A New Integrated Finite Volume–Finite Volume Hydrodynamic Modelling Framework for Wave-Structure Interactions

Ranjodh Singh Rai

PhD 2023

A New Integrated Finite Volume–Finite Volume Hydrodynamic Modelling Framework for Wave-Structure Interactions

Ranjodh Singh Rai

A thesis submitted in partial fulfilment of the requirements of the Manchester Metropolitan University for the degree of Doctor of Philosophy

Department of Computing and Mathematics

Manchester Metropolitan University

2023

Abstract

This thesis presents a new integrated hydrodynamic modelling framework for and long-time and large-scale wave-structure interaction problems. It is developed by coupling a finite-volume-based fully-nonlinear potential-flow (FNPF) solver with the native OpenFOAM incompressible 'interFoam' solver in a numerical wave tank (NWT). This new model, named IntegratedFoam, has the primary advantage that each constituent solver has been developed in the same numerical framework (OpenFOAM), and consequently, are both also based on the same numerical method, i.e., the finite-volume method (FVM). Consequently, the method for transferring information is made simple and the coupling stable. Indeed, the coupling procedure follows a domain decomposition approach in which an overlapping relaxation zone is utilised to implement a one-way coupling. Hence, given that both solvers have been developed in OpenFOAM and are finite-volume-based, only a method to calculate the volume fraction from the free-surface elevation needs to be implemented: the velocity and pressure are already calculated as part of the FNPF solution and can be transferred accordingly in one direction—simplifying things greatly and avoiding unwanted errors. In addition, existing advanced OpenFOAM functionalities can be used for the required interpolation—easily addressing the problem of nonconforming meshes. These functionalities then also allow for the easy implementation of an overlapping relaxation zone which is key to a stable coupling because it ensures that there is a smooth transition from the FNPF to interFoam solution. Without it, there is a danger of there being a lack of continuity between each solution due the underlying physics of each solver being different. This could potentially then lead to errors and subsequently make the coupling unstable. Moreover, this zone also absorbs any reflected waves in the NWT, again aiding stability. In conjunction with the development of this new integrated model, a new stabilisation method for finite-volume or finite-difference FNPF models, motivated by a total variation diminishing (TVD) approach, is also presented.

The accuracy and efficiency of the new IntegratedFoam model are then systematically validated through a series of wave propagation and wave-structure interaction test cases. In particular, the sensitivity of the model to its main coupling parameters is first assessed through fifth-order Stokes wave propagation. The model is then applied to a number of test cases involving wave interaction with offshore structures: fifth-order Stokes waves interaction with a 2-D T-shaped floating body acting as simplified midship section with superstructure, focused wave

interaction with a fixed 3-D cylinder acting as a simplified monopile foundation, and focused wave interaction with a 3-D wave energy converter (WEC) device. It is shown to produce accurate numerical solutions that agree well with existing theoretical results and experimental data, all whilst significantly improving computational efficiency. Therefore, given that OpenFOAM is open source, the new integrated model can readily be used by researchers as a more efficient model for complex wave-structure interaction problems than interFoam. The new stabilisation method is then also systematically validated through fifth-order Stokes wave propagation, focused wave propagation, and wave shoaling. Again, it is shown to produce accurate numerical solutions that agree well with existing theoretical results and experimental data, all whilst reducing excessive numerical dissipation and thus significantly improving energy conservation.

Acknowledgements

I'd first like to thank my supervisor Dr Zhihua Ma. He's always been on hand for help, guidance, and general encouragement. For that, I'm grateful. I'd also like to thank my other supervisors, Dr Wei Bai and Professor Ling Qian, whose advice is always appreciated. Special mention also goes to Dr Zaibin Lin, whose advice and guidance on OpenFOAM was essential to this project. Thank you to you all.

I'd also like to thank all my friends who encouraged me and have always been a source of comfort and relief. Special mention to Georgie, who has always provided love and support. Thanks for also always showing an interest, even if you may not have had a clue what I was going on about. Honourable mention goes to Sahara and Edd. Not entirely sure why.

Thanks to my sister Jasbir for the grammatical advice, I hope all hyphens are in the right place! Thanks also to my brother Steve. I think you quizzing me about my proficiency in Maths as a 10-year-old may have sparked something...

Finally, I'd like to most of all thank me mother and father. Their constant encouragement to be 'as educated as possible' is ultimately what led me here. Without them, this would never have been possible.

Contents

Abstract **2**

Acknowledgements **3**

List of Figures **14**

List of Tables **16**

1 Introduction **17**

1.1 Background . . . 18

1.1.1 Global outlook for electricity generation . . . 18

1.1.2 Offshore renewable energy in the United Kingdom . . . 19

1.1.3 Challenges faced by offshore renewables . . . 21

1.2 Hydrodynamic modelling for wave-structure interaction . . . 22

1.3 Fully-nonlinear potential-flow models . . . 23

1.3.1 Numerical methods . . . 24

1.3.2 Stabilisation techniques for FNPF models . . . 26

1.4 Navier-Stokes models . . . 28

1.5 Integrated/Hybrid Models . . . 29

1.5.1 Domain decomposition . . . 30

1.5.2 Functional decomposition . . . 33

1.5.3 Important considerations . . . 34

1.6 OpenFOAM . . . 35

1.7 Objectives and contributions of the present work . . . 36

1.7.1 Development a new integrated hydrodynamic model . . . 36

1.7.2 Introduction of a new stabilisation technique for FNPF models . . . 38

1.8 Outline of the remainder of the thesis . . . 38

2 Incompressible Two-Phase Navier-Stokes Model **40**

2.1 Volume-of-fluid method . . . 41

2.1.1 Governing equations . . . 41

2.1.2 Indicator function . . . 41

2.1.3 Final formulation . . . 42

2.2 Finite-volume method . . . 42

2.2.1 Spatial and temporal discretisation . . . 42
2.2.2 Equation discretisation . . . 44
2.3 Finite-volume formulation and solution procedure for the Navier-Stokes system . 48
2.3.1 Equation discretisation . . . 48
2.3.2 Boundary conditions . . . 49
2.3.3 Solution procedure . . . 50
2.4 Dynamic mesh . . . 53
2.4.1 Equation formulation . . . 53
2.4.2 Rigid-body motion solver . . . 54

3 Fully-Nonlinear Potential-Flow Model Based on the Finite-Volume Method 56
3.1 Methodology of the original FNPF model . . . 57
3.1.1 Mathematical formulation of the boundary-value problem . . . 57
3.1.2 Numerical implementation . . . 59
3.2 Hypothesis on why the sawtooth instability occurs in the Lin FNPF model . . . 61
3.3 Computational formulation of the new TVD-based scheme . . . 62
3.3.1 Updating the free-surface variable η in time . . . 62
3.3.2 TVD property . . . 63
3.3.3 Flux limiter . . . 64
3.3.4 Final formulation . . . 66
3.4 Validation of the new stabilised model . . . 66

4 Integrated Methodology 68
4.1 Advantages of the proposed integrated model . . . 69
4.1.1 Implementation of an overlapping relaxation zone . . . 69
4.1.2 Handling a mismatch in variables . . . 69
4.1.3 Handling non-conforming meshes . . . 70
4.1.4 Handling of mismatching time steps . . . 71
4.2 Coupling procedure . . . 71
4.2.1 Transferring $\mathbf{u}$ and p . . . 71
4.2.2 Estimating the water-volume fraction α from the free-surface variable η . . . 72
4.2.3 Relaxation correction and damping . . . 73
4.3 Computational procedure . . . 74
4.4 Parallelisation . . . 75
4.5 Validation of IntegratedFoam . . . 75

5 Regular and Extreme Wave Propagation 76
5.1 Wave theories . . . 77
5.1.1 Regular wave characteristics . . . 77
5.1.2 Stokes wave theory . . . 78

5.1.3 Irregular random waves . . . 80
5.1.4 Focused waves . . . 81
5.2 Stabilised FNPF model . . . 83
5.2.1 Regular fifth-order Stokes wave propagation . . . 83
5.2.2 Energy considerations . . . 83
5.2.3 Mesh sensitivity . . . 87
5.2.4 Temporal sensitivity . . . 90
5.2.5 Choice of flux limiter . . . 94
5.2.6 Focused wave propagation . . . 97
5.3 IntegratedFoam . . . 100
5.3.1 Testing the length of relaxation and damping zones Ω_{OZ} and Ω_{DZ} . . . 100
5.3.2 Mesh sensitivity . . . 115
5.3.3 Temporal sensitivity . . . 119

6 Wave-Structure Interaction 126
6.1 Wave shoaling . . . 127
6.1.1 2-D wave shoaling . . . 127
6.1.2 3-D wave shoaling . . . 131
6.2 Regular wave interaction with a 2-D floating body . . . 133
6.2.1 Geometric and computational setups . . . 133
6.2.2 Numerical results . . . 134
6.3 Focused wave-interaction with a fixed cylinder . . . 137
6.3.1 Experimental setup . . . 137
6.3.2 Geometric setup . . . 138
6.3.3 Case 1 . . . 140
6.3.4 Case 3 . . . 150
6.4 Focused wave-interaction with a point absorber wave energy converter . . . 161
6.4.1 Experimental setup . . . 161
6.4.2 Geometric setup . . . 163
6.4.3 Computational setup for Ω_{FNPF} . . . 164
6.4.4 Computational setup for Ω_{NS} . . . 167
6.4.5 Setup of remaining computational parameters . . . 170
6.4.6 Numerical results . . . 170

7 Conclusion 175
7.1 Summary of research outcomes . . . 176
7.1.1 Development and validation of a new finite volume–finite volume integrated hydrodynamic model . . . 176
7.1.2 Introduction of a new stabilisation technique for FNPF models . . . 178
7.2 Recommendations for future work . . . 179

Bibliography **180**

A Publications **195**

List of Figures

1.1 Gross electricity generated by source from 1974–2020 by OECD countries. Figure from the International Energy Agency (IEA (2021) [71]). 19

1.2 Floating offshore wind turbine designs by Equinor: spar-substructure foundation (left), semi-submersible foundation (right). Image by Equinor ASA (Equinor (2021) [41]). 20

2.1 Example OpenFOAM control volumes with key mesh parameters 43

3.1 Schematic of a three-dimensional numerical wave tank. 57

3.2 Lin model computational procedure (without numerical damping). 60

3.3 (a) TVD region for the flux limiter function $\psi(r)$, (b) First and second-order regions, (c) Popular functions. 65

4.1 Example 2-D IntegratedFoam domain. 72

4.2 IntegratedFoam computational procedure. 74

5.1 Time histories of free-surface elevation for the stabilised model, Lin et al. (2021) [90] model, and analytical fifth-order Stokes solution at various wave gauges in the numerical wave tank. Please note that the upper limits of the time intervals in these panels are not the same. 84

5.2 (a) Time histories of free-surface elevation for the stabilised model, Lin et al. (2021) [90] model, and fifth-order Stokes solution at WG1 = 430 m. (b) Time histories of total energy E_T in the damping zone of the numerical wave tank for the stabilised model and Lin et al. (2021) [90] model. (c) Time histories of total energy E_T in the middle portion of the numerical wave tank for the stabilised model and Lin et al. (2021) [90] model. 86

5.3 Time histories of free-surface elevation for meshes C and E at wave gauge 2 (WG2), along with the analytical fifth-order Stokes wave solution: (a) $t/T \in [0, 20]$, (b) $t/T \in [15, 20]$. 88

5.4 Time histories of free-surface elevation for meshes C and E at wave gauge 5 (WG5), along with the analytical fifth-order Stokes wave solution: (a) $t/T \in [10, 20]$, (b) $t/T \in [45, 50]$. 89

5.5 Time histories of free-surface elevation for meshes A, B, C and D at wave gauge 2 (WG2), along with the analytical fifth-order Stokes wave solution: (a) $t/T \in [0, 20]$, (b) $t/T \in [15, 20]$. 89
5.6 Time histories of free-surface elevation for meshes A, B, C and D at wave gauge 5 (WG5), along with the analytical fifth-order Stokes wave solution: (a) $t/T \in [10, 50]$, (b) $t/T \in [45, 50]$. 90
5.7 (a) Time histories of free-surface elevation for $C_{\max} = 0.05$, 0.1, 0.2, and 0.4 at wave gauge 2 (WG2) in $t/T \in [10, 20]$, along with the analytical fifth-order Stokes solution. (b) Normalised crest amplitude error e^a_{crest}, (c) normalised trough amplitude error e^a_{trough}, (d) normalised crest phase shift e^θ_{crest}, and (e) normalised trough phase shift e^θ_{trough} for $C_{\max} = 0.05$, 0.1, 0.2, and 0.4 at WG2 in $t/T \in [10, 20]$. 92
5.8 (a) Time histories of free-surface elevation for $C_{\max} = 0.05$, 0.1, 0.2, and 0.4 at wave gauge 5 (WG5) in $t/T \in [30, 50]$, along with the analytical fifth-order Stokes solution. (b) Normalised crest amplitude error e^a_{crest}, (c) normalised trough amplitude error e^a_{trough}, (d) normalised crest phase shift e^θ_{crest}, and (e) normalised trough phase shift e^θ_{trough} for $C_{\max} = 0.05$, 0.1, 0.2, and 0.4 at WG5 in $t/T \in [30, 50]$. 93
5.9 Time histories of free-surface elevation for the first-order upwind scheme (FOU), the Min-mod (MM), Van Leer (VL), Van Albada 1 (VA1), Van Albada 2 (VA2), and SuperBee (SB) limiters at wave gauge 2 (WG2), along with the analytical fifth-order Stokes solution: (a) $t/T \in [0, 20]$, (b) $t/T \in [15, 20]$, (c) $t/T \in [17.5, 18.5]$. 95
5.10 Time histories of free-surface elevation for the first-order upwind scheme (FOU), the Min-mod (MM), Van Leer (VL), Van Albada 1 (VA1), Van Albada 2 (VA2), and SuperBee (SB) limiters at wave gauge 5 (WG5), along with the analytical fifth-order Stokes solution: (a) $t/T \in [30, 50]$, (b) $t/T \in [45, 50]$, (c) $t/T \in [47.5, 48.5]$. 96
5.11 Time histories of free-surface elevation at the input focus location x_0 for different mesh configurations and experimental solution from Ning et al. (2009) [111]. . . 98
5.12 (a.) Free-surface profile at input focus time t_0 and real focus time t_1. (b.) Time histories of free-surface elevation at input focus location x_0 and real focus location x_1. (c.) Time histories of free-surface elevation at real focus location x_1 and experimental solution from Ning et al. (2009) [111]. 99
5.13 Schematic in the xy-plane of the reference IntegratedFoam numerical wave tank used in the long case (not to scale). All dimensions are in meters. 102
5.14 Time histories of free-surface elevation for Ω_{OZ} lengths $1/2\lambda$, λ, and 2λ, and FNPFFoam at wave gauges 1–4 (WGs 1–4) in the long case numerical wave tank. 104

5.15 Time histories of free-surface elevation for Ω_{OZ} lengths $1/2\lambda$, λ, and 2λ, and FNPFFoam at wave gauge 1 (WG1) in the long case: (a) $t/T \in [14, 19]$, (b) $t/T \in [24, 29]$, (c) $t/T \in [33, 38]$. 105
5.16 Time histories of free-surface elevation for Ω_{OZ} lengths $1/2\lambda$, λ, and 2λ, and FNPFFoam at wave gauge 2 (WG2) in the long case: (a) $t/T \in [15, 20]$, (b) $t/T \in [24, 29]$, (c) $t/T \in [33, 38]$. 105
5.17 Time histories of free-surface elevation for Ω_{OZ} lengths $1/2\lambda$, λ, and 2λ, and FNPFFoam at wave gauge 3 (WG3) in the long case: (a) $t/T \in [16, 21]$, (b) $t/T \in [24, 29]$, (c) $t/T \in [33, 38]$. 106
5.18 Time histories of free-surface elevation for Ω_{OZ} lengths $1/2\lambda$, λ, and 2λ, and FNPFFoam at wave gauge 4 (WG4) in the long case: (a) $t/T \in [17, 22]$, (b) $t/T \in [24, 29]$, (c) $t/T \in [33, 38]$. 106
5.19 Time histories of free-surface elevation for Ω_{DZ} lengths $1/2\lambda$, λ, and 2λ, and FNPFFoam at wave gauges 1–4 (WGs 1–4) in the long case numerical wave tank. 108
5.20 Time histories of free-surface elevation for Ω_{DZ} lengths $1/2\lambda$, λ, and 2λ, and FNPFFoam at wave gauge 1 (WG1) in the long case: (a) $t/T \in [14, 19]$, (b) $t/T \in [24, 29]$, (c) $t/T \in [33, 38]$. 109
5.21 Time histories of free-surface elevation for Ω_{DZ} lengths $1/2\lambda$, λ, and 2λ, and FNPFFoam at wave gauge 2 (WG2) in the long case: (a) $t/T \in [15, 20]$, (b) $t/T \in [24, 29]$, (c) $t/T \in [33, 38]$. 109
5.22 Time histories of free-surface elevation for Ω_{DZ} lengths $1/2\lambda$, λ, and 2λ, and FNPFFoam at wave gauge 3 (WG3) in the long case: (a) $t/T \in [16, 21]$, (b) $t/T \in [24, 29]$, (c) $t/T \in [33, 38]$. 110
5.23 Time histories of free-surface elevation for Ω_{OZ} lengths $1/2\lambda$, λ, and 2λ, and FNPFFoam at wave gauge 4 (WG4) in the long case: (a) $t/T \in [17, 22]$, (b) $t/T \in [24, 29]$, (c) $t/T \in [33, 38]$. 110
5.24 Time histories of free-surface elevation for Ω_{OZ} lengths $1/2\lambda$, λ, and 2λ, and FNPFFoam at wave gauge (WG) $x = 64$ m in the short case numerical wave tank: (a) $t/T \in [10, 39]$, (b) $t/T \in [18, 23]$, (c) $t/T \in [25, 30]$, (d) $t/T \in [33, 38]$. 113
5.25 Time histories of free-surface elevation for Ω_{DZ} lengths $1/2\lambda$, λ, and 2λ, and FNPFFoam at wave gauge (WG) $x = 64$ m in the short case numerical wave tank: (a) $t/T \in [10, 39]$, (b) $t/T \in [18, 23]$, (c) $t/T \in [25, 30]$, (d) $t/T \in [33, 38]$. 114
5.26 Time histories of free-surface elevation for meshes IntegratedFoam A, B, C, and D, and FNPFFoam at wave gauge 1–4 (WGs 1–4). 116
5.27 Time histories of free-surface elevation for IntegratedFoam meshes A, B, C, and D, and FNPFFoam at wave gauge 1 (WG1): (a) $t/T \in [14, 19]$, (b) $t/T \in [24, 29]$, (c) $t/T \in [33, 38]$. 117

5.28 Time histories of free-surface elevation for IntegratedFoam meshes A, B, C, and D, and FNPFFoam at wave gauge 2 (WG2): (a) $t/T \in [15, 20]$, (b) $t/T \in [24, 29]$, (c) $t/T \in [33, 38]$. 117
5.29 Time histories of free-surface elevation for IntegratedFoam meshes A, B, C, and D, and FNPFFoam at wave gauge 3 (WG3): (a) $t/T \in [16, 21]$, (b) $t/T \in [24, 29]$, (c) $t/T \in [33, 38]$. 118
5.30 Time histories of free-surface elevation for IntegratedFoam meshes A, B, C, and D, and FNPFFoam at wave gauge 4 (WG4): (a) $t/T \in [17, 22]$, (b) $t/T \in [24, 29]$, (c) $t/T \in [33, 38]$. 118
5.31 Relationship between the number of mesh cells in meshes A, B, C, and D, and computational time: (a) Coupling, (b) interFoam and Total. Note that the number of mesh cells for the coupling is less so the x-axis limits are different. However, the y-axis has the same limits, so the proportion of actual time taken by each part of the solver is illustrated to scale. 119
5.32 Normalised crest and trough amplitude errors ϵ^a_{crest} and ϵ^a_{trough} for $C_{\max} = 0.05$, 0.1, 0.2, and 0.4 at wave gauges 1–4 (WGs 1–4) in the long case. 121
5.33 Normalised crest and trough phase shifts ϵ^θ_{crest} and ϵ^θ_{trough} for $C_{\max} = 0.05$, 0.1, 0.2, and 0.4 at wave gauges 1–4 (WGs 1–4) in the long case. 122
5.34 (a) Relationship between $C_{\max}$ and computational time for different parts of the IntegratedFoam model. (b) Relationship between number for time steps N and computational time for differing values of $C_{\max}$ and for different parts of the IntegratedFoam model. 123
5.35 Normalised crest and trough amplitude errors ϵ^a_{crest} and ϵ^a_{trough} for $C_{\max} = 0.05$, 0.1, 0.2, and 0.4 at wave gauge (WG) $x = 64$ m in the short case. 124
5.36 Normalised crest and trough phase shifts ϵ^θ_{crest} and ϵ^θ_{trough} for $C_{\max} = 0.05$, 0.1, 0.2, and 0.4 at wave gauge (WG) $x = 64$ m in the short case. 125

6.1 Sketch of numerical wave tank for the 2-D wave shoaling test case (not to scale). 128
6.2 Time histories of free-surface elevation for the stabilised model, Lin et al. (2021) [90] model, and experimental solution of Beji and Battjes (1994) [4] at various wave gauges in the NWT for input B1. 129
6.3 Time histories of free-surface elevation for the stabilised model, Lin et al. (2021) [90] model, and experimental solution of Beji and Battjes (1993) [3] at various wave gauges in the NWT for input B2. 130
6.4 Harmonic components of numerical results from the stabilised model, Shao and Faltinsen (2014) [123], Engsig-Karup et al. (2009) [37], and experimental results of Whalin (1971) [143] at the streamwise central line of the NWT: (a.) input W1, (b.) input W2, (c.) input W3. 132

6.5 Snapshots of the free surface for input W3 at times (a.) 11 seconds (s), (b.) 16 s, (c.) 21 s, and (d.) 31 s. (Not to scale—exaggerated 20 times in the y-direction).132
6.6 Schematic of the 2-D numerical wave tank in the floating body test case (not to scale). The black cross marks the centre of rotation and the dot marks the centre of mass. All dimensions are in meters. 133
6.7 Time histories of (a) roll motion, (b) heave motion, and (c) free-surface elevation for IntergratedFoam, interFoam, the experimental Zhao and Hu solution [153], and the numerical Zhao and Hu solution [153]. 135
6.8 Time histories of pressure, measured 0.01 m above deck, for IntegratedFoam, interFoam, the experimental Zhao and Hu solution [153], and the numerical Zhao and Hu solution [153]. 136
6.9 Schematic in the xy-plane of the IntegratedFoam numerical wave tank used in the fixed cylinder test cases (not to scale). The black rectangle represents the cylinder and all dimensions are in meters. 139
6.10 (a) Schematic in the xz-plane of Ω_{NS}, and locations of wave gauges 5–7, in the fixed cylinder test cases. All dimensions in meters. (b) Locations of all pressure gauges on the surface of the cylinder. The dashed line indicates the still water level $y = 0$. 139
6.11 Case 1 FNPFFoam time histories of free-surface elevation for meshes A and B at wave gauge 4 (WG4), along with the experimental solution of Sriram et al. (2021) [126]: (a) $t \in [20,\ 50]$, (b) $t \in [30,\ 36]$. 141
6.12 Case 1 FNPFFoam time histories of free-surface elevation for meshes A and B at wave gauge 5 (WG5), along with the experimental solution of Sriram et al. (2021) [126]: (a) $t \in [20,\ 50]$, (b) $t \in [36,\ 42]$. 142
6.13 Case 1 FNPFFoam time histories of free-surface elevation for meshes C, B, and D at wave gauge 4 (WG4), along with the experimental solution of Sriram et al. (2021) [126]: (a) $t \in [20,\ 50]$, (b) $t \in [30,\ 36]$. 142
6.14 Case 1 FNPFFoam time histories of free-surface elevation for meshes C, B, and D at wave gauge 5 (WG5), along with the experimental solution of Sriram et al. (2021) [126]: (a) $t \in [20,\ 50]$, (b) $t \in [36,\ 42]$. 143
6.15 Initially constructed Ω_{NS} mesh in the xz-plane (A and B) and the xy-plane (C). 144
6.16 Case 1 IntegratedFoam time histories of free-surface elevation for meshes E, F, G, and H at wave gauge 5 (WG5), along with the experimental solution of Sriram et al. (2021) [126]: (a) $t \in [20,\ 55]$, (b) $t \in [36,\ 42]$, (c) $t \times \eta \in [38.8,\ 39.4] \times [0.04,\ 0.05]$.144
6.17 Case 1 IntegratedFoam time histories of free-surface elevation for meshes I, F, and J at wave gauge 5 (WG5), along with the experimental solution of Sriram et al. (2021) [126]: (a) $t \in [20,\ 55]$, (b) $t \in [36,\ 42]$, (c) $t \times \eta \in [38.8,\ 39.4] \times [0.04,\ 0.05]$.146
6.18 Final Ω_{NS} mesh in the xz-plane for Case 1. 146

6.19 Case 1 time histories of free-surface elevation for IntegratedFoam, and the experimental solution of Sriram et al. (2021) [126], at wave gauges 5–7 (WG5–WG7). . 148
6.20 Case 1 time histories of body-surface pressure for IntegratedFoam, and the experimental solution of Sriram et al. (2021) [126], at pressure gauges 2–8 (PG2–PG8).149
6.21 Case 3 FNPFFoam time histories of free-surface elevation for meshes A, B, C, and D at wave gauge 4 (WG4), along with the experimental solution of Sriram et al. (2021) [126]: (a) $t \in [20, 50]$, (b) $t \in [28, 36]$. 151
6.22 Case 3 IntegratedFoam time histories of free-surface elevation for meshes A, B, C, and D at wave gauge 5 (WG5) in Ω_{FNPF}, along with the experimental solution of Sriram et al. (2021) [126]: (a) $t \in [20, 50]$, (b) $t \in [36, 42]$, (c) $t \times \eta \in [38.6, 39.2] \times [0.12, 0.22]$. 152
6.23 Case 3 IntegratedFoam time histories of free-surface elevation for meshes E, F, G, and H at wave gauge 5 (WG5) in Ω_{NS}, along with the experimental solution of Sriram et al. (2021) [126]: (a) $t \in [20, 55]$, (b) $t \in [36, 42]$, (c) $t \times \eta \in [38.6, 39.2] \times [0.12, 0.22]$. 153
6.24 Final Ω_{NS} mesh for Case 3 in the xz-plane (A, B, C, and E) and the xy-plane (D).154
6.25 Case 3 time histories of free-surface elevation for IntegratedFoam, and the experimental solution of Sriram et al. (2021) [126], at wave gauges 5–7 (WG5–WG7). . 156
6.26 Case 3 time histories of body-surface pressure for IntegratedFoam, and the experimental solution of Sriram et al. (2021) [126], at pressure gauges 2–8 (PG2–PG8).157
6.27 Snapshots of the free-surface profile at $t = 38.75$, 38.9, 39.05, and 39.2 s in Case 3. The wave propagates from left to right. Left panel: front left view. Right panel: rear left view. 158
6.28 Snapshots of the free-surface profile at $t = 39.4$, 39.75, and 40 s in Case 3. The wave propagates from left to right. Left panel: front left view. Right panel: rear left view. 159
6.29 Snapshots of free-surface velocity magnitude at $t = 38.75$, 39.2, and 39.75 s in Case 3. The wave propagates from left to right. Left panel: front left view. Right panel: rear left view. 160
6.30 Schematic in the xy-plane of the hemispherical-bottomed wave energy converter (WEC). All dimensions are in metres. 162
6.31 Schematic in the xy-plane of the IntegratedFoam numerical wave tank used in the wave energy converter (WEC) test case (not to scale). All dimensions are in metres. 164
6.32 Schematic in the xz-plane of Ω_{NS} in the wave energy converter (WEC) test case (not to scale). All dimensions in metres. 164
6.33 FNPFFoam time histories of free-surface elevation for meshes A, B, and C at wave gauge 5 (WG5), along with the experimental solution from CCP-WSI (2020) [15]: (a) $t \in [35, 55]$, (b) $t \in [40, 50]$. 165

6.34 FNPFFoam time histories of free-surface elevation using mesh B at wave gauges (WGs) 1, 3, 5, and 8, along with the experimental solution from CCP-WSI (2020) [15]. 166
6.35 Initial background Ω_{NS} mesh in the xy-plane (A) and the xz-plane (B) in the wave energy converter (WEC) test case. 167
6.36 Wave energy converter (WEC) mesh. 168
6.37 Cross section (in the xy-plane) of the final constructed mesh in a small region around the wave energy converter (WEC). 168
6.38 IntegratedFoam time histories of free-surface elevation for meshes D, E, and F at wave gauge 5 (WG5), along with the experimental solution from CCP-WSI (2020) [15]: (a) $t \in [35, 55]$, (b) $t \in [40, 50]$. 169
6.39 IntegratedFoam time histories of surge displacement (a), heave displacement (b), pitch angle (c), and mooring force magnitude (d) of the WEC, along with the experimental solution from CCP-WSI (2020) [15]. Initial attempt. 171
6.40 Time histories of free-surface elevation and the experimental solution from CCP-WSI (2020) [15] at wave gauge 5 (WG5). 171
6.41 IntegratedFoam time histories of sway displacement (a) and yaw angle (b) of the WEC in the initial attempt. 172
6.42 IntegratedFoam time histories of surge displacement (a), heave displacement (b), pitch angle (c), and mooring force magnitude (d) of the WEC, along with the experimental solution from CCP-WSI (2020) [15]. Refined attempt. 173

List of Tables

2.1 Name of OpenFOAM boundary conditions used for interFoam in the present work. 49

3.1 Expressions for some popular flux limiter functions. 65

5.1 Fifth-order Stokes wave coefficients 79
5.2 Wave parameters for the generated fifth-order Stokes waves. 83
5.3 Mesh configurations used in mesh sensitivity studies for the stabilised model. . . 88
5.4 Time taken by the stabilised model for each value of $C_{\max}$. 94
5.5 Input wave parameters for cases NING1 and NING3: Input focused wave parameters for the WEC test case: f_p is the peak frequency, T_p is the characteristic wave period, A_I is the input focused wave amplitude, and λ_p is the characteristic wavelength. 97
5.6 Dimensions of numerical wave tank for cases NING1 and NING3. 97
5.7 Input and actual focusing properties for cases NING1 and NING3. 97
5.8 Mesh configurations used in mesh sensitivity study for case NING1. 98
5.9 Wave parameters for the generated fifth-order Stokes waves. 101
5.10 Wave gauge locations in the long case. 102
5.11 Lengths of Ω_{OZ}, dimensions of Ω_{OZ}, corresponding dimensions of Ω_{NS}, and corresponding mesh configurations of Ω_{NS} in the long case. 103
5.12 Lengths of Ω_{DZ}, dimensions of Ω_{DZ}, corresponding dimensions of Ω_{NS}, and corresponding mesh configurations of Ω_{NS} in the long case. 103
5.13 Time taken by different parts of the solver for each Ω_{OZ} length in the long case. 107
5.14 Time taken by interFoam for each Ω_{DZ} length in the long case. 111
5.15 Lengths of Ω_{OZ}, dimensions of Ω_{OZ}, corresponding dimensions of Ω_{NS}, and corresponding mesh configurations of Ω_{NS} in the short case. 111
5.16 Lengths of Ω_{DZ}, dimensions of Ω_{DZ}, corresponding dimensions of Ω_{NS}, and corresponding mesh configurations of Ω_{NS} in the short case. 111
5.17 Time taken by different parts of the solver for each Ω_{OZ} length in the short case. 112
5.18 Time taken by interFoam for each Ω_{DZ} length in the short case. 112
5.19 Mesh configurations used in mesh sensitivity studies for IntegratedFoam. 115
5.20 Time taken by different parts of the solver for meshes A, B, C, and D. 116
5.21 Time taken by different parts of the solver for each value of $C_{\max}$ in the long case. 123
5.22 Time taken by different parts of the solver for each value of $C_{\max}$ in the short case. 125

6.1 Wave parameters for 2-D and 3-D shoaling cases. 128
6.2 Mesh configurations for 2-D and 3-D shoaling cases 128
6.3 Wave parameters for the generated fifth-order Stokes waves. 134
6.4 Mechanical Characteristics of the 2-D floating body. 134
6.5 Time taken by different parts of the solver in 2-D floating body case. 136
6.6 Input focused wave parameters for the fixed cylinder test cases. 138
6.7 Wave gauge locations in the fixed cylinder test cases. Note that wave gauge 4 is only in Ω_{FNPF}. 139
6.8 Pressure gauge locations on the surface of the cylinder. 139
6.9 Dimensions of each domain and zone in the fixed cylinder test cases. 140
6.10 Mesh configurations used in mesh sensitivity studies for Case 1. 140
6.11 Time taken by different parts of the solver in Case 1. 147
6.12 Mesh configurations used in mesh sensitivity studies for Case 3. 150
6.13 Time taken by different parts of the solver in Case 3. 155
6.14 Mechanical Characteristics of the hemispherical-bottomed wave energy converter (WEC). 162
6.15 Input focused wave parameters for the wave energy converter (WEC) test case: A_I is the input focused wave amplitude, f_p is the peak frequency, H_s is the significant wave height, x_f is the focusing location, and t_f is the focusing time. . 163
6.16 Wave gauge locations in the WEC test case. Note that wave gauge 5 is the focusing location. 163
6.17 Dimensions of each domain and zone in the WEC test case. 164
6.18 Mesh configurations used in empty-tank Ω_{FNPF} mesh sensitivity studies in the wave energy converter (WEC) case. 165
6.19 Mesh configurations used in empty-tank Ω_{NS} mesh sensitivity studies in the wave energy converter (WEC) case. 169
6.20 Time taken by different parts of the solver in the wave energy converter (WEC) test case. 173

1

Introduction

1.1 Background

1.1.1 Global outlook for electricity generation

Electrical power generation is arguably the bedrock of modern industrial society. Traditionally, since the time of the second industrial revolution, the majority of demand for this power has been met by burning fossil fuels, such as coal, oil, and more recently natural gas. However, these are finite and polluting resources; their use has done irreparable damage to our planet and has been the majority contributing factor to global greenhouse gas emissions. The Intergovernmental Panel on Climate Change (IPCC) recently stated that, 'More than a century of burning fossil fuels as well as unequal and unsustainable energy and land use has led to global warming of 1.1°C above pre-industrial levels' (Intergovernmental Panel on Climate Change (2023) [20]). It is due to this dangerous level of warming that 194 nation states and the European Union came together in 2015 to sign the landmark Paris Agreement (United Nations (2015) [108]). This legally binding international treaty compelled nations to limit the increase in global temperatures to 'well below' 2°C above pre-industrial levels whilst also endeavouring to limit the rise to just 1.5°C above pre-industrial levels. To achieve this, the parties agreed on the need to reach 'net-zero' greenhouse gas emissions by the year 2050 with at least a 45% reduction in emissions by 2030.

The primary anthropogenic greenhouse gas that accounts for the largest proportion of emissions is carbon dioxide (CO_2), and approximately one third of CO_2 emissions globally comes from electricity generation (IEA (2022) [72]). This means that decarbonising electricity generation is the key objective on the road to net zero by 2050. Consequently, low-carbon—and specifically renewable—sources of energy have become more prominent around the world, with the accompanying economic opportunities presented by green industry becoming a major part of future industrial strategies of nation states. Many different sources of renewable energy have been explored to varying degrees of success. Hydropower has long been the worlds largest and most successful, with Three Gorges Dam in China even being the largest electrical power station of any type in the world with an installed capacity of 22,500 megawatts (MW) (Brittanica (2023) [12]). However, in recent years, wind and solar have become more prominent, and in 2022 they were estimated to account for approximately 12% of all electricity generated. They are also the fasting growing forms of energy, with installed capacity increasing 17% and 24% respectively from 2021 to 2022 (Ember (2023) [34]). Other forms—such as geothermal, tidal, and biomass—have also been explored. Figure 1.1 from the International Energy Agency (IEA (2021) [71]) shows the gross electricity generated by source as a percentage of total electricity from 1974–2020 by OECD countries. There is a clear uptick in renewable energy—solar, wind, geothermal, etc.—from 2.4% in 2008 to 13.4% in 2020. Moreover, this is accompanied by a significant downward trend in the use of coal, the most polluting fossil fuel, from a peak of 42.6% in 1985 to just 19.3% in 2020. Ultimately, the success of any form of renewable energy will

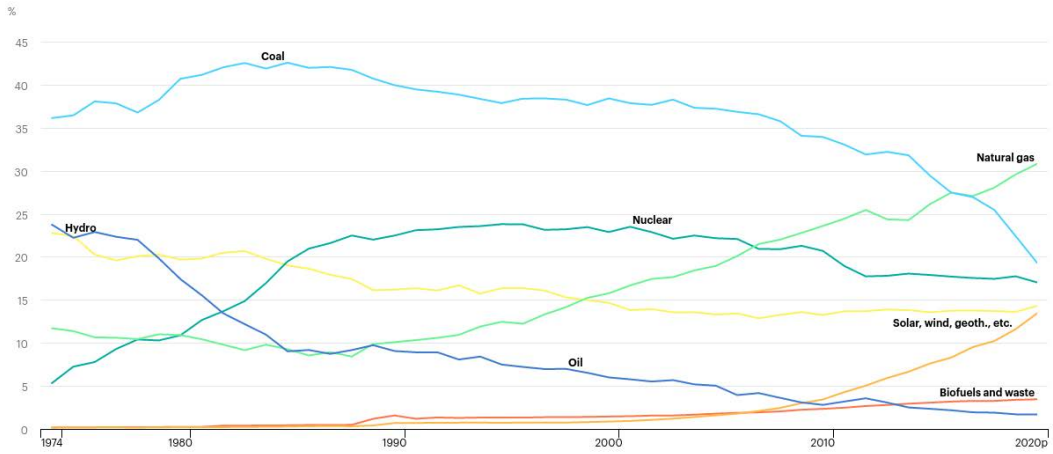

Figure 1.1: Gross electricity generated by source from 1974–2020 by OECD countries. Figure from the International Energy Agency (IEA (2021) [71]).

come down to practical, and financial, viability and sustainability, meaning that technological advancements through research and development are key to the driving up efficiency for success in the future.

1.1.2 Offshore renewable energy in the United Kingdom

One proven source of renewable energy is the marine environment. For example, most wind energy installations globally have customarily been onshore, but in recent years, offshore installations have markedly increased. In 2019, offshore wind accounted for 29 out of 651 gigawatts (GW) total installed capacity globally—approximately 4.5% (Global Wind Energy Council (2022) [24]). However, by 2023, offshore accounted for 64.3 out of 906.3 GW total installed capacity—approximately 7.1% (Global Wind Energy Council (2023) [25]). This increase can in part be explained by the fact that offshore wind holds a significant advantage over its onshore counterpart in that the wind resource in the ocean environment tends to be much larger and more consistent, in turn making electricity generation more efficient. The recognition of this fact has meant substantial investment has gone into developing new technologies, leading to a gradual increase in share of total capacity.

The United Kingdom (UK) is very much a leader in offshore wind; it is second only to China as the largest offshore wind market globally and is comfortably the largest in Europe. In 2023, the UK had 21.6% (13.9 GW) of global capacity installed in its waters, generating 13.8% (45 terrawatt hours (TWh)) of all electricity in the UK in 2022 (Department for Energy Security and Net Zero (2023) [36]). This was aided by the worlds largest offshore wind farm, Hornsea 2, becoming fully operational in August 2022 with an installed capacity of 1.3 GW. In April 2022, the UK government announced that it will be targeting an installed capacity of 50 GW by 2030, part of the wider pledge to be carbon neutral by 2050. An additional target to deliver up to 5 GW of electricity from *floating* offshore wind by 2030 was also introduced. In 2020 the

Global Wind Energy Council estimated that 80% of global offshore wind resource lies in waters deeper than 60 metres (m), whereas almost all development up until now has been bottom fixed structures in waters less than 60 m deep (Global Wind Energy Council (2020) [23]). This highlights the huge potential for floating offshore wind, and the UK's target clearly demonstrates their recognition of this. However, many practical and financial challenges currently hinder the development of new floating technologies and subsequent large scale construction of farms, meaning extensive research and development is still required to help hit targets. Nevertheless, the potential of floating win can be seen in the worlds first fully operational floating wind farm, Hywind Scotland, that was commissioned in 2017. Owned by Equinor, it consists of five 6 MW turbines that utilise the Hywind floating spar-substructure foundation shown in Figure 1.2. Crucially, it achieved on average a capacity factor of 54% over its five years of operations (Equinor (2022) [40]). This is in contrast to fixed farms which report capacity factors of around 39%. This difference is remarkable given that floating technology is in its infancy and it clearly highlights the potential increase in efficiency that can come with technological advancements. Indeed, Equinor have even announced a new semi-submersible foundation design called 'The Wind Semi', also shown in Figure 1.2, that will be deployed in future Scottish floating wind projects. Therefore, it is clear that floating wind has the potential to play a key part on the route to net zero.

Offshore wind is the most successful offshore form of renewable energy and arguably has the most commercial potential. However, the most theoretical potential arguably comes from the ocean itself in the form of wave and tidal power, particularly for island nations like the UK. It is estimated that the UK has an exploitable wave resource of between 40–50 TWh/year (Jin and Greaves (2021) [80]) which has the potential to generate between 12.3–15.4% of the UK's

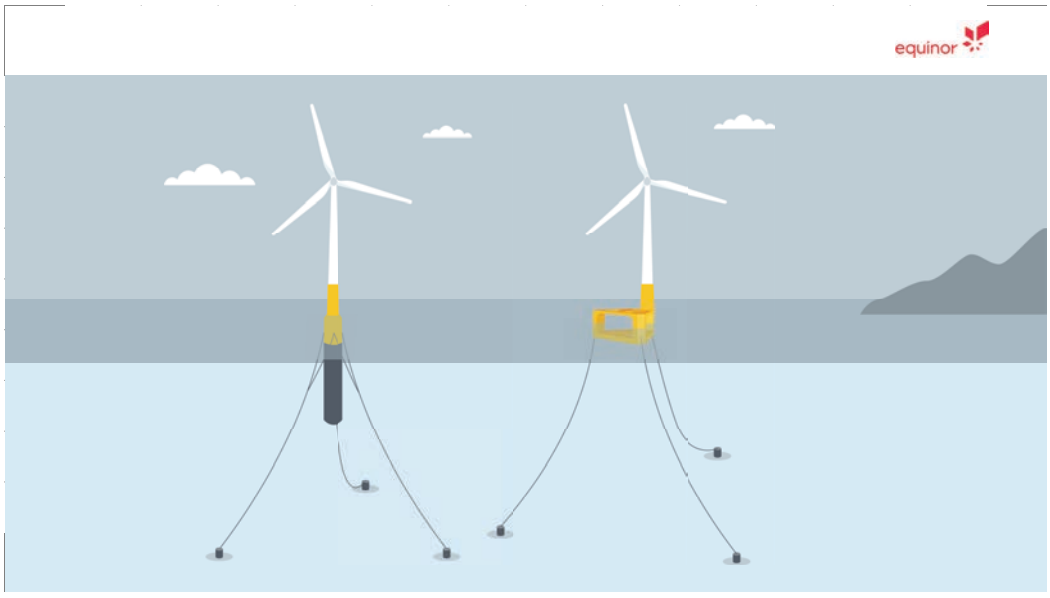

Figure 1.2: Floating offshore wind turbine designs by Equinor: spar-substructure foundation (left), semi-submersible foundation (right). Image by Equinor ASA (Equinor (2021) [41]).

electricity based on 2022 consumption. However, wave power has never been properly exploited due to the scale of complex challenges that come with development. Ocean waves can hold enormous amounts of energy, meaning that the survivability of any structure is immediately challenged. This is then compounded by the fact that energy then also has to be extracted to consequently generate electricity with high enough efficiency to make it viable. The sheer complexity of this process means that the practical, and financial, sustainability and scalability of wave power has never been definitively proven. A similar story can be told for tidal power which is the most consistent of all renewable resources: the rise and fall of tides daily is guaranteed. Tidal power can in general be classified by three electricity generation methods: tidal stream, tidal barrage, and tidal lagoon. It is estimated that tidal stream in particular has an exploitable resource of 34 Twh/year (Coles et al. (2021) [21]) which has the potential to generate 10.5% of the UK's electricity based on 2022 consumption. However, as with wave power, progress to commercial viability has been sluggish for similar reasons. Regardless, the UK is very much the world leader in tidal power and, in contrast to wave power, has shown signs of taking the next step. Total installed capacity is expected to increase from 10.1 to 50.9 MW by 2027 given current developments (Serin et al. (2023) [122]), with innovative designs from developers such as Simec Atlantic Energy being deployed (Simec Atlantic Energy (2023) [35]).

1.1.3 Challenges faced by offshore renewables

As already mentioned, offshore renewable development often faces a number of complex but interconnected challenges. For example, political challenges regularly manifest in the form of policymakers making short-term decisions to garner political capital rather than taking long-term decisions that provide the economic and regulatory environment for offshore renewable development to thrive. For example, the latest round of 'contracts for difference' auctions by the UK government failed to secure any new offshore wind projects for the first time since the scheme came into existence. This was blamed on ministers setting the guaranteed strike price too low, even though developers had indicated that increased supply chain and inflationary pressures had pushed costs up by as much 40% in the previous year (Carbon Brief (2023) [11]). The failure of the auction consequently puts the UK's 2030 target of 50 GW of installed offshore wind capacity at risk.

Ecological impacts also need to be considered so that offshore renewables do not have a significant adverse affect on the surrounding marine environment. For example, several studies, such as Galparsoro et al. (2022) [48], have found that offshore wind farms can have negative ecological impacts, with one such impact being excess noise that occurs during construction, operation, and decommissioning. However, significant efforts have been made to develop noise abatement systems, a review of which in the UK context can be found in Verfuss et al. (2019) [133]. Financial challenges are also often a hindrance. Securing both state-funded and private-sector investment through every stage of development, from feasibility studies to the design

process, construction, and even insurance can be a challenge. However, it is indisputable that the key for offshore renewables is tackling technical and engineering challenges. For example, as already discussed with wave and tidal power, technological progress is hampered by the complexity of engineering challenges faced. Even with the success of offshore wind, significant advancements in efficiency and output are still needed if future demand for electricity is to be met. Moreover, all the other factors mentioned also have to be taken into account when designing and constructing any offshore structure: it cannot be a haphazard and vague endeavour. Consistently tackling these technical and engineering challenges through research and innovation is therefore the single most important thing that will deem offshore renewable electricity generation a success on the road to net zero.

1.2 Hydrodynamic modelling for wave-structure interaction

The majority of technical and engineering challenges stem from the fact that the marine environment in which offshore renewable structures operate is naturally subject to harsh and potentially inconsistent wave conditions over the long term, posing a significant challenge to the survivability of any such structure and its performance. Given this, to achieve excellent performance over the long term, there must be a thorough and robust design process, followed by extensive numerical and experimental testing. Consequently, one of the pivotal tools required at a fundamental level is an advanced hydrodynamic model that deals with complex wave-structure interactions, the quality of which will also help ensure that the structure is as efficient as possible, both in a practical and financial sense.

Naturally, the above does not only apply to offshore renewables: hydrodynamic modelling of wave-structure interaction more widely is an important topic in several branches of marine/ocean research and engineering. For example, wave-structure is evidently a crucial consideration in the design of vessels for industries such as shipping, tourism, and defence. Moreover, safety in the oil and gas industry also relies on modelling of structures such as floating production storage and offloading (FPSO) vessels. However, the scope is not limited to just engineering but also extends to the study of the natural marine environment. For example, it is important to understand the extent to which wave interaction affects the distribution of sea ice and how that then affects the global climate. In addition, study of wave interaction with vegetation—such as mangroves—is beneficial in understanding how these natural structures can be used as 'nature-based' coastal defences. These examples can also then be intrinsically linked back to offshore renewables as well, e.g., the towing of wind turbines to their operating location will involve modelling beforehand to ensure it can be done safely and efficiently. Overall, regardless of application, hydrodynamic modelling is always required at some fundamental level.

In general it is required that any numerical model is capable of simulating large regions of waves stretching far from the structure as well as small regions on and around the structure in

which the flow is characteristically different. This approach is necessary in order to strike an optimal balance between accuracy and computational efficiency. It is not sufficient to have a model that cannot accurately calculate important physical effects, such as hydrodynamic loads, or six degrees of freedom motion (for floating structures). However, it is also not sufficient to have a model that can quantify such things but is unfeasibly computationally inefficient. Instead, industry requires a combination of both for optimal systematic analyses of survivability and performance, even if they are invariably more complex to construct, because the advantages are clear.

Traditionally, numerical models for wave hydrodynamics have largely been based on potential flow theory. However, fully-nonlinear potential flow (FNPF) is also a popular area of research. This type of model has been proven to provide sufficiently accurate solutions to a number of problems involving wave propagation, wave-wave interaction, and wave transformation whilst remaining computationally efficient. This makes them especially applicable to long-time and large-scale problems in marine areas spanning deep to shallow water. Other types of wave models are also regularly used for wave propagation, such as Boussinesq-type models based on Boussinesq approximations. These models are efficient and are adept at capturing wave transformation, but like FNPF models, cannot directly account for viscous effects apparent during wave-structure interaction. Models based on the nonlinear shallow water wave equations are also used for wave propagation in shallow water but again run into the same problems as FNPF and Boussinesq models when it comes to wave-structure interaction. The inability of the aforementioned models to take into account viscosity, vorticity, and other important physical effects means that in recent years, Navier-Stokes (NS) equations based computational fluid dynamics (CFD) models have become essential for modelling complex wave-structure interactions. However, CFD models in general are computationally expensive, making them practically unfeasible for long-time and large-scale wave simulations.

Naturally, due to the deficiencies of all the aforementioned models, it is appealing to instead develop integrated (or hybrid) models that aim to utilise the advantages of each through some sort of coupling between each individual solver. This is exactly the type of model described previously that was stated to be necessary for long-time and large-scale simulations and is also the main motivation of the present work. In particular, the primary objective of the present work is to develop a new integrated hydrodynamic model for large-scale and long-time wave-structure interaction problems by coupling an FNPF solver with a N-S solver. A detailed literature review discussing the key aspects of FNPF, NS, and integrated models hence follows.

1.3 Fully-nonlinear potential-flow models

As previously mentioned, FNPF models have long been used in the field of wave hydrodynamics due to their efficiency. They are well suited to long-time and large-scale problems involving wave propagation, wave-wave interaction, and wave transformation, with some also being able

to model basic wave-structure interaction. Mathematically, this efficiency is as a result of a one-phase simplification; that is, under potential flow theory, it is assumed that the flow is incompressible, inviscid, and irrotational. A mixed boundary-value problem (BVP), in which Laplace's equation is the governing equation, is then solved to obtain the velocity potential in the single fluid (water in this case) domain. However, the free-surface boundary is not known a priori; this means that a pair of coupled nonlinear free-surface boundary condition equations also have to be evolved in time to obtain the instantaneous free-surface elevation and potential at each step.

1.3.1 Numerical methods

Many different numerical methods have been purposed to yield solutions to these BVP's, but the most commonly utilised has certainly been the boundary-element method (BEM). In their seminal work, Longuet-Higgins and Cokelet (1976) [93] were the first to use a boundary integral equation formulation for 2-D steep overturning waves, solved via their mixed Eulerian-Lagrangian (MEL) time marching procedure. The crux of boundary-integral methods is to reduce the dimensionality of the problem by projecting the motion of the fluid body to its boundary. The entire motion of the fluid can then be determined by calculating the motion of the boundary alone—simplifying things greatly by reducing the amount of unknowns. The projection is most commonly done by making use of Green's second identity, such as the work of Grill et al. (2001) [54] where an accurate and efficient 3-D high-order BEM NWT was developed and utilised for various applications including wave shoaling and overturning waves. Approaches using Cauchy's integral formula, such as Dold (1992) [29], have also been shown to produce accurate and efficient models but are limited to 2D. The reduced dimensionality approach of BEM models and their ability to easily handle complex geometries means they are widely used for problems involving wave-structure interaction, e.g., Xue et al. (2001) [145] and Liu et al. (2001) [92], Bai and Eatock-Taylor (2007, 2009) [2, 1], and Zhou et al. (2015) [154]. The main disadvantage of traditional large-scale 3-D BEM models is the high computational cost and subsequent inefficiency of the method due to the influence coefficient matrix being very dense. However, there have been many advancements in finding a solution to this problem, most commonly by utilising the fast-multipole method (FMM) by Greengard and Rokhlin (1987) [52], e.g., Harris et al. (2022) [60].

Another traditional numerical method for FNPF models is the finite-element method (FEM) which, in constrast to the BEM, involves discretisation of the entire computational domain. An early use of the FEM was by Wu and Eatock-Taylor (1994) [144] who developed a 2-D model that simulated transient waves. Ma et al. (2001a, 2001b) [96, 97] then developed a 3-D model that simulated steep wave interaction with vertical cylinders. This model used finite differences to calculate the velocity only on the free surface and body surface rather than in the whole fluid domain, requiring far less computational time whilst achieving similar accuracy. In addition, a patch recovery technique was used to improve the accuracy of the FEM solution. In general,

FEM-based models are more computationally efficient than their BEM counterparts due to the relative sparsity of the influence coefficient matrix. However, a common disadvantage of some FEM models is the necessity of a complex unstructured mesh that has to regularly be regenerated for accurate solutions when modelling waves and bodies; this inevitably increases the computational time. To combat this, Ma and Yan (2006) [99] developed the quasi arbitrary Lagrangian-Eulerian finite-element method (QALE-FEM) which bypassed this problem of mesh regeneration. Instead, the QALE-FEM requires generation of the complex mesh only at the beginning of the simulation and is moved to conform to the motion of boundaries at other time steps—significantly reducing the computational time. Ma and Yan (2007, 2009) [98, 148] then successfully applied the QALE-FEM to simulate steep-wave interaction with 2-D and 3-D floating bodies.

Another well-utilised volume discretisation method is the finite-difference method (FDM). Li and Fleming (1997) [83] were the first to develop a second-order 3-D FDM model that was applied to wave shoaling problems. They made use of the well-known σ-transformation that transformed the Laplace equation and corresponding boundary conditions from the complex physical domain to a regular computational domain. The multigrid method (Brandt (1977) [10]) was then applied to efficiently solve the transformed Laplace equation whilst a stable implicit scheme was used to integrate the free-surface boundary equations. Bingham and Zhang (2007) [9] extended the Li and Fleming (1997) [83] model by allowing arbitrary order FDM's and non-uniform mesh spacing in 2D. It was found that a high-order method on a stretched vertical mesh was advantageous in terms of accuracy and stability compared to the original second-order method on a uniform mesh. Engsig-Karup et al. (2009) [37] then further extended the Bingham and Zhang (2007) [9] model into 3D. It was successfully tested using cases involving standing waves, highly nonlinear periodic waves, and nonlinear waves on a semi-circular shoal. More recently, Bihs et al. (2020) [8] developed the 2-D REEF3D::FNPF model that applied a second-order central difference (CD) scheme to discretise the σ-transformed Laplace equation, along with a third-order TVD Runge-Kutta scheme for time integration. The model was fully parallelised and was shown to accurately and efficiently simulate regular wave propagation, focused wave propagation, and wave transformation (shoaling) over a submerged bar.

As well as these traditional methods, several other models have been developed based on less-conventional methods. For example, Shao and Faltinsen (2014) [123] introduced the harmonic polynomial cell (HPC) method where the velocity potential within each cell of the volume-discretised computational domain is represented by the linear superposition of a set of harmonic polynomials. The 3-D model was used to simulate liquid sloshing, regular waves, wave shoaling, and wave diffraction of a bottom-mounted free-surface piercing cylinder. Hanssen et al. (2022) [58] also applied the HPC method to efficiently model various large-scale free-surface wave simulations including both short-crested and long-crested irregular waves. Another example is the high-order spectral method (HOS) (Dommermouth and Yue (1987) [31], Ducrozet et al. (2016) [33]) which is a pseudo-spectral method based on Taylor expansions and fast Fourier transform

(FFT). The spectral-element method (SEM) (Engsig-Karup et al. (2016) [38], Engsig-Karup et al. (2019) [39]) is a combination of the HOS and FEM methods and aims to utilise the advantages of both. Moreover, Clamond and Grue (2001) [19] introduced the pseudo-spectral 2-D spectral boundary integral (SBI) method which combines boundary integrals with FFT. Fructus et al. (2005) [46] extended this method to 3D and Wang and Ma (2015) [135] introduced techniques to enhance their efficiency. Lin et al. (2021) [90] also recently developed a finite-volume method FNPF model within the framework of the open-source CFD software OpenFOAM. A key advantage of this model is that it is capable of dealing with complex geometries not aligned with mesh lines/surfaces. It also allows for easier development of an integrated model through coupling with already available finite-volume-based multi-phase incompressible and compressible Navier-Stokes solvers in the same framework. The model itself was found to accurately simulate wave generation, propagation, and interaction with structures.

1.3.2 Stabilisation techniques for FNPF models

One problem that commonly arises in FNPF models—and has been extensively reported regardless of numerical method—is the so called 'sawtooth instability' which was first observed by Longuet-Higgins and Cokelet (1976) [93] in their seminal work. The consequence of this instability is that the free-surface boundary develops a sawtooth like wave profile after some time, particularly when simulating steep waves. The direct source of this instability has not been definitively proven; few authors in the literature attempt to verify the source and instead elect only to mitigate the problem. However, Dias and Bridges (2006) [28] suggested, 'The presence of sawtooth instabilities can be expected in the theory for nonlinear systems without dissipation, wherein energy flows from low to high wavenumbers and accumulates at the highest wavenumber associated with the discretisation.' This does not necessarily source the instability, but does suggest that it may be inherent in FNPF models, whilst also giving a basis from which mitigating measures can be developed. Dold (1992) [29] also split the occurring instability into three types: weak, strong, and steep wave. Through this he attempted to investigate how each type materialises, leading to suggestions of how each could be mitigated. Nevertheless, regardless of source, it is clear that some sort of stabilisation technique has to be utilised to ensure that any given model is free from the sawtooth instability.

By far the most popular technique in the literature for stabilising FNPF models is to use some form of numerical damping, such as smoothing. Indeed, as well as developing the MEL method, Longuet-Higgins and Cokelet (1976) [93] also outlined a 5-point smoothing formula which has regularly been used by other authors such as Wu and Eatock-Taylor (1994) [144] and Mehmood et al. (2016) [103]. A variety of other damping techniques also exist, such as the fourth-order damping correction used by Lin et al. (2021) [90] and the volume-conservative smoother proposed by Ferrand and Harris (2021) [43]. In general, smoothing is usually carried out on the free-surface variables—elevation and velocity potential—in order to act as a form of artificial dissipation, just like the type described by Dias and Bridges (2006) [28] previously.

However, these sorts of artificial techniques, particularly the common low order types mentioned, are not desirable because they can potentially cause superfluous dissipation, resulting in overall loss in energy in the system. This in turn can then make FNPF models inaccurate, particularly for large-scale and long-time simulations. Moreover, these techniques can involve a number of parameters that have to be tuned for any given application in order to achieve an optimal balance between stability and accuracy, resulting in a very sluggish and drawn-out process of trial and error if the values are not known a priori. However, it should also be noted that high-order techniques formulated on large stencils, such as the original tenth-order 13-point Savitzky-Golay (S-G) filter [121] utilised by Engsig-Karup et al. (2009) [37] and Hanssen et al. (2022) [58], and improved S-G filters developed by Shao et al. (2022) [124], can stabilise large-scale FNPF models with negligibly small energy loss for a number of applications. This is also without explicitly requiring tuning of any parameters like the low-order filters.

Even though most FNPF models suffer from the sawtooth instability, subsequently requiring some form of numerical damping, there are examples of models that do not. For example, Grilli et al. (1989, 2001) [55, 54] developed a 2-D and 3-D model, both of which did not report the instability and hence required no smoothing or remeshing. The authors attributed the high accuracy and stability of the models to a unique high-order BEM and a second-order Taylor series-based time-integration scheme, further details of which can be found in [54]. This Taylor series scheme was actually first utilised by Dold et al. (1986) [30], a model also based on the BEM. Again, the sawtooth instability did not appear, but only so long as a sufficiently small time step was adopted, a point Dold expands on in [29]. However, in the latter article he also stated that for steep waves, the instability always appears when the simulation is allowed to continue over a sufficiently long period of time, and that smoothing is required in this situation. This indicates that Grilli et al. (1989, 2001) [55, 54] may be correct in their aspersion that it is a combination of factors that stabilised their models, and that a high-order time-integration scheme in itself may not be sufficient.

There are also examples of FEM models that do not suffer from the sawtooth instability and hence require no smoothing or remeshing. Early FEM models such as Wu and Eatock-Taylor (1994) [144] and Ma et al. (2001a, 2001b) [96, 97] did require smoothing and remeshing respectively, but the latterly developed QALE-FEM (Ma and Yan (2006, 2007, 2009) [99, 148, 98]) avoided it. This is likely due to the precisely controlled mesh movement and highly accurate free-surface velocity calculation, aspects which some other FNPF models may under perform in. The finite difference-based FNPF model of Bihs et al. (2020) [8] also avoided the explicit use of numerical damping; this is likely down to the use of a fifth-order weighted essentially non-oscillatory (WENO) scheme to discretise the convection terms in the free-surface boundary condition equations. Mola et al. (2013) [104] used the streamwise upwind Petrov–Galerkin scheme to remove the sawtooth instability. This was accomplished by introducing weighted projections in the free-surface boundary condition equations. Furthermore, spectral methods-based models in the literature often attribute numerical instability to aliasing effects, hence

usually some sort of anti-aliasing technique is utilised in order to mitigate these effects and any consequent numerical instability. For example, Frcutus et al. (2005) [46] produced a 3-D SBI model that used an anti-aliasing technique involving zero padding, meaning it therefore required no smoothing or remeshing, and importantly showed no signs of the sawtooth instability. However, there is an argument to suggest that some anti-aliasing techniques, such as the spectral filtering used by Engsig-Karup et al. (2016) [38], are themselves a form of numerical damping as dissipation is being artificially added to the model.

1.4 Navier-Stokes models

Advancements in computing power and numerical analysis in recent decades has paved the way for computational fluid dynamics models based on the Navier-Stokes equations. CFD models have the advantage of being able to take into account rotational, viscous, and turbulent effects, as well as being able to simulate post wave-breaking flows. This makes them particularly useful for modelling wave-structure interactions where it's required to calculate things such as hydrodynamic loads or six degree of freedom motions, as well as model vortex shedding or air entrainment. However, CFD models are generally computationally expensive, making them practically unfeasible for large-scale wave simulations. CFD models based on the N-S equations have been researched in depth and various models exist for a number of applications involving wave-structure interaction. Therefore, methods, rather than applications, are the primary focus of this section, with a focus on two-phase models in particular due to their practicality to model the aforementioned physical effects.

Two-phase N-S CFD models can primarily be categorised into two groups based on the method for determining the free-surface interface: interface capturing and interface tracking. Interface-capturing methods are mesh-based methods that calculate the flow solution in a combined two-fluid domain. The fluid interface is then 'captured' by solving a transport equation for an additional variable. This additional variable depends on the specific method, with the two most popular being the volume-of-fluid (VOF) method (Hirt and Nichols (1981) [68], Martínez Ferrer et al. (2016) [101]), for which the volume fraction of a single phase (such as water or air) is the variable, and the level-set (LS) method (Osher and Sethian (1988) [112], Bihs et al. (2016) [7]), for which an implicit field related to the distance to the interface is the variable. The VOF method has excellent mass conservation properties but can be complex as the interface position is not explicitly calculated and has to be reconstructed. Special emphasis has to also be placed on maintaining a sharp interface for an accurate solution. In contrast, the LS method does explicitly calculate the interface, leading to a smoother solution, but does not have the same conservation properties.

Interface-tracking methods can be mesh based—either fixed or moving—or meshless. Mesh-based approaches include using the marker-and-cell (MAC) method (Harlow and Welch (1965) [59], Wang et al. (2007) [134]) and the arbitrary Lagrangian-Eulerian (ALE) technique (Ferrand

and Harris (2021) [43]), whilst meshless methods include particle tracking methods such as smoothed particle hydrodynamics (SPH) (Gingold and Monaghan (1977) [49], Monaghan (1994) [105], Lind et al. (2012) [91]) and meshless local Petrov-Galerkin (MLPG) (Lin and Atluri (2001) [87]). Meshless methods are powerful because they allow for the simulation of highly complex flows without mesh constraints, whereas mesh-based methods cannot simulate post wave breaking. However, meshless methods also have a very high computational cost.

1.5 Integrated/Hybrid Models

As previously outlined in detail in Sections 1.3 and 1.4, both FNPF and N-S solvers have their advantages and disadvantages when applied to a variety of problems in offshore and coastal engineering, but no single model can be considered universally applicable to any large-scale and long-time problem. As a consequence, in order to negate the deficiencies of the both of the aforementioned models and instead exploit the benefits, it is appealing to instead develop a single integrated (or hybrid) model through some sort of coupling between each individual solver. This approach is then favourable in the sense that each solver can be utilised to the fidelity which it performs best—ultimately striking an optimal balance between accuracy and computational efficiency. More precisely, in regions where viscous/turbulent effects play a significant role, such as on and around structures, a N-S model can be used; whereas, the rest of the computational domain, where viscous/turbulent effects play no significant role, is governed by an FNPF model which is utilised primarily to generate, propagate, and absorb computational waves.

Integrated models in the context of wave-structure interaction can broadly be categorised into two groups based on the method used to achieve the coupling: domain (or zonal) decomposition and functional (or velocity) decomposition. Domain decomposition—as the name suggests—is whereby the whole computational domain is physically split into separate subdomains (or zones) governed by one of the two models. Each domain is then separated by a coupled interface, or an overlapping zone, through which relevant information is exchanged. On the other hand, functional decomposition is different in that the governing equations, boundary conditions, and variables themselves are changed. That is, a 'complementary equation' is derived as the difference between the FNPF and N-S equations. The FNPF equations are then solved over the entire computational domain, whilst the complementary equation is solved in a designated N-S subdomain (e.g., around a structure) to obtain a 'complementary solution'. The summation of the FNPF and complementary solutions then gives a complete solution in the entire computational domain.

Another important characteristic by which integrated models can be categorised is the direction of coupling, i.e., one-way or two-way. For the former, information only travels one way, i.e., the FNPF solver essentially generates the inflow condition and provides information to the N-S solver but does not receive any feedback. In this sense, the FNPF solver runs

independent of the NS. In contrast, for the latter, information can travel either way and affect either solution. Hence, in this respect, the two solvers instead have to run simultaneously.

1.5.1 Domain decomposition

1.5.1.1 One-way coupling

Many domain decomposed models have been previously developed and successfully applied to various problems in offshore and coastal engineering. This includes both one-way and two-way couplings, as well as myriad numerical methods utilised for the constituent solvers. One-way coupled models are more prevalent, most probably due to them being easier to implement than two-way coupled methods. Guignard et al. (1999) [57] is an early example of a one-way coupled 2-D model that coupled a BEM-based FPNF solver with a VOF-based N-S solver and used it to model the transformation and breaking of solitary waves over plane slopes. The coupling itself was achieved via a single interface, a procedure again used and extended by Lachaume et al. (2003) [82]. However, a single interface has been perceived by some authors to be insufficient if we wish to achieve an accurate and stable one-way coupling. For example, Li et al. (2018) [84] suggested that there are two specific problems. First is the issue of reflected waves when modelling interaction with structures: any such reflected wave will be re-reflected at the interface back into the N-S domain and affect the accuracy of the solution while also affecting the stability of the coupling by interfering with the solution at the interface itself. Secondly, the fundamental physics of each model is different, i.e., the FNPF model assumes the flow is inviscid and irrotational whereas the N-S model does not. This will inevitably affect the continuity of the solution at the interface. To combat these problems, a number of authors instead implement an overlapping relaxation zone (Mayer et al. (1998) [102], Jacobsen et al. (2012) [75]) at the boundary between the two solvers; the relaxation zone will then have the dual effect of damping out any reflected waves whilst also ensuring a smooth transition in the solution between each subdomain. Li et al. (2018) [84] themselves utilised this method by coupling the QALE-FEM FNPF solver (Ma and Yan (2006, 2007, 2009) [99, 148, 98]) with the native VOF incompressible N-S 'interFoam' solver in OpenFOAM to create the 3-D 'qaleFOAM' model. This integrated model has then been successfully used for a number of applications, such as focused wave interaction with fixed and moving cylinders (Gong et al. (2021) [51], Li et al. (2021) [85], and Yan et al. (2020) [147]), investigating the added resistance and seakeeping performance of trimarans in oblique waves (Gong et al. (2020) [50]), and simulating a floating offshore wind turbine in waves (Yu et al. (2022) [151]).

Paulsen et al. (2014) [113] coupled one way the OceanWave3D FNPF model by Engsig-Karup et al. (2009) [37] with an extended version of the OpenFOAM interFoam solver. They also used the overlapping relaxation zone method and validated the model by computing wave loads on surface piercing cylinders in a variety of wave conditions, e.g., multi-directional irregular waves on a sloping bed. Wang et al. (2022) [138] developed another one-way cou-

pled integrated model via the overlapping relaxation zone in their 'REEF3D' framework. This model is interesting in that both constituent models are developed and coupled within the same framework—potentially bringing a number of advantages. The authors themselves remarked that 'Since both solvers are part of the same numerical framework, the numerics are more consistent and the coupling interface can be more robust and straightforward.' The model itself tested breaking waves over a submerged reef but did not test any wave-structure interaction.

All one-way coupled models mentioned previously involved mesh-based constituent N-S solvers. However, there are also significant contributions involving meshless (or particle) methods. Fourtakas et al. (2017) [45] coupled one way the QALE-FEM with an incompressible smoothed particle hydrodynamics (ISPH) solver using an overlapping 'buffer zone' at the coupling boundary. It was validated through the propagation of regular waves but not tested for wave-structure interaction. However, Zhang et al. (2020) [152] also developed a one-way coupled QALE-FEM–ISPH model which was capable of simulating extreme wave interaction with wave energy converter (WEC) devices moving in six degrees of freedom.

More recently, Higuera et al. (2018) [64] coupled one way a fully-Lagrangian FDM solver (Buldakov et al. (2019) [14]) with 'olaFlow'—a VOF-based N-S solver developed in OpenFOAM. It was used to determine wave run up and pressure on a fixed FPSO structure after interaction with a focused wave. The coupling was achieved through a single interface boundary through which information was transferred, but which also included active wave absorption so that any reflected waves were still absorbed even as the target waves were generated. However, Higuera et al. (2021) [65] then edited this coupling and instead used an overlapping relaxation zone to simulate extreme wave interaction with a fixed cylinder. They also did the same experiment with the original single interface boundary model and found that there was no significant discrepancies in results between the two. However, they did find that using the relaxation zone technique did result in slightly increased computational time. This shows the importance of picking the correct size of the zone when using this technique; i.e., it is sufficiently large enough to ensure proper absorption and continuity, but not too large as to have a detrimental affect on efficiency. Nevertheless, the authors do also remark that the relaxation zone method is advantageous in that it is proven to allow the generation of much steeper waves than the single interface method.

1.5.1.2 Two-way coupling

Two-way coupled models are less common than their one way counterparts. The main difference between the two types is the fact that information is instead exchanged two ways rather than being transferred solely from the FNPF solver to the NS. This adds an extra layer of complexity in that variables have to be calculated in the opposite direction (for example, the velocity potential in the FNPF domain has to be derived from the velocity in the N-S domain) and the boundary conditions also have to be satisfied simultaneously to ensure continuity.

Iafrati and Campana (2003) [70] provided an early example of a two-way coupled 2-D model.

The domain was split into two subdomains: one enclosing the free-surface region in which the N-S equations were solved with the level-set method used to capture the interface, and another below the free-surface region which was governed by a boundary integral-based FNPF solver. Two different coupling methods, categorised by how information is exchanged at the coupling boundary between the two subdomains, were outlined: Neumann type (NT) and Dirichlet type (DT). In both methods, the solution in the FNPF region provides the boundary condition for the N-S solver at the coupling boundary—similar to a one-way coupling. However, the reverse exchange is where the two differ. For the NT coupling, a Neumann boundary condition for the velocity potential is imposed on the coupling boundary so that the normal velocity from the N-S solver is given as the normal derivative of the velocity potential on said boundary. For this method, an overlapping zone is also used so that there are two coupling boundaries, one for each direction of information transfer. To ensure continuity, an iterative procedure is then required so that the solutions in the overlapping zone are obtained simultaneously with the boundary conditions satisfied. On the other hand, for the DT coupling, the normal stress calculated from the N-S solver is imposed as a pressure condition on the coupling boundary. Bernoulli's condition is then integrated in time to obtain the velocity potential field which is used a Dirichlet boundary condition for the FNPF solver. In contrast to the NT coupling, a single coupling boundary is satisfactory for continuity but an iterative procedure is again required. Both coupling methods were used to study a wave breaking flow generated by a hydrofoil moving close to the free surface. It should be noted that this model required no explicit coupling of the free surface as it is entirely enclosed by the N-S domain.

Colicchio et al. (2006) [22] applied the NT method with overlapping zone to couple two ways a two-phase BEM-based FNPF solver with a level-set N-S solver. It was validated for a dam break and wave impact problem. This 2-D model is different to Iafrati and Campana (2003) [70] in that the coupling boundaries and overlapping zone are oriented vertically in the domain so that the free surface transitions from one subdomain to the next. In addition, free-surface position and pressure, as well as velocity, are exchanged at the coupling boundaries. The temporal coupling is also different; rather than using an iterative procedure to achieve convergence, an intrinsic algorithm is presented in which the solution at the coupling boundaries accounts for both of the subdomains at several instances per time step. The authors suggested that this led to better stability properties than an iterative procedure. They also reported that, in their work, the NT method with overlapping zone was shown to be more robust in terms of continuity and stability compared to the DT method with a single coupling boundary. However, they also noted that an overlapping zone may decrease the computational efficiency of the model, so it is important to pick the correct size of the zone; i.e., it is sufficiently large enough to ensure continuity at the interface, but not too large as to have a detrimental affect on efficiency.

Sriram et al. (2014) [128] coupled two way an FEM-based FNPF solver with an Improved Meshless Local Petrov Galerkin with Rankine Source (IMLPG-R) N-S solver using the NT

method and a moving overlapping zone. The temporal coupling was done via an intrinsic algorithm and the model itself was used to simulate the propagation and breaking of regular, solitary, and cnoidal waves. The authors also gave a review of the different types of fixed/moving interfaces and overlapping zones for a two-way coupling and reached similar conclusions to Colicchio (2003) et al. [22] in that a single coupling boundary is not satisfactory for continuity and stability. For their model, they also concluded that a fixed overlapping zone was not sufficient and hence developed the moving overlapping zone which was actually used. Yan and Ma (2017) [146] also coupled two ways a (IMLPG-R) N-S solver with their QALE-FEM FNPF solver. The model was validated by simulating a 2-D unidirectional focused wave. Kim et al. (2010) [81] coupled two ways a BEM-based FNPF solver with a VOF N-S solver, again via the NT method, to produce a 2-D model that simulated fifth-order Stokes waves and random waves. It was found to produce results as accurate as the solely VOF model but for a fraction of the computational time.

1.5.2 Functional decomposition

Functional decomposition is fundamentally different to domain decomposition. Instead of decomposing the domain, the actual governing equations, boundary conditions, and variables themselves are 'decomposed'. This method is sometimes also called velocity decomposition because it involves decomposing the total velocity into its irrotational (potential) and vortical parts, i.e.,

$$\mathbf{u} = \nabla\phi + \mathbf{v}, \tag{1.1}$$

where $\mathbf{u}$ is the total fluid velocity, ϕ is the velocity potential, and $\mathbf{v}$ is the vortical velocity. The potential solution $\nabla\phi$ is then sought in the entire computational domain, whereas the vortical solution $\mathbf{v}$ is sought from the derived 'complementary' equation in the N-S region. The total fluid velocity $\mathbf{u}$ is then calculated through summing $\nabla\phi$ and $\mathbf{v}$. The same decomposition can also be done for other variables such as pressure.

Ferrant et al. (2003) [44] outlined a functional decomposition method in which the velocity, pressure, and free-surface elevation are split into incident and diffracted components. Then, at any given time step, the incident flow solution is first obtained in the entire domain (disregarding any structure) from a BEM-based FNPF solver. A set of complementary equations, named the spectral wave explicit Navier-Stokes equations (SWENSE), are then derived by explicitly including the incident solution at that time step in the single-phase N-S equations. From this, the new set of equations is then solved to obtain the diffracted flow solution and hence the complete solution. The subsequent 2-D model was inherently a one-way coupling as the FNPF solution was solely used as the incident wave field: there was no feedback to the FNPF solver. Ferrant et al. (2003) [44] tested this model by computing hydrodynamic loads on a submerged square body due to regular wave interaction. Since the development of the original SWENSE method, it has been successfully applied to myriad test cases involving wave-structure interaction; for example, Monroy et al. (2009) [107] used it for seakeeping by calculating

ship motions in regular and irregular head waves, Luquet et al. (2007) [95] simulated regular and irregular wave interaction with a tension-leg platform (TLP), and Monroy et al. (2009) [106] modelled a catenary anchor leg mooring (CALM) buoy in multi-directional regular and irregular sea states. Moreover, the SWENSE method was also recently extended to two-phase N-S models; for example, Li et al. (2021) [86] coupled a high-order spectral method-based FNPF solver with an OpenFOAM VOF N-S solver. This model was comprehensively validated through test cases involving regular and irregular wave interaction with a vertical cylinder and a CALM buoy. The authors also mention use of a relaxation scheme, similar to the one-way domain decomposition couplings, to absorb reflected waves from structures. Other functional decomposition models have also been developed such as Janssen et al. (2010) [76] who coupled a BEM FNPF solver with particle-based Lattice-Boltzmann solver to study solitary wave shoaling and breaking over a plane slope.

1.5.3 Important considerations

From the review of integrated models, a number of important points arise that have to be considered in detail when developing such a model. Firstly, it has to be remembered that the fundamental physics underlying each constituent model is different, meaning the task of information exchange is not simple because there will often be a mismatch in variables; i.e., in the FNPF model, the free-surface elevation and velocity potential are the main physical quantities, whereas in the N-S model, it is the velocity, pressure, and water-volume fraction. To illustrate why this may be a problem, consider the one-way coupling of Li et al.(2018) [84]. In order to transfer the velocity, they had to implement a scheme to calculate the gradient of the FNPF velocity potential—namely, the quadric semi-analytical finite-difference interpolation (QSFDI) scheme by Yan et al. (2020) [149]. However, implementing this scheme also brings some constraints such as requiring a finer mesh near the coupling boundary and making sure that the displacement of FNPF nodes near the coupling boundary is not too large. In general, implementing a scheme like this that can accurately and efficiently derive the relevant variable can often be challenging and time consuming. Moreover, care has to be taken so that no significant numerical errors are accumulated that could affect the accuracy of the solution and stability of the coupling.

There is also the inherent problem of mismatching time steps: N-S models often need smaller time steps for a stable and accurate solution when compared to FNPF models. Similarly, for volume discretised domain decomposed models, there will also be a problem with nonconforming meshes: N-S models require a finer mesh for a stable and accurate solution compared to FNPF models. Both these problems also have to be overcome when developing integrated models.

1.6 OpenFOAM

OpenFOAM® [141, 79] is an open-source C++ CFD toolbox that is widely employed in research and industry due to its robustness and advanced range of features. It is capable of solving a vast range of continuum mechanics problems with in-built numerical solvers as well allowing for the development of user-built customised solvers. In terms of numerical method, OpenFOAM implements a cell-centred, collocated finite-volume method (FVM) on a structured or unstructured polyhedral mesh. In addition, it has advanced features for mesh generation, spatial and temporal discretisation, MPI for parallelisation, and much more.

OpenFOAM has also been applied to a wide range of wave propagation, wave-wave interaction, and wave-structure interaction problems. The most commonly used in-built OpenFOAM solver is 'interFoam', an incompressible two-phase pressure-based solver based on the volume-of-fluid (VOF) method. For example, Jacobsen et al. (2012) [75] introduced wave generation and absorption techniques using relaxation zones into the interFoam solver. It was validated through generation, propagation, absorption, and breaking of regular waves. Higuera et al. (2013a, 2013b) [66, 67] also introduced a number of other wave generation and absorption techniques, e.g., piston-type wavemaker and active wave absorption, into interFoam and tested it by simulating a wide range of coastal engineering processes, e.g., solitary wave interaction with a vertical structure and rip current on a barred beach. Chen et al. (2014) [18] assessed how the interFoam solver performed when applied to the problem of regular and focused wave interaction with a surface piercing cylinder. The work concluded that OpenFOAM is very capable of accurately modelling the nonlinear wave interaction with this offshore structure. However, no comment was made about computational time.

One of the key advantages of OpenFOAM is the flexibility it provides in creating customised solvers for specific problems. For example, Mehmood et al. (2015) [103] and Lin et al. (2021) [90] developed the first FNPF solvers in OpenFOAM, with Lin et al. (2021) [90] in particular applying it to a number of problems such as 3-D wave shoaling and regular wave interaction with a fixed cylinder. In addition, the coupling of individual solvers is also made possible. For example, Martínez Ferrer et al. (2016) [101] coupled the interFoam solver with the compressible version of interFoam called 'compressibleInterFoam', whilst Di Paolo et al. (2021) [27] coupled the interFoam solver with itself in different dimensions, i.e., 2D–3D. Another more recent development in OpenFOAM is the use of the overset meshing technique with interFoam in the solver 'overInterDyMFoam'. Using an overset mesh has the major advantage over the standard dynamic mesh in that it allows for much larger deformations. This greater flexibility in motion makes it an attractive technique for complex wave-structure interaction problems. Chen et al. (2019) [17] applied overInterDyMFoam to a number of problems involving structures, e.g., a 2-D horizontal floating cylinder in regular waves, regular wave interaction with a 2-D T-shaped floating body, 2-D wedge-shaped body impact at constant speed, and many more.

1.7 Objectives and contributions of the present work

1.7.1 Development a new integrated hydrodynamic model

The literature shows that a breadth of research exists in the area of integrated models for wave structure interaction, each with their own advantages and disadvantages. Nevertheless, a new integrated hydrodynamic modelling framework for large-scale and long-time wave-structure interaction problems is proposed in this work. In particular, the primary objective is to develop the new integrated model by coupling the finite-volume-based FNPF solver by Lin et al. (2021) [90] with the native OpenFOAM incompressible 'interFoam' solver in a numerical wave tank (NWT). This proposed model has the primary advantage that each constituent solver has been developed in the same numerical framework (OpenFOAM), and consequently, are both also based on the same numerical method, i.e., the FVM. Very few models in the literature can report this advantage; recall from Section 1.5.1.1 that Wang et al. (2022) [138] developed an integrated model in their 'REEF3D' framework and remarked that this brought the advantage that 'the numerics are more consistent and the coupling interface can be more robust and straightforward'. However, the constituent models in Wang et al. (2022) [138] were not also based on the same numerical method like the proposed model. Indeed, the model by Lin et al. (2021) [90] is one of very few FVM-based FNPF solvers in the literature. Hence, the proposed model would be one of the first finite volume–finite volume integrated models. Lu et al. (2017) [94] also presented a FVM–FVM coupling in OpenFOAM that was applied to some basic problems including the sinking of a semi-submersible platform. This model is interesting as it is a hybrid one-way/two-way coupling in that information is only transferred in one direction, and not back, but the direction could be either way, i.e., FNPF to NS or NS to FNPF. However, no analysis is given on the computational efficiency of the model and there is no indication that it is parallelised. In addition, the hybrid one-way/two-way coupling procedure outlined is quite complex and cumbersome, and the model was not tested for any wave-structure interaction problems. Given this, it is unclear whether this model provides any advantage over other models for large-scale and long-time wave-structure interaction problems. Moreover, given that OpenFOAM is open source, the major benefit of the proposed integrated model would be that it could readily be used by researchers as a more efficient model for complex wave-structure interaction problems than the native incompressible solver 'interFoam'.

In the present work, a one-way domain decomposed coupling is implemented via an overlapping relaxation zone. Domain decomposition is the logical choice of decomposition method due to the fact that both constituent models are volume discretised, based on the same numerical method, and developed in the same framework. Moreover, the primary purpose of the proposed model is to apply it to complex wave-structure interaction problems whereby the actual interaction is achieved through the open-source interFoam solver that has been extensively advanced and tested over a number years. With this in mind, it would be illogical to try and edit

the interFoam solver itself as would have to be done for a functionally decomposed coupling. This would be needlessly complex and directly contravene the advantages of the proposed coupling outlined earlier. Instead, domain decomposition would only require an amendment of the boundary conditions to achieve the coupling, something that is made simple through readily available OpenFOAM features.

In addition to the choice of coupling method, the choice of strength and the argument for a one-way coupling is also cogent. For wave-structure interaction problems, it's essential to consider the crux of the problem and the reason why the model is being used. As mentioned previously in Section 1.2, the main emphasis of the present work is to model wave interaction with offshore renewable structures, e.g., fixed monopile foundations, wave energy converter devices, or floating offshore wind turbines. The key characteristic that needs investigating is the survivability of any such object under a variety of wave conditions, with extreme conditions being of particular importance. In a modelling context, this amounts to determining extreme hydrodynamic loads on the structure under harsh sea states. These conditions can be replicated in a variety of different ways, such as by generating focused waves in a numerical wave tank, from which hydrodynamic loads can then be determined when they reach the structure. However, under this context, the wave response from the structure as it radiates away from the structure, after the extreme wave event has occurred, does not need to be quantified. Therefore, a two-way coupling is not necessary as the physical quantities do not need to be transferred back into the original FNPF domain or on into another FNPF domain. Implementing a two-way coupling would add extra complexity to the proposed coupling—again contravening the advantages. For example, a method for reconstructing the velocity potential from the velocity would have to be implemented and an iterative procedure would be necessary to achieve convergent solutions in the overlapping zone. Nevertheless, a two-way coupling would however be applicable in contexts where the reverse is true, for example, if we have an array of fixed or floating wind turbines, or even if there is an array of combined wind and wave energy devices such as the types reviewed by Pérez-Collazo et al. (2015) [115]. In this context, a two-way coupling would be necessary.

The chosen coupling methodology also exploits a number of other consequential advantages that stem from the aforementioned primary advantage of each constituent solver being developed in the same framework and based on the same numerical method. These advantages are linked to the 'important considerations' mentioned in Section 1.5.3 and are essential in ensuring that the method for transferring information is simple and that the coupling is stable and accurate. Indeed, given that both solvers have been developed in OpenFOAM and are finite-volume-based, only a method to calculate the volume fraction from the free-surface elevation needs to be implemented: the velocity and pressure are already calculated as part of the FNPF solution (explained in Section 3.2 during the outline of the FNPF methodology) and can be transferred accordingly in one direction—simplifying things greatly and avoiding unwanted errors. In addition, existing advanced OpenFOAM functionalities can be used for the required interpolation—easily addressing the problem of nonconforming meshes. These functionalities

then also allow for the easy implementation of an overlapping relaxation zone which is key to a stable coupling because it ensures that there is a smooth transition from the FNPF to interFoam solution. Without it, there is a danger of there being a lack of continuity between each solution due the underlying physics of each solver being different. This could potentially then lead to errors and subsequently make the coupling unstable. Moreover, this zone also absorbs any reflected waves in the NWT, again aiding stability and accuracy. These advantages of the proposed models are expanded on in more detail in Chapter 4 where the coupling methodology is outlined.

1.7.2 Introduction of a new stabilisation technique for FNPF models

As detailed in Section 1.3.2, a problem that commonly arises in FNPF models is the so called 'sawtooth instability'. Reasons as to why this instability may occur is discussed in detail in Section 3.2, but a review of existing stabilisation techniques to deal with the instability suggested that the most popular technique was to use some form of numerical damping, such as smoothing. One such model that used numerical damping for stabilisation was Lin et al. (2021) [90] by way of a fourth-order damping correction scheme—a low-order scheme. Given the reasons discussed previously, this is not desirable, and it would be beneficial if the model did not have to use it. Indeed, no test cases were done over a large scale to examine if the model suffered from the sort of energy loss that is known to occur when using this type of technique. For this reason, there is a degree of uncertainty as to whether the model is applicable to large-scale and long-time simulations. Given this, a secondary but preliminary objective in the present work is to develop a new method that can stabilise the computation of the Lin et al. (2021) [90] model, and any other finite-volume or finite-difference FNPF model, without using any of the aforementioned undesirable techniques that involve artificial dissipation. Therefore, a new method based on a total variation diminishing (TVD) approach is developed. The methodology of this new method is discussed in Chapter 3, and it is validated through test cases in Chapter 5 and 6.

1.8 Outline of the remainder of the thesis

The remainder of thesis is organised as follows:

- In Chapter 2, the methodology of the interFoam solver and its implementation in OpenFOAM is presented. A detailed description of the governing equations in the volume-of-fluid method is first given, followed by an outline of the finite-volume formulation, including spatial, temporal, and equation discretisation. Finally, the solution procedure is presented, including derivation of the pressure-velocity coupling and description of the Pressure-implicit with splitting of operators (PISO) algorithm. Solution control features such as adaptive time stepping are also outlined.

- In Chapter 3, the FNPF methodology is outlined. As mentioned in Section 1.7, the FNPF model of Lin et al. (2021) [90] is the focus of the present work, so both its mathematical formulation and numerical implementation based on the finite-volume method in OpenFOAM is detailed. In addition to this, the methodology behind the new stabilisation technique motivated by a TVD approach is also presented. This includes reasons as to why the sawtooth instability may be occurring in the original Lin et al. (2021) [90] model and how to solve it, as well as the new computational formulation arising from this.

- Chapter 4 then focuses on the methodology of the new integrated model. It is first discussed in detail how the chosen coupling methodology exploits a number of consequential advantages that stem from the fact the two constituent models have been developed in OpenFOAM and are based on the finite-volume method. This includes how an overlapping relaxation zone can adeptly be implemented, how a mismatch in variables can easily be handled, how the issue of non-conforming meshes can be solved, and how the problem of mismatching time steps can be mitigated. The full coupling procedure is then presented, including how information is transferred, and how the relaxation correction is applied. Finally, the computational procedure is described and the method for parallelisation is briefly discussed.

- In Chapter 5, the accuracy, efficiency, and sensitivity to parameters are tested for both the refined FNPF model and new integrated model via test cases involving regular and irregular wave propagation in the form of fifth-order Stokes and focused waves respectively. For the FNPF model, temporal and mesh sensitivity are tested, and the superiority of the new stabilisation technique in terms of energy conservation over the old Lin et al. (2021) [90] model is proven. For the integrated model, temporal and mesh sensitivity are also tested, as well as sensitivity to the primary coupling parameters. Two different sized domain are considered and detailed analyses of computational time are given throughout.

- Chapter 6 then validates the accuracy and efficiency of the two models through wave-structure interaction test cases. For the FNPF model, 2-D and 3-D wave shoaling are considered. For the integrated model the test cases are fifth-order Stokes wave interaction with a 2-D floating body, focused wave interaction with a fixed cylinder, and focused wave interaction with a 3-D floating wave energy converter (WEC) device. Again, detailed analyses of computational time are given throughout.

- Finally, conclusions are drawn in Chapter 7, with some discussion on the potential for future work.

2

Incompressible Two-Phase Navier-Stokes Model

The native 'interFoam' solver in OpenFOAM is a pressure-based incompressible two-phase Navier-Stokes (NS) solver. It is based on the volume-of-fluid (VOF) method which solves the 3-D equations for two phases, i.e., air and water, and has a special emphasis on maintaining a sharp free surface (interface-capturing) through use of an indicator function and artificial compression terms. This chapter is focused on outlining the methodology of the interFoam solver and its implementation in OpenFOAM. As mentioned previously in Section 1.6, OpenFOAM implements a cell-centred, collocated finite-volume method (FVM) on an unstructured (or structured) polyhedral mesh, so this is also gone over in detail. The majority of this chapter is based on the works of Jasak (1996) [78], Rusche (2003) [119], Ubbink (1997) [132], and Berberovic et al. (2009) [5].

2.1 Volume-of-fluid method

2.1.1 Governing equations

The system of equations for an incompressible two-phase flow mixture consists of a mass conservation equation, momentum conservation equation, and transport equation for the volume fraction α, each respectively given by

$$\nabla \cdot \mathbf{u} = 0, \tag{2.1}$$

$$\frac{\partial \rho \mathbf{u}}{\partial t} + \nabla \cdot (\rho \mathbf{u}\mathbf{u}) = -\nabla p + \nabla \cdot \mathbf{T} + \rho \mathbf{g}, \tag{2.2}$$

$$\frac{\partial \alpha}{\partial t} + \nabla \cdot (\mathbf{u}\alpha) = 0, \tag{2.3}$$

where $\mathbf{u}$ is the mixture velocity, ρ is the mixture density, p is the pressure, $\mathbf{T}$ is the viscous stress tensor, and $\mathbf{g}$ is the gravitational acceleration. Given that the constituent fluids of the mixture are Newtonian, the stress tensor $\mathbf{T}$ is also linearly related to the rate of strain tensor by the dynamic viscosity μ, meaning that $\nabla \cdot \mathbf{T}$ in Equation (2.2) can be rewritten as

$$\nabla \cdot \mathbf{T} = \nabla \cdot (\mu \nabla \mathbf{u}) + (\nabla \mathbf{u}) \cdot \nabla \mu. \tag{2.4}$$

In order to also simplify the definition of the pressure boundary conditions, a modified pressure p', defined as

$$p' = p - \rho \mathbf{g} \cdot \mathbf{x}, \tag{2.5}$$

where $\mathbf{x}$ is the position vector, is introduced. This modified pressure has no actual physical meaning but is used as an advantageous numerical technique, as explained by Rusche (2003) [119] and Higuera (2015) [63]. The pressure gradient in Equation (2.2) is then consequently modified as

$$-\nabla p = -\nabla p' - \rho \mathbf{g} - \mathbf{g} \cdot \mathbf{x} \nabla \rho. \tag{2.6}$$

2.1.2 Indicator function

The indicator function for the VOF method in interFoam is the water-volume fraction $\alpha \in [0, 1]$. It takes the value 1 in regions containing solely water and 0 in regions containing solely air. At the phase interface between the two fluids, there is a transitional region in which α can take any value between 0 and 1 according to the distribution of the phases throughout the domain. In the VOF method, a special emphasis has to be placed on maintaining a sharp free surface interface because proper calculation of the surface curvature is essential for determining other important physical properties such as the pressure gradient. The way that this sharp interface is maintained in OpenFOAM is by introducing the artificial compression term of Weller (2002, 2008) [140, 139] into Equation (2.3) so that it becomes

$$\frac{\partial \alpha}{\partial t} + \nabla \cdot \mathbf{u}\alpha + \nabla \cdot \mathbf{u}_c \alpha(1 - \alpha) = 0, \tag{2.7}$$

where $\mathbf{u}_c = \mathbf{u}_w - \mathbf{u}_a$ is called the 'compression velocity', and where the subscripts w and a denote the water and air phases respectively. By definition, this compression term is only applied within the bounds of the transitional phase interface region and does not affect the solution outside this region. The key to deriving this artificial term is to take the mixture velocity as a weighted average based on the volume fraction:

$$\mathbf{u} = \alpha \mathbf{u}_w + (1 - \alpha)\mathbf{u}_a. \tag{2.8}$$

Similarly, the physical properties of the mixture; namely, the density ρ and dynamic viscosity μ, are also expressed as a weighted average, i.e.,

$$\rho = \alpha \rho_w + (1 - \alpha)\rho_a, \tag{2.9}$$

$$\mu = \alpha \mu_w + (1 - \alpha)\mu_a. \tag{2.10}$$

2.1.3 Final formulation

Using Equations (2.4) and (2.6), the momentum conservation equation (2.2) can be rewritten as

$$\frac{\partial \rho \mathbf{u}}{\partial t} + \nabla \cdot (\rho \mathbf{u}\mathbf{u}) - \nabla \cdot (\mu \nabla \mathbf{u}) = -\nabla p' + (\nabla \mathbf{u}) \cdot \nabla \mu - \mathbf{g} \cdot \mathbf{x} \nabla \rho. \tag{2.11}$$

Therefore, to conclude, the VOF method implemented in interFoam consists of simultaneously solving the mass conservation equation (2.1), the momentum conservation equation (2.11), and volume fraction transport equation (2.7), together with the constitutive relations for the density (2.9) and dynamic viscosity (2.10).

2.2 Finite-volume method

As mentioned at the start of this chapter, OpenFOAM implements a cell-centred, co-located FVM on an unstructured polyhedral mesh. The FVM is a commonly utilised method in CFD due to it being naturally conservative. The method itself involves discretising the integral form of the governing equations over a finite number of control volumes. The crux of the method is to then use Gauss' theorem to convert volume integrals into surface integrals so that each term in the discretised equations can be evaluated as fluxes at the surfaces of each control volume. This then generates a corresponding system of algebraic equations whose solution provides an approximate solution to the original equations at some fixed locations in space and time. For a finite volume formulation of the problem outlined in Section 2.1, spatial, temporal, and equation discretisation all have to be considered separately.

2.2.1 Spatial and temporal discretisation

Spatial discretisation involves subdividing the computational domain into a finite number of control volumes (cells). Each of these cells is bounded by a set of faces so that the cell is

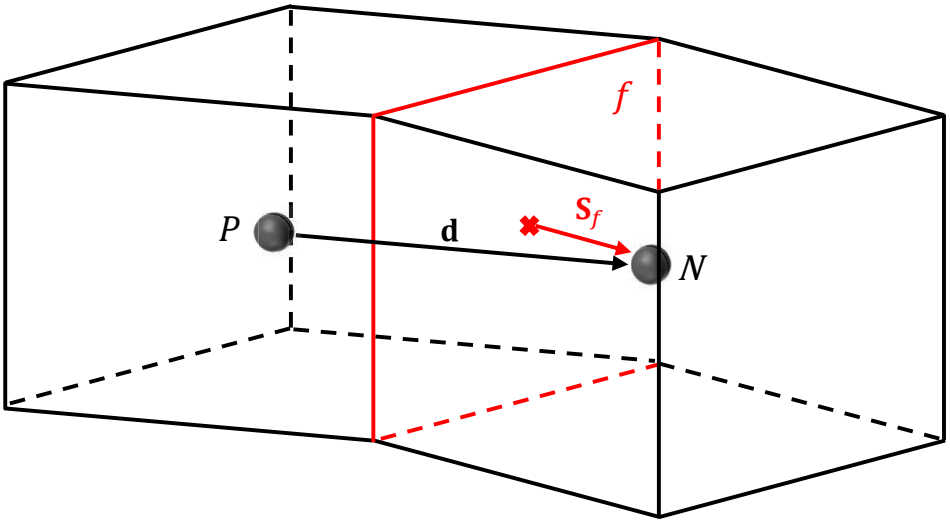

Figure 2.1: Example OpenFOAM control volumes with key mesh parameters

convex and no two cells overlap. Consequently, each face is shared by only two cells—the control volume cell (or owner cell) and the neighbouring cell (or the donor cell). In general, OpenFOAM allows the use of an unstructured mesh which means that any number of faces can bound a single cell. However, in this work, a structured mesh of hexahedral cells is primarily used, an example of which is shown in Figure 2.1. Here, two cells with centres labelled P (owner) and N (neighbour) are each bounded by a set of faces, with only face f in common. Given that the FVM in OpenFOAM is collocated and cell centred, all information is stored at these cell centres. The position vector $\mathbf{x}_P$ of cell centre P is defined such that the volume integral

$$\int_{V_P} (\mathbf{x} - \mathbf{x}_P)\, dV = 0, \tag{2.12}$$

where V_P is the volume of the cell P. Correspondingly, the position vector $\mathbf{x}_f$ of the centre of face f is defined such that the surface integral

$$\oint_{S_f} (\mathbf{x} - \mathbf{x}_S)\, dS = 0, \tag{2.13}$$

where S_f is the surface area of f. With regards to the other mesh parameters labelled in Figure 2.1, $\mathbf{S}_f$ is the outward pointing face area vector defined as

$$\mathbf{S}_f = S_f \hat{\mathbf{n}}, \tag{2.14}$$

where $\hat{\mathbf{n}}$ is the outward pointing normal of f. The vector $\mathbf{d}$ is defined as the distance between the points P and N, i.e., $\mathbf{d} = \mathbf{x}_N - \mathbf{x}_P$.

Temporal discretisation is simple and consists of splitting the time interval into a finite number of time steps, i.e., $t \in [t_0, t_1, ..., t_{n-1}, t_n, t_{n+1}, ..., t_{N-1}, t_N]$. These time steps can either be fixed or they can change during a simulation subject to some condition.

2.2.2 Equation discretisation

As mentioned previously, the governing equations are transformed into a solvable system of algebraic equations using the FVM. The following section first summarises the procedure for a general transport equation, and then applies the method to the problem outlined in Section 2.1.

2.2.2.1 Discretisation of general transport equation

The general form of a transport equation for a scalar quantity ϕ is given as

$$\frac{\partial \rho\phi}{\partial t} + \nabla \cdot (\rho \mathbf{u}\phi) - \nabla \cdot (\rho\Gamma\nabla\phi) = S_\phi(\phi), \tag{2.15}$$

where the first term on the left hand side is the temporal term, the second is the convection term, the third is the diffusion term with Γ being the diffusivity, and the right hand side is a source term. A finite volume discretisation of Equation (2.15) is then formulated by integrating over the control volume P, and a time interval $t + \Delta t$, so that

$$\int_t^{t+\Delta t} \left[\int_{V_P} \frac{\partial \rho\phi}{\partial t} dV + \int_{V_P} \nabla \cdot (\rho \mathbf{u}\phi)\ dV - \int_{V_P} \nabla \cdot (\Gamma \nabla\phi)\ dV \right] dt = \int_t^{t+\Delta t} \left[\int_{V_P} S_\phi(\phi)\ dV \right] dt. \tag{2.16}$$

Each of these volume integrals in Equation (2.16) then have to be evaluated by using Gauss' theorem. However, the integral over the control volume P of the variable ϕ is also required, and hence is evaluated as

$$\begin{aligned} \int_{V_P} \phi(\mathbf{x})\ dV &\approx \int_{V_P} \Big[\phi_P + (\mathbf{x} - \mathbf{x}_P) \cdot (\nabla\phi)_P \Big] dV \\ &= \phi_P \left(\int_{V_P} dV \right) + \left[\int_{V_P} (\mathbf{x} - \mathbf{x}_P)\ dV \right] \cdot (\nabla\phi)_P \\ &= \phi_P V_P. \end{aligned} \tag{2.17}$$

The first line in Equation (2.17) is due to the fact that, in order to obtain a second-order accurate FVM, is has to be assumed that the spatial variation of ϕ is linear. The second term on line two is then equal to zero due to Equation (2.12). As an aside, it has to also be assumed that the temporal variation is also linear—a point that will be returned to later.

2.2.2.2 Gauss' theorem

As mentioned previously, the crux of the FVM is to use Gauss' theorem to convert volume integrals into surface integrals over cell surfaces. The generalised form of Gauss' theorem for any tensor field Φ is expressed as

$$\int_V \nabla * \Phi\ dV = \oint_S \Phi * d\mathbf{S}, \tag{2.18}$$

where S is the closed surface bounding the volume V, and $d\mathbf{S}$ is the infinitesimal area vector associated with a surface element dS and outward pointing normal $\hat{\mathbf{n}}$. The symbol $*$ represents any tensor product, e.g., inner, outer, or cross.

2.2.2.3 Gradient calculation

Using Gauss' theorem (2.18), the volume integral for the gradient $\nabla\phi$ can be converted into a surface integral, i.e.,

$$\int_{V_P} \nabla\phi \; dV = \oint_S \phi \; d\mathbf{S}. \tag{2.19}$$

Given that the control volume V_P is bounded by a set of faces S, the surface integral in Equation (2.19) can then be transformed into a sum of integrals over all faces of the cell so that

$$\oint_S \phi \; d\mathbf{S} = \sum_f \Big(\oint_{S_f} \phi_f \; d\mathbf{S} \Big), \tag{2.20}$$

where S_f is the surface area of face f and ϕ_f is the value of the variable ϕ evaluated on f. Moreover, given the assumption of linear variation of ϕ, and in a similar way to (2.17),

$$\begin{aligned} \oint_{S_f} \phi_f \; d\mathbf{S} &\approx \oint_{S_f} \Big[\phi_f + (\mathbf{x} - \mathbf{x}_f) \cdot (\nabla\phi)_f \Big] d\mathbf{S} \\ &= \phi_f \Big(\oint_{S_f} d\mathbf{S} \Big) + \oint_{S_f} \Big[\phi_f + (\mathbf{x} - \mathbf{x}_f) \; d\mathbf{S} \Big] \cdot (\nabla\phi)_f \\ &= \mathbf{S}_f \phi_f, \\ \implies \oint_S \phi \; d\mathbf{S} &= \sum_f \mathbf{S}_f \phi_f. \end{aligned} \tag{2.21}$$

Here, $\mathbf{S}_f$ is the outward pointing face area vector defined in Equation (2.14). Note that the second term on line two of Equation (2.21) is equal to zero due to Equation (2.13). Note that only the linear gradient scheme in OpenFOAM is described here, but other gradient schemes are available, such as least-squares, fourth-order least squares, and limited versions of each. Regardless of scheme, it can be seen in Equation (2.21) that the values of ϕ_f also have to be estimated via interpolation from cell centres to faces. A variety of different schemes are available in OpenFOAM to do this and are described in Section 2.2.2.5 after the discretisation of the convection term, for which interpolation is important, is first outlined.

2.2.2.4 Convection term

Using Gauss' theorem (2.18) and Sections 2.2.2.1–2.2.2.3, the volume integral for the convection term $\nabla \cdot (\rho\mathbf{u}\phi)$ in Equation (2.16) is transformed and evaluated as

$$\begin{aligned} \int_{V_P} \nabla \cdot (\rho\mathbf{u}\phi) \; dV &= \oint_S (\rho\mathbf{u}\phi) \cdot d\mathbf{S} \\ &\approx \sum_f \mathbf{S}_f \cdot (\rho\mathbf{u})_f \phi_f \\ &= \sum_f F_f \phi_f, \end{aligned} \tag{2.22}$$

where $F_f = \mathbf{S}_f \cdot (\rho\mathbf{u})_f$ is the mass flux through the face f.

2.2.2.5 Face interpolation

As mentioned previously, interpolation of ϕ from cell centres to face centres is required. In general, there are three types of scheme that can be used in OpenFOAM. The first, central

differencing (CD), is primarily used during linear gradient calculation in Equation (2.21) and for the convection term (2.22) in non convection-dominated problems. This scheme assumes a linear variation of ϕ between cell centres P and N (Figure 2.1), meaning that ϕ_f can be calculated as

$$\phi_f = f_x \phi_P + (1 - f_x)\phi_N, \tag{2.23}$$

where

$$f_x = \frac{|\mathbf{x}_f - \mathbf{x}_N|}{|\mathbf{x}_f - \mathbf{x}_N| + |\mathbf{x}_f - \mathbf{x}_P|}. \tag{2.24}$$

This scheme is second-order accurate but is known to cause unphysical oscillations in the solution and hence violates the boundedness of the solution for convection-dominated problems. However, for gradient calculation like Equation (2.21), the CD scheme is accurate and stable. Other similar schemes are also available.

The second and third schemes are primarily used in conjunction with specific divergence schemes for the convection term (2.22) in convection-dominated problems. The first of these schemes is upwind differencing (UD); this determines ϕ_f according to the direction of flow, i.e.,

$$\phi_f = \begin{cases} \phi_P & \text{for} \quad F_f \geq 0, \\ \phi_N & \text{for} \quad F_f < 0, \end{cases} \tag{2.25}$$

where F_f is the flux from Equation (2.22). This scheme guarantees boundedness but is only first-order accurate. The second of these schemes is blended differencing (BD) (Jasak (1996) [78]); this aims to ensure both boundedness and accuracy of the solution by combining both CD and UD schemes through the linear combination

$$\phi_f = \gamma(\phi_f)_{\text{CD}} + (1 - \gamma)(\phi_f)_{\text{UD}}, \tag{2.26}$$

where $\gamma \in [0, 1]$ is the blending factor. The choice of γ then determines the exact scheme, but the primary schemes available in OpenFOAM are high resolution total variation diminishing (TVD) schemes.

2.2.2.6 Diffusion term

Similar to the convection terms, the diffusion term is transformed and evaluated as

$$\begin{aligned} \int_V \nabla \cdot (\Gamma \nabla \phi)\, dV &= \oint_S (\Gamma \nabla \phi) \cdot d\mathbf{S} \\ &\approx \sum_f \Gamma_f \mathbf{S}_f \cdot (\nabla \phi)_f. \end{aligned} \tag{2.27}$$

The term $\mathbf{S}_f \cdot (\nabla \phi)_f$ here is called the surface normal gradient, and if the mesh is orthogonal, it can be approximated to second order accuracy by

$$\mathbf{S}_f \cdot (\nabla \phi)_f = |\mathbf{S}_f| \frac{\phi_N - \phi_P}{|\mathbf{d}|}. \tag{2.28}$$

However, for non-orthogonal meshes, an additional correction term is needed to maintain second-order accuracy. In this case, Equation (2.28) becomes

$$\mathbf{S}_f \cdot (\nabla \phi)_f = \boldsymbol{\Delta}_f \cdot (\nabla \phi)_f + \mathbf{k}_f \cdot (\nabla \phi)_f, \tag{2.29}$$

where

$$\mathbf{S}_f = \boldsymbol{\Delta}_f + \mathbf{k}_f. \tag{2.30}$$

The first term on the right hand side in Equation (2.30) is the orthogonal contribution, whereas the second the term is the non-orthogonal contribution. Both vectors $\boldsymbol{\Delta}_f$ and $\mathbf{k}_f$ must then be determined by some sort of non-orthogonality treatment. In OpenFOAM, this is the over-relaxed approach (Jasak (1996) [78], Ubbink (1997) [132]) in which

$$\boldsymbol{\Delta}_f = \frac{\mathbf{d}}{\mathbf{d} \cdot \mathbf{S}_f} |\mathbf{S}_f|^2. \tag{2.31}$$

2.2.2.7 Source term

The source term $S_\phi(\phi)$ in Equation (2.16) can be a general function of ϕ and can hence be linearised as

$$S_\phi(\phi) = S_A \phi + S_B, \tag{2.32}$$

where S_A and S_B can also depend on ϕ. The volume integral can then be evaluated as

$$\begin{aligned} \int_{V_P} S_\phi(\phi)\ dV &= \int_{V_P} S_A \phi + S_B\ dV, \\ &= S_A \phi_P V_P + S_B V_P, \end{aligned} \tag{2.33}$$

where Equation (2.17) has been used to get from the first line to the second.

2.2.2.8 Temporal discretisation

The spatial discretisation of the temporal term in Equation (2.16) is simple and is given as

$$\int_{V_P} \frac{\partial \rho \phi}{\partial t} dV = \left(\frac{\partial \rho \phi}{\partial t} \right)_P V_P. \tag{2.34}$$

Using Equations (2.22), (2.27), (2.33), and (2.34), and assuming that the control volumes do not change in time, the general transport (2.16) equation can now be rewritten as

$$\int_t^{t+\Delta t} \left[\left(\frac{\partial \rho \phi}{\partial t} \right)_P V_P + \sum_f F_f \phi_f - \sum_f \Gamma_f \mathbf{S}_f \cdot (\nabla \phi)_f \right] dt = \int_t^{t+\Delta t} (S_A \phi_P V_P + S_B V_P) dt. \tag{2.35}$$

For temporal discretisation, evaluation of the time integrals and time derivative in (2.35) are done through the implicit Euler method. The implicit Euler method is only first order accurate in time but is unconditionally stable and guarantees boundedness of the solution. Therefore, Equation (2.35) can be rewritten as

$$\rho_P \frac{\phi_P^{n+1} - \phi_P^n}{\Delta t} V_P + \sum_f F_f \phi_f^{n+1} - \sum_f \Gamma_f \mathbf{S}_f \cdot (\nabla \phi)_f^{n+1} = S_A \phi_P^{n+1} V_P + S_B V_P. \tag{2.36}$$

This linear algebraic equation applies to any control volume P in the computational domain. Moreover, given that any value of ϕ_f and $(\nabla \phi)_f$ in Equation (2.36) can be calculated using the neighbouring cells of P, the equation itself can be written in generic form as

$$a_P \phi_P^{n+1} + \sum_N a_N \phi_N^{n+1} = r_P, \tag{2.37}$$

where a_P represents the coefficients of cell P, a_N represents the coefficients of neighbouring cells, and r_P represents the source terms (Rusche (2003) [119]). This can then be expanded to the whole computational domain to create a system of linear algebraic equations:

$$\mathbf{A}\boldsymbol{\phi} = \mathbf{r}, \tag{2.38}$$

where $\mathbf{A}$ is a matrix with the values of a_P on the diagonal and a_N off the diagonal, $\boldsymbol{\phi}$ is the dependent variable vector, and $\mathbf{r}$ is the source vector.

2.3 Finite-volume formulation and solution procedure for the Navier-Stokes system

2.3.1 Equation discretisation

The discretisation procedure outlined in Section 2.2 can then be used to discretise the momentum equation for the Navier-Stokes system outlined in Section 2.1. Indeed, Equation (2.11) for the mixture velocity $\mathbf{u}$ is discretised over a control volume P, and a time interval $t + \Delta t$, so that

$$\rho_P V_P \frac{\mathbf{u}_P^{n+1} - \mathbf{u}_P^n}{\Delta t} + \sum_f F_f^{n+1}\mathbf{u}_f^{n+1} - \sum_f \mu_f \mathbf{S}_f \cdot (\nabla \mathbf{u})_f^{n+1} = (\nabla \mathbf{u})_P^n \cdot (\nabla \mu)_P - (\nabla p')_P - \mathbf{g} \cdot \nabla(\rho)_P. \tag{2.39}$$

The water-volume fraction transport equation can also be discretised in the same way. Hence, Equation (2.7) for the water-volume fraction α is discretised over a control volume P, and a time interval $t + \Delta t$, so that

$$\frac{\alpha_P^{n+1} - \alpha_P^n}{\Delta t} V_P + \sum_f \phi_f \alpha_f^{n+1} + \sum_f \phi_{c,f}[\alpha(1-\alpha)]_f^{n+1} = 0, \tag{2.40}$$

where ϕ_f is the volumetric flux (to be distinguished from the scalar variable ϕ in Section 2.2) and $\phi_{c,f} = \mathbf{S}_f \cdot \mathbf{u}_{c,f}$ is the compressive volumetric flux with

$$\mathbf{u}_{c,f} = n_f \min\left[K_c \frac{|\ \phi_f\ |}{|\ \mathbf{S}_f\ |}, \max\left(\frac{|\ \phi_f\ |}{|\ \mathbf{S}_f\ |}\right)\right]. \tag{2.41}$$

The coefficient K_c in (2.41) is an adjustable parameter that determines the magnitude of compression and n_f is the face unit normal flux given by

$$n_f = \frac{(\nabla \alpha)_f}{|\ (\nabla \alpha)_f + \delta_n\ |} \cdot \mathbf{S}_f, \tag{2.42}$$

where δ_n is the stabilisation parameter which takes into account mesh non uniformity. It usually takes the value 10^{-5}. It is important to note here that the volumetric flux ϕ_f in Equations (2.40) and (2.41) is not evaluated using the interpolated face velocity, but is instead determined using the calculated velocity resulting from the pressure-velocity solution procedure that will be outlined in the next section.

2.3.2 Boundary conditions

To complete the boundary-value problem, boundary conditions (BCs) are needed at each boundary of the computational domain for each variable. Proper choice of BCs is essential to the stability and accuracy of the solution to any given problem. Moreover, they also depend on the specific problem at hand, hence OpenFOAM offers a variety of different conditions that can be used at the users discretion. In the present work, interFoam is used as a constituent solver in an integrated model of the type proposed in Section 1.7.1. Given the proposed methodology briefly outlined (it is outlined in more detail in Chapter 4), it is clear that the inlet and outlet BCs will be modified through the coupling and damping procedure, so the user chosen BCs for the physical boundaries can be simplified. Therefore, only standard Dirichlet and Neumann BCs are required in this work and are detailed in Table 2.1 for each variable.

In Table 2.1, the 'zeroGradient' condition is the basic Neumann condition where the normal gradient of any given variable ϕ is equal to zero, i.e.,

$$\frac{\partial \phi}{\partial n} = 0. \tag{2.43}$$

The 'noSlip' condition is a Dirichlet velocity condition that sets the velocity at a rigid wall to zero, i.e.,

$$\mathbf{u} = 0, \tag{2.44}$$

whereas the 'movingWallVelocity' is the analogue in the case of a moving wall, i.e.,

$$\mathbf{u} = \mathbf{u}_{\text{wall}}. \tag{2.45}$$

The atmospheric BCs for each variable are slightly different. The 'pressureInletOutletVelocity' condition for the velocity assigns a zeroGradient condition for flow out of the domain, but assigns a velocity based on the normal flux for flow into the domain. The 'inletOutlet' for the water-volume fraction is similar apart from that the inlet is uniformly set to zero (air). The 'totalPressure' condition is given as

$$p' = p_0 - \frac{1}{2}|\mathbf{u}|^2, \tag{2.46}$$

where all values are calculated at the boundary and p_0 is the total pressure. In this work, p_0 is equal to the atmospheric pressure $p_{\text{atm}} \approx 100,000$ Pascals (Pa).

Variable	Inlet	Outlet	Rigid walls	Atmosphere	Moving walls
$\mathbf{u}$	zeroGradient	zeroGradient	noSlip	pressureInletOutletVelocity	movingWallVelocity
p'	zeroGradient	zeroGradient	zeroGradient	totalPressure	zeroGradient
α	zeroGradient	zeroGradient	zeroGradient	inletOutlet	zeroGradient

Table 2.1: Name of OpenFOAM boundary conditions used for interFoam in the present work.

2.3.3 Solution procedure

2.3.3.1 Solution for the water-volume fraction

A solution to the water-volume fraction equation (2.40) is obtained through the 'multidimensional universal limiter for explicit solution' (MULES) procedure that is implemented in OpenFOAM (Greenshields (2023) [53]). Thorough details of the procedure can be found in Damián (2013) [26], but the important thing to note is that it guarantees the boundedness of $\alpha \in [0, 1]$. In more recent versions of OpenFOAM, a semi-implicit version of the procedure was introduced that loosened the criteria to ensure stability of the solution.

2.3.3.2 Pressure-velocity coupling

There are two specific problems that need to be tackled to obtain both velocity and pressure solutions to the Navier-Stokes system. The first is that there is no equation for the pressure, and second is that the mass conservation equation (2.1) acts a restriction on the calculated velocity solution, hence any solution must satisfy it. Together this is known as the pressure-velocity coupling problem and it has to be solved in order to obtain a proper solution.

Given that there is no pressure equation, one first has to be derived. The derivation here follows Jasak (1996) [78] and Rusche (2003) [119]. To start, the momentum equation (2.39) is expressed as a system of algebraic equations in the same way as Equations (2.37) and (2.38) for the general transport equation in Section 2.3. However, given that an equation for pressure is being derived, the pressure gradient term is not discretised at this point. Therefore:

$$\mathbf{A}_{\mathrm{D}}\mathbf{u}_P^{n+1} = \mathbf{H} - \nabla p', \tag{2.47}$$

where

$$\mathbf{H} = \mathbf{A}_{\mathrm{O}}\mathbf{u}_N^{n+1} + \frac{\mathbf{u}^n}{\Delta t} + (\nabla \mathbf{u})_P^n \cdot (\nabla \mu)_P - \mathbf{g} \cdot \nabla(\rho)_P. \tag{2.48}$$

The matrix $\mathbf{A}_{\mathrm{D}}$ here in Equation (2.47) is a diagonal matrix constructed from the diagonal entries of matrix $\mathbf{A}$ in Equation (2.38) but for this problem; i.e., it is a diagonal matrix with the a_P coefficients for the owner cells on its diagonal. In contrast, matrix $\mathbf{A}_{\mathrm{O}}$ in Equation (2.48) is the matrix constructed from the off-diagonal entries of matrix $\mathbf{A}$ in Equation (2.38) but for this problem; i.e., it is a matrix that contains the a_N coefficients for the neighbour cells. Consequently, the matrix $\mathbf{H}$ defined in Equation (2.48) can be split into two parts: the 'transport part', which comprises of the $\mathbf{A}_{\mathrm{O}}$ matrix and the neighbour cells coefficients multiplied by the corresponding velocity; and the 'source part', which comprises of all the source terms in the momentum equation bar the pressure. This $\mathbf{H}$ matrix is important because it will be used to calculate the source terms for the derived pressure equation.

To derive the aformentioned pressure equation, the first step is to multiply Equation (2.47) by the inverse of matrix $\mathbf{A}_{\mathrm{D}}$, which is easy to find given that $\mathbf{A}_{\mathrm{D}}$ is diagonal. This then gives

$$\mathbf{u}_P^{n+1} = \mathbf{A}_{\mathrm{D}}^{-1}\mathbf{H} - \mathbf{A}_{\mathrm{D}}^{-1}\nabla p', \tag{2.49}$$

which is an equation for cell centre velocity. The face centre velocity can then be found via interpolation (as outlined in Section 2.2.2.5 and is given as

$$\mathbf{u}_f^{n+1} = (\mathbf{A}_\mathrm{D}^{-1}\mathbf{H})_f - (\mathbf{A}_\mathrm{D}^{-1})_f(\nabla p')_f. \tag{2.50}$$

As of yet, the mass conservation equation (2.1) has not been discretised. However, it can be discretised in the same way as the other equations in the system via the procedure detailed in Section 2.2. Hence, Equation (2.1) for the mixture velocity $\mathbf{u}$ is discretised over a control volume P so that

$$\sum_f \mathbf{S}_f \cdot \mathbf{u}_f = 0. \tag{2.51}$$

The expression for the face centre velocity (2.50) can then be substitued into the discretised mass conservation equation (2.51) to give

$$\sum_f \mathbf{S}_f \cdot \Big[(\mathbf{A}_\mathrm{D}^{-1})_f(\nabla p)_f\Big] = \sum_f \mathbf{S}_f \cdot (\mathbf{A}_\mathrm{D}^{-1}\mathbf{H})_f, \tag{2.52}$$

which is clearly a Poisson equation for the pressure. Hence, rather than the mass conservation equation being a restriction on the velocity field, it now instead provides an equation for the pressure. The left hand side of Equation (2.52) can then be further discretised in the same way as the diffusion term in Section 2.2.2.6. The final equation required is for the conservative volumetric fluxes ϕ_f, which can be calculated using the face velocities in Equation (2.50) such that

$$\begin{aligned} \phi_f &= \mathbf{S}_f \cdot \mathbf{u}_f^{n+1}, \\ &= \mathbf{S}_f \cdot \Big[(\mathbf{A}_\mathrm{D}^{-1}\mathbf{H})_f - (\mathbf{A}_\mathrm{D}^{-1})_f(\nabla p')_f\Big]. \end{aligned} \tag{2.53}$$

The final discretised system for the pressure-velocity coupling is then given by the momentum predictor equation

$$\mathbf{A}_\mathrm{D}\mathbf{u}_P^{n+1} = \mathbf{H} - \sum_f \mathbf{S}_f\, p'_f, \tag{2.54}$$

where the pressure is now discretised; the $\mathbf{H}$ matrix defintion (2.48); the cell-centre velocity equation (2.49); the derived pressure equation (2.52); and the flux calculation (2.53).

2.3.3.3 Pressure-implicit with splitting of operators (PISO) algorithm

The pressure-velocity coupling system for transient flows in the present work is primarily solved via the PISO algorithm that was originally proposed by Issa (1986a, 1986b) [73, 74]. The procedure is as follows:

1. The momentum predictor equation (2.54) is solved using the pressure field from the previous time step. This step is called the momentum 'predictor' step because the velocity is essentially being guessed (or predicted) as it does not yet satisfy the mass conservation equation.

2. The predicted velocity field is then used to compute a new $\mathbf{H}$ matrix using Equation (2.48) which, along with the $\mathbf{A}_\mathrm{D}^{-1}$ matrix, will be the source term in the pressure equation. Once

this has been computed, the pressure equation (2.52) can be solved to obtain the pressure field solution.

3. A new set of conservative fluxes can then be calculated using the new pressure solution and Equation (2.53). Moreover, the velocity field is also corrected explicitly using (2.49) so that it now satisfies the mass conservation equation.

At this point, solutions for pressure and velocity have both been obtained. However, after the velocity correction, the pressure equation (2.52) is no longer satisfied because the **H** matrix is dependent on the velocity—which has just been corrected. Therefore, the pressure is no longer correct. Given this, it is necessary to go back to step 2, correct the **H** matrix, and repeat the procedure. To summarise, the PISO algorithm consists of an implicit momentum predictor step 1, followed by a number of pressure solutions and explicit velocity corrections 2 and 3 until a user-determined tolerance is achieved. One loop of steps 2 and 3 is know as an *inner corrector* in OpenFOAM.

The other common algorithm used is semi-implicit method for pressure-linked equations (SIMPLE) where, instead of looping over just steps 2 and 3, the loop goes back to step 1 and the momentum predictor equation (2.54). This is known as an *outer corrector*. The SIMPLE algorithm is mainly used for steady-state flows and in conjunction with the under-relaxation technique that artificially increases diagonal dominance in the system. For an unsteady flow, the SIMPLE algorithm is practically unfeasible because it requires a very large amount of iterations to achieve a convergent solution. This is compared the PISO algorithm for which most problems only require one momentum predictor step and 2–3 inner correctors as long as the time step is sufficiently small. The other algorithm in OpenFOAM is the PIMPLE algorithm which is a combination of both SIMPLE and PISO and allows for the use of larger time steps.

2.3.3.4 Adaptive time step control

OpenFOAM handily allows the use of adaptive time stepping to ensure stability of the solution procedure. The time step algorithm adjusts the time step size at the start of every time loop based on the Courant number C which is defined as

$$C = \frac{\mathbf{u}_f \cdot \mathbf{S}_f}{\mathbf{d} \cdot \mathbf{S}_f} \Delta t, \tag{2.55}$$

where $\mathbf{d}$ is the distance vector defined in Figure 2.1 (Rusche (2003) [119]). Using values $\mathbf{u}_f^n$ and Δt^n from the previous time step n, a maximum local Courant number C^n is calculated and the new time step is evaluated from

$$\Delta^{n+1} = \min\left\{ \frac{C_{\max}}{C^n}\Delta t^n,\ \left(1 + \lambda_1 \frac{C_{\max}}{C^n}\right)\Delta t^n,\ \lambda_2 \Delta t^n,\ \Delta t_{\max} \right\}, \tag{2.56}$$

where $\Delta t_{\max}$ and $C_{\max}$ are user-prescribed limits for the time step and Courant number respectively, and λ_1 and λ_2 are damping factors. In interFoam, $\lambda_1 = 0.1$ and $\lambda_2 = 1.2$ (Berberovic (2009) [5]).

2.3.3.5 Temporal subcycling

As mentioned in Chapter 1, the stability and accuracy of the VOF method relies on there being a sharp phase interface. Given this, the transport equation for α (2.40) is solved in several subcycles during a single time step (Berberovic (2009) [5]). The time step used in a single subcycle $\Delta t_{\text{subcycle}}$ is given as

$$\Delta t_{\text{subcycle}} = \frac{\Delta t}{n_{\text{subcycle}}}, \tag{2.57}$$

n_{subcycle} is the number of subcycles.

2.3.3.6 Full interFoam solution procedure

The full interFoam solution procedure for a given time step is summarised as follows:

1. Calculate the Courant number from Equation (2.55) and adjust the time step using Equation (2.56).

2. Solver the water-volume fraction transport equation (2.41) via the MULES procedure mentioned in Section 2.3.3.1 and using the volumetric fluxes from the previous time step.

3. Use the new values of α to calculate the new mixture density via Equation (2.9) and the new mixture viscosity using Equation (2.10).

4. Assemble the momentum predictor equation (2.47) and go through the PISO algorithm described in Section 2.3.3.3 until a convergent solution is obtained.

2.4 Dynamic mesh

2.4.1 Equation formulation

Dynamic meshing in OpenFOAM allows the computational mesh to change during simulations. Dynamic meshing is essential in the present work because it is required in examples involving rigid-body motion where the mesh has to be morphed in response to the motion of the body. Moreover, it is also required in the fully-nonlinear potential-flow model that will be outlined in Chapter 3 where the mesh has to be morphed in response to the motion of the free surface. The two main differences compared to a static mesh is that cell volume and cell velocity varies in time. Following Jasak (2009) [77] and Guerrero (2022) [56], the volume integral formulation of the general transport equation (2.16) changes to ALE form

$$\frac{\partial}{\partial t}\int_{V_P} \rho\phi dV + \int_{V_P} \nabla\cdot\left[\rho\phi(\mathbf{u}-\mathbf{u}_s)\right]\, dV - \int_{V_P} \nabla\cdot(\Gamma\nabla\phi)\, dV = \int_{V_P} S_\phi(\phi)\, dV, \tag{2.58}$$

where $\mathbf{u}_s$ is the mesh velocity and the volume dV now depends on time. Given this time dependence, the implicit Euler method (the same as in Section 2.2.2.8) now gives

$$\frac{\partial}{\partial t}\int_{V_P} \rho\phi dV = \rho_P \frac{(V\phi)_P^{n+1} - (V\phi)_P^n}{\Delta t}, \tag{2.59}$$

where V_P^{n+1} can be calculated by

$$V_P^{n+1} = V_P^n + \frac{dV_P}{dt}\Delta t. \tag{2.60}$$

The relationship between the rate of change of the cell volume V_P and the mesh velocity $\mathbf{u}_s$ is given by the space conservation law:

$$\frac{\partial}{\partial t}\int_{V_P} dV - \int_{V_P} \nabla \cdot \mathbf{u}_s \; dV = 0. \tag{2.61}$$

Using Section 2.2.2.4, Equation (2.61) then becomes

$$\frac{dV}{dt} = \sum_f \mathbf{S}_f \cdot \mathbf{u}_{sf}, \tag{2.62}$$

where $\mathbf{u}_{sf}$ is the velocity of the face f. The quantity on the right hand side of Equation (2.62) can then be computed by calculating the volume V_f 'swept out' by face f over a time step, i.e.,

$$\mathbf{S}_f \cdot \mathbf{u}_{sf} = \frac{\Delta V_f}{\Delta t}. \tag{2.63}$$

Using Equations (2.62)–(2.63) in Equations (2.58)–(2.60) and following the same procedure outlined throughout this chapter then gives the dynamic-mesh methodology.

2.4.2 Rigid-body motion solver

For cases involving floating bodies, the native rigid-body motion 'sixDoFRigidBodyMotion' solver in OpenFOAM is applied to solve the six DoF (degree of freedom) motion. The motion equation is formulated based on the conservation of linear and angular momentum:

$$\mathbf{a}_f = \frac{\mathbf{f}_f}{m_f}, \tag{2.64}$$

$$\boldsymbol{\alpha}_f = \mathbf{I}_f^{-1}\boldsymbol{\tau}_f, \tag{2.65}$$

where f denotes the floating body; $\mathbf{a}_f$ and $\boldsymbol{\alpha}_f$ are the linear and angular acceleration respectively; m_F is the mass of the body; and $\mathbf{I}_f$ is the moment of inertia. In addition, $\boldsymbol{f}_f$ and $\boldsymbol{\tau}_f$ are the external force and torque which are calculated as

$$\mathbf{f}_f = \iint_S (p\mathbf{I}_3 + \mathbf{T}) \cdot \mathrm{d}\mathbf{S} + m_f\mathbf{g}, \tag{2.66}$$

$$\boldsymbol{\tau}_f = \iint_S \mathbf{r}_\mathrm{S} \times (p\mathrm{I}_3 + \mathbf{T}) \cdot \mathrm{d}\mathbf{S} + \mathbf{r}_\mathrm{G} \times m_f\mathbf{g}, \tag{2.67}$$

where p is the pressure, $\mathbf{I}_3$ is the 3-D identity matrix, $\mathbf{T}$ is the viscous stress tensor, and S denotes the boundary surface of the floating body. Furthermore, $\mathbf{g}$ is the gravitational acceleration, and $\mathbf{r}_\mathrm{S}$ and $\mathbf{r}_\mathrm{G}$ are the lever arm vectors of the hydrodynamic and gravitational forces respectively. Based on the accelerations from Eqs. (2.64)–(2.65), the Newmark scheme (Newmark (1959) [109]) is applied to obtain the displacement, velocity, and orientation of the body. The body displacement is then linearly diffused into the domain by solving the Laplacian equation:

$$\nabla \cdot (k\nabla \mathbf{u}_{fS}) = 0, \tag{2.68}$$

where $\mathbf{u}_{fS}$ is the velocity of the moving body boundary and k is the distance-based diffusivity parameter derived from the user-specified parameters *inner* and *outer* distance, between which mesh morphing is allowed.

3

Fully-Nonlinear Potential-Flow Model Based on the Finite-Volume Method

In this chapter, the fully-nonlinear potential-flow (FNPF) methodology is outlined. As mentioned in Section 1.7, the FNPF model of Lin et al. (2021) [90] is the focus of the present work, so both its mathematical formulation and numerical implementation based on the finite-volume method (FVM) in OpenFOAM is detailed. In addition to this, the methodology behind the new stabilisation technique is also presented. This includes reasons as to why the sawtooth instability may be occurring in the original Lin et al. (2021) [90] model and how to solve it, as well as the new computational formulation arising from this. Note that, henceforth, the Lin et al. (2021) [90] model will simply be referred to as the 'Lin model' unless there is a direct reference, e.g., numerical results.

3.1 Methodology of the original FNPF model

3.1.1 Mathematical formulation of the boundary-value problem

Under potential flow theory, it is assumed that the flow is incompressible, inviscid, and irrotational. In the computational domain, a 3-D numerical wave tank (NWT) is defined with a Cartesian coordinate system where the y-axis points vertically upwards and the still free-surface water level is defined as the xz-plane—as shown in Figure 3.1. Furthermore, the free-surface elevation from the still water level is defined as the function $\eta(x, z, t)$ where t is the time. Throughout this work, the still water level is always defined as $y = 0$.

The governing equation in the fluid domain is Laplace's equation

$$\nabla^2 \phi = 0, \tag{3.1}$$

where $\phi(x, y, z, t)$ is the velocity potential. The nonlinear kinematic and dynamic boundary conditions (KBC and DBC respectively)—both satisfied at the free surface—are given as

$$\frac{\partial \eta}{\partial t} = \frac{\partial \phi}{\partial y} - \frac{\partial \phi}{\partial x}\frac{\partial \eta}{\partial x} - \frac{\partial \phi}{\partial z}\frac{\partial \eta}{\partial z} \quad \text{at} \quad y = \eta(x, z, t), \tag{3.2}$$

$$\frac{\partial \phi}{\partial t} = -g\eta - \frac{1}{2}\nabla\phi \cdot \nabla\phi \quad \text{at} \quad y = \eta(x, z, t), \tag{3.3}$$

where g is the gravitational acceleration.

As mentioned in the Section 1.3.1, the majority of FNPF models adopt the mixed Eulerian-Lagrangian (MEL) approach first outlined by Longuet-Higgins and Cokelet (1976) [93]. To understand why it is favoured, consider the free-surface boundary condition equations (3.2)–(3.3) which are given in the Eulerian description. For the simulation of water-wave problems, the equations clearly need to be satisfied on a moving boundary surface, in which case a Lagrangian description must be used. Consequently, in the mixed approach, the Laplace problem is solved in the fluid domain from an Eulerian point of view, whilst the moving free-surface boundary

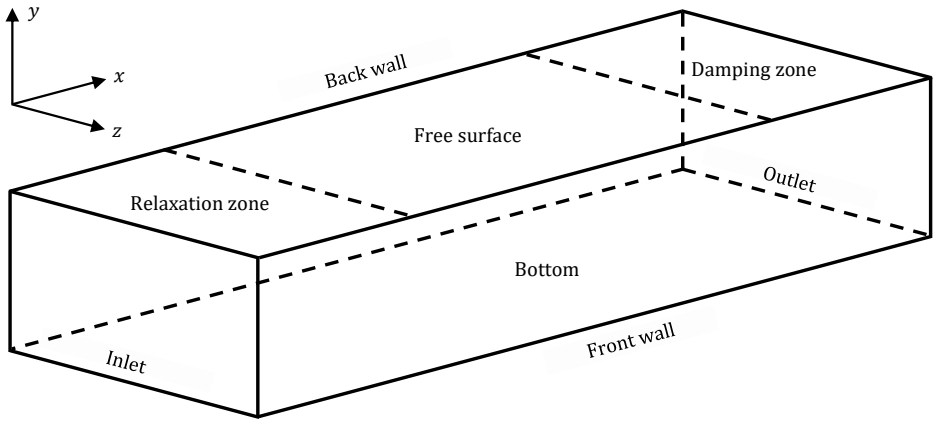

Figure 3.1: Schematic of a three-dimensional numerical wave tank.

is updated from a Lagrangian point of view. Thus, when a free-surface node is moving with velocity $\boldsymbol{v}$, the free-surface equations (3.2)–(3.3) can be modified by considering the material derivative

$$\frac{\delta()}{\delta t} = \frac{\partial()}{\partial t} + \mathbf{v} \cdot \nabla(). \tag{3.4}$$

In a full-Lagrangian approach, nodes move with the motion of water particles, i.e., $\mathbf{v} = \nabla\phi$. However, this then requires the nodes to be rearranged at every time step to prevent them from piling up. In contrast, free-surface nodes in a semi-Lagrangian approach move only with the vertical motion of water particles, i.e., $\mathbf{v} = (0, \frac{\delta\eta}{\delta t}, 0)$, in which case the method much simpler because rearrangement of nodes is unnecessary. This semi-Lagrangian approach is the one adopted by Lin et al. (2021) [90], meaning that the free-surface boundary conditions are rewritten as

$$\frac{\delta\eta}{\delta t} = \frac{\partial\phi}{\partial y} - \frac{\partial\phi}{\partial x}\frac{\partial\eta}{\partial x} - \frac{\partial\phi}{\partial z}\frac{\partial\eta}{\partial z} \quad \text{at} \quad y = \eta(x, z, t), \tag{3.5}$$

$$\frac{\delta\phi}{\delta t} = -g\eta - \frac{1}{2}\nabla\phi \cdot \nabla\phi + \frac{\delta\eta}{\delta t}\frac{\partial\phi}{\partial y} \quad \text{at} \quad y = \eta(x, z, t). \tag{3.6}$$

Lin et al. (2021) [90] then use a different but equivalent form of the KBC, presented in terms of the fluid particle velocity $\mathbf{U}_\eta$ at the free surface and the unit normal vector $\mathbf{n}$ of the free surface, as shown by Mayer et al. (1998) [102]. This leads to the KBC being rewritten as

$$\frac{\delta\eta}{\delta t} = \frac{\mathbf{U}_\eta \cdot \mathbf{n}}{n_y}, \tag{3.7}$$

where n_y is the vertical component of $\mathbf{n}$.

To complete the boundary value problem in the NWT, additional conditions are required at the remaining boundaries. For problems involving wave generation, a relaxation zone is placed at the inlet boundary, i.e., if f is either ϕ or η, then

$$f = \alpha_R f_{\text{computed}} + (1 - \alpha_R) f_{\text{analytical}} \tag{3.8}$$

where f_{computed} is the computed value from the solver, $f_{\text{analytical}}$ is the analytical value of target wave, and α_R is the relaxation function. Lin et al. (2021) [90] specifically use an exponential relaxation function [47, 75]

$$\alpha_R(\sigma) = 1 - \frac{\exp(\sigma^{3.5}) - 1}{\exp(1) - 1} \tag{3.9}$$

where σ is a function that is equal to 1 at the start of the relaxation zone and 0 at the end; namely,

$$\sigma = \frac{x_{\text{end}} - x}{x_{\text{end}} - x_{\text{start}}}. \tag{3.10}$$

Conversely, for wave absorption, a damping zone is placed at the outlet, i.e., if f is either ϕ or η and $\nu(x)$ is a damping function, an extra term $-\nu(x)f$ is added to the free-surface boundary equations (3.6) and (3.7). In Lin et al. (2021) [90], $\nu(x)$ is defined as

$$\nu(x) = \begin{cases} \alpha\omega\left(\frac{x - x_0}{\beta\lambda}\right)^2 & \text{for } x \geq x_0, \\ 0 & \text{for } x < x_0, \end{cases} \tag{3.11}$$

where x_0 is the start of the damping zone, α is the damping strength, β is the length of the zone (in multiples of wavelength), λ is the wavelength, and ω is the angular wave frequency. Finally, at fixed solid boundaries such as the bottom of the NWT, the impermeable boundary condition for ϕ is used:

$$\frac{\partial \phi}{\partial \mathbf{n}} = 0, \tag{3.12}$$

where $\mathbf{n}$ is the unit normal vector.

Once the velocity potential has been determined by solving the boundary-value problem, the pressure field p can be predicted throughout the domain by using Bernoulli's equation:

$$p = \rho\left(\frac{\partial \phi}{\partial t} + \frac{1}{2}\nabla\phi \cdot \nabla\phi + gy\right), \tag{3.13}$$

where ρ is the water density.

3.1.2 Numerical implementation

As mentioned previously, the Lin model was developed in OpenFOAM and is based on the FVM. A detailed description of the finite-volume formulation in OpenFOAM was given in Chapter 2, albeit for the Navier-Stokes sytem. However, something similar is done to solve Laplace's equation (3.1) in the Lin FNPF model. To be specific, the discretisation is done in the same way as the diffusion term in Section 2.2.2.6, i.e., it is first integrated over a control volume P,

$$\int_{V_P} \nabla^2\phi = \int_{V_P} \nabla \cdot (\nabla\phi), \tag{3.14}$$

then converted into a surface integral using Gauss' theorem,

$$\int_{V_P} \nabla \cdot (\nabla\phi) = \oint_S (\nabla\phi) \cdot d\mathbf{S}, \tag{3.15}$$

and finally discretised by summing over the cell face values,

$$\oint_S (\nabla\phi) \cdot d\mathbf{S} = \sum_f \mathbf{S}_f \cdot (\nabla\phi)_f, \tag{3.16}$$

where $\mathbf{S}_f$ is the outward pointing face area vector defined in Equation (2.14). The specialised `fvm::laplacian` function solver is then used, along with a non-orthognal correction scheme, to solve throughout the fluid domain to obtain the velocity potential solution.

The free-surface boundary equations (3.7) and (3.6) also have to be advanced in time to obtain the instantaneous free-surface elevation and potential at each time step. In the Lin model, this is done using the first-order explicit Euler scheme. The FNPF model is of course a single-phase model, so the mesh nodes on the free surface also have to be to moved to account for the motion of the free-surface calculated by the KBC. In the Lin model, the semi-Lagrangian approach is adopted (as detailed in Section 3.1.1), so the mesh nodes move only in the vertical y-direction. However, the free-surface variable η is theoretically stored at free-surface faces, so the value of η has to first be interpolated to the free-surface nodes before they can be moved. This is done via an inverse distance-weighted interpolation scheme available in OpenFOAM.

After the free-surface nodes have been moved, the rest of the mesh nodes also have be moved so that the motion is distributed properly throughout the domain. In the Lin model, the distribution (or 'diffusivity' in OpenFOAM) is done according to the quadratic inverse of the distance from from the free-surface boundary. Moreover, the velocity $\mathbf{u}$ is explicitly required during the mesh update procedure and for the adaptive time-stepping procedure outlined in Section 2.3.3.4, so the gradient of ϕ has to also be calculated in the fluid domain before the mesh can be moved. This is done using the `fvc::grad` function in OpenFOAM, which is talked about in more detail in Chapter 4. In addition to the KBC, the DBC is also then needed to obtain the velocity potential solution in the fluid domain, otherwise the potential boundary condition at the free surface would be incorrect. However, given that the two equations are coupled via the temporal derivative of η, this can only be done after the mesh has been updated. Finally, as mentioned previously, the Lin model also implements a fourth-order damping correction scheme to ensure stability. Full details of this scheme and its implementation can be found in Lin et al. (2021) [90] but are omitted here because most are not important to this work. However, two things that are important are the key parameters that control the amount of dissipation: the

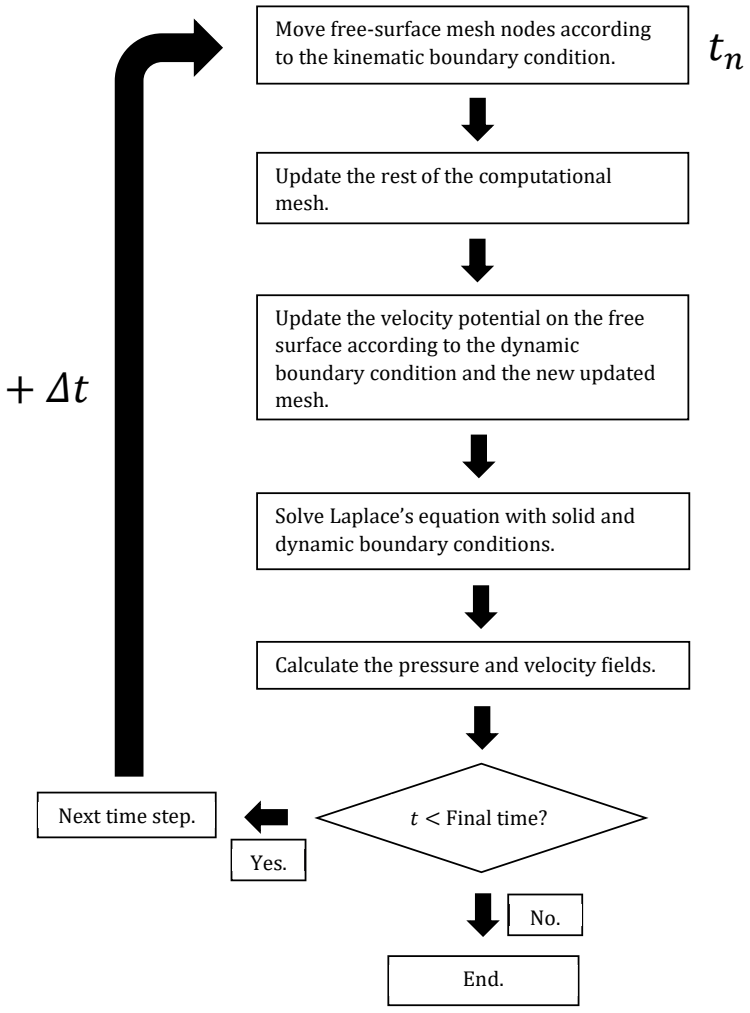

Figure 3.2: Lin model computational procedure (without numerical damping).

'correction coefficient' β_{FODC}, shown in equation (16) of [90], and the damping frequency (in time steps). These parameters are referred to during the validation test cases in this work.

A flowchart that summarises the full Lin model computational procedure for a general time step, without the numerical damping, is shown in Figure 3.2. First, the free-surface mesh nodes are updated using the KBC (3.7), followed by the rest of the computational mesh. Next, Laplace's equation is solved in the fluid domain along with the solid boundary condition and the DBC (3.6) which can now be updated given that the KBC and the mesh has been updated. The velocity and pressure (using Equation (3.13)) are then calculated: the velocity will be used to calculate the next time step and for the next mesh update.

3.2 Hypothesis on why the sawtooth instability occurs in the Lin FNPF model

As mentioned Section 1.3.2, the direct source of the sawtooth instability in FNPF models has never been definitively proven. It is clear that there could an accumulation of numerical error in the model, at the free-surface, that arises during numerical integration of the free-surface boundary conditions. Indeed, it is well known that the numerical solution procedure for problems governed by Laplace's equation with Dirichlet and/or Neumann boundary conditions generally provides smooth results, but in the case of FNPF models, the free-surface boundary equations are nonlinear and coupled which instead poses significant difficulties in ensuring accurate evaluation during the numerical integration procedure. Moreover, from the literature review in Section 1.3.2, it is clear that many semi-Lagrangian models—like Lin et al. (2021) [90]—encounter such instabilities, indicating that this is a problem inherent to them. Given the reformulation of the free-surface boundary equations in semi-Lagrangian models, the aforementioned accumulation of errors will most likely be present, especially if the physical characteristics of these equations—particularly the KBC equation—are not considered. This is the hypothesised cause of the instability in the Lin et al. (2021) [90] model with the use of the alternative KBC (3.7).

To expand on this hypothesis, the characteristics of the original KBC (3.5) are considered. This equation is very similar to the 2-D advection equation but instead has a source term $F(y) = \frac{\partial \phi}{\partial y}$. Moreover, given that the free-surface equations are a coupled set of equations, the evolution of the free-surface elevation η over time is dependent on the evolution of the velocity potential ϕ. As a consequence, the KBC is not strictly hyperbolic like the advection equation, but can instead be considered as *advection dominated* due to its similarity. It is well known that these sorts of equations are notoriously difficult to handle by using classical numerical schemes such as central differences; hence, in this work it is proposed that a different method be used to discretise the advection terms in the KBC in the Lin et al. (2021) [90] model.

In order to match the order of numerical solution accuracy of the governing equation (3.1), the new method for the KBC equation should be at least second order. The new method

should also be physically sound, accurate, and robust for wave hydrodynamics. At the same time, it should not be over complicated, but simple and easy to implement, and economic for use. Considering these requirements, a second-order scheme motivated by a total variation diminishing (TVD) approach is proposed. TVD schemes are a class of *high-resolution schemes* for hyperbolic partial differential equations that are known to produce solutions free from spurious oscillations whilst remaining accurate around shocks and discontinuities. In particular, they are proven to produce oscillation-free solutions when used to discretise advection terms in advection-dominated equations like the KBC. In view of this, it will be investigated whether such a method can effectively discretise the advection terms in the KBC, and consequently successfully stabilise the Lin FNPF model.

A key advantage of TVD schemes is that they can also aptly handle sharp gradients, which is of particular importance when it comes to modelling steep waves. In this situation, the proposed TVD method is the perfect fix due to its montonicity-preserving property. This is whereby, in the face of a sharp gradient, the numerical solution remains monotone before and after the advection terms are calculated, ensuring that there are no new local extrema—which is exactly what occurs in the formation of a sawtooth. The key to ensuring the scheme is monotonicity preserving is the flux limiter which directly modifies the advective fluxes in the scheme so that the total variation of the solution does not increase in time. Furthermore, as already outlined, the TVD method is robust and computationally efficient, as well as retaining second-order solution accuracy. Finally, the TVD method is simple and suited to a wide range of applications—no tuning of parameters is required. This is in contrast to a number of FNPF models, such as the Lin model, in which the amount of artificial dissipation needs to be tuned for different cases in order to ensure stability.

3.3 Computational formulation of the new TVD-based scheme

3.3.1 Updating the free-surface variable η in time

Time integration in the Lin model was carried out using the first-order Euler scheme, so the same is done in the present work. Moreover, for simplicity, only a 2-D NWT is considered in this formulation. However, the extension to three dimensions is straightforward by following the same logic. The computational mesh in OpenFOAM is three dimensional, but it can still be used for 2-D models by using a single cell in the z-direction. Clearly this works because the FVM is cell centred, so all information is stored in the same two-dimensional xy-plane. Furthermore, in this work, only a structured computational mesh is considered due to the fact this FNPF model is only used for wave propagation and wave-wave interaction. Finally, as already mentioned, the proceeding method for the advection terms is constructed by closely following the TVD methodology.

To start, the KBC (3.5) is written in 2-D form as

$$\frac{\delta\eta}{\delta t} = v - u\frac{\partial\eta}{\partial x}, \quad \text{where } v = \frac{\partial\phi}{\partial y} \text{ and } u = \frac{\partial\phi}{\partial x}. \tag{3.17}$$

Now, if $i-\frac{1}{2}$ and $i+\frac{1}{2}$ denote the left and right edge respectively of a computational free-surface mesh face i, then the Euler method for time integration leads to the update for η on face i being

$$\eta_i^{n+1} = \eta_i^n + v_i^n\Delta t - \frac{u_i^n\Delta t}{\Delta x}(\eta_{i+\frac{1}{2}}^n - \eta_{i-\frac{1}{2}}^n). \tag{3.18}$$

If $u_i \geq 0$, setting $\eta_{i+\frac{1}{2}} = \eta_i$ and $\eta_{i-\frac{1}{2}} = \eta_{i-1}$ recovers the First Order upwind (FOU) scheme—a first-order TVD scheme that is known to be the most numerically stable but suffers severely from numerical dissipation. For a second-order evaluation of $\eta_{i+\frac{1}{2}}$ and $\eta_{i-\frac{1}{2}}$, a correction term needs to be added. This is where the idea of a flux limiter and the TVD property comes in.

3.3.2 TVD property

To construct a TVD scheme for the advection terms, it first needs to be outlined what actually makes a scheme TVD. First, an explicit numerical scheme used to calculate some variable f in cell x_i and at time t_{n+1} has the general form

$$f_i^{n+1} = G(f)_i^n = G(f_{i-p}^n, ..., f_i^n, ..., f_{i+q}^n), \quad p = 1, 2, ..., q = 1, 2, ... \tag{3.19}$$

This scheme is said to be *monotone* if and only if the function G is an increasing (or decreasing) function of all its arguments, i.e., G is monotonically increasing if

$$\forall\ f_i, f_j \text{ such that } f_i \leq f_j, \text{ we have } G(f_i) \leq G(f_j) \quad \text{(and vice versa)}. \tag{3.20}$$

The scheme is then also said to be *monotonicity preserving* if

$$f_{i+1}^n \geq f_i^n \quad \forall i \implies f_{i+1}^{n+1} \geq f_i^{n+1} \quad \forall i. \tag{3.21}$$

A monotonicity-preserving scheme creates no new undershoots or overshoots in the solution, meaning that it should be free of spurious oscillations, and is therefore the type of scheme that should be constructed. To construct this sort of scheme, the total variation TV of a data set $\{f_1, f_2, ..., f_{n-1}, f_n\}$ is first defined as

$$TV(f) = \sum_{i=1}^{n-1} \mid f_{i+1} - f_i \mid . \tag{3.22}$$

The scheme is then said to be *total variation diminishing (TVD)* if

$$TV(f^{n+1}) \leq TV(f^n), \tag{3.23}$$

which will clearly be monotonicity preserving. Furthermore, it can be shown that a monotone scheme is TVD, and hence monotonicity preserving. Therefore, to construct a TVD scheme, it is sufficient for the scheme to be monotone. For more details, please refer to the work of Harten (1983) [61].

3.3.3 Flux limiter

Referring back to the update for η (3.18), it is clear that the second-order correction must ensure that the scheme for the advection terms is monotone, and hence TVD. The way this is done is by using a flux limiter; a function defined by the generalised second-order upwind-biased evaluation of $\eta_{i+\frac{1}{2}}$ when $u_i \geq 0$:

$$\eta_{i+\frac{1}{2}} = \eta_i + \frac{1}{2}\psi(r_{i+\frac{1}{2}})(\eta_{i+1} - \eta_i). \tag{3.24}$$

Here, ψ is called the *flux limiter function* and is dependent on r, which is the ratio of upwind to downwind gradients of η for face i. For example, given that $u_i \geq 0$ in (3.18) and (3.24), the ratio of upwind to downwind gradients is

$$r_{i+\frac{1}{2}} = \frac{\eta_i - \eta_{i-1}}{\eta_{i+1} - \eta_i}. \tag{3.25}$$

For the scheme to then be monotone and therefore TVD, as well as second order, the flux limiter function $\psi(r)$ must satisfy certain constraints derived by Sweby (1984) [130]:

- If $0 < r < 1$, the upper limit is $\psi(r) = 2r$, so for TVD schemes $\psi(r) \leq 2r$.
- If $r \geq 1$, the upper limit is $\psi(r) = 2$, so for TVD schemes $\psi(r) \leq 2$.

These constraints result in the TVD region visualised in Figure 3.3 (a). From this it can be deduced that, the key to ensuring that the numerical scheme is TVD is to construct a flux limiter function $\psi(r)$ that remains in this region for all r. Moreover, Sweby (1984) [130] also deduced that the choice of $\psi(r)$ dictates the order of the scheme. For a scheme to be second order, $\psi(r)$ must satisfy further constraints:

- If $0 < r < 1$, the lower limit is $\psi(r) = r$, the upper limit is $\psi(r) = 1$, so for TVD schemes $r < \psi(r) < 1$.
- If $r \geq 1$, the lower limit is $\psi(r) = 1$, the upper limit is $\psi(r) = r$, so for TVD schemes $1 \leq \psi(r) \leq r$.
- $\psi(r)$ must pass through the point (1, 1) in the $r - \psi(r)$ diagram.

These additional constraints result in a partition of the larger TVD region into separate second and first-order regions, as shown in Figure 3.3(b). Figure 3.3(c) then also shows some popular flux limiter functions plotted on a $r - \psi(r)$ diagram, with the corresponding expressions shown in Table 3.1.

For the choice of flux limiter in the present work, the Van Albada 2 limiter, defined as

$$\psi(r) = \begin{cases} \frac{2r}{r^2+1}, & r > 0 \\ 0, & r \leq 0, \end{cases} \tag{3.26}$$

is chosen. Incidentally, this limiter is actually only first-order accurate for $r > 1$. However, it still successfully produced sufficiently accurate results in the present work. Nevertheless, for completeness, an analysis of different flux limiter functions will be done in Chapter 5.

Limiter	$\psi(r)$
Van Leer	$\frac{r+\|r\|}{1+\|r\|}$
Van Albada 1	$\frac{r^2+r}{r^2+1}$
Van Albada 2	$\frac{2r}{r^2+1}$
MinMod	$\max[0, \min(1, r)]$
SuperBee	$\max[0, \min(1, 2r), \min(2, r)]$
Sweby	$\max[0, \min(1, \beta r), \min(\beta, r)]$

Table 3.1: Expressions for some popular flux limiter functions.

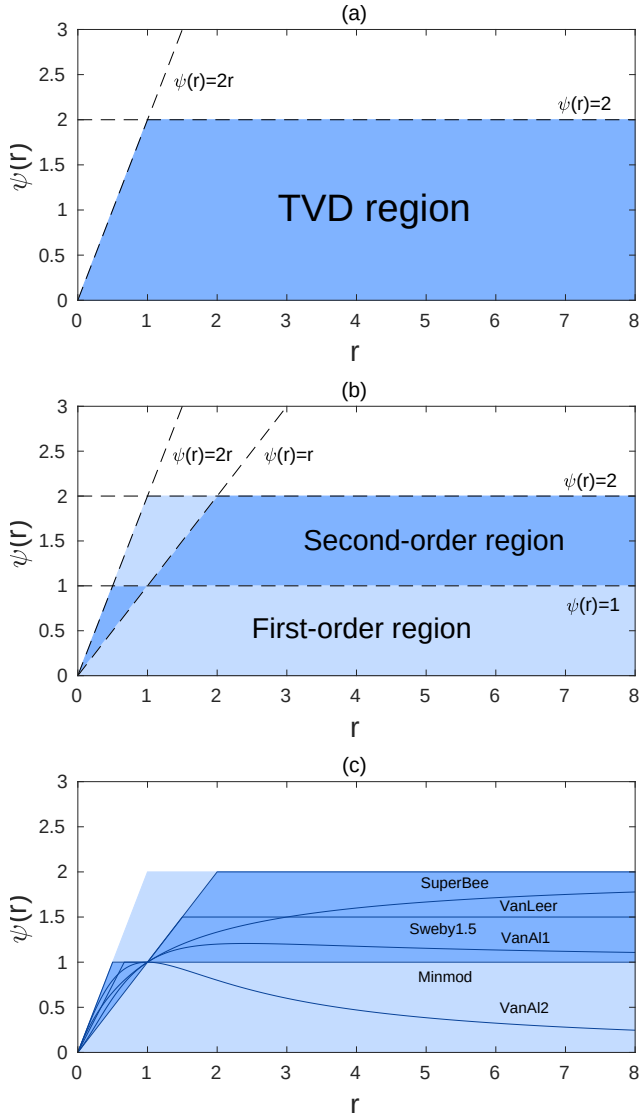

Figure 3.3: (a) TVD region for the flux limiter function $\psi(r)$, (b) First and second-order regions, (c) Popular functions.

3.3.4 Final formulation

In addition to (3.24) and (3.25) at the right edge $i+\frac{1}{2}$, at the left edge $i-\frac{1}{2}$

$$\eta_{i-\frac{1}{2}} = \eta_{i-1} + \frac{1}{2}\psi(r_{i-\frac{1}{2}})(\eta_i - \eta_{i-1}), \tag{3.27}$$

where

$$r_{i-\frac{1}{2}} = \frac{\eta_{i-1} - \eta_{i-2}}{\eta_i - \eta_{i-1}}. \tag{3.28}$$

Finally, using(3.24), (3.25), (3.26), (3.27), and (3.28) in (3.18) gives the update for η on face i given that $u_i \geq 0$:

$$\eta_i^{n+1} = \eta_i^n + v_i^n \Delta t - \frac{u_i^n \Delta t}{\Delta x}\left\{[\eta_i^n + \frac{1}{2}\psi(r_{i+\frac{1}{2}})(\eta_{i+1}^n - \eta_i^n)] - [\eta_{i-1}^n + \frac{1}{2}\psi(r_{i-\frac{1}{2}})(\eta_i^n - \eta_{i-1}^n)]\right\}, \tag{3.29}$$

where $\psi(r_{i+\frac{1}{2}})$ and $\psi(r_{i+\frac{1}{2}})$ are calculated accordingly. Note that an equivalent result can be derived in the same way for when $u_i < 0$ but is omitted here. Equation (3.29) is then used in the original KBC (3.5) for the mesh update. The KBC version (3.7) is consequently discarded.

3.4 Validation of the new stabilised model

To comprehensively validate the proposed method, three test cases are considered in this work and will be discussed in Chapters 5 and 6. The first, is regular fifth-order Stokes wave propagation in a two-dimensional numerical wave tank, with results compared to analytical solutions and those of Lin et al. (2021) [90]. The second is focused wave propagation in which irregular extreme wave events are simulated. For this case, the numerical and practical experiments of Ning et al. (2009) [111] are investigated and results compared. All the above are discussed in Section 5.2. For the third test case, 2-D and 3-D wave shoaling is considered to test the ability of the new model to capture the transformation of propagating waves due to variable bathymetry. In 2D, the experiments of Beji and Battjes (1993, 1994) [3, 4] are investigated, whereas in 3D the experiments of Whalin (1971) [143] are investigated. These cases are discussed in Section 6.1. In addition to this, the superiority of the new model over the Lin model in terms of energy conservation is also proven and the choice of flux limiter is investigated.

It should be noted that, for each case, the first thing established is whether the sawtooth instability has been eliminated without using numerical damping. Only then are the accuracy of the results explored. As already stated, numerical damping is required for each validation test case when it comes to the Lin model, and hence any Lin et al. (2021) [90] results used for comparison are when damping is being used—unless of course stated otherwise. The choice of test cases for validation is also primarily for comparison to the work of Lin et al. (2021) [90], i.e., fifth-order Stokes wave propagation and wave shoaling. However, an additional focused waved case is also included because of its importance in achieving the primary goal on this work; namely, investigating complex wave structure interaction via an integrated hydrodynamic model. For most of these test cases, unless stated otherwise, a value of $C_{\max} = 0.2$ is also used in the adaptive time stepping procedure (2.56) for both the new and Lin models.

Henceforth, the new improved model will be referred to as the 'stabilised model' in any validation cases so as to clearly distinguish it from the original Lin model. Furthermore, the validation of the new stabilised model in this work is done in conjunction with the validation of the proposed integrated model. This is purely the authors choice as the best structure to present their work. Consequently, when it comes to validation for the integrated model, the stabilised model will instead then be referred to as the FNPF model or 'FNPFFoam' so as to distinguish it from the Navier-Stokes.

4

Integrated Methodology

It was stated in Section 1.7.1 that a one-way domain decomposed coupling will applied in the present work via an overlapping relaxation zone. This proposed model, which will be called 'IntegratedFoam' has the primary advantage that both constituent solvers—namely, FNPFFoam and interFoam—have been developed in the same numerical framework, OpenFOAM, and are consequently also both based on the same numerical method, i.e., the finite volume method (FVM). Why this is advantageous is discussed in further detail in this chapter. In particular, it will be discussed how it makes the choice of coupling method simple to implement, with specific references to OpenFOAM features and functionalities. In addition, it will be illustrated how a number of consequential advantages are exploited to ensure that the method for transferring information is simple and that the coupling is stable and accurate. The full coupling procedure is then presented, including how information is transferred, and how the relaxation correction is applied. Finally, the computational procedure is described and the method for parallelisation is briefly discussed.

4.1 Advantages of the proposed integrated model

4.1.1 Implementation of an overlapping relaxation zone

The key to the proposed model and the coupling procedure is an overlapping relaxation zone. This will ensure that information can be transferred smoothly from FNPFFoam to interFoam. Without it, there is a danger of there being a lack of continuity between each solution due the underlying physics of each solver being different. This could potentially then lead to errors and subsequently make the coupling unstable. Moreover, this zone will also absorb any reflected waves in the numerical wave tank (NWT), again aiding stability and accuracy. The pivotal OpenFOAM functionality required to implement this overlapping relaxation zone is 'region-Properties' which allows for the development of 'multi-region' solvers. It is most commonly used for the problems involving both solids and fluids, such as conjugate heat transfer, whereby different numerical solvers operate in different regions and information is transferred from one region to another through coupled boundary conditions. However, it can also be used in the development of NWTs; the interFoam–compressibleInterFoam coupling by Martínez Ferrer et al. (2016) [101] was done using this functionality. Although, the coupled boundary conditions in this case were via an interface—not an overlapping region. However, Ma et al. (2018) [100] used the regionProperties functionality to create an overset mesh solver in OpenFOAM which did indeed generate two separate regions which overlapped in the way that is required in this work, but it only involved two separate interFoam regions, not different solvers.

In terms of the proposed IntegratedFoam model, the regionProperties functionality allows for the generation of two separate and independent computational meshes: one on which a N-S region Ω_{NS} is defined and which is governed by the interFoam solver, and one on which an FNPF region Ω_{FNPF} region is defined and which is governed by the FNPFFoam solver. Crucially, these meshes can then be overlapped or 'overset' to create an overlapping region through which information can be transferred and corrected via relaxation. The key thing to note here is that this process is very straightforward; a single OpenFOAM functionality has to be used to couple the two solvers, with only minor edits having to be made to each solver to fit the 'regionProperties' framework. This would undoubtedly be more complex if both constituent solvers had not been developed in OpenFOAM.

4.1.2 Handling a mismatch in variables

As discussed in Sections 1.5.3 and 1.7.1, a critical problem that arises during the transfer of information is that the fundamental physics underlying each constituent model is different, meaning there is a mismatch in variables. In FNPFFoam, the free-surface variable η and the velocity potential ϕ are the primary physical quantities; whereas, in interFoam, it is the velocity $\mathbf{u}$, pressure p, and volume fraction α. Given a one-way coupling, with information being transferred from FNPFFoam to interFoam, the velocity $\mathbf{u}$ must be calculated from the

potential ϕ and α has to be derived from η. The pressure can be transferred using Bernoulli's equation (3.13) but this may still be discontinuous given the potential flow assumptions.

Given the definition of the velocity potential ϕ, $\mathbf{u} = \nabla\phi$, it is clear a gradient scheme has to be applied to calculate the velocity $\mathbf{u}$. However, doing this accurately and efficiently can often be challenging and time consuming. Moreover, care has to be taken so that no significant numerical errors are accumulated that could affect the accuracy of the solution and stability of the coupling. Tackling this challenge is not then made any easier if the two solvers are based on different numerical methods and have been developed in different frameworks, and in some cases it could make it even harder. However, with the proposed IntegratedFoam model, this problem is easily avoided; the velocity $\mathbf{u}$ is already calculated through the finite-volume FNPFFoam solution procedure and can be transferred accordingly. Specifically, it is calculated in the entire computational domain using the OpenFOAM function `fvc::grad()` and is needed to update the position of the computational mesh to account for the fluid motion. In terms of the actual scheme that is implemented by this function, OpenFOAM has a range of different options: Gauss linear, least squares, fourth-order least squares, and limited versions of each. The function is also fully parallelised and has been proven to provide accurate, stable, and efficient results. This clearly simplifies things greatly and avoids any added complexity and risk. This means that the method for transferring the velocity is simple and consequently helps ensure the coupling is stable and accurate.

4.1.3 Handling non-conforming meshes

A further problem discussed in Sections 1.5.3 and 1.7.1—linked to the problem of mismatching variables—is the problem of nonconforming meshes: interFoam generally require a finer mesh for stable and accurate solutions compared to FNPFFoam. Again, if the two solvers were based on different numerical methods and had been developed in different frameworks, information transfer and associated gradient calculations would be made even more challenging than they already would be to achieve a stable and accurate coupling. Methods to tackle this problem include the 'spatial-temporal interpolation scheme' for qaleFOAM by Yan et al. (2019) [150]. However, designing and implementing such schemes again adds an extra layer of complexity, with extra care having to be taken to ensure that stability, accuracy, and efficiency is maintained. However, with the proposed IntergratedFoam model, this problem is again easily avoided through the use of existing an OpenFOAM functionality that makes the required interpolation straightforward and accurate. The exact interpolation function used, and its underlying method, will be outlined in Section 4.2.1 but the advantage here is clear in that the interpolation can be done easily because each constituent solver has been developed in OpenFOAM. Overall, this functionality in conjunction with the 'regionProperties' functionality and the `fvc::grad()` function is the core of what makes the method for transferring information simple, accurate, and efficient.

4.1.4 Handling of mismatching time steps

The last problem discussed in Sections 1.5.3 and 1.7.1 is the inherent problem of mismatching time steps: interFoam needs smaller time steps for a stable and accurate solution when compared to FNPFFoam. This is another problem that the Yan et al. (2019) [150] 'spatial-temporal interpolation scheme' tackles for qaleFOAM alongside the problem of nonconforming meshes. Another way to mitigate this problem is to use the max allowed time step for the N-S solver as the global time step for both constituent solvers. Yan et al. (2019) [150] stated that any detrimental effects on efficiency are probably negligible using this method given that FNPF solvers are generally much faster than the NS ones. This is also true in the present work; hence, the max allowed local time step for interFoam will be used as the global time step for IntergatedFoam and, consequently, the local time step for FNPFFoam. To what extent this does or does not affect the efficiency of the model will be explored further in Chapters 5–6.

4.2 Coupling procedure

4.2.1 Transferring u and p

To demonstrate the method for transferring information in more detail, an example 2-D IntegratedFoam governed NWT is illustrated in Figure 4.1. Two independent meshes, Ω_{FNPF} and Ω_{NS}, are generated with an overlapping zone Ω_{OZ} defined on Ω_{NS}, i.e., $\Omega_{\mathrm{OZ}} \subset \Omega_{\mathrm{NS}}$. In addition, an interface $\partial\Omega$ is defined as the left-hand-side boundary of Ω_{NS}. The process of information transfer then has two stages:

1. Establishing the *domain connectivity information (DCI)*.
2. Interpolating the values of $\mathbf{u}$ and p.

4.2.1.1 Establishing the domain connectivity information

Recall that a one-way coupling is being implemented so information is being transferred from Ω_{FNPF} to Ω_{OZ}. Hence, for every cell $i \in \Omega_{\mathrm{OZ}}$, the DCI stage involves locating the corresponding cell $\mathrm{I} \in \Omega_{\mathrm{FNPF}}$ from which the information is being transferred. Logically, this will be the closest such cell in the computational space. For example, in Figure 4.1, consider cell $a \in \Omega_{\mathrm{OZ}}$ with its centre marked by the red cross. Recall that OpenFOAM is cell centred, so the cell in Ω_{FNPF} whose centre is closest to the centre of cell a is located: this is clearly cell $\mathrm{A} \in \Omega_{\mathrm{FNPF}}$ whose centre is marked by the black circular point. The index of this cell is then recorded as the piece of information that *connects* these two cells on two independent domains. The same process can then be carried out for each cell in Ω_{OZ}, e.g., b, c, and d which would all also record the index of cell A. This stage is completed before either solver is run for the current time step.

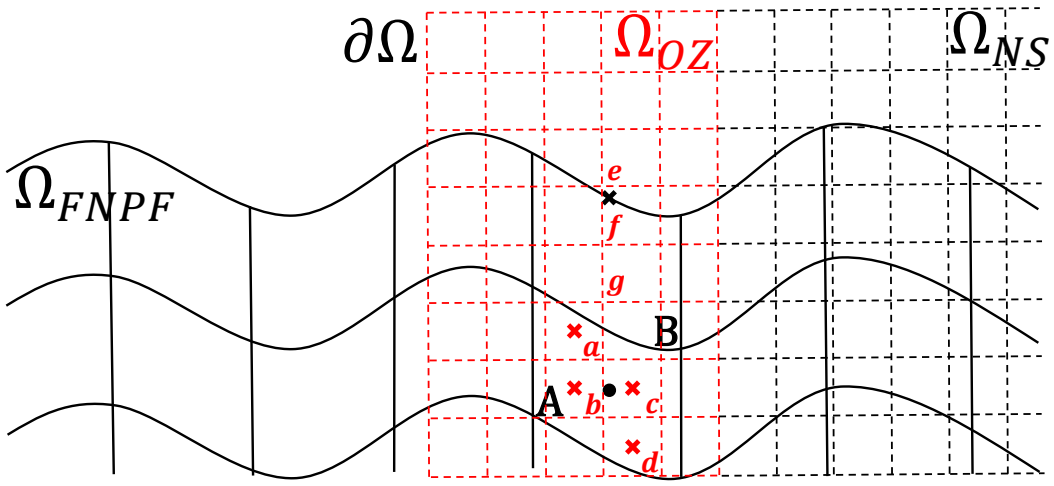

Figure 4.1: Example 2-D IntegratedFoam domain.

4.2.1.2 Interpolating the relevant information

The second stage is then actually interpolating the values of $\mathbf{u}$ and p from every documented Ω_{FNPF} cell to each corresponding Ω_{OZ} cell. The particular interpolation class used in OpenFOAM is `interpolationCellPoint` which interpolates from the centre to an arbitrary location within a cell. It works by first decomposing each face of the cell into triangles which can then be used to define tetrahedra connected to the cell centre. The specific tetrahedron which encloses the point is then located and the values are interpolated using inverse distance weights calculated from the barycentric coordinates of the point. To see how this works in the present work, again consider Figure 4.1. Cells a, b, c, and $d \in \Omega_{\text{FNPF}}$ all locate cell A $\in \Omega_{\text{OZ}}$ during the DCI stage. These cells also all lie within the same computational space as cell A and hence their positions are all arbitrary locations within it. Therefore, the `interpolationCellPoint` class is applicable here. This interpolation stage is done after the DCI stage with all values being stored for the relaxation correction at the end of the time step.

4.2.2 Estimating the water-volume fraction α from the free-surface variable η

As mentioned previously, one problem that cannot be avoided is having to estimate the water-volume fraction α from the free-surface variable η. Nevertheless, this can still be easily done in OpenFOAM given that the physical location of the Ω_{FNPF} free-surface boundary relative to any cell $i \in \Omega_{\text{OZ}}$ is easily obtainable. For example, consider cells $e, f, g \in \Omega_{\text{OZ}}$ in Figure 4.1. For each of these cells, the first thing that has to be done is find the closest free-surface face centre in Ω_{FNPF}: this is where the variable η is stored and is also the point at which it is defined in the discretisation (i.e., the calculated value of η is equal to the physical y-coordinate of this point). In this example, the closest such face is clearly the one marked by the black cross on the

boundary of cell B $\in \Omega_{\text{FNPF}}$. The y-coordinates of cells e, f, and g can then be compared with the value of η at this point. Clearly, for cells like e and g, $\alpha = 1$ and 0 respectively as the whole cell lies above or below the free surface. However, for cells like f where the Ω_{FNPF} free-surface boundary actually passes through the cell, the ratio of the wetted area against the total cell area can instead be calculated. In the present work, this method of estimation works regardless of whether a 2-D or 3-D NWT is considered because the input waves are always 2D. Therefore, a cell such as f can always be considered as a 2-D square from which the wetted area can then be found through simple area integration. To do this, the equation of the straight line that the Ω_{FNPF} free surface makes through the cell, and the two points at which the line intersects the boundaries (of the cell), have to be found. In the case that the free surface does not make a perfect straight line through the cell, i.e., when two Ω_{FNPF} cells meet, an approximation to a single straight line can be made instead. Given that the Ω_{FNPF} mesh is always much coarser than the Ω_{NS}, this approximation has a negligible affect on the accuracy of the estimation. The only other information then required is the coordinates of the cell vertices which can again be easily obtained in OpenFOAM.

4.2.3 Relaxation correction and damping

A relaxation correction is applied in Ω_{OZ} to ensure that there is a smooth transition from the FNPFFoam to interFoam solution and to absorb any reflected waves from the interFoam domain. The correction itself is applied in the same way as wave generation in FNPFFoam using Equations (3.8)–(3.10). Hence, if f is either $\mathbf{u}, p$, or α, then

$$f_{\text{OZ}} = \alpha_R f_{\text{NS}} + (1 - \alpha_R) f_{\text{FNPF}}, \tag{4.1}$$

where α_R is the exponential relaxation function

$$\alpha_R(\sigma) = 1 - \frac{\exp(\sigma^{3.5}) - 1}{\exp(1) - 1}, \tag{4.2}$$

σ is

$$\sigma = \frac{x_{\text{end}} - x}{x_{\text{end}} - x_{\text{start}}}, \tag{4.3}$$

and the subscripts *start* and *end* denote the start and end locations of Ω_{OZ}. Moreover, given that a one-way coupling is being applied in this work, waves also need to be damped out at the outlet of the interFoam domain to prevent reflection back in. Given this, an additional relaxation zone is placed at the end of Ω_{NS} in which the relaxation function is the opposite of Equation (4.2) so that $\alpha_R = 1$ at the start of the zone and $\alpha_R = 0$ at the right Ω_{NS} boundary. To do this, the function σ is also changed to

$$\sigma = \frac{x - x_{\text{start}}}{x_{\text{end}} - x_{\text{start}}}, \tag{4.4}$$

and the target value of each variable f is 0. Note that the size of the two zones is not discussed here but is analysed in detail in Chapter 5.

4.3 Computational procedure

A flowchart that summarises the full computational procedure of IntegratedFoam is shown in Figure 4.2. First, the two meshes are generated, the initial field values are initialised, and the boundary conditions are set. Next is the process of information transfer. The DCI information is first established, the volume fields $\mathbf{u}$ and p are then interpolated, and the water-volume fraction is estimated. Each of these interpolated/estimated values are stored ready for the relaxation correction. Note that these values can be interpolated/estimated and stored before interFoam is run due to fact it is a one-way coupling and the two solvers do not run simultaneously. FNPFFoam is then run and the free-surface position on Ω_{FNPF} is updated for the first time step. Note that, as mentioned previously, a single global time step is used. Given that interFoam usually requires a smaller time step, this global time step is chosen to be the maximum allowed time step for interFoam. Next, interFoam is run for the first time step to obtain the solution on Ω_{NS}. Finally, the relaxation (and damping) correction is applied and the values of $\mathbf{u}, p$, and α are updated in Ω_{OZ} on Ω_{NS}. The process is then repeated for the next time step until the final time.

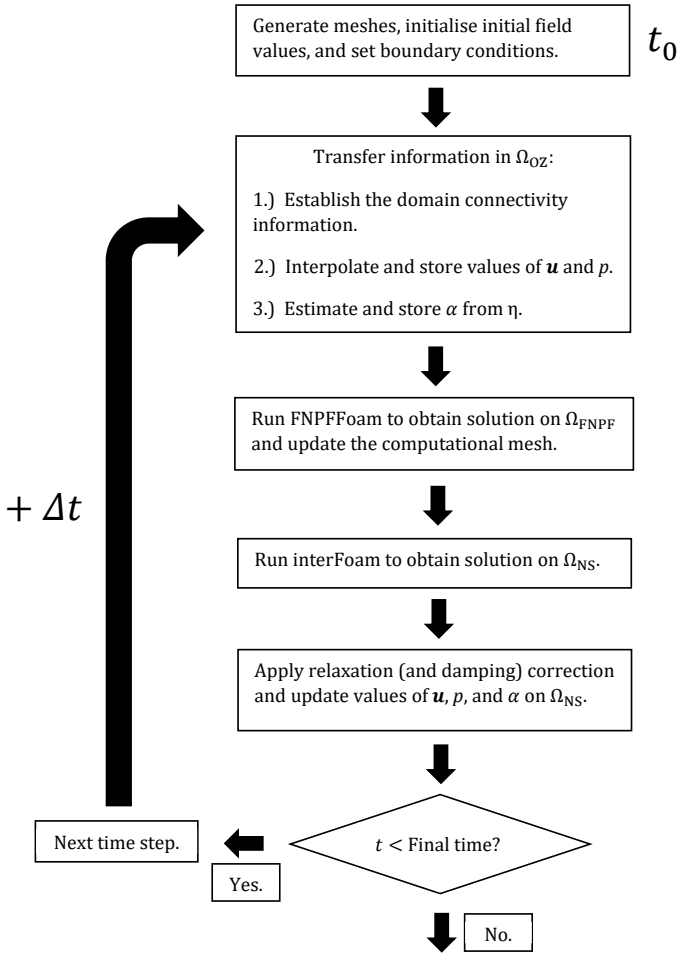

Figure 4.2: IntegratedFoam computational procedure.

4.4 Parallelisation

OpenFOAM fully supports parallel computing: each feature and functionality is fully parallelised. Parallelisation is implemented using domain decomposition: this is whereby the computational domain is decomposed into n non-overlapping subdomains which are each assigned to n separate processors. Each processor has its own independent process and communicates with other processors through the openMPI implementation of the standard message passing interface (MPI). The exchange of information between each subdomain is then done specifically through a zero-halo approach in which processors exchange information through a shared interface described by the '`processor`' boundary condition.

In IntegratedFoam, the decomposition is done manually depending on the specific geometric and computational setup for the case. Decomposition can be done arbitrarily, but as will be seen in Chapters 5 and 6, different parts of the solver, such as the coupling or interFoam, can take longer than others, so more or less processors may need to be assigned to each. An analysis of this will be alongside the test cases in proceeding chapters.

4.5 Validation of IntegratedFoam

To comprehensively validate the new integrated model in terms of its accuracy and efficiency, a number of test cases are considered. In Chapter 5, regular fifth-order Stokes wave propagation in a two-dimensional numerical wave tank is considered to test the model for all its relevant coupling parameters and to test mesh and temporal sensitivity. Chapter 6 then focuses on three wave-structure interaction cases. The first, discussed in Section 6.2, is fifth-order Stokes wave interaction with a 2-D floating body which tests the ability of the model to accurately compute the body motions in 2 degrees of freedom. The second, discussed in Section 6.3, is focused wave interaction with a fixed cylinder on which the hydrodynamic loads are calculated. The third, discussed in Section 6.4, is focused wave interaction with a 3-D floating wave energy converter device which tests the ability of the model to accurately compute the body motions in 6 degrees of freedom. A key thing that is also discussed throughout is computational time. As mentioned throughout, the whole point of developing integrated models is to increase efficiency whilst still being able to model wave-structure interaction. Therefore, a thorough analysis of computational time is given with each case.

5

Regular and Extreme Wave Propagation

As mentioned in Chapter 1, the main emphasis of the present work is to model wave interaction with offshore renewable structures, e.g., fixed monopile foundations, wave energy converter devices, or floating offshore wind turbines. The long-term performance of any such structure is dependent on its survivability due to the marine area in which they operate being naturally subject to harsh wave conditions. Ocean waves can hold enormous amounts of energy, so a structure will need to be able to withstand the force subjected on it by the largest in particular. However, the consistency of wave climate also needs to be taken into account as it is well known that ocean waves are generally random in nature: a structure will encounter a wide range of wave conditions but the likelihood of encountering the harshest may be very low. This can make the design and engineering process incredibly challenging, particularly if the structures are to be practically and financially feasible. Nevertheless, contemporary methods for predicting the *sea state*—the general state of the irregular free-surface for a large area of water—at any given location and point in time are very accurate and employ a deeper understanding of the ocean environment than was the case over recent decades. However, deterministic wave theories can still be used to describe regular free-surface waves. Although these theories are idealistic and do not accurately represent the randomness and irregularity of real-world sea states, they are still regularly used in the design of offshore structures interaction because of the useful information that can be garnered with relative ease and simplicity. In this chapter, the accuracy, efficiency, and sensitivity to parameters are tested for both the stabilised model and new integrated model via test case involving regular and irregular wave propagation.

5.1 Wave theories

5.1.1 Regular wave characteristics

According to Chakrabati (2005) [16], regular waves are characterised by the fact each wave cycle has exactly the same form, i.e., the wave parameters that describe the wave are invariant from cycle to cycle. For any regular wave theory, three key parameters are needed to describe a wave:

1. *period* T, which is the time taken for one wave cycle, i.e., the time taken to for two successive crests to pass a fixed point;
2. *height* H, which is the vertical distance between a crest and neighbouring trough;
3. and *water depth* h, which is the mean vertical distance from the still free-surface water level to the seabed.

From these key parameters, other useful parameters can also be derived. These include:

- *wavelength* λ, which is the horizontal distance between two adjacent crests or troughs;
- *celerity* (or *phase velocity*) c, which is the velocity of a crest;
- *frequency* $\omega = \dfrac{2\pi}{T}$, which is the number of repeating units of a propagating wave per unit of time;
- *wavenumber* $k = \dfrac{2\pi}{\lambda}$, which is the number of repeating units of a propagating wave per unit space.

Ocean waves are in general generated by a variety of different disturbing and restoring forces and occur over a wide range of scales. In the context of this work, the primary type of wave in question are *wind waves*, or *surface gravity waves*, which are generated by wind and where gravity is the main restoring force. The simplest and most widely used regular wave theory for the propagation of wind waves is Airy wave theory which provides a linear description of low amplitude (and steepness) sinusoidal waves in deep water (usually defined as water with $h > 1/2\lambda$). It assumes that the flow is incompressible, inviscid, irrotational and that there is constant mean depth. It can be used for a number of applications but obviously fails to take into account nonlinear effects and starts to break down in intermediate to shallow water depth ($h > 1/2\lambda$). However, this theory can also be used to derive the *dispersion relation* which provides a relationship between the frequency ω and wavenumber k. For finite water depth h, this is given as

$$\omega^2 = gk\tanh(kh), \tag{5.1}$$

from which the celerity c can be defined as

$$c = \frac{\omega}{k} = \frac{gT}{2\pi}\tanh(kh). \tag{5.2}$$

Interesting properties of ocean waves can then be derived by examining the limits of shallow and deep water. In deep water, $\tanh(kh) \to 1$ as $kh \to \infty$. Using this in Equations (5.1) and (5.2) then leads to the deep-water wave celerity

$$c = \sqrt{\frac{g\lambda}{2\pi}} = \frac{gT}{2\pi}. \tag{5.3}$$

This implies that ocean waves propagate faster with increasing wavelength and wave period—an effect known as frequency dispersion. On the other hand, in shallow water, $\tanh(kh) \to kh$ as $kh \to 0$. Again using this in Equations (5.1) and (5.2) then leads to the shallow-water wave celerity

$$c = \sqrt{gh}. \tag{5.4}$$

Since the celerity is now independent of the wavelength and period, shallow-water waves are not dispersive. Therefore, a different type of wave theory is needed for shallow water; for example, shallow water-wave theory.

Frequency dispersion also leads to the velocity of energy propagation, known as the group velocity c_g, being different to the phase velocity c. For finite water depth h,

$$c_g = \frac{d\omega}{dk} = \frac{1}{2}\left(1 + \frac{2kh}{\sinh(2kh)}\right)c. \tag{5.5}$$

In deep water, the group velocity is equal to half the phase velocity, i.e., as $kh \to \infty$, $\dfrac{2kh}{\sinh(2kh)} \to 0$, $\implies c_g \to \dfrac{1}{2}c$. On the other hand, in shallow water, the group velocity is equal to the phase velocity, i.e., as $kh \to 0$, $\dfrac{2kh}{\sinh(2kh)} \to 1$, $\implies c_g \to c$. This again shows that shallow water waves are not dispersive.

5.1.2 Stokes wave theory

Stokes waves are a type of nonlinear regular wave for an inviscid fluid on constant mean depth. Stokes wave theory was first established in 1847 by George Stokes (Stokes (1847) [129]) when he obtained approximate solutions for nonlinear regular wave motion through perturbation expansions now known as the 'Stokes expansion'. In general, Stokes wave theory is applicable from intermediate to deep water, with solutions of increasing nonlinearity up to fifth order having been derived since the original work of Stokes. As the solution is a perturbation expansion, the contribution from each successive component to the full wave solution is an order of magnitude smaller than the previous. In addition, the frequency of each successive higher-order component is a multiple of the fundamental wave frequency corresponding to the order of the component itself. The higher-order components also decay quicker as the water depth increases, meaning their contribution becomes negligible in deeper water. This is to be expected given that a linear approximation is essentially a first-order Stokes wave and is only valid in deep water.

$$
\begin{aligned}
S=&\quad \operatorname{sech}(2kh)\\
A_{11}=&\quad \operatorname{cosech}(kh)\\
A_{22}=&\quad \frac{3S^2}{2(1-S)^2}\\
A_{31}=&\quad \frac{(-4-20S+10S^2-13S^3)\,\operatorname{cosech}(kh)}{8(1-S)^3}\\
A_{33}=&\quad \frac{(-2S^2+11S^3)\,\operatorname{cosech}(kh)}{8(1-S)^3}\\
A_{42}=&\quad \frac{12S-14S^2-264S^3-45S^4-13S^5}{24(1-S)^5}\\
A_{44}=&\quad \frac{10S^3-174S^4+291S^5+278S^6}{48(3+2S)(1-S)^5}\\
A_{51}=&\quad \frac{(-1184+32S+13232S^2+21712S^3+20940S^4)\,\operatorname{cosech}(kh)}{64(3+2S)(4+S)(1-S)^6}\\
+&\quad \frac{(12554S^5-500S^6-3341S^7-670S^8)\,\operatorname{cosech}(kh)}{64(3+2S)(4+S)(1-S)^6}\\
A_{53}=&\quad \frac{(4S+105S^2+198S^3-1376S^4-1302S^5-117S^6+58S^7)\,\operatorname{cosech}(kh)}{32(3+2S)(1-S)^6}\\
A_{55}=&\quad \frac{(-6S^3+272S^4-1552S^5+852S^6+2029S^7+430S^8)\,\operatorname{cosech}(kh)}{64(3+2S)(4+S)(1-S)^6}\\
B_{22}=&\quad \frac{(1+2S)\,\coth(kh)}{2(1-S)}\\
B_{31}=&\quad \frac{-3(1+3S+3S^2+2S^3)}{8(1-S)^3}\\
B_{42}=&\quad \frac{(6-26S-182S^2-204S^3-25S^4+26S^5)\,\coth(kh)}{6(3+2S)(1-S)^4}\\
B_{44}=&\quad \frac{(24+92S+122S^2+66S^3+67S^4+34S^5)\,\coth(kh)}{24(3+2S)(1-S)^4}\\
B_{53}=&\quad \frac{9(132+17S-2216S^2-5897S^3-6292S^4-2687S^5+194S^6+467S^7+82S^8)}{128(3+2S)(4+S)(1-S)^6}\\
B_{55}=&\quad \frac{5(300+1579S+3176S^2+2949S^3+1188S^4+675S^5+1326S^6+827S^7+130S^8)}{384(3+2S)(4+S)(1-S)^6}\\
C_0=&\quad \tanh^{\frac{1}{2}}(kh)\\
C_2=&\quad \frac{(2+7S^2)\,\tanh^{\frac{1}{2}}(kh)}{4(1-S)^2}\\
C_4=&\quad \frac{(4+32S-116S^2-400S^3-71S^4+146S^5)\,\tanh^{\frac{1}{2}}(kh)}{32(1-S)^5}\\
D_2=&\quad -\frac{\coth^{\frac{1}{2}}(kh)}{2}\\
D_4=&\quad \frac{(2+4S+S^2+2S^2)\,\coth^{\frac{1}{2}}(kh)}{8(1-S)^3}\\
E_2=&\quad \frac{(2+2S+5S^2)\,\tanh(kh)}{4(1-S)^2}\\
E_4=&\quad \frac{(8+12S-152S^2-308S^3-42S^4+77S^5)\,\tanh(kh)}{32(1-S)^5}
\end{aligned}
$$

Table 5.1: Fifth-order Stokes wave coefficients

5.1.2.1 Fifth-order Stokes waves

Fifth-order Stokes waves are the type of regular wave considered in this work, with the solution of Fenton (1985) [42] being utilised in particular. Only the solution is presented here: a full derivation can be found in the cited work. The key to the Fenton (1985) [42] solution is that the Stokes expansion is determined by using the nondimensional wave steepness as the perturbation parameter, i.e.,

$$\epsilon = \frac{kH}{2}, \tag{5.6}$$

where ϵ is the perturbation parameter, H is the wave height, and k is the wavenumber. Note these last two parameters were defined in 5.1.1. The velocity potential $\phi(x, y, t)$ is then given as

$$\phi(x,y,t) = (c-\bar{u})x + C_0\left(\frac{g}{k^3}\right)^{\frac{1}{2}} \sum_{i=1}^{5} \epsilon^i \sum_{j=1}^{i} A_{ij} \cosh(jkY)\sin(j\theta) + \mathcal{O}(\epsilon^6), \tag{5.7}$$

with the mean fluid speed $\bar{u}$ defined as

$$\bar{u}\left(\frac{k}{g}\right)^{\frac{1}{2}} = C_0 + \epsilon^2 C_2 + \epsilon^4 C_4 + \mathcal{O}(\epsilon^6). \tag{5.8}$$

The coefficients C_i and A_{ij} here are all nondimensional and can be calculated from the formulas listed in Table 5.1. In addition, the phase $\theta = kx - \omega t$ and $Y = y + h$. Similarly, the free-surface elevation $\eta(x, t)$ is given as

$$\begin{aligned} k\eta(x,t) = {} & \epsilon\cos(\theta) + \epsilon^2 B_{22}\cos(2\theta) + \epsilon^3 B_{31}\Big(\cos(\theta) - \cos(3\theta)\Big) + \epsilon^4\Big(B_{42}\cos(2\theta) + B_{44}\cos(4\theta)\Big) \\ & + \epsilon^5\Big(- \big(B_{53} + B_{55}\big)\cos(\theta) + B_{53}\cos(3\theta) + B_{55}\cos(5\theta)\Big) + \mathcal{O}(\epsilon^6), \end{aligned} \tag{5.9}$$

where it is assumed that the still water level is $\eta = 0$. Again, the coefficients B_{ij} are nondimensional and are calculated using the formulae in Table 5.1.

5.1.3 Irregular random waves

As mentioned previously, the real-world ocean surface is not regular but highly irregular. An irregular sea state in any given region is random and consists of many different incident regular waves, each with different heights, frequencies, and directions. Mathematically, the random ocean free-surface can consequently be considered the as the linear superposition of all such regular components, i.e.,

$$\eta = \sum_{i}^{\infty} A_i \cos\left(k_i x - \omega_i t\right). \tag{5.10}$$

As explained by authors such as Pecher and Kofoed (2017) [114] and Holthuijsen (2007) [69], the idea of a *wave spectrum* can then be introduced through Fourier analysis. This spectrum describes the distribution of wave energy over each frequency in the sea state and is represented by the function $S(f)$ which is called the *spectral variance density*. Importantly, all parameters that statistically characterise the sea state can be derived from this spectrum.

Integrating $S(f)$ over all frequencies then gives the total energy transported:

$$\int_0^\infty S(f)\, df = \frac{H_s^2}{16}, \tag{5.11}$$

where H_s is known as the significant wave height (SWH) which is traditionally defined as the mean wave height of the highest third of waves in a given sea state. However, from Equation (5.11), H_s can also be defined as

$$H_s = 4\sqrt{m_0}, \tag{5.12}$$

where m_0 is the zeroth moment of $S(f)$, i.e., the left-hand side of Equation (5.11). The SWH is the key parameter in characterising any given sea state. It is important to note that common waves will be smaller in height than H_s, but it is still statistically possible to encounter a wave with height much larger than H_s.

In terms of the actual spectra themselves, several have been developed. The formulae ultimately have to be derived from the observations of actual ocean waves and are hence empirical in nature. The most commonly used spectrum is the Pierson-Moskowitz spectrum (Pierson and Moskowitz (1964) [116]) which assumes that the sea-state is fully developed and so that the spectrum is dependent on only the wind speed. The JONSWAP spectrum (Hasselmann et al. (1973) [62]) is then an extension of this to represent sea states that are not fully developed. This spectrum is used in the present work and will be described in the next section.

5.1.4 Focused waves

Of particular importance to wave-structure models is the existence of extreme waves. As mentioned previously, even though most waves will be smaller in height that the SWH H_s, it is still possible to encounter ones that are much larger: these are called extreme waves. In order to replicate these extreme wave events in a numerical wave tank (NWT), the most widely utilised method is to use NewWave theory (Tromans et al. (1991) [131]) to generate focused waves. When using NewWave theory, a group of localised regular waves are derived from a measured or theoretical waves spectrum such as JONSWAP or Pierson-Moskowitz. These individual wave components are then superposed so that they constructively interfere to build up a larger irregular wave. In addition, the phase of each wave component is adjusted so that they each focus simultaneously at a specific time and location. The result is a *focused* extreme wave representative of the underlying spectrum.

In a similar way to Equation (5.10), focused wave generation is realised through the linear superposition of a finite number of regular wave components. Hence, the first-order free-surface wave elevation using N components is defined as

$$\eta^{(1)} = \sum_{i=1}^{N} A_i \cos\theta_i, \tag{5.13}$$

where A_i is the amplitude of each component and θ_i is the phase of each component. Moreover, the phase is defined as

$$\theta_i = k_i x - \omega_i t - \epsilon_i, \tag{5.14}$$

where k_i is the wavenumber, and ω_i the angular frequency, of each component. As also previously mentioned, the phase of each component is adjusted so that the waves focuses at a specific time and location. To do this, ϵ_i in Equation (5.14) is defined as

$$\epsilon_i = k_i x_0 - \omega_i t_0, \tag{5.15}$$

where t_0 is called the *focus time* and x_0 is called the *focus location*. Similarly, the first-order velocity potential is defined as

$$\phi^{(1)} = \sum_{i=1}^{N} \frac{gA_i}{\omega_i} \frac{\cosh(k_i[y+h])}{\cosh(k_i h)} \sin(k_i(x - x_0) - \omega_i(t - t_0)). \tag{5.16}$$

The amplitude A_i for each wave component is then calculated as

$$A_i = A_I \frac{S_i(f)\Delta f}{\sum_{i=1}^{N} S_i(f)\Delta f}, \tag{5.17}$$

where A_I is the input amplitude of the focused wave, $S_i(f)$ is the spectral variance density, and Δf is the increment frequency. In the present work, $S_i(f)$ refers to the JONSWAP spectrum mentioned in 5.1.3. It is defined as

$$S_i(f) = \frac{5}{16} H_s^2 f_p^4 f_i^{-5} \exp\left(-\frac{5}{4}\left(\frac{f_p}{f_i}\right)^4 \right) \gamma^{\exp\left(\frac{-(f_i - f_p)^2}{2\sigma^2 f_p^2}\right)}, \tag{5.18}$$

where H_s is again the SWH, $\gamma = 3.3$ is the peak-enhancement factor, f_p is the peak spectral frequency, and σ is the spectral width parameter defined as

$$\sigma = \begin{cases} 0.07 & \text{for} \quad f_i \leq f_p, \\ 0.09 & \text{for} \quad f_i > f_p. \end{cases} \tag{5.19}$$

It can be seen from Equation (5.18) that, in order to generate each wave component, only H_s (which is just A_I), f_p, and a frequency bandwidth $f \in [f_{\min}, f_{\max}]$ are required.

In the present work, the second-order free-surface elevation and velocity potential are also added so that

$$\eta = \eta^{(1)} + \eta^{(2)}, \tag{5.20}$$

$$\phi = \phi^{(1)} + \phi^{(2)}. \tag{5.21}$$

Details of the formulation for $\eta^{(2)}$ and $\phi^{(2)}$ can be found in papers by Ning et al. (2008, 2009) [110, 111], but are omitted here.

5.2 Stabilised FNPF model

5.2.1 Regular fifth-order Stokes wave propagation

The first validation test case for the new stabilised model is fifth-order Stokes wave propagation. For a specific comparison, the particular case and initial computational setup considered here is identical to that of Lin et al. (2021) [90]. However, the computational setup is adjusted later on for a more in depth analysis of the new model. The NWT in Lin et al. (2021) [90] has dimensions $x \times y \times z \in [0,\ 100] \times [-0.7,\ 0] \times [0,\ 1]$ (metres) with a mesh configuration of $x \times y \times z = 1080 \times 30 \times 5$. The input wave parameters are listed Table 5.2, meaning the mesh configuration corresponds to 50 cells per wavelength in the x-direction. The relaxation and damping zones are one wavelength long, and the mesh is uniform in the x-direction but is refined in the y-direction so that the cell at the top has vertical width 1/10 of the cell at the bottom. The simulation time is 100 seconds.

Figure 5.1 then shows the time histories of the free-surface elevation for the stabilised model, Lin et al. (2021) [90] model, and analytical fifth-order Stokes solution at various wave gauges (WGs) in the NWT. The key thing to note is that the simulation is stable with no sawtooth instability present—all without using numerical damping or smoothing. This provides clear evidence that the stabilised model has the capacity to remain stable in the face on highly nonlinear waves. In addition, the solution is clearly also very accurate, even for the wave gauge furthest down the tank. There is also negligible difference with the Lin et al. (2021) [90] model (for which a value $\beta_{FODC} = 0.05$ with a frequency of 5 time steps is used to ensure stability) with both models showing similar levels of accuracy. However, some interference can clearly be seen at WG3 and WG4 which is most likely down to reflection from the outlet and inlet.

Wave	Amplitude: A(m)	Period: T(s)	Wavelength: λ(m)	Water depth: h(m)	Steepness: $2A/\lambda$
Stokes 5^{th}	0.125	2	4.62	0.7	0.054

Table 5.2: Wave parameters for the generated fifth-order Stokes waves.

5.2.2 Energy considerations

As mentioned in Section 1.3.2, the use of artificial dissipation by way of a low-order numerical damping or smoothing scheme in FNPF models is undesirable due to overall loss in energy in the NWT. This in turn can then make the models inaccurate, particularly for large-scale and long-time simulations. In addition, this technique usually involves certain parameters that have to be tuned for any given application in order to achieve an optimal balance between stability and accuracy, leading to a very sluggish and drawn-out process if the values are not known a priori. These clear disadvantages of artificial dissipation are the primary reason why a second-

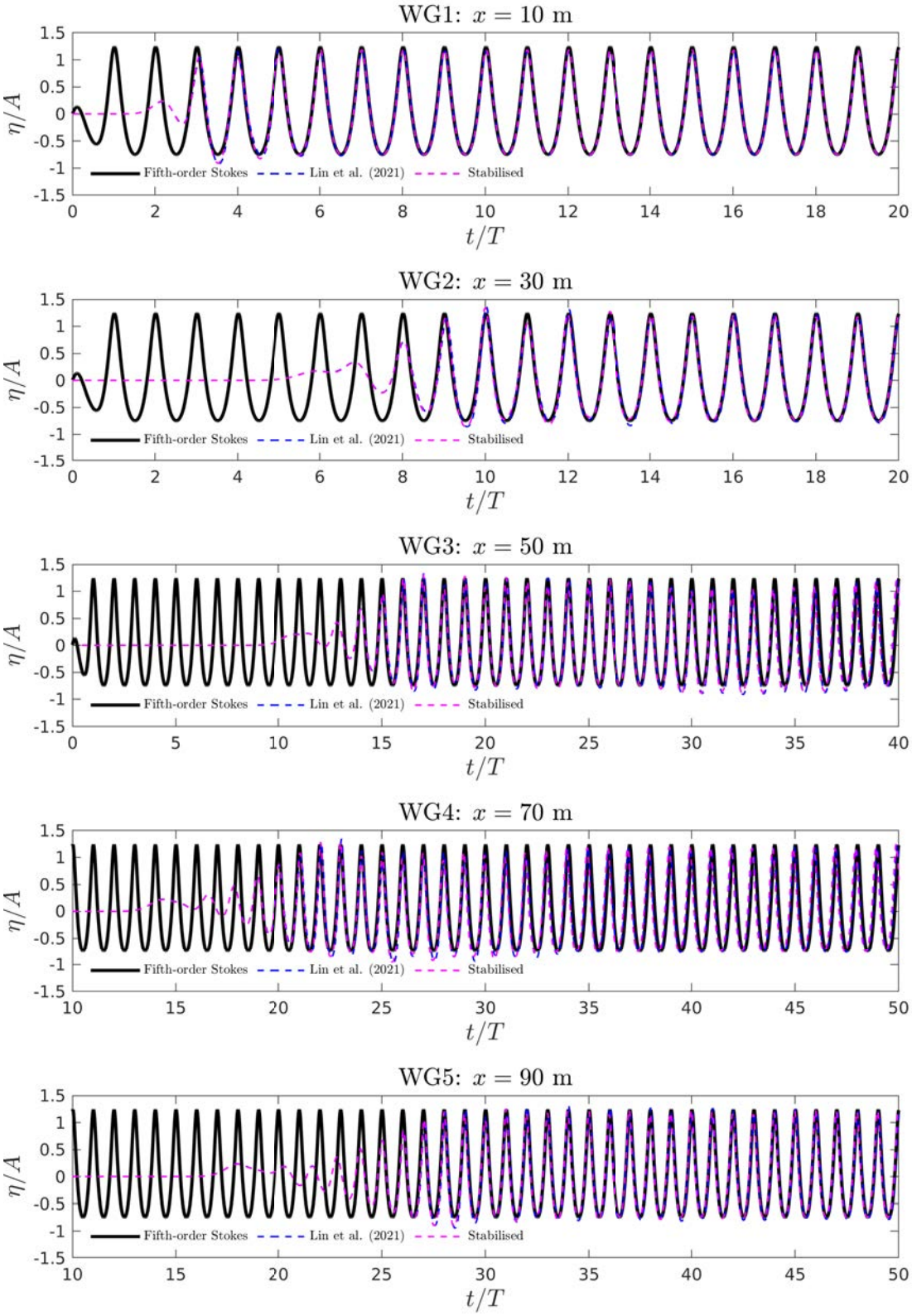

Figure 5.1: Time histories of free-surface elevation for the stabilised model, Lin et al. (2021) [90] model, and analytical fifth-order Stokes solution at various wave gauges in the numerical wave tank. Please note that the upper limits of the time intervals in these panels are not the same.

order TVD method was instead proposed. Indeed, the stabilised model requires no tuning of any parameters—only a certain flux limiter has to be chosen. This is in contrast to the Lin model for which carefully chosen values of the damping parameters were required to ensure stability and good accuracy. If instead these parameters were poorly chosen, the simulation would have either been unstable, or there would have been excessive damping and overall loss in energy. The stabilised model avoids this process of trial and error in pursuing the optimal damping parameters, so in this sense, it is reasonable to conclude that it is superior to the Lin model. Nevertheless, to validate this conclusion further, new examples are considered through which the superiority of the stabilised model over the Lin model in terms of energy conservation is proven.

The most straightforward and heuristic way of verifying the loss in energy due to artificial dissipation is to observe the growing reduction in amplitude of progressive waves as they get further from the inlet. Furthermore, the total energy E_T in the NWT over time can be explicitly calculated and compared with the prior heuristic observations. To calculate E_T, the total kinetic and potential energies in the NWT can be summed, i.e.,

$$E_T = E_k + E_p. \tag{5.22}$$

Then, if 0 and X denote the limits of the computational domain in the x-direction and ρ_w is the density of water, E_k and E_p are given by

$$E_k = \frac{1}{2}\rho_w \int_0^X \int_{-h}^{\eta} (\nabla\phi \cdot \nabla\phi)\, dydx \quad \text{and} \quad E_p = \rho_w g \int_0^X \int_{-h}^{\eta} y\, dydx, \tag{5.23}$$

which in turn implies that

$$E_T = \frac{1}{2}\rho_w \int_0^X \int_{-h}^{\eta} (\nabla\phi \cdot \nabla\phi)\, dydx \; + \; \frac{1}{2}\rho_w g \int_0^X (\eta^2 - h^2) dx. \tag{5.24}$$

The potential energy below the initial free-surface position $y = 0$, given by $-\frac{1}{2}\rho_w g \int_0^X h^2\, dx$, is a constant that will be the same for each of the two models, and hence is discarded from the calculation for E_T as it has no relation to the wave motion. The total wave energy E_T then becomes

$$E_T = \frac{1}{2}\rho_w \int_0^X \left(\int_{-h}^{\eta} (\nabla\phi \cdot \nabla\phi)\, dy \; + \; g\eta^2 \right) dx. \tag{5.25}$$

Given that OpenFOAM implements a cell-centred and co-located FVM, calculating the total energy is straightforward, i.e.,

$$E_T = \frac{1}{2}\rho_w \left(\sum_n^N (\nabla\phi_n \cdot \nabla\phi_n)\; A_n + g \sum_i^I y_i^2 x_i \right), \tag{5.26}$$

where N is the total number of mesh cells, A_n the vertical cross-sectional area of cell n, I the number of cells in the x-direction, x_i the x-directional width of free-surface cell face i, and y_i the y-coordinate of face i.

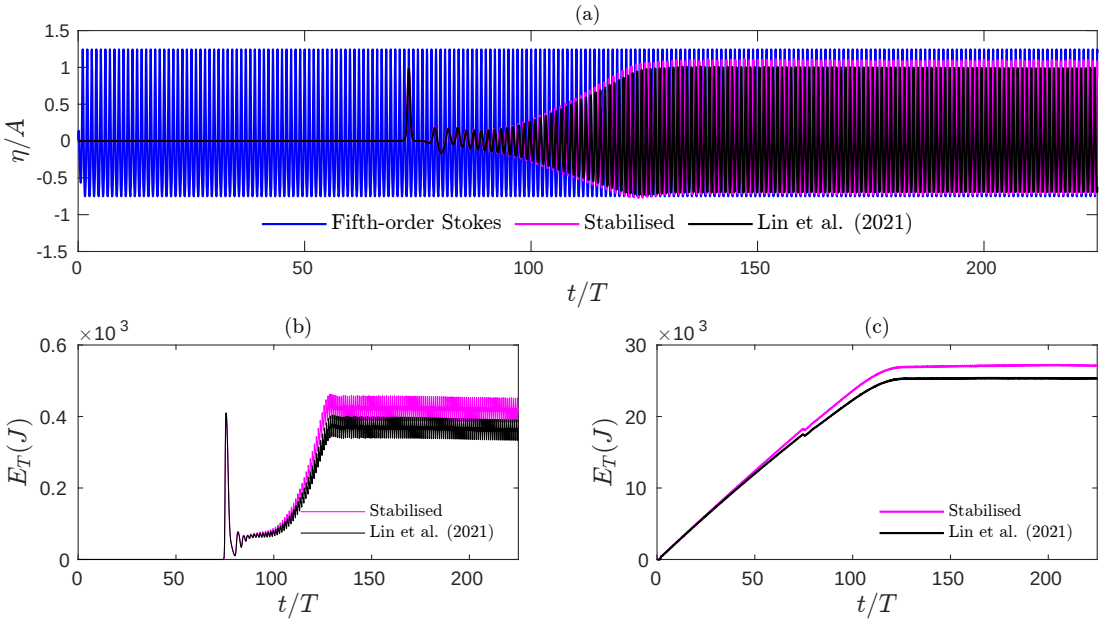

Figure 5.2: (a) Time histories of free-surface elevation for the stabilised model, Lin et al. (2021) [90] model, and fifth-order Stokes solution at WG1 = 430 m. (b) Time histories of total energy E_T in the damping zone of the numerical wave tank for the stabilised model and Lin et al. (2021) [90] model. (c) Time histories of total energy E_T in the middle portion of the numerical wave tank for the stabilised model and Lin et al. (2021) [90] model.

Given that a large-scale and long-time simulation is wanted, the fifth-order Stokes wave example in Section 5.2.1 is extended so that the NWT in this case is 100 wavelengths long with a final time of 450 s. The example is also changed to 2D given that the input waves are 2D. All wave parameters are the same as in Table 5.2 meaning the NWT now has dimensions $x \times y \in [0,\ 462] \times [-0.7,\ 0]$ (m). In addition, the relaxation and damping zones are both 5 wavelengths long and the mesh configuration is $x \times y = 5000 \times 30$ (50 cells per λ). For the Lin model, the same values of the damping parameter $\beta_{FODC} = 0.05$ and frequency of 5 time steps, which were found to be optimal for stability, are used. Finally, the energy E_T is considered in two separate regions in the NWT: the damping zone and the 'middle portion' which is the region that does not include both the relaxation and damping zones (and is hence 90 wavelengths long).

Figure 5.2(a) then shows the time histories of free-surface elevation for the stabilised model, Lin et al. (2021) [90] model, and analytical fifth-order Stokes solution at WG1 = 430 m. Note this wave gauge is near the end of the NWT, just before the damping zone begins. It can be seen from the results that the Lin model experiences a greater reduction in amplitude—and hence a greater loss in energy—of propagating waves than the stabilised model. Although the stabilised model also experiences a reduction in amplitude, the loss is smaller than the Lin model; hence, in this sense, the new model outperforms the old one. The results when the energy is explicitly calculated are also in agreement with this heuristic observation. Figure 5.2(b) shows the time

histories of E_T for the stabilised model and Lin et al. (2021) [90] model in the damping zone of the NWT. These results clearly show that the amount of energy having to be transferred out of the NWT in this zone is higher for the stabilised model than the Lin model, clearly indicating that the waves in the stabilised model are propagating more energy at the point which they reach the damping zone for all time—a result corroborated by the results in Figure 5.2(a). In addition, Figure 5.2(c) shows analogous results for the middle portion of the NWT where waves are not being generated or damped but only propagated. It clearly shows that the stabilised model conserves more energy over time than the Lin model.

According to Dong et al. (2020) [32], the theoretical total wave energy per unit horizontal area for this fifth-order Stokes wave in the middle portion of the NWT can be found at about $\overline{E} = 75.9$ J/m^2. The corresponding computed values are 65.4 J/m^2 and 60.9 J/m^2 for the stabilised and Lin models, respectively. These energy calculations also clearly corroborate the prior heuristic observations and hence further cement the superiority of the stabilised model over the Lin et al. (2021) [90] model in terms of energy conservation and accuracy for large-scale and long-time simulations.

5.2.3 Mesh sensitivity

As of yet, the new stabilised model has only been tested under the same conditions as the Lin model for comparison. However, the computational configurations used may not be optimal for the new stabilised model in terms of accuracy and efficiency. For example, it may be possible to use a coarser mesh but still have a convergent solution. This is what will be tested in this section.

The first thing to note about about the original test case in Section 5.2.1, and in the work of Lin et al. (2021) [90], is that a density of 30 cells in the y-direction is used. This was needed by the Lin model to ensure accuracy in the face of the relatively high nonlinearity and steepness of the fifth-order Stokes waves. However, such a high number may not be necessary for the stabilised model and a lot of computational time could potentially be saved. Therefore, the same test case is redone but using half the number of cells in the y-direction. However, given that the input waves are 2D, the NWT is changed so that it is 2D. Mesh E in Table 5.3 refers to the original configuration but in 2D, and mesh C refers to the new configuration with only 15 cells in the y-direction. Again, the mesh is refined in the y-direction so that the cell at the top has vertical width 1/10 of the cell at the bottom. Figures 5.3 and 5.4 then show the time histories of free-surface elevation for meshes C and E at WGs 2 and 5, along with the analytical fifth-order Stokes solution. It can clearly be seen that mesh C achieves pretty much the same solution accuracy as mesh E, even at WG5 near the end of the NWT. Moreover, the total computational time for mesh C was 0.42 times that of mesh E, so it is much quicker as well. Therefore, 15 cells in the y-direction is found to be sufficient.

For the x-direction, three additional meshes—A, B, and D listed in Table 5.3—are chosen. These constitute 30, 40, and 60 cells per wavelength in addition to the original 50. These meshes are again uniform in the x-direction but refined in the y-direction as mentioned previously. Figures 5.5 and 5.6 then show the time histories of free-surface elevation for meshes A, B, C, and D at WGs 2 and 5, along with the analytical fifth-order Stokes solution. At WG2 (Figure 5.5), meshes C and D clearly provide an accurate and convergent solution. However, meshes A and B show slight dissipation and consequent reduction crest amplitude, with mesh A being particularly bad. This effect is more pronounced at WG5 (Figure 5.6) where meshes C and D are remarkably accurate, but meshes A and B clearly suffer severe dissipation in the form of amplitude decay and phase shift. Therefore, if accurate solutions are required on large scales, the original mesh density of 50 cells per wavelength is recommended. However, given the results at WG3, it may be possible to use slightly coarser mesh if a solution is required on a much smaller scale.

ID	Configuration $x \times y$	Cells per λ
A	648×15	30
B	864×15	40
C	1080×15	50
D	1296×15	60
E	1080×30	50

Table 5.3: Mesh configurations used in mesh sensitivity studies for the stabilised model.

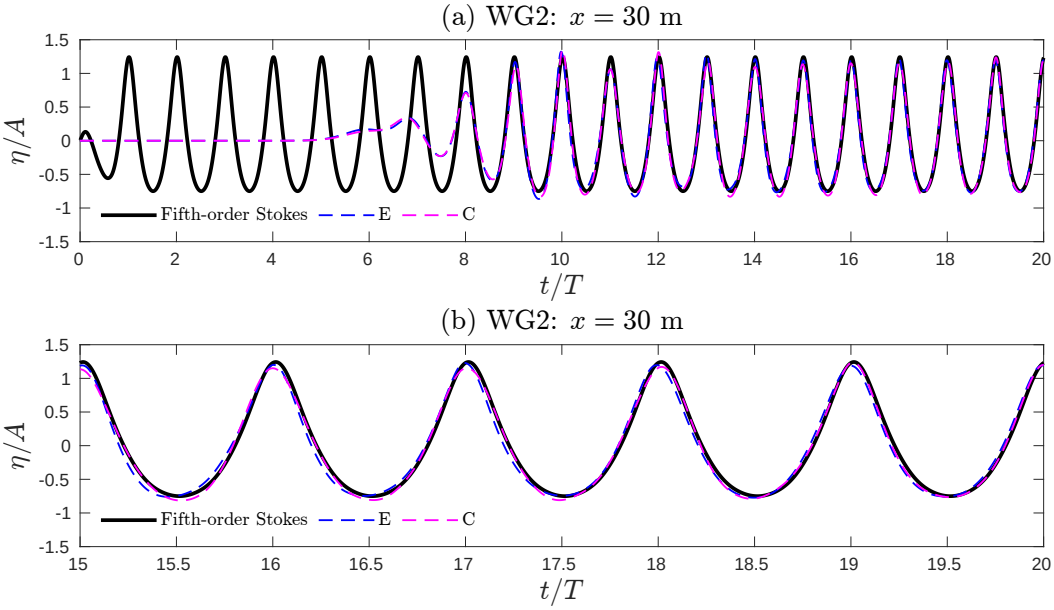

Figure 5.3: Time histories of free-surface elevation for meshes C and E at wave gauge 2 (WG2), along with the analytical fifth-order Stokes wave solution: (a) $t/T \in [0, 20]$, (b) $t/T \in [15, 20]$.

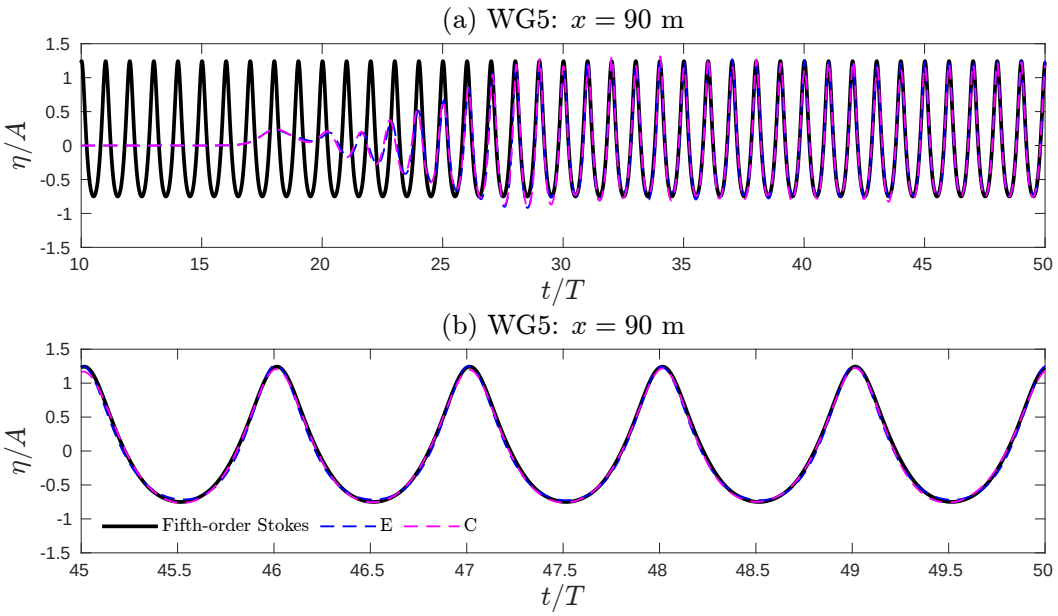

Figure 5.4: Time histories of free-surface elevation for meshes C and E at wave gauge 5 (WG5), along with the analytical fifth-order Stokes wave solution: (a) $t/T \in [10, 20]$, (b) $t/T \in [45, 50]$.

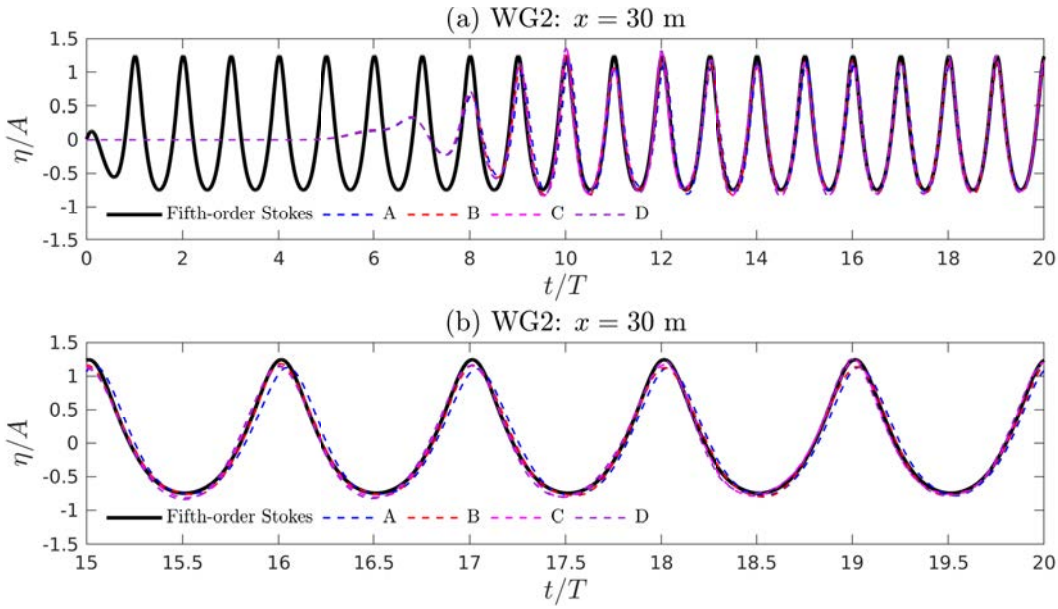

Figure 5.5: Time histories of free-surface elevation for meshes A, B, C and D at wave gauge 2 (WG2), along with the analytical fifth-order Stokes wave solution: (a) $t/T \in [0, 20]$, (b) $t/T \in [15, 20]$.

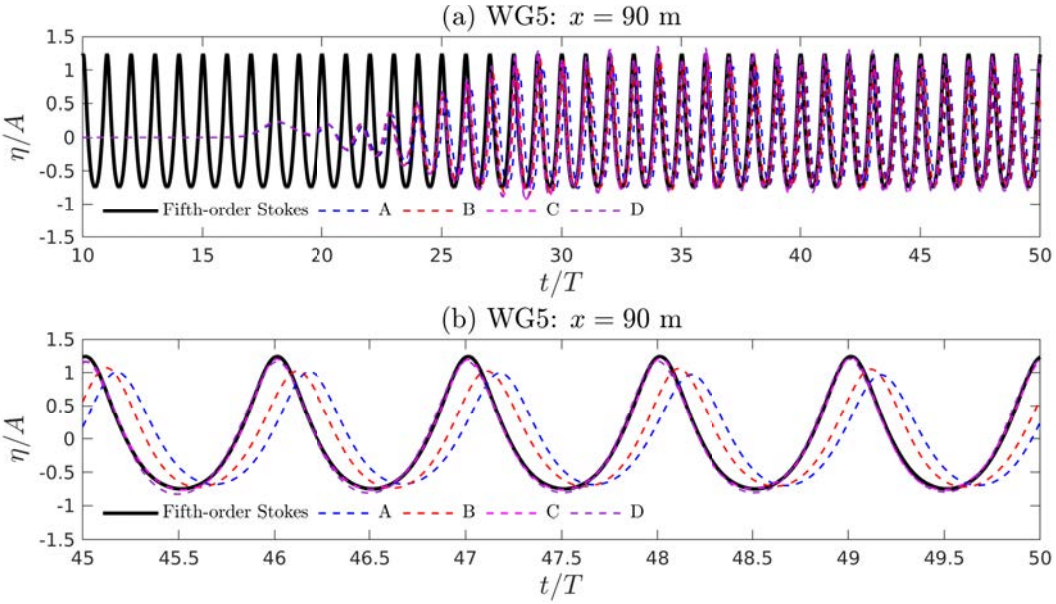

Figure 5.6: Time histories of free-surface elevation for meshes A, B, C and D at wave gauge 5 (WG5), along with the analytical fifth-order Stokes wave solution: (a) $t/T \in [10, 50]$, (b) $t/T \in [45, 50]$.

5.2.4 Temporal sensitivity

Another key test for the new stabilised is temporal sensitivity and convergence. Recall that the adaptive time-stepping control procedure explained in Section 2.3.3.4 is implemented in OpenFOAM. This procedure is dependent on the user-prescribed max Courant number $C_{\max}$, from which the time step is calculated accordingly from Equation (2.56). Given this, the stabilised model is tested here by prescribing different values of $C_{\max}$.

5.2.4.1 Geometric and computational setups

The geometric and computational setups are the same as in the previous section 5.2.3, with mesh C from Table 5.3 being used. Moreover, the input fifth-order Stokes wave parameters are the same as those listed in Table 5.1, and the same wave gauges are used for validation. The values of $C_{\max}$ tested are 0.05, 0.1, 0.2, and 0.4. Note that $C_{\max} = 0.2$ is the value that has been used in all test cases so far, and hence is the reference case. Finally, four error measures are introduced: the normalised crest and trough amplitude errors e^a_{crest} and e^a_{trough}, each defined by

$$e^a_{crest} = \frac{\eta^{\text{stabilised}}_{crest} - \eta^{\text{analytical}}_{crest}}{A} \tag{5.27}$$

and

$$e^a_{trough} = \frac{\eta^{\text{stabilised}}_{trough} - \eta^{\text{analytical}}_{trough}}{A} \tag{5.28}$$

respectively, where $\eta^{\text{stabilised}}$ and $\eta^{\text{analytical}}$ are the stabilised and fifth-order Stokes free-surface elevations respectively; and the normalised crest and trough phase shifts e^θ_{crest} and e^θ_{trough}, each

defined by

$$e^{\theta}_{crest} = \frac{t^{\text{stabilised}}_{crest} - t^{\text{analytical}}_{crest}}{T} \tag{5.29}$$

and

$$e^{\theta}_{trough} = \frac{t^{\text{stabilised}}_{trough} - t^{\text{analytical}}_{trough}}{T} \tag{5.30}$$

respectively, where $t^{\text{stabilised}}$ and $t^{\text{analytical}}$ are the stabilised and fifth-order Stokes times respectively at each crest and trough instance.

5.2.4.2 Effects of changing $C_{\max}$ on free-surface elevation and computational time

Figure 5.7(a) shows the time histories of free-surface elevation for varying values of $C_{\max}$ at WG2, along with the analytical fifth-order Stokes solution. The solutions are all clearly reasonably accurate but show an apparent underestimation of the wave crest amplitudes and overestimation of trough amplitudes. However, the solution for $C_{\max} = 0.4$ looks to be slightly different to the others. This is backed up in Figures 5.7 (b) and (c) which indicate that the normalised crest and trough amplitude errors e^{a}_{crest} and e^{a}_{trough} show a similar pattern. However, although all crest errors fluctuate, $C_{\max} = 0.4$ clearly shows a smaller error for the crests over time, but larger error for the troughs over time. The other solutions for $C_{\max} = 0.05$, 0.1, and 0.2 show a slightly larger—but similar—crest error over time but smaller trough error. This behaviour might seem counter intuitive but most likely indicates that the $C_{\max} = 0.4$ does not provide a fully 'convergent' solution. Any numerical method will show some level of dissipation, particularly given that the explicit Euler method used in the stabilised model is first order, so the wave solution will not necessarily converge exactly to the analytical. Instead it may converge to something slightly different, which is clearly the case here as solutions for $C_{\max} = 0.05$, 0.1, and 0.2 seem to be doing. Given this, the crest error solution for $C_{\max} = 0.4$ shows a clear overestimation, even if it closer to 0. This is then backed up by the trough error where the overestimation lead to a larger error than the other solutions. The crest and trough phase shifts—e^{θ}_{crest} and e^{θ}_{trough} respectively—are also shown in Figures 5.7 (d) and (e). The crest shifts are very small and can be considered negligible, whereas the trough shifts show slightly larger fluctuations, with a similar counter-intuitive pattern to e^{a}_{crest} present. However, this is explainable for the same reason, i.e., the solution is still converging with decreasing $C_{\max}$.

Figure 5.8 then shows the analogous results at WG5. The solutions show a much more regular pattern than those at WG2, but still show similar behaviour. For example, Figures 5.8 (b) and (c) shows a distinct overestimation of crest and trough amplitudes for $C_{\max} = 0.4$, but the overestimation decreases with decreasing $C_{\max}$. Furthermore, Figures 5.8 (d) and (e) show a greater negative phase shift with increasing $C_{\max}$. This shows that increasing values of $C_{\max}$ leads to greater dissipation over this large-scale, most likely in the form of kinetic energy loss in the NWT. Given the dispersion relations (5.1) and (5.2), this likely leads to this negative shift.

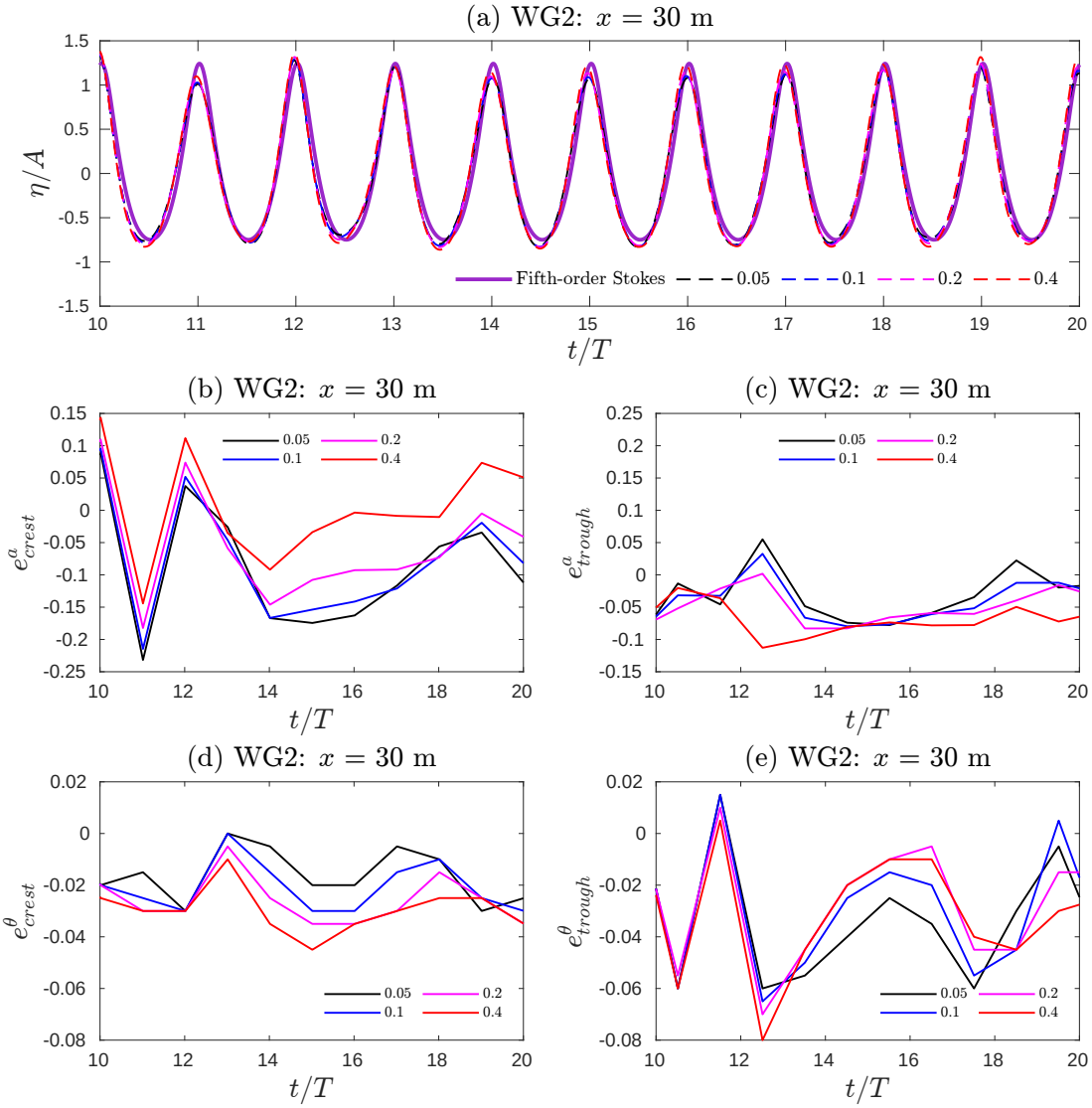

Figure 5.7: (a) Time histories of free-surface elevation for $C_{\max} = 0.05$, 0.1, 0.2, and 0.4 at wave gauge 2 (WG2) in $t/T \in [10,\ 20]$, along with the analytical fifth-order Stokes solution. (b) Normalised crest amplitude error e^a_{crest}, (c) normalised trough amplitude error e^a_{trough}, (d) normalised crest phase shift e^θ_{crest}, and (e) normalised trough phase shift e^θ_{trough} for $C_{\max} = 0.05$, 0.1, 0.2, and 0.4 at WG2 in $t/T \in [10,\ 20]$.

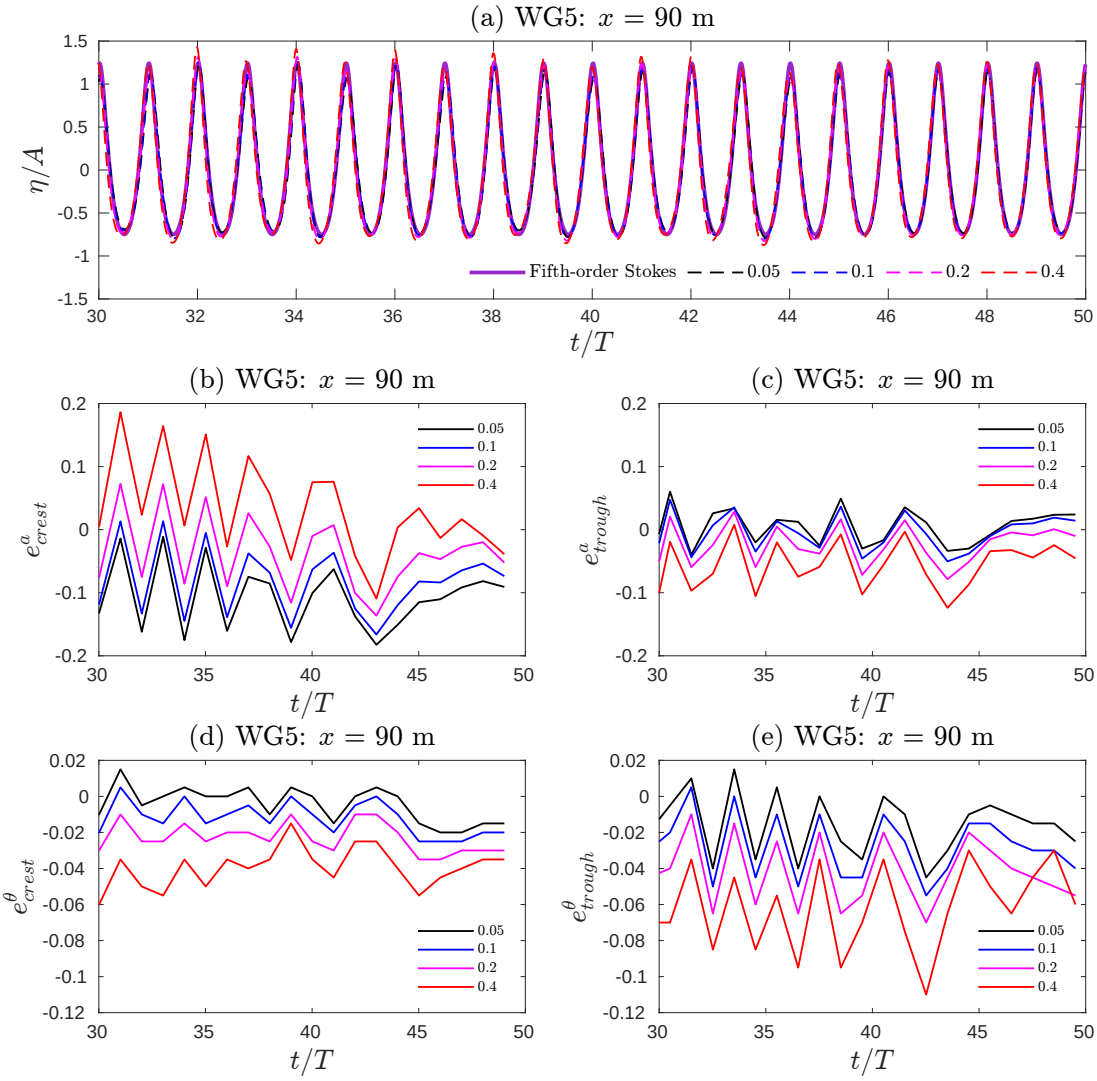

Figure 5.8: (a) Time histories of free-surface elevation for $C_{\max} = 0.05$, 0.1, 0.2, and 0.4 at wave gauge 5 (WG5) in $t/T \in [30, 50]$, along with the analytical fifth-order Stokes solution. (b) Normalised crest amplitude error e^a_{crest}, (c) normalised trough amplitude error e^a_{trough}, (d) normalised crest phase shift e^θ_{crest}, and (e) normalised trough phase shift e^θ_{trough} for $C_{\max} = 0.05$, 0.1, 0.2, and 0.4 at WG5 in $t/T \in [30, 50]$.

Another key factor that has to be taken into account when choosing the value of $C_{\max}$ is the computational time: lower values of $C_{\max}$ will invariably lead to greater computational time. Table 5.4 shows the total simulation time (s) for each value of $C_{\max}$. Using $C_{\max} = 0.2$ as the reference time, $C_{\max} = 0.05$ takes approximately 2.97 times as long, $C_{\max} = 0.1$ takes approximately 1.55 as long, and $C_{\max} = 0.4$ takes approximately 0.52 times as long. This indicates that decreasing the value of $C_{\max}$ can greatly increase the computational time, hence this also has to be taken into account for a balance between accuracy and efficiency. However, as will be seen in Chapter 6, the FNPF time is far outweighed by the coupling and interFoam times in the integrated model, so the value $C_{\max}$ will ultimately be decided by interFoam.

To conclude, it is clear that decreasing the value of $C_{\max}$ results in a more accurate and convergent solution but a large increase in computational time. The chosen value should then be discretionary on the specific case; it should be noted that the choice of $C_{\max} = 0.2$ used for the all test cases previously efficiently provided sufficiently accurate solutions.

$C_{\max}$	0.05	0.1	0.2	0.4
Simulation time (s)	2957	1579	921	514

Table 5.4: Time taken by the stabilised model for each value of $C_{\max}$.

5.2.5 Choice of flux limiter

Another key parameter in the new stabilised FNPF model is the flux limiter function $\psi(r)$ defined in Equation (3.24). It was also mentioned in Section 3.3.3 that the Van Albada 2 limiter—defined in Equation (3.26)—is the one used in the present work. Nevertheless, for completeness, an analysis of the other flux limiter functions defined in Table 3.1, as well as the first-order upwind (FOU) scheme, is done here via fifth-order Stokes wave propagation. The same geometric and computational setups as Sections 5.2.3 and 5.2.4 are used. Moreover, the optimal mesh density found through the mesh sensitivity study—mesh C in Table 5.3—and optimal value of $C_{\max} = 0.2$ found through the temporal sensitivity study are used.

Figures 5.10 and 5.9 then show the time histories of free-surface elevation for each flux limiter listed in Table 3.1 at WGs 2 and 5, along with the analytical fifth-order Stokes solution. At WG2: $x = 30$ m (5.10), the Min-mod (MM), Van Leer (VL), Van Albada 1 (VA1), and Van Albada 2 (VA2) limiters provide similarly accurate results with minimal phase shifts or reduction in crest and trough amplitudes. However, the SuperBee (SB) limiter gives an overestimation at some troughs and crests, whilst the FOU scheme (as expected) shows significant dissipation. This overestimation and dissipation is amplified respectively at WG5: $x = 90$ m to the point of severe inaccuracy. However, the other limiters remain very accurate, with only the MM limiter showing any noticeably large dissipation. If anything, the VA2 limiter seems to be slightly more accurate than the others but the differences are small. Hence, this justifies the decision to choice the VA2 limiter in this work.

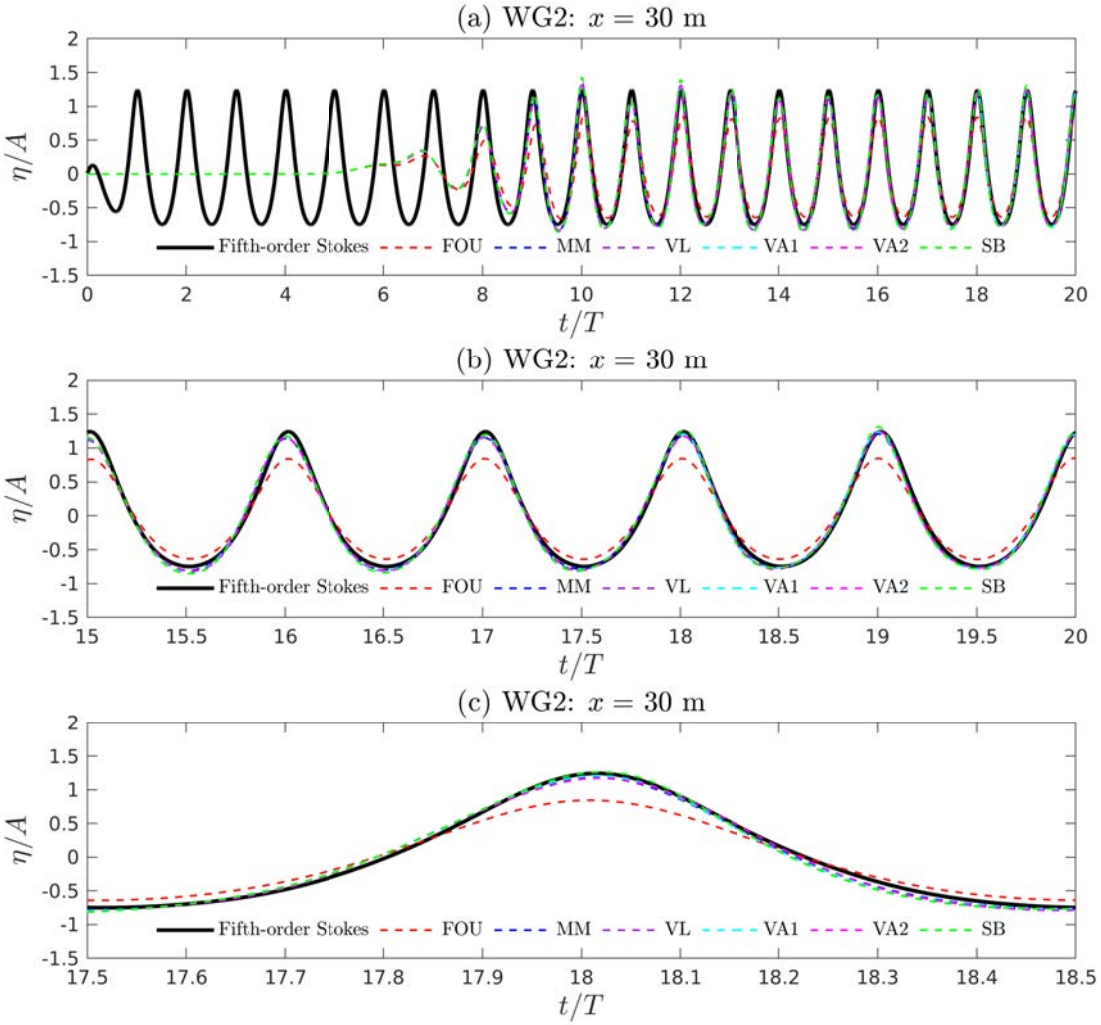

Figure 5.9: Time histories of free-surface elevation for the first-order upwind scheme (FOU), the Min-mod (MM), Van Leer (VL), Van Albada 1 (VA1), Van Albada 2 (VA2), and SuperBee (SB) limiters at wave gauge 2 (WG2), along with the analytical fifth-order Stokes solution: (a) $t/T \in [0,\ 20]$, (b) $t/T \in [15,\ 20]$, (c) $t/T \in [17.5,\ 18.5]$.

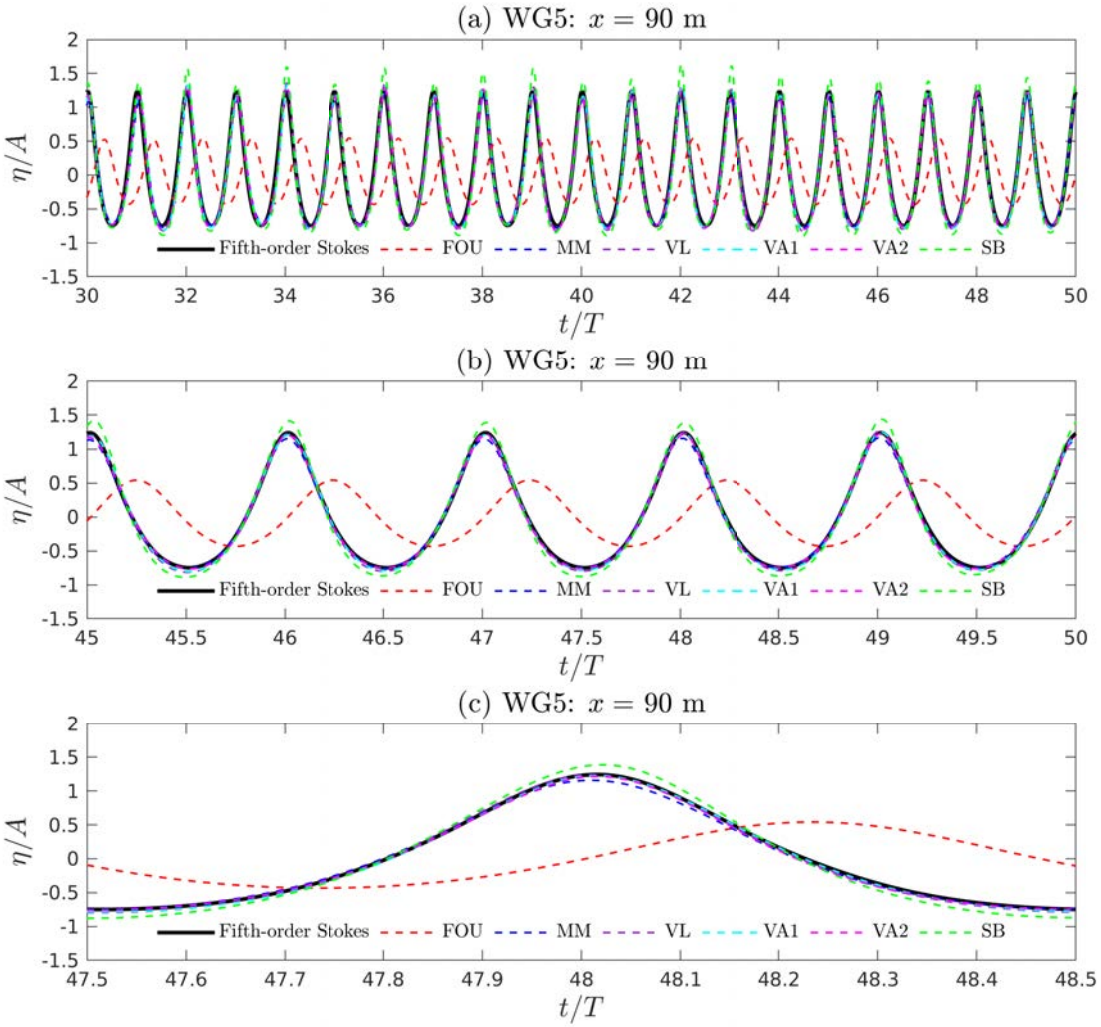

Figure 5.10: Time histories of free-surface elevation for the first-order upwind scheme (FOU), the Min-mod (MM), Van Leer (VL), Van Albada 1 (VA1), Van Albada 2 (VA2), and SuperBee (SB) limiters at wave gauge 5 (WG5), along with the analytical fifth-order Stokes solution: (a) $t/T \in [30,\ 50]$, (b) $t/T \in [45,\ 50]$, (c) $t/T \in [47.5,\ 48.5]$.

5.2.6 Focused wave propagation

The second validation test case for the stabilised model is focused wave propagation. In this case, the physical and numerical experiments by Ning et al. (2009) [111] are considered. Four extreme wave cases—based on NewWave theory—were investigated with different input amplitudes. In the present work, the stabilised model is validated using cases 1 and 3 in particular, with the corresponding input wave characteristics listed in Table 5.5, and with the focused waves generated in the same way as Ning et al. (2009) [111] as detailed in Section 5.1.4. Note that T_p and λ_p are the period and wavelength for the characteristic wave for that particular group, which is taken as the wave corresponding to the peak amplitude (for that group). In the numerical experiments of Ning et al. (2009) [111], the 3-D NWT had dimensions $x \times y \times z = 5\lambda_p \times 0.5 \times \lambda_p/10$ (m). However, the input focused waves are 2D, so a 2-D NWT with dimensions $x \times y = 5\lambda_p \times 0.5$ (m) is used in this work instead. Moreover, the relaxation and damping layer are the same length as Ning et al. (2009) [111], i.e., λ_p and $2\lambda_p$ respectively. All these dimensions are more clearly listed for each case in Table 5.6. The corresponding focus location and time are also given by Ning et al. (2009) [111] as $x_0 = 1.5\lambda_p$ and $t_0 = 8T_p$ respectively. These are also listed for each case in Table 5.7. Finally, 31 wave components are used in case NING1, whereas 41 are used in case NING3. The difference is owed to the increased steepness and nonlinearity of the focused wave in NING3.

Case	Frequency band (Hz)	f_p (Hz)	T_p (s)	A_I (m)	λ_p (m)
NING1	$f \in [0.6, 1.2]$	0.83	1.2	0.0313	2
NING3	$f \in [0.6, 1.4]$	0.8	1.25	0.0875	2.18

Table 5.5: Input wave parameters for cases NING1 and NING3: Input focused wave parameters for the WEC test case: f_p is the peak frequency, T_p is the characteristic wave period, A_I is the input focused wave amplitude, and λ_p is the characteristic wavelength.

Case	Dimensions $x \times y$ (m)	Relaxation zone	Damping zone
NING1	10×0.5	[0, 2]	[6, 10]
NING3	10.9×0.5	[0, 2.18]	[6.54, 10.9]

Table 5.6: Dimensions of numerical wave tank for cases NING1 and NING3.

Case	Input x_0(m)	Input t_0(s)	Actual x_1(m)	Actual t_1(s)
NING1	3	9.6	3	9.6
NING3	3.27	10	3.575	10.16

Table 5.7: Input and actual focusing properties for cases NING1 and NING3.

5.2.6.1 Case NING1

To begin, a mesh sensitivity study is undertook for case NING1 to assess accuracy and to determine the best mesh configuration for the steeper case NING3. Four different mesh configurations are chosen and are listed in Table 5.8. Again, the mesh is refined in the y-direction so that the cell at the top has vertical width 1/10 of the cell at the bottom. Figure 5.11 then shows the time histories of free-surface elevation at the focus location x_0, plotted with the experimental solution from Ning et al. (2009) [111]. Again, the simulation is stable with no sawtooth instability. In terms of convergence, the solution is clearly converging with there being minimal difference between the results for configurations N1, N2, N3, and N4—all of which are very accurate. Therefore, the middle configuration N3—corresponding to 25 cells per wavelength—is chosen for case NING3.

Mesh	Configuration ($x \times y$)	Cells per wavelength
N1	75×10	15
N2	100×10	20
N3	125×10	25
N4	150×10	30

Table 5.8: Mesh configurations used in mesh sensitivity study for case NING1.

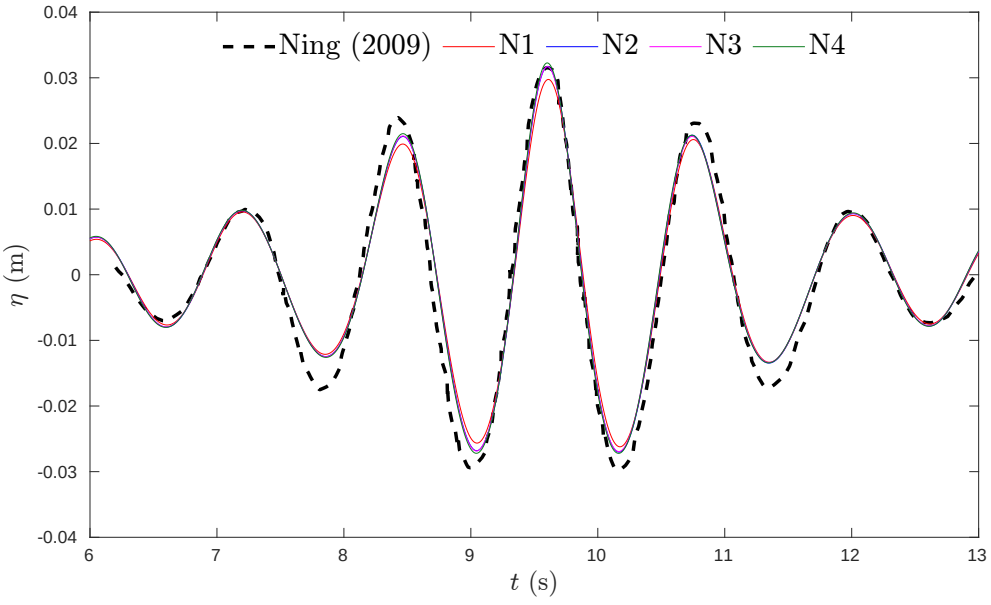

Figure 5.11: Time histories of free-surface elevation at the input focus location x_0 for different mesh configurations and experimental solution from Ning et al. (2009) [111].

5.2.6.2 Case NING3

Moving on to NING3, it can be seen from Table 5.5 that the input amplitude A_I is almost three times larger than for case NING1. This means that the focused wave will also be steeper and be more strongly nonlinear. Consequently, it is expected that the focusing time will be delayed and the focusing location will be shifted downstream. This is an effect reported not only by Ning et al. (2009) [111], but also other authors such as Westphalen et al. (2012) [142], Bihs et al. (2017) [6], and Wang et al. (2019) [137], with the cause in main being attributed to nonlinear wave-wave interaction as the wave group evolves—something that becomes more prominent with increased nonlinearity. Given this, the true focus time t_1 and location x_1 need to be found. To do this, the wave profile at time intervals close to the input focus time $t_0 = 10$ are outputted, as done by Wang et al. (2019) [137]. By doing this, the wave profile with the largest peak amplitude, its corresponding focusing location (x_1), and the corresponding focusing time (t_1) can be found. By this method, t_1 is found to be 10.16 s and x_1 is found to be 3.575

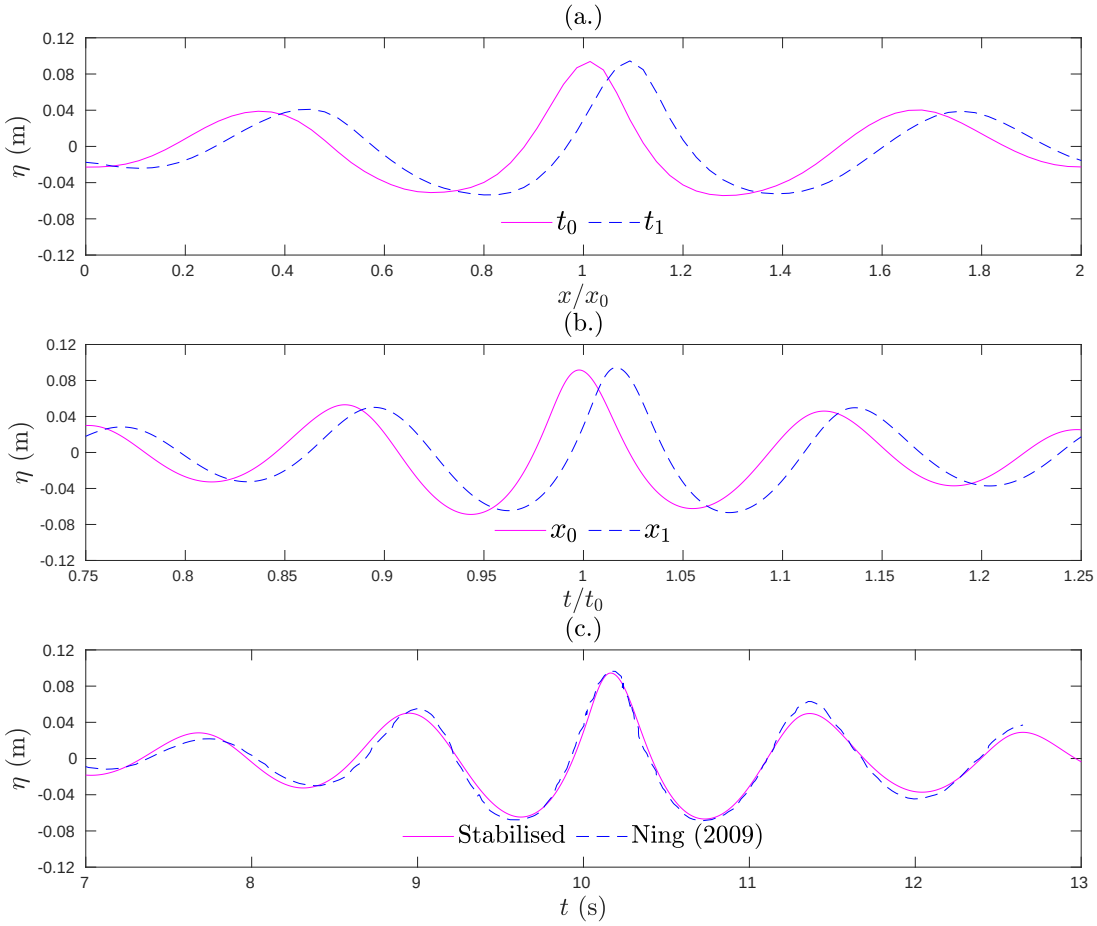

Figure 5.12: (a.) Free-surface profile at input focus time t_0 and real focus time t_1. (b.) Time histories of free-surface elevation at input focus location x_0 and real focus location x_1. (c.) Time histories of free-surface elevation at real focus location x_1 and experimental solution from Ning et al. (2009) [111].

m, both of which are also listed in Table 5.7. Figure 5.12(a) then shows the wave profiles for both t_0 and t_1 where it can be seen that the central crest at t_1 is slightly higher than at t_0. Figure 5.12(b) then also shows the time histories of free-surface elevation at both x_0 and x_1 where the delay in focal time due to increased nonlinearity can clearly be seen. Finally, Figure 5.12(c) compares the time history of free-surface elevation at the real focal location x_1 with the experimental results from Ning et al. (2009) [111], from which a good agreement in results can be seen. Note that the delay in time and shift downstream is slightly smaller than the other works cited. It is reasonable to assume that this is due to the fact a relaxation zone is used to generate the focused wave in this work, whereas the others use either a piston or paddle wavemaker.

It can be concluded then from this case that the stabilised model can accurately replicate extreme wave events in a NWT without encountering the sawtooth instability. This is of particular importance when assessing the survivability of offshore structures: any structure must be able to survive the harshest conditions, no matter how rare they may be. Hence, when it comes to designing integrated models, it has been demonstrated that this stabilised model can successfully act as the FNPF part when is comes to replicating these events.

5.3 IntegratedFoam

The success of any integrated model is dependent on the stability, accuracy, and efficiency of the coupling. In particular, the key requirement is to accurately and efficiently transfer propagating waves from the FNPF domain and successfully reproduce them in the N-S domain. How successfully this can be done is sensitive to a change in certain parameters that govern the coupling. For the IntegratedFoam model, a number of different of factors could affect the coupling, such as the type of interpolation method, accuracy of the alpha calculation method, and type of relaxation function. However, these are all predetermined and part of the given methodology, the primary parameters that will directly affect the accuracy are the mesh density, the global time step, and length of the relaxation overlapping zone Ω_{OZ}. Moreover, although not directly linked to the coupling, the length of the damping zone Ω_{DZ} will also directly affect the solution. Therefore, in this section, all the aforementioned parameters will tested for the IntegratedFoam model through test cases involving fifth-order Stokes wave propagation. Furthermore, given that a change in these parameters will also directly affect the computational time of the model, the efficiency is also simultaneously analysed.

5.3.1 Testing the length of relaxation and damping zones Ω_{OZ} and Ω_{DZ}

The first thing tested is the length of relaxation and damping zones Ω_{OZ} and Ω_{DZ}. It may seem counter intuitive to do this before the mesh and temporal sensitivity, but the length of Ω_{OZ} in particular is the main coupling parameter on which the coupling is dependent. The mesh and time step can be studied separately for the constituent FNPF and interFoam solvers, whereas

the length of Ω_{OZ} cannot. Therefore, the lengths of Ω_{OZ} and Ω_{DZ} are studied first.

Based on the works of other authors such as Paulsen et al. (2014) [113] and Li et al. (2018) [84], and through prior work with relaxation zones, a length of one wavelength for both Ω_{OZ} and Ω_{DZ} is generally assumed to be optimal for both accuracy and efficiency. Therefore, the reference case in this section is one in which Ω_{OZ} and Ω_{DZ} are both chosen to be 1 wavelength long. The other tested lengths for both Ω_{OZ} and Ω_{DZ} are 1/2 a wavelength and 2 wavelengths. Moreover, for the tests involving changing Ω_{OZ}, Ω_{DZ} is controlled at 1 wavelength, and vice versa. The dimensions of the interFoam domain Ω_{NS} are then also altered depending on the lengths of Ω_{OZ} and Ω_{DZ}, but the end location of Ω_{OZ} and start location of Ω_{DZ} are kept constant. This is to also simultaneously test how the efficiency of the model is affected by changing the lengths of the zones; it was was noted in Section 1.5.1.1 that increasing the length of the overlapping relaxation zone will inevitably increase computational time. In contrast, the dimensions of the FNPFFoam domain Ω_{FNPF} are kept constant throughout this section.

As mentioned previously in Chapters 1 and 4, the primary purpose of the constituent interFoam solver is to model wave-structure interaction, meaning only a small interFoam domain is required on and around any such structure. It would never be solely used to model wave propagation—this is left the FNPFFoam solver. However, as mentioned previously, the purpose of these tests is to see how accurately and efficiently the waves are transferred from Ω_{FNPF} and reproduced in Ω_{NS} with regards to the length of Ω_{OZ}. Given this, a relatively large ($> 6\lambda$) interFoam domain is first used in order to allow the waves to fully develop and so useful information about the coupling can be garnered before there is any potentially significant interference due to reflection from Ω_{DZ}. However, a second, more practically useful example is then considered in which the interFoam domain is much smaller ($< 2.5\ \lambda$) to see how this then compares. These cases will be called the 'long case' and 'short case' respectively.

5.3.1.1 Geometric and computational setup of FNPFFoam

The wave parameters, geometries, and computational setups for both cases in this section are all conveniently chosen to easily and properly illustrate any significant results arising from the numerical tests. The fifth-order Stokes waves generated are controlled and are the same throughout. The input wave parameters and corresponding wave steepness is similar to the fifth-order waves generated in Section 5.2.1 but are slightly adjusted to give rounder numbers; they are listed in Table 5.9. It then follows that $\Omega_{\mathrm{FNPF}} = [0,\ 100] \times [-1,\ 0]$ (m), meaning the total length of the NWT is exactly 20 wavelengths long, whereas the water depth is 1/5 of the wavelength. Following the discussion in Section 5.2, the relaxation and damping zones in

Wave	Amplitude: A(m)	Period: T(s)	Wavelength: λ(m)	Water depth: h(m)
Stokes 5^{th}	0.15	1.94	5	1

Table 5.9: Wave parameters for the generated fifth-order Stokes waves.

FNPFFoam are both chosen to be one wavelength long, and the mesh configuration is $x \times y = 800 \times 15$. This constitutes 40 cells per wavelength in the x-direction. This is slightly less than the 50 in Section 5.2.3 but was found to be sufficient through a mesh sensitivity study that is omitted here. The mesh is also refined in the y-direction so that the cell at the top has vertical width 1/10 of the cell at the bottom. The geometric and computational setup for Ω_{FNPF} is kept the same throughout this section.

5.3.1.2 Geometric and computational setups of Ω_{NS} in the long case

For the reference long case in which both Ω_{OZ} and Ω_{DZ} are 1 wavelength long, $\Omega_{\text{NS}} = [35,\ 70] \times [-1,\ 0.4]$ (m), meaning the length of Ω_{NS} is exactly 7 wavelengths long. The full IntegratedFoam NWT is then illustrated for the first time in Figure 5.13. It is important note that the vertical size of the interFoam domain is greater than FNPFFoam because it also has to allow for the air phase. The mesh configuration in this case is 850×75 where the mesh is refined in the y-direction so that 50% of cells are concentrated in the region $y \in [-0.23,\ 0.232]$ (m) around the free-surface. This is to ensure that there is sufficient mesh resolution to accurately calculate the water-volume fraction α; insufficient resolution could potentially lead to significant numerical dissipation. This configuration constitutes approximately 120 cells per wavelength in the x-direction—three times more than Ω_{FNPF}. This was found through a sensitivity study that is done in Section 5.3.2. The Ω_{OZ} lengths, dimensions, and mesh configurations for each of the three cases used to test the length of Ω_{OZ} are then all listed in Table 5.11. Analogously, the Ω_{DZ} lengths, dimensions, and mesh configurations for each of the three cases used to test the length of the Ω_{DZ} are then all listed in Table 5.12. Note that the reference case is common to both. Finally, the simulation time is 75 s, the max global Courant number $C_{\max}$ used here is 0.2, and four wave gauges, all listed in Table 5.10, are placed in both Ω_{FNPF} and Ω_{NS} to measure free-surface elevation.

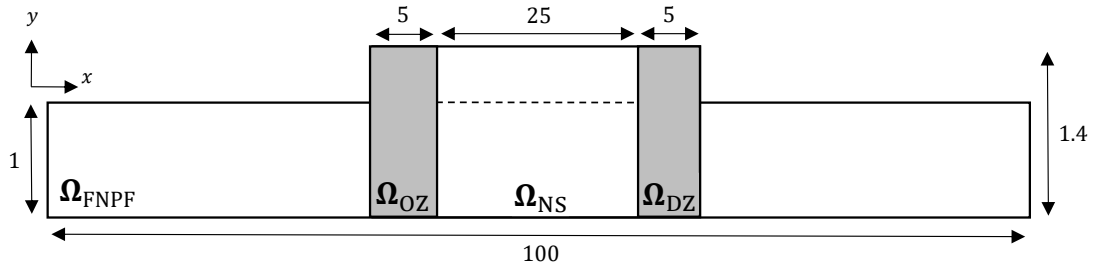

Figure 5.13: Schematic in the xy-plane of the reference IntegratedFoam numerical wave tank used in the long case (not to scale). All dimensions are in meters.

Wave Gauge	1	2	3	4
x-location (m)	45	50	55	65

Table 5.10: Wave gauge locations in the long case.

Ω_{OZ} length	Ω_{OZ} dimensions (m)	Ω_{NS} dimensions (m)	Mesh configuration
$1/2\lambda$	$[37.5,\ 40] \times [-1,\ 0.4]$	$[37.5,\ 70] \times [-1,\ 0.4]$	789×75
λ	$[35,\ 40] \times [-1,\ 0.4]$	$[35,\ 70] \times [-1,\ 0.4]$	850×75
2λ	$[30,\ 40] \times [-1,\ 0.4]$	$[30,\ 70] \times [-1,\ 0.4]$	971×75

Table 5.11: Lengths of Ω_{OZ}, dimensions of Ω_{OZ}, corresponding dimensions of Ω_{NS}, and corresponding mesh configurations of Ω_{NS} in the long case.

Ω_{DZ} length	Ω_{DZ} dimensions (m)	Ω_{NS} dimensions (m)	Mesh configuration
$1/2\lambda$	$[65,\ 67.5] \times [-1,\ 0.4]$	$[35,\ 67.5] \times [-1,\ 0.4]$	789×75
λ	$[65,\ 70] \times [-1,\ 0.4]$	$[35,\ 70] \times [-1,\ 0.4]$	850×75
2λ	$[65,\ 75] \times [-1,\ 0.4]$	$[35,\ 75] \times [-1,\ 0.4]$	971×75

Table 5.12: Lengths of Ω_{DZ}, dimensions of Ω_{DZ}, corresponding dimensions of Ω_{NS}, and corresponding mesh configurations of Ω_{NS} in the long case.

5.3.1.3 Effects of changing the length of Ω_{OZ} in the long case

Considering the change in Ω_{OZ} first, Figure 5.14 shows the time histories of free-surface elevation for FNPFFoam, and each IntegratedFoam Ω_{OZ} length, at all wave gauges. Overall, the integrated solution for each Ω_{OZ} shows good agreements with the FNPF solution at each wave gauge. However, dissipation and interference can clearly be seen after some time at every wave gauge. For closer inspection, Figures 5.15–5.18 show the same time histories at each wave gauge separately and for smaller ranges of t/T. Figures 5.15(a)–5.18(a) show the first 5 periods after the there is a fully formed wave solution. Clearly there is an increasing negative phase shift in the solution as the distance from Ω_{OZ} increases; this is the same for each length of Ω_{OZ}. This is to be expected for interFoam due to its inherent increase in dissipation over larger scales. In the same was as FNPFFFoam, this is most likely due to kinetic energy loss which leads to a negative shift given the dispersion relations (5.1) and (5.2). Figures 5.15(b)–5.18(b) then show the solutions in a middle range $t/T \in [24,\ 29]$. Again a similar pattern of phase shifting can be seen at successive wave gauges, but the difference between the solutions of varying Ω_{OZ} is negligible. Finally, Figures 5.15(c)–5.18(c) show solutions near the end of the simulation in the range $t/T \in [33,\ 38]$. A minor reduction in crest and trough amplitude can be seen at every wave gauge; this is probably down to a combination of interference due to reflection over time, and the prior observed dissipation. However, small differences can now also be observed between the solutions of varying Ω_{OZ}. In general, the solutions where $\Omega_{OZ} = \lambda$ and $\Omega_{OZ} = 2\lambda$ show better accuracy than $\Omega_{OZ} = 1/2\lambda$, particularly at the later wave gauges. This is perhaps obvious given that a larger relaxation zone should mean there is less reflection and hence should have less affect on the long-term behaviour of the solution.

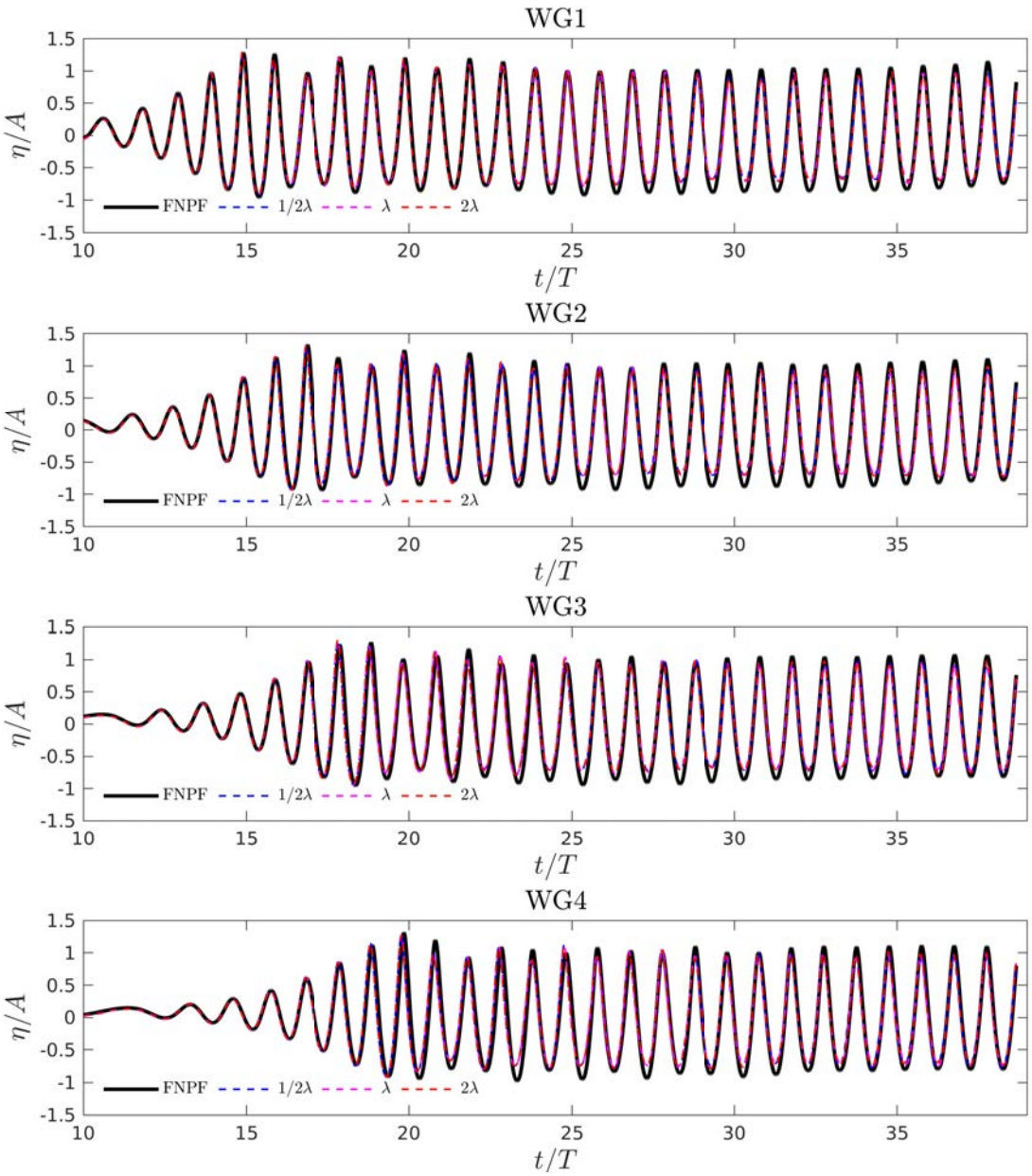

Figure 5.14: Time histories of free-surface elevation for Ω_{OZ} lengths $1/2\lambda$, λ, and 2λ, and FNPFFoam at wave gauges 1–4 (WGs 1–4) in the long case numerical wave tank.

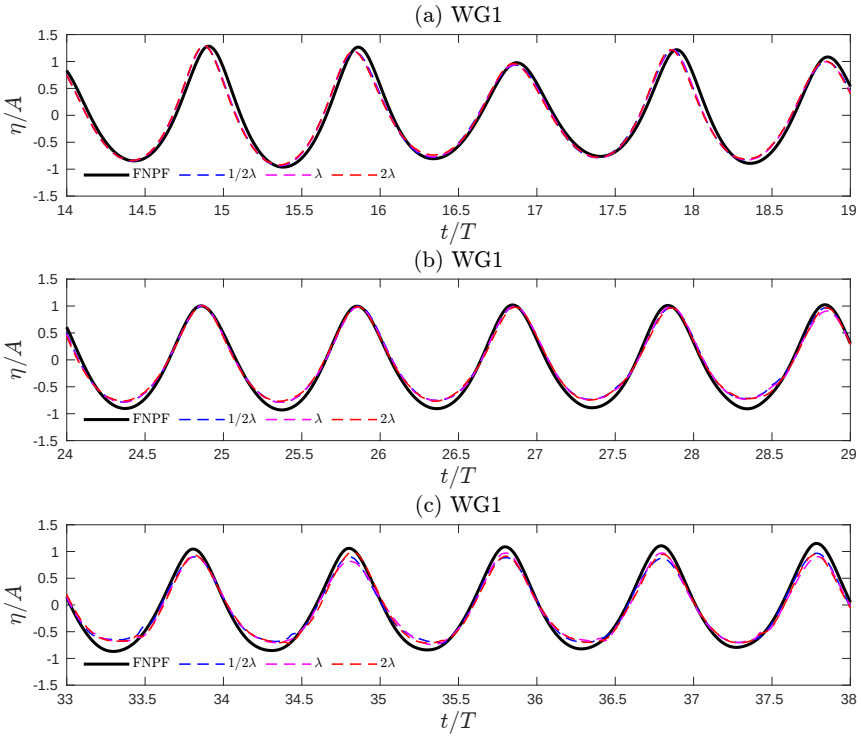

Figure 5.15: Time histories of free-surface elevation for Ω_{OZ} lengths $1/2\lambda$, λ, and 2λ, and FNPFFoam at wave gauge 1 (WG1) in the long case: (a) $t/T \in [14, 19]$, (b) $t/T \in [24, 29]$, (c) $t/T \in [33, 38]$.

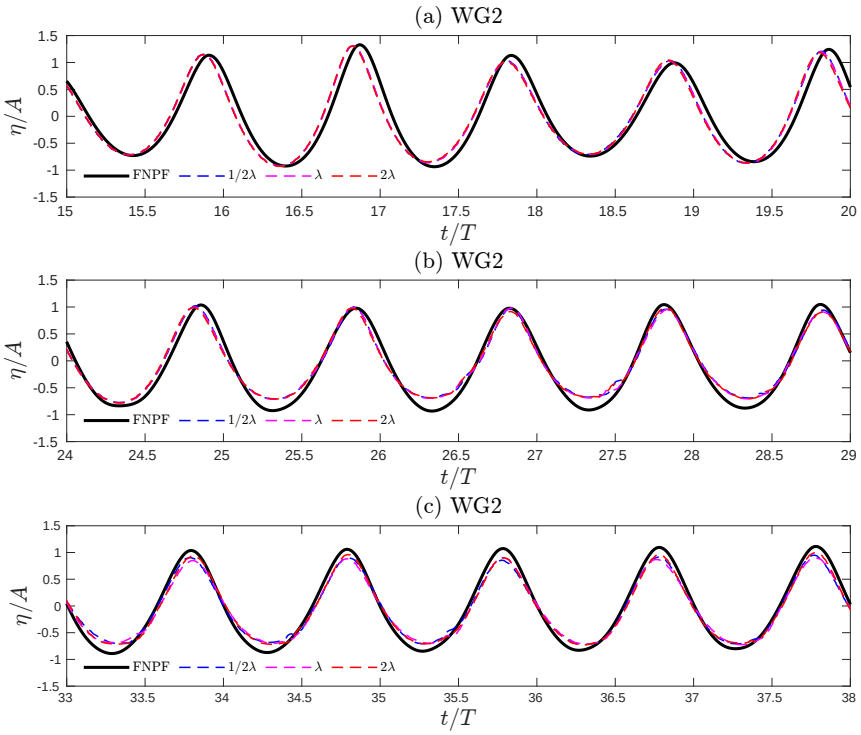

Figure 5.16: Time histories of free-surface elevation for Ω_{OZ} lengths $1/2\lambda$, λ, and 2λ, and FNPFFoam at wave gauge 2 (WG2) in the long case: (a) $t/T \in [15, 20]$, (b) $t/T \in [24, 29]$, (c) $t/T \in [33, 38]$.

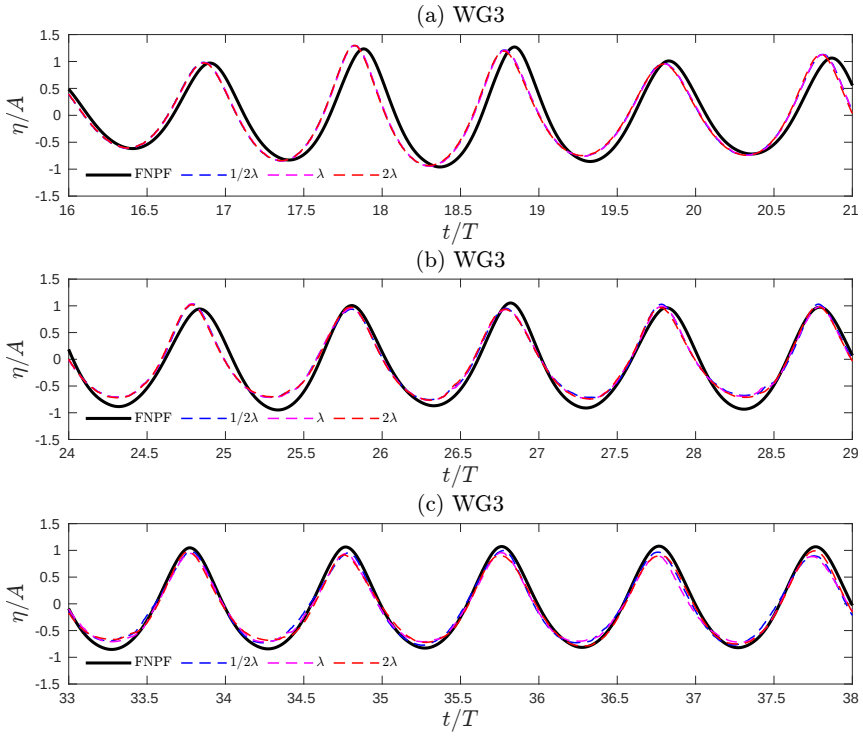

Figure 5.17: Time histories of free-surface elevation for Ω_{OZ} lengths $1/2\lambda$, λ, and 2λ, and FNPFFoam at wave gauge 3 (WG3) in the long case: (a) $t/T \in [16, 21]$, (b) $t/T \in [24, 29]$, (c) $t/T \in [33, 38]$.

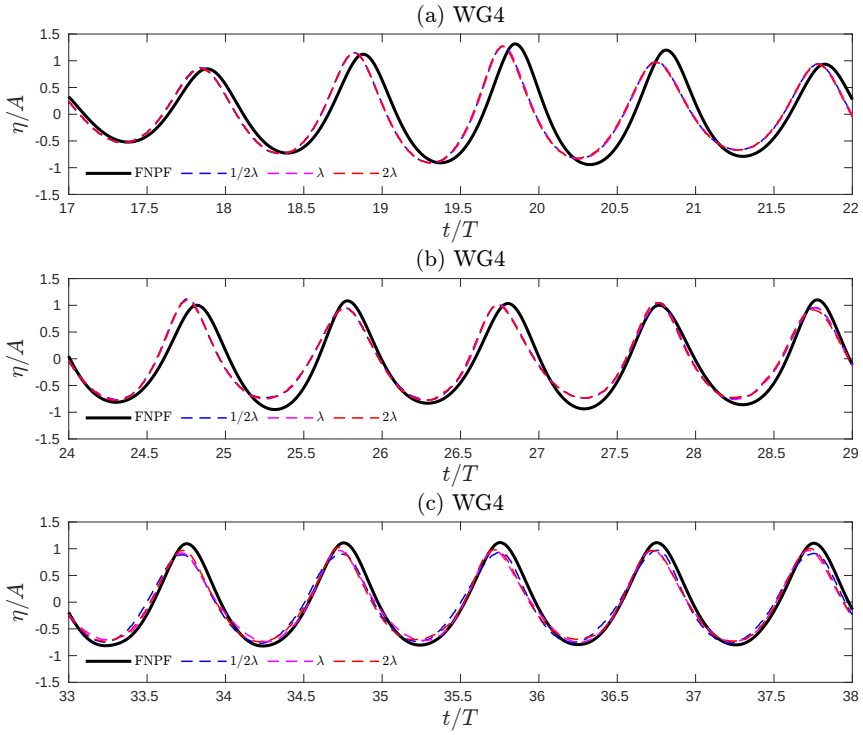

Figure 5.18: Time histories of free-surface elevation for Ω_{OZ} lengths $1/2\lambda$, λ, and 2λ, and FNPFFoam at wave gauge 4 (WG4) in the long case: (a) $t/T \in [17, 22]$, (b) $t/T \in [24, 29]$, (c) $t/T \in [33, 38]$.

It can be concluded then from the results that, all tested lengths of Ω_{OZ} produce similar results in this long case where Ω_{NS} is relatively large: only slight discrepancies can be seen as you get further from Ω_{OZ} over time. However, one thing that has not been considered yet is computational time. The total interFoam and coupling times are shown in Table 5.13 (note the FNPF time is similar for each so is omitted). Using 1 wavelength as the reference time, the 1/2 wavelength case takes approximately 0.75 times as long whilst the 2 wavelength case takes approximately 1.18 times as long. Moreover, in all cases the coupling accounts for approximately 73% of total time: a relatively large portion. These differences clearly indicate that computational time also needs to be taken into account in order for a proper balance between accuracy and efficiency, particularly for complex 3-D cases where the mesh density Ω_{NS} in the transverse direction is large. However, a question could be posed as to why an integrated model is necessary in the first place given the coupling time far outweighs the interFoam time. However, as already mentioned at the start of this section, the integrated model will never be solely used for wave propagation: its primary purpose is for wave-structure interaction. In those cases, as will be seen in Chapter 6, the interFoam time is far higher. For solely wave propagation, the FNPFFoam solver is sufficient and that is clearly much more efficient.

Another question that arises when considering these computational times is how to best decompose the domain for parallel simulations. Given that the coupling takes up most of the time, it is clear that more processors need to be dedicated to it. How this optimally balanced is then dependent on the specific case. For example, in this long case, 10 processors were used in total. The $1/2\lambda$ example dedicated 2 processors to the coupling, the λ example 3, and the 2λ example 5. This was found to optimally balance the computational time. However, as mentioned previously, in cases where the interFoam time is far higher, less processors will have to be dedicated to the coupling. On the other hand, the FNPFFoam time is far lower than both the coupling and interFoam, so how it is decomposed does not make any difference to the computational time.

Ω_{OZ} length	$1/2\lambda$	λ	2λ
Coupling time (s)	6701	9310	10,624
interFoam time (s)	2436	2948	3872
Total (s)	9137	12258	14,496

Table 5.13: Time taken by different parts of the solver for each Ω_{OZ} length in the long case.

5.3.1.4 Effects of changing the length of Ω_{DZ} in the long case

Changing the length of Ω_{DZ} is now considered. Recall that the length of Ω_{OZ} is kept constant at 1 wavelength and the dimensions in each test are displayed in Table 5.12. Figure 5.19 shows the time histories of free-surface elevation for FNPFFoam, and each IntegratedFoam Ω_{DZ} length, at all wave gauges. Initial observations indicate that the solution for $\Omega_{DZ} = 1/2\lambda$ shows some

significant interference at WGs 3 and 4, meaning reflection from the Ω_{DZ} is greater. For closer inspection, Figures 5.20–5.23 again show the same time histories at each wave gauge separately and for smaller ranges of t/T. Similar to the test for Ω_{OZ}, a phase shift can again be seen in Figures 5.15(a)–5.18(a). However the results in Figures 5.15(b)–5.18(b) are slightly different. At WGs 1 and 2 the solutions progressively get more accurate with increasing Ω_{DZ} length. This is also true for WGs 3 and 4 but all solutions generally become more inaccurate, with the $1/2\lambda$ solution being more inaccurate than the others. Similar effects can be seen in Figures 5.15(c)–5.18(c). Overall, these results confirm what is already assumed; namely, increasing the length Ω_{DZ} results in less reflection and better accuracy. However, the extent to which this is the case is not discernible. At most it can be concluded that a length $\Omega_{DZ} = 1/2\lambda$ should not be used if it can be avoided.

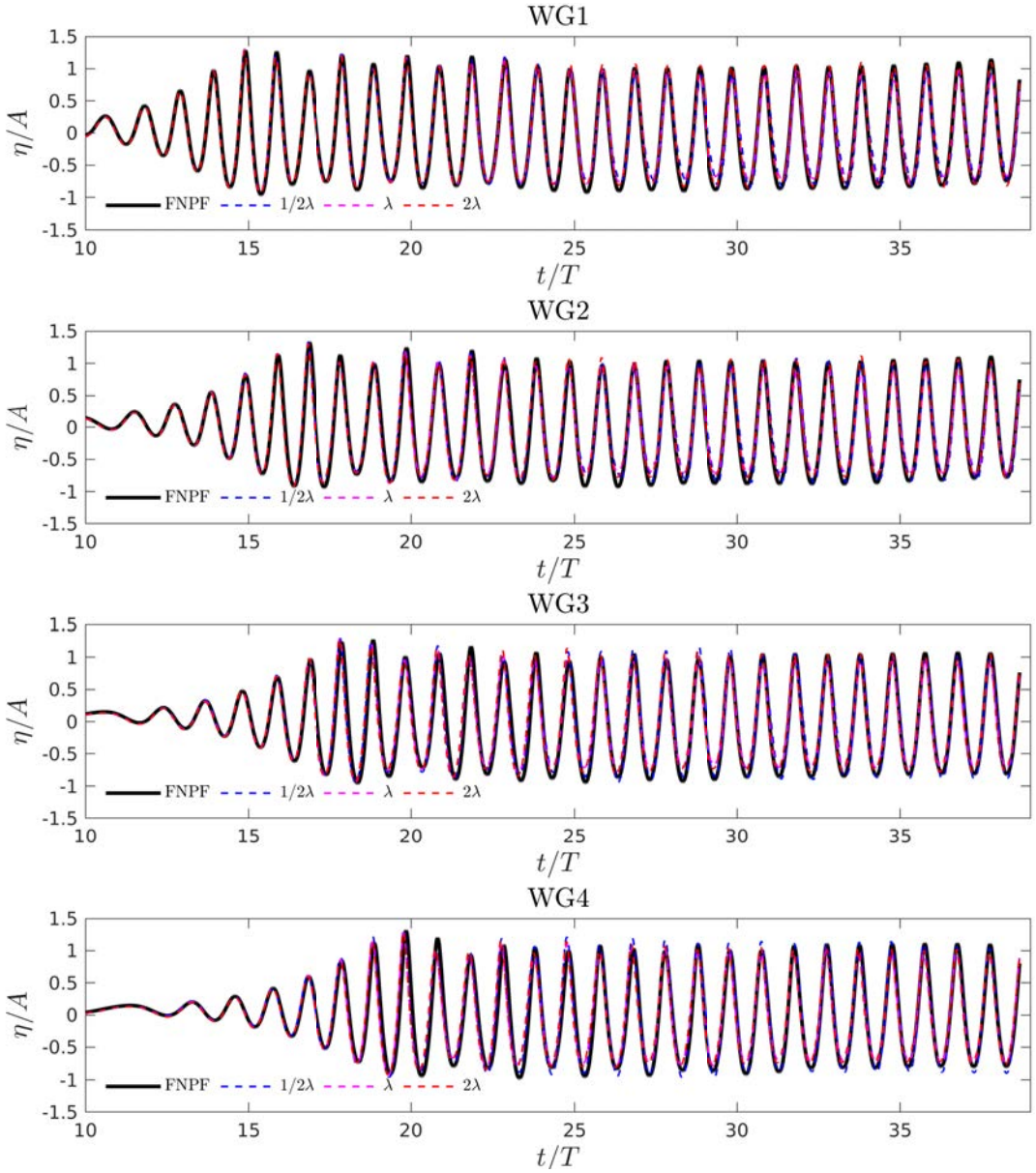

Figure 5.19: Time histories of free-surface elevation for Ω_{DZ} lengths $1/2\lambda$, λ, and 2λ, and FNPFFoam at wave gauges 1–4 (WGs 1–4) in the long case numerical wave tank.

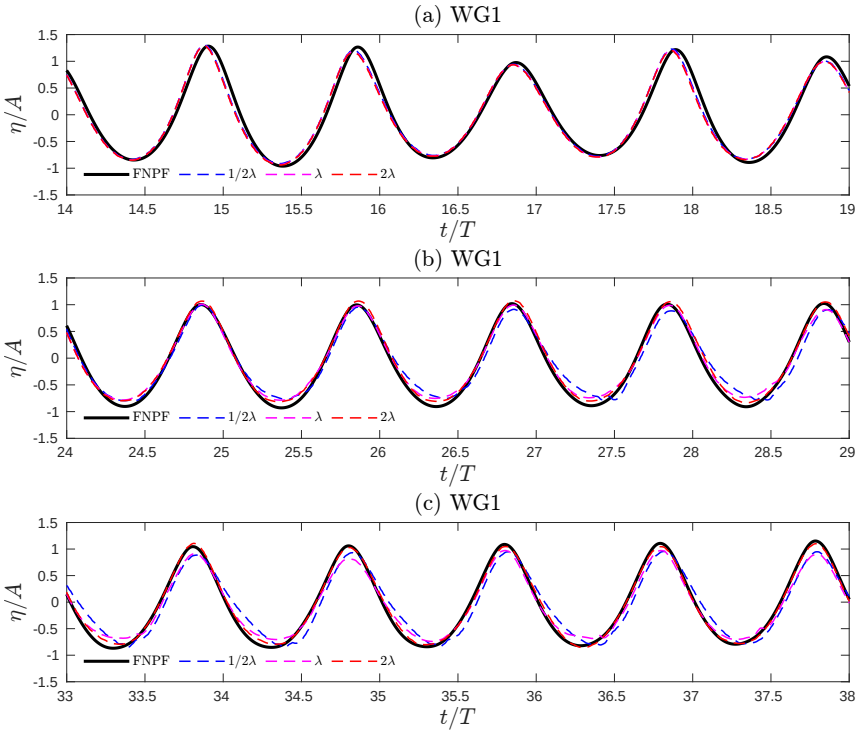

Figure 5.20: Time histories of free-surface elevation for Ω_{DZ} lengths $1/2\lambda$, λ, and 2λ, and FNPFFoam at wave gauge 1 (WG1) in the long case: (a) $t/T \in [14, 19]$, (b) $t/T \in [24, 29]$, (c) $t/T \in [33, 38]$.

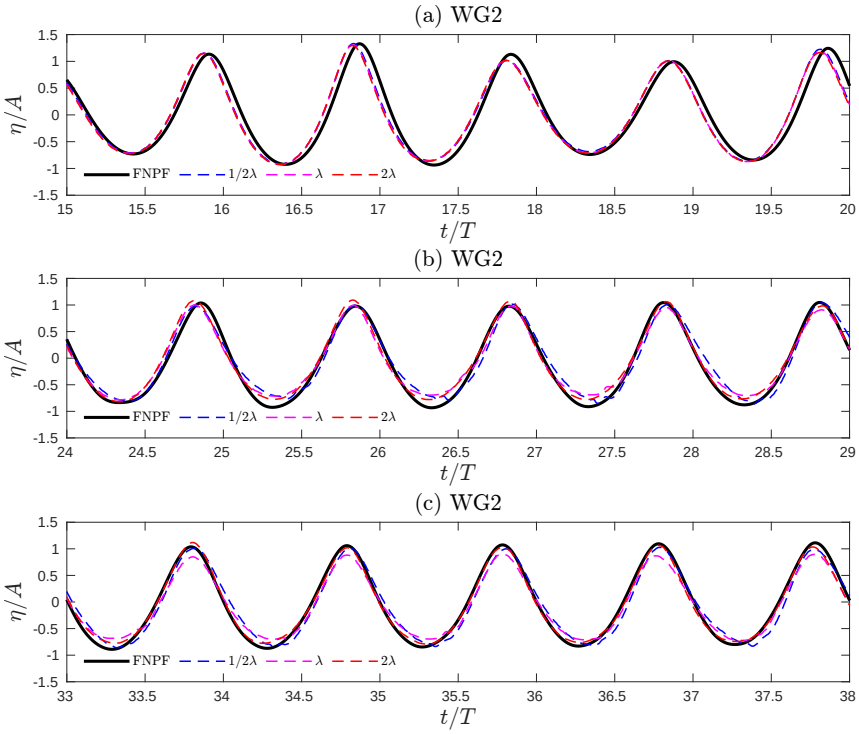

Figure 5.21: Time histories of free-surface elevation for Ω_{DZ} lengths $1/2\lambda$, λ, and 2λ, and FNPFFoam at wave gauge 2 (WG2) in the long case: (a) $t/T \in [15, 20]$, (b) $t/T \in [24, 29]$, (c) $t/T \in [33, 38]$.

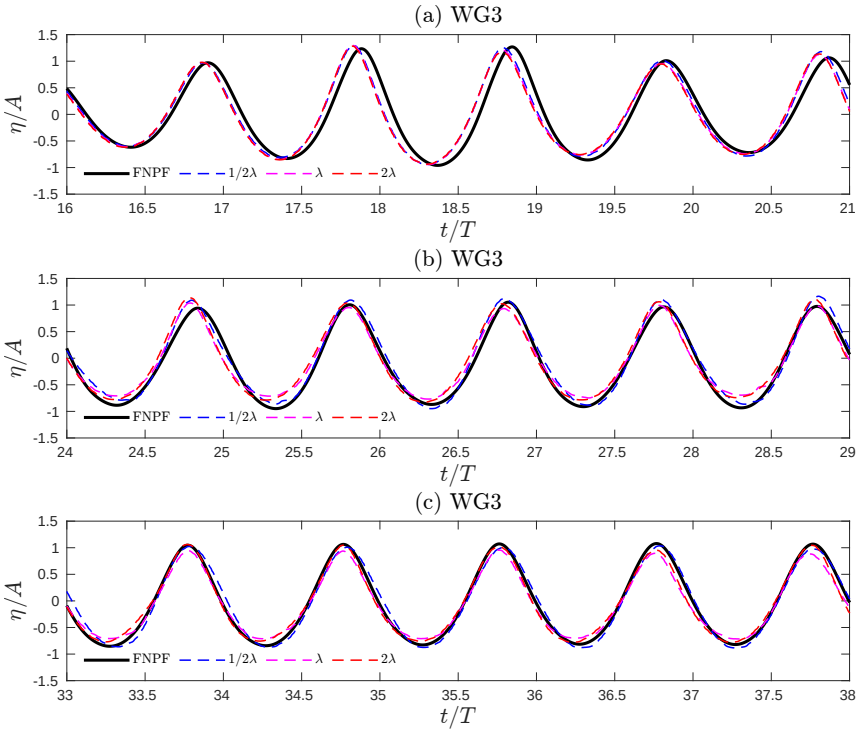

Figure 5.22: Time histories of free-surface elevation for Ω_{DZ} lengths $1/2\lambda$, λ, and 2λ, and FNPFFoam at wave gauge 3 (WG3) in the long case: (a) $t/T \in [16, 21]$, (b) $t/T \in [24, 29]$, (c) $t/T \in [33, 38]$.

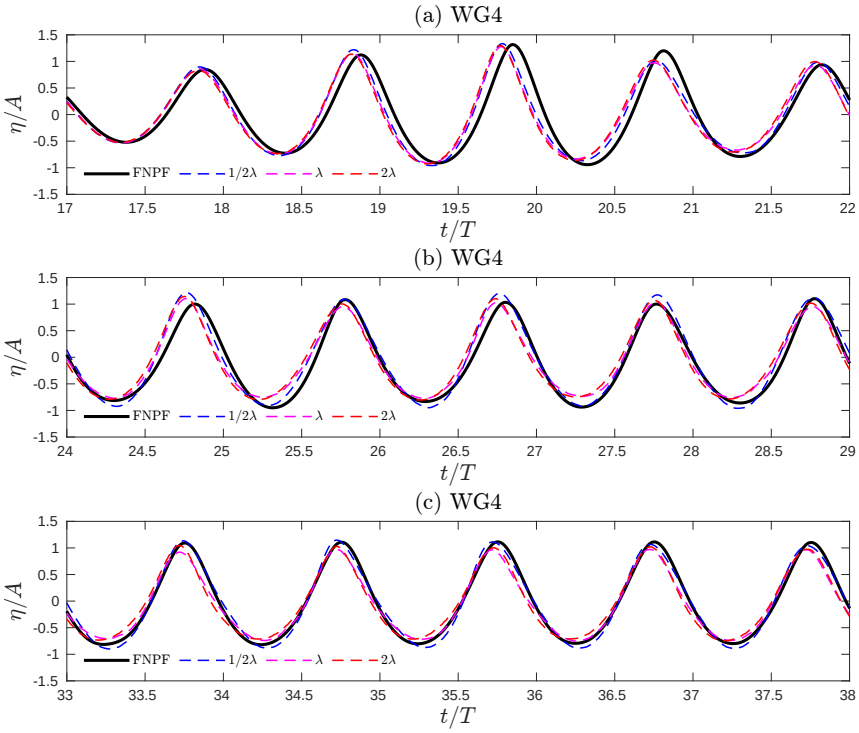

Figure 5.23: Time histories of free-surface elevation for Ω_{OZ} lengths $1/2\lambda$, λ, and 2λ, and FNPFFoam at wave gauge 4 (WG4) in the long case: (a) $t/T \in [17, 22]$, (b) $t/T \in [24, 29]$, (c) $t/T \in [33, 38]$.

Table 5.14 then shows the differences in interFoam time. The differences here clearly are not that great with the 2λ case taking approximately 1.15 times as long and the $1/2\lambda$ case taking approximately 0.96 times as long. Therefore, it is discretionary depending on the case which length is chosen. However, as was the case with Ω_{OZ}, the time will be vastly increased in 3D or if the wavelength is long, so this also has to be taken into account.

Ω_{DZ} length	$1/2\lambda$	λ	2λ
interFoam time (s)	2842	2948	3372

Table 5.14: Time taken by interFoam for each Ω_{DZ} length in the long case.

5.3.1.5 Geometric and computational setups of Ω_{NS} in the short case

As mentioned previously, the short case is a more practically useful example because it is more representative of the Ω_{NS} setup that will be used for wave-structure interaction problems. For the reference short case in which both Ω_{OZ} and Ω_{DZ} are again 1 wavelength long, $\Omega_{\mathrm{NS}} = [58,\ 70] \times [-1,\ 0.4]$ (m), meaning the length of Ω_{NS} is 2.4 wavelengths long—as opposed to the long case which was 7. The mesh configuration is 291×75 and the mesh is again refined in the y-direction so that 50% of cells are concentrated in the region $y \in [-0.23,\ 0.232]$ (m). The Ω_{OZ} lengths, dimensions, and mesh configurations for each of the three cases used to test the length of the Ω_{OZ} are then all listed in Table 5.15. The analogous for Ω_{DZ} are then all also listed in Table 5.16. Note that the reference case is again common to both. Finally, the simulation time is 75 s, the max global Courant number $C_{\max}$ is 0.2, and there is one wave gauge at $x = 64$ m in both Ω_{FNPF} and Ω_{NS}.

Ω_{OZ} length	Ω_{OZ} dimensions (m)	Ω_{NS} dimensions (m)	Mesh configuration
$1/2\lambda$	$[60.5,\ 63] \times [-1,\ 0.4]$	$[60.5,\ 70] \times [-1,\ 0.4]$	230×75
λ	$[58,\ 63] \times [-1,\ 0.4]$	$[58,\ 70] \times [-1,\ 0.4]$	291×75
2λ	$[53,\ 63] \times [-1,\ 0.4]$	$[53,\ 70] \times [-1,\ 0.4]$	412×75

Table 5.15: Lengths of Ω_{OZ}, dimensions of Ω_{OZ}, corresponding dimensions of Ω_{NS}, and corresponding mesh configurations of Ω_{NS} in the short case.

Ω_{DZ} length	Ω_{DZ} dimensions (m)	Ω_{NS} dimensions (m)	Mesh configuration
$1/2\lambda$	$[65,\ 67.5] \times [-1,\ 0.4]$	$[58,\ 67.5] \times [-1,\ 0.4]$	230×75
λ	$[65,\ 70] \times [-1,\ 0.4]$	$[58,\ 70] \times [-1,\ 0.4]$	291×75
2λ	$[65,\ 75] \times [-1,\ 0.4]$	$[58,\ 75] \times [-1,\ 0.4]$	412×75

Table 5.16: Lengths of Ω_{DZ}, dimensions of Ω_{DZ}, corresponding dimensions of Ω_{NS}, and corresponding mesh configurations of Ω_{NS} in the short case.

5.3.1.6 Effects of changing the length of Ω_{OZ} and Ω_{DZ} in the short case

Considering Ω_{OZ} first, Figure 5.24 shows the time histories of free-surface elevation for FNPFFoam, and each IntegratedFoam Ω_{OZ} length, at the sole wave gauge and for varying ranges of t/T. Overall, the λ and 2λ integrated solutions show very good agreements with the FNPF solution. However, the $1/2\lambda$ solution shows a clear phase shift, but the crest and trough amplitudes are still accurate. Interestingly, the long term behaviour of the solution for each length does not show as significant dissipation or interference as the long case and instead remains very accurate. Therefore, given that this short case is more representative of what will be used for wave-structure interaction problems, it can be concluded with confidence the integrated model would be able to accurately reproduce the wave solution in Ω_{NS} over a large time scale.

The total interfoam and coupling times are then shown in Table 5.17. Using 1 wavelength as the reference time, the 1/2 wavelength case takes approximately 0.74 times as long whilst the 2 wavelength case takes approximately 1.2 times as long. Moreover, the coupling accounts for approximately 82–84% of total time: an even larger portion than the long case. However, this is to expected given that the proportion of Ω_{OZ} relative to Ω_{NS} is larger. Again, it must be emphasised that the integrated model will never be solely used for wave propagation: its primary purpose is for wave-structure interaction. In those cases, as will be seen in Chapter 6, the interFoam time is far higher. For solely wave propagation, the FNPFFoam solver is sufficient and that is clearly much more efficient.

Figure 5.25 then shows the analogous time histories of free-surface elevation for FNPFFoam, and each IntegratedFoam Ω_{DZ} length, at the sole wave gauge and for varying ranges of t/T. Again, the λ and 2λ integrated solutions shows very good agreements with the FNPF solution, but the $1/2\lambda$ solution shows a reduction in both crest and trough amplitude in all time intervals. Moreover, the interFoam times displayed in Table 5.18 show no major difference between each length, hence a length of $1/2\lambda$ can easily be avoided. However, as already mentioned, this does also depend on the specific case and should be discretionary.

Ω_{OZ} length	$1/2\lambda$	λ	2λ
Coupling time (s)	4570	6161	7285
interFoam time (s)	854	1169	1563
Total (s)	5424	7330	8848

Table 5.17: Time taken by different parts of the solver for each Ω_{OZ} length in the short case.

Ω_{DZ} length	$1/2\lambda$	λ	2λ
interFoam time (s)	923	945	982

Table 5.18: Time taken by interFoam for each Ω_{DZ} length in the short case.

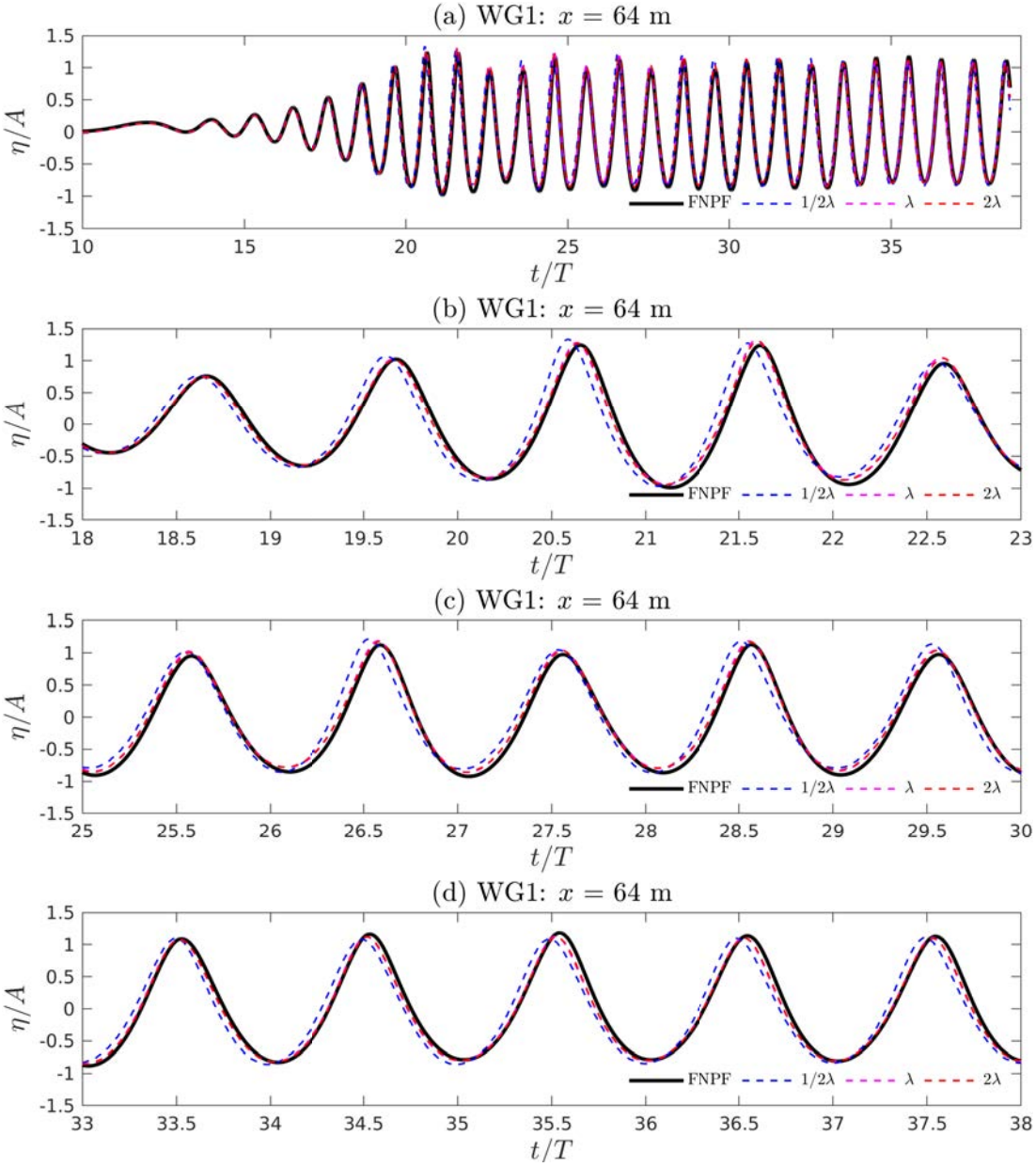

Figure 5.24: Time histories of free-surface elevation for Ω_{OZ} lengths $1/2\lambda$, λ, and 2λ, and FNPFFoam at wave gauge (WG) $x = 64$ m in the short case numerical wave tank: (a) $t/T \in [10, 39]$, (b) $t/T \in [18, 23]$, (c) $t/T \in [25, 30]$, (d) $t/T \in [33, 38]$.

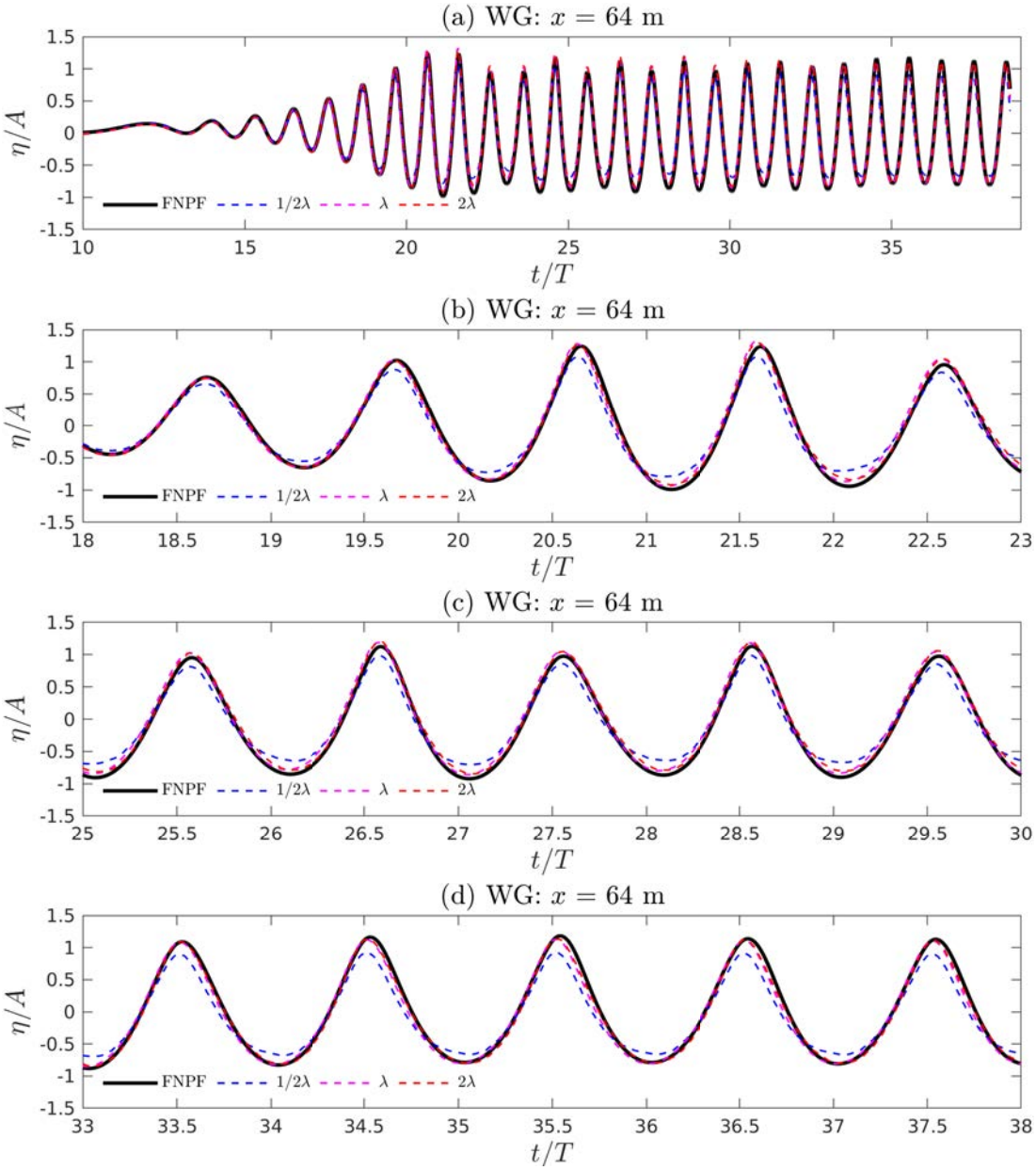

Figure 5.25: Time histories of free-surface elevation for Ω_{DZ} lengths $1/2\lambda$, λ, and 2λ, and FNPFFoam at wave gauge (WG) $x = 64$ m in the short case numerical wave tank: (a) $t/T \in [10, 39]$, (b) $t/T \in [18, 23]$, (c) $t/T \in [25, 30]$, (d) $t/T \in [33, 38]$.

5.3.2 Mesh sensitivity

The next thing tested mesh sensitivity. Proper mesh density is required for the interFoam solver to provide a sufficiently accurate solution, but efficiency also has to be taken into account. In addition, for IntegratedFoam, proper density is also required in the overlapping relaxation zone. Testing in this section is done using the reference long case NWT outlined in Section 5.3.1.2 with the same input wave parameters and computational setup. Prior work with interFoam suggests that at least double the density of cells is required per wavelength for sufficient accuracy when compared to FNPFFoam. Therefore, four meshes—A, B, C, and D listed in Table 5.19—are considered. These constitute 80, 100, 120, and 140 cells per wavelength. Note that mesh C is the mesh that was used in the prior long case.

ID	Configuration $x \times y$	Cells per λ	Total no. of cells	No. of cells in Ω_{OZ}
A	562×75	80	42,150	6021
B	702×75	100	52,650	7521
C	850×75	120	63,750	9107
D	982×75	140	73,650	10,521

Table 5.19: Mesh configurations used in mesh sensitivity studies for IntegratedFoam.

Figure 5.26 then shows the time histories of free-surface elevation for FNPFFoam, and each IntegratedFoam mesh, at all wave gauges. Overall, every mesh shows good agreements with the FNPF solution at each wave gauge, but some dissipation is present (which is top be expected as discussed previously). For closer inspection, Figures 5.27–5.30 show the same time histories at each wave gauge separately and for smaller ranges of t/T. These figures paint a slightly different story. At WG1 (Figure 5.27), each mesh is reasonably accurate, but mesh D counter intuitively shows slight amplitude decay and phase shift. This looks like an anomalous result because the mesh D solution at WGs 2–4 is actually the most accurate. Mesh C also performs well and provides similar solution accuracy to mesh D at every wave gauge. However, meshes A and B show increased dissipation at each progressive wave gauge. Their solutions at WG3 and WG4 in particular show noticeable amplitude decay and negative phase shift.

Table 5.20 then also shows the computational times. As expected, the increased number of cells increases both coupling and interFoam times. However, the coupling time seems to be increasing at a faster rate than interFoam. This is backed up by Figure 5.31 which shows the relationship between the number of cells and computational time for the coupling and interFoam. The times for both interFoam and the coupling are clearly increasing exponentially as the number of cells increases, but the coupling time is increasing much faster. This clearly then has to be taken into account when balancing accuracy and efficiency. A further analysis could even be done by refining the mesh to see whether less cells can be used for the coupling, whilst keeping the same amount in the rest of the domain, without a loss in accuracy.

Mesh	A	B	C	D
Coupling time (s)	4166	5570	9310	13831
interFoam time (s)	1214	1812	2948	5007
Total (s)	5380	7382	12258	18838

Table 5.20: Time taken by different parts of the solver for meshes A, B, C, and D.

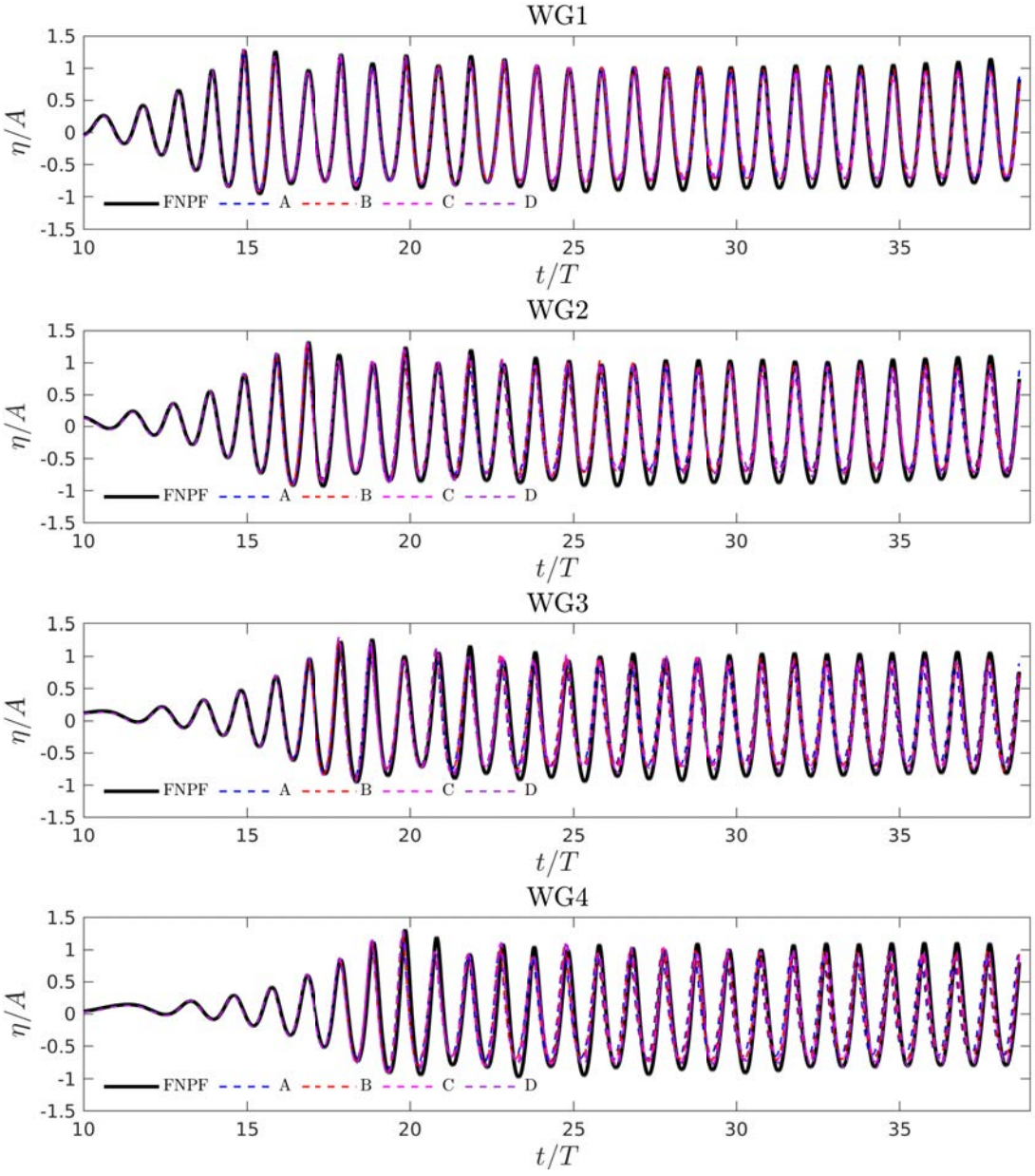

Figure 5.26: Time histories of free-surface elevation for meshes IntegratedFoam A, B, C, and D, and FNPFFoam at wave gauge 1–4 (WGs 1–4).

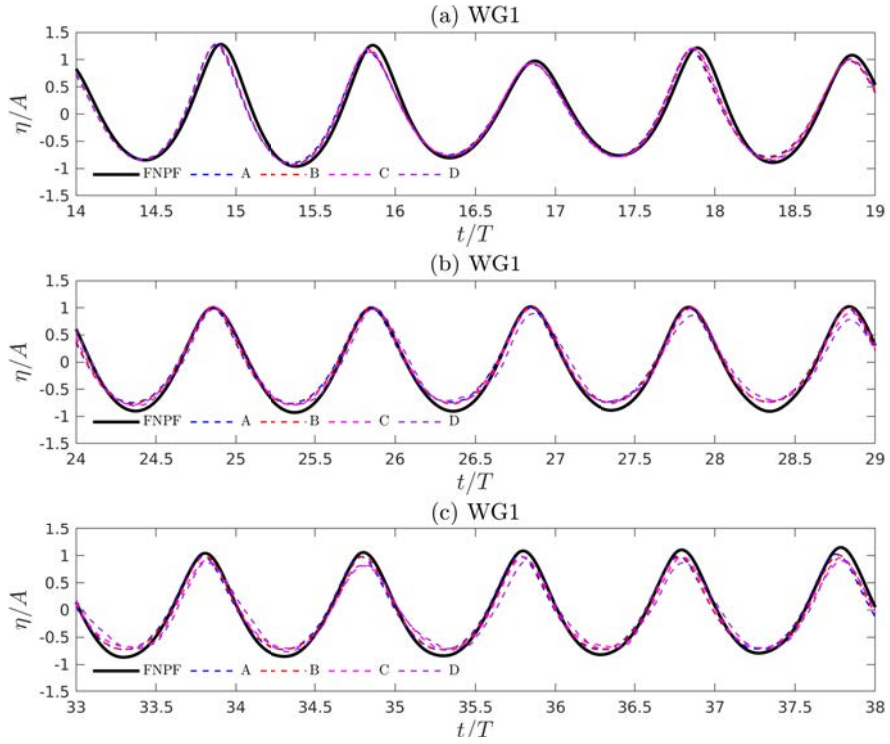

Figure 5.27: Time histories of free-surface elevation for IntegratedFoam meshes A, B, C, and D, and FNPFFoam at wave gauge 1 (WG1): (a) $t/T \in [14, 19]$, (b) $t/T \in [24, 29]$, (c) $t/T \in [33, 38]$.

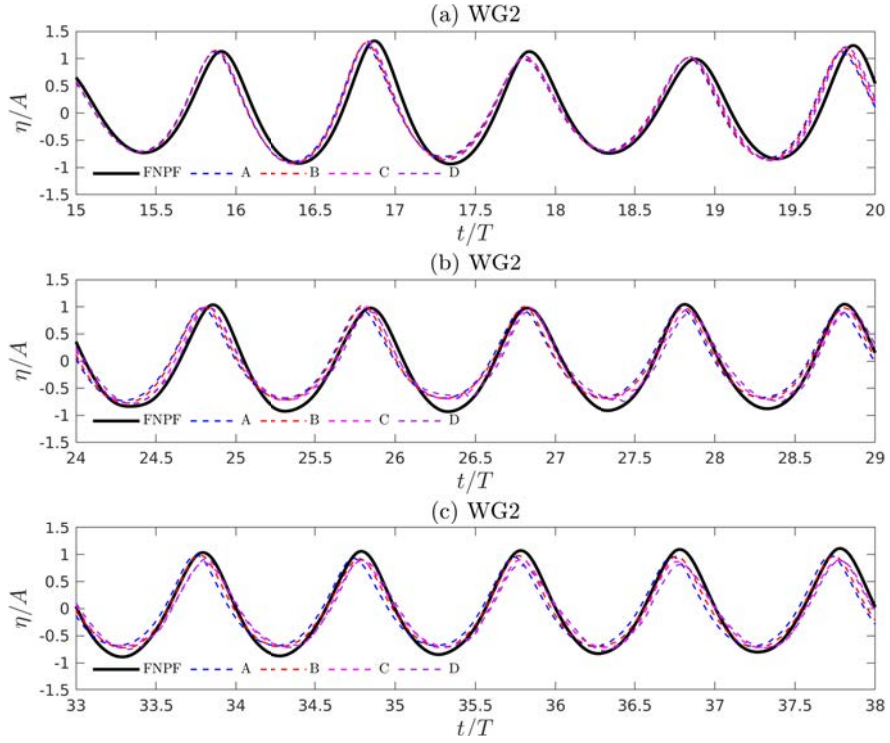

Figure 5.28: Time histories of free-surface elevation for IntegratedFoam meshes A, B, C, and D, and FNPFFoam at wave gauge 2 (WG2): (a) $t/T \in [15, 20]$, (b) $t/T \in [24, 29]$, (c) $t/T \in [33, 38]$.

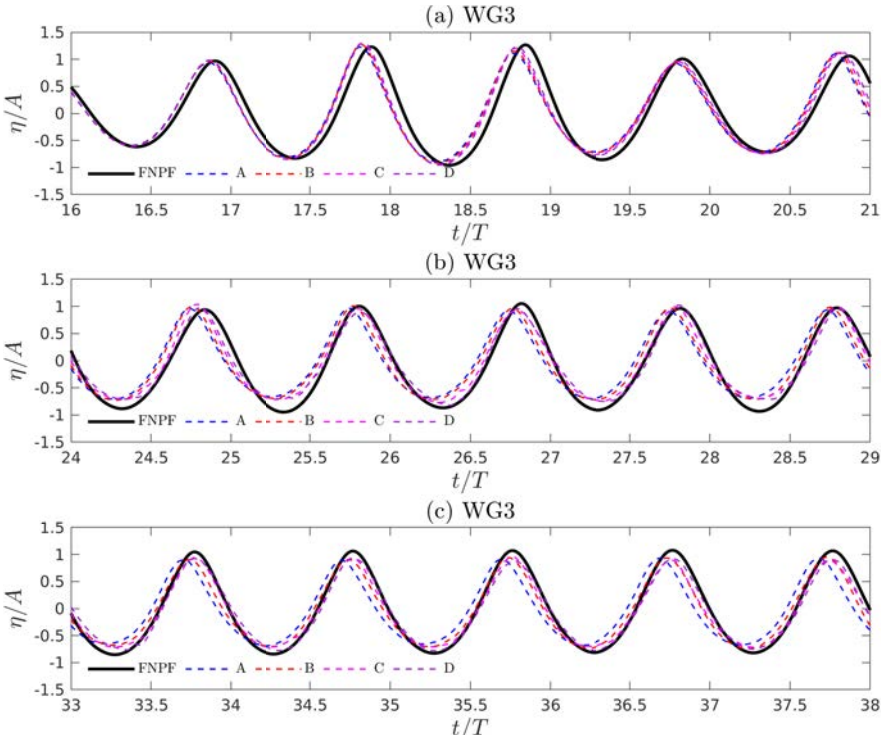

Figure 5.29: Time histories of free-surface elevation for IntegratedFoam meshes A, B, C, and D, and FNPFFoam at wave gauge 3 (WG3): (a) $t/T \in [16, 21]$, (b) $t/T \in [24, 29]$, (c) $t/T \in [33, 38]$.

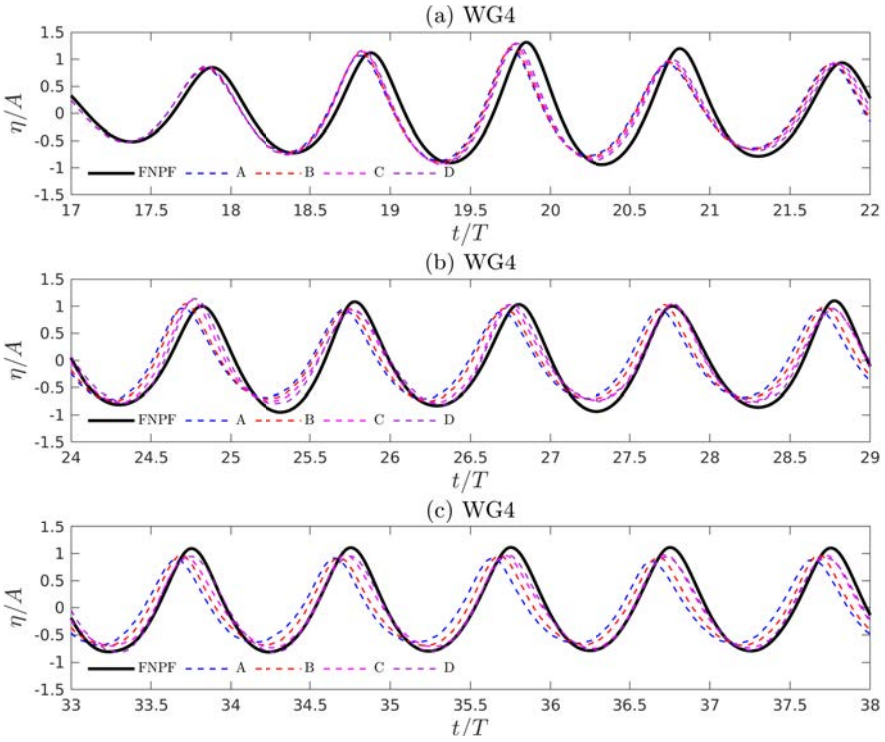

Figure 5.30: Time histories of free-surface elevation for IntegratedFoam meshes A, B, C, and D, and FNPFFoam at wave gauge 4 (WG4): (a) $t/T \in [17, 22]$, (b) $t/T \in [24, 29]$, (c) $t/T \in [33, 38]$.

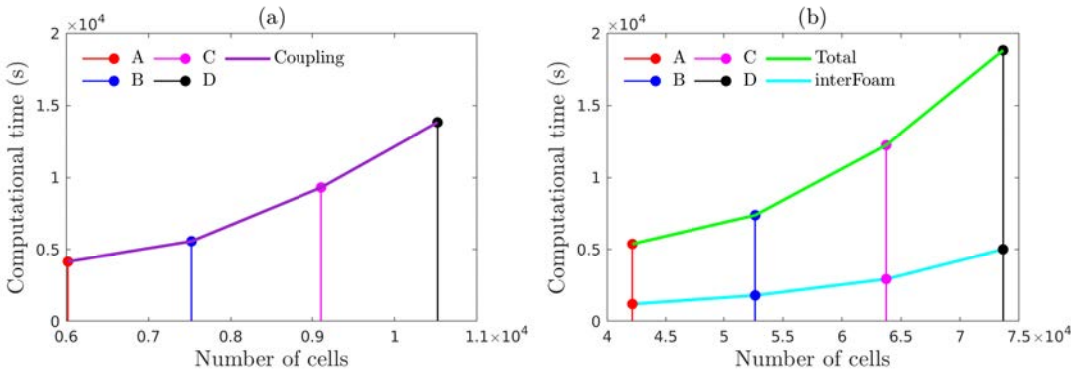

Figure 5.31: Relationship between the number of mesh cells in meshes A, B, C, and D, and computational time: (a) Coupling, (b) interFoam and Total. Note that the number of mesh cells for the coupling is less so the x-axis limits are different. However, the y-axis has the same limits, so the proportion of actual time taken by each part of the solver is illustrated to scale.

5.3.3 Temporal sensitivity

As previously mentioned, and similar to the FNPFFoam model, temporal sensitivity and convergence with respect to the global time step is a key parameter that will affect the accuracy of the coupling in the IntegratedFoam model. Recall that the adaptive time-stepping control procedure explained in Section 2.3.3.4 is implemented in the IntegratedFoam model and its constituent FNPFFoam and interFoam solvers. This procedure is dependent on the user-prescribed max Courant number $C_{\max}$, from which the time step is calculated separately for each solver accordingly from Equation (2.56). The global time step is then calculated as the minimum value out of the two. Given this, the IntegratedFoam model is tested here for both the long and short cases by prescribing different global values of $C_{\max}$.

5.3.3.1 Geometric and computational setup for the long case

The geometric and computational setup is the same as the long case in the Section5.3.1.2, with Ω_{OZ} and Ω_{DZ} both chosen as 1 wavelength long. The corresponding dimensions and mesh configurations are shown in Tables 5.11 and 5.12. Moreover, the input fifth-order Stokes wave parameters are the same as those listed in Table 5.9, the same FNPFFoam setup outlined in Section 5.3.1.1 is again used, and the same wave gauges listed in Table 5.10 are placed in the NWT. The values of $C_{\max}$ tested are 0.05, 0.1, 0.2, and 0.4. Note that $C_{\max} = 0.2$ is the value that has been used in all test cases so far, and hence is the reference case.

Given that the change in $C_{\max}$ also affects the FNPFFoam solution as well as the coupling, an error measure that compares the IntegratedFoam solution to its corresponding FNPFFoam solution is used for analysis rather by directly analysing the free-surface elevation. Therefore, similar to Section 5.2.4.1, four error measures are introduced: the normalised crest and trough

amplitude errors ϵ^a_{crest} and ϵ^a_{trough}, each defined by

$$\epsilon^a_{crest} = \frac{\eta^{\text{Integrated}}_{crest} - \eta^{\text{FNPF}}_{crest}}{A} \tag{5.31}$$

and

$$\epsilon^a_{trough} = \frac{\eta^{\text{Integrated}}_{trough} - \eta^{\text{FNPF}}_{trough}}{A} \tag{5.32}$$

respectively, where $\eta^{\text{Integrated}}$ and η^{FNPF} are the IntegratedFoam and corresponding FNPFFoam free-surface elevations respectively; and the normalised crest and trough phase shifts ϵ^θ_{crest} and ϵ^θ_{trough}, each defined by

$$\epsilon^\theta_{crest} = \frac{t^{\text{Integrated}}_{crest} - t^{\text{FNPF}}_{crest}}{T} \tag{5.33}$$

and

$$\epsilon^\theta_{trough} = \frac{t^{\text{Integrated}}_{trough} - t^{\text{FNPF}}_{trough}}{T} \tag{5.34}$$

respectively, where $t^{\text{Integrated}}$ and t^{FNPF} are the IntegratedFoam and FNPFFoam times respectively at each crest and trough instance.

5.3.3.2 Effects of changing $C_{\max}$ on free-surface elevation in the long case

Figure 5.32 shows the normalised crest and trough amplitude errors over time at WGs 1–4 for varying values of $C_{\max}$. The crest errors ϵ^a_{crest} are shown in Figure 5.32(a) and the trough errors ϵ^a_{trough} are shown in Figure 5.32(b). For the crest errors, it is clear at WGs 1–3 that the crest amplitude fluctuates between underestimation and overestimation during the 10 or so periods, with the degree of fluctuation increasing with increasing $C_{\max}$. All solutions then gradually tend towards increased underestimation as time goes by with minimal difference between solutions, but a slight trend of increased underestimation with increasing $C_{\max}$ persists. The results at WG4 are slightly different in that the $C_{\max} = 0.4$ solution shows a much greater underestimation than the other solutions. For the trough errors, a more distinct pattern of underestimation is seen at progressive wave gauges. Moreover, besides WG1, the underestimation increases with increasing $C_{\max}$ with $C_{\max} = 0.4$ again showing greater underestimation, particularly at WGs 3 and 4. This confirms that the coupling and interfoam are indeed sensitive to a change in $C_{\max}$ and consequently the time step. In general, a smaller value of $C_{\max}$ leads to a more accurate solution, particularly over a larger scale. However, the results also show that the difference between the solutions for $C_{\max} = 0.05$, 0.1, and 0.2 is small—$C_{\max} = 0.4$ is the main outlier.

Moving on to the phase shifts, Figure 5.33 shows the normalised crest and trough phase shifts over time at WGs 1–4 for varying values of $C_{\max}$. Again, the crest shifts ϵ^θ_{crest} are shown in Figure 5.33(a) and the trough shifts ϵ^θ_{trough} are shown in Figure 5.33(b). For the crest shifts, a clear pattern emerges with each progressive wave gauge: $C_{\max} = 0.05$, 0.1, and 0.2 show very slight fluctuations with the magnitude of the phase shift increasing slightly with increasing $C_{\max}$, whereas $C_{\max} = 0.4$ shows a large negative phase shift at every wave gauge, with the divergence from the other solutions becoming larger at progressive gauges. The trough shifts show a similar but slightly different pattern. The solutions of $C_{\max} = 0.05$, 0.1, and 0.2 all

show a slight positive phase shift that decreases with each wave gauge. This can most likely be put down to significant interference from reflection given that it starts to increase at similar times for each wave gauge. On the other hand, $C_{\max} = 0.4$ shows a negative phase shift that again increases with each wave gauge, clearly showing it does not provide an accurate solution.

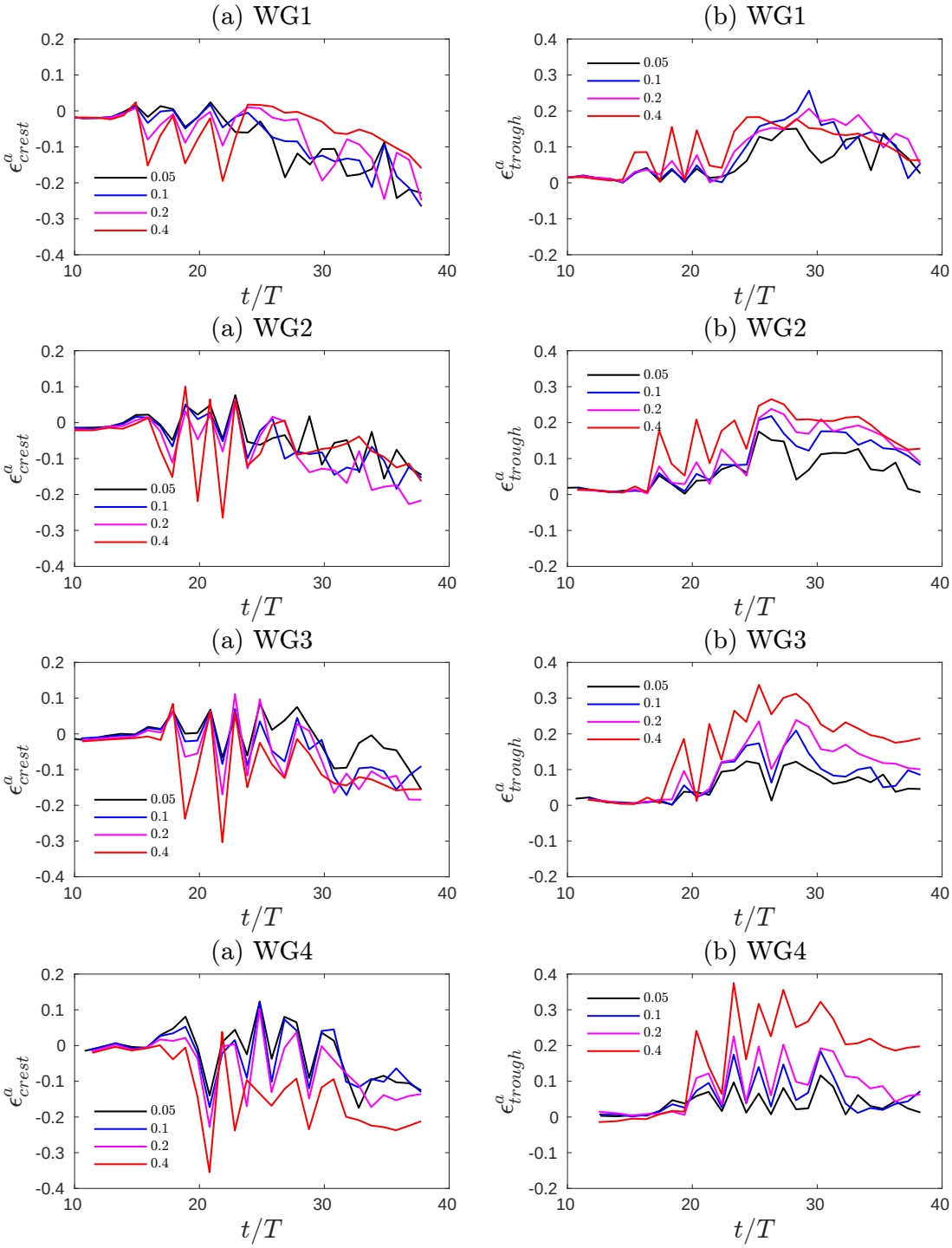

Figure 5.32: Normalised crest and trough amplitude errors ϵ^a_{crest} and ϵ^a_{trough} for $C_{\max} = 0.05$, 0.1, 0.2, and 0.4 at wave gauges 1–4 (WGs 1–4) in the long case.

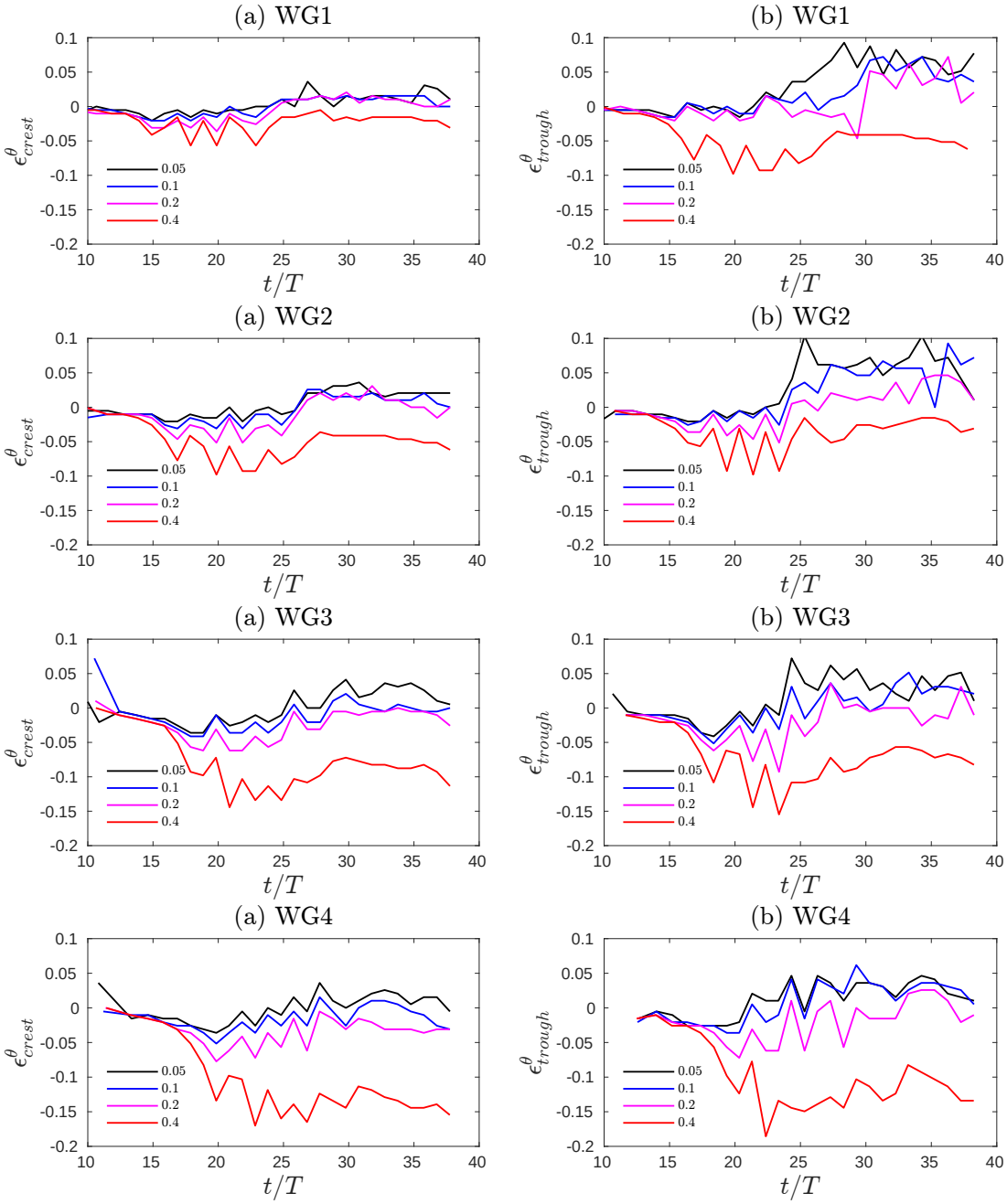

Figure 5.33: Normalised crest and trough phase shifts $\epsilon^{\theta}_{crest}$ and $\epsilon^{\theta}_{trough}$ for $C_{\max} = 0.05$, 0.1, 0.2, and 0.4 at wave gauges 1–4 (WGs 1–4) in the long case.

5.3.3.3 Effects of changing $C_{\max}$ on computational time in the long case

Table 5.21 then shows the time taken by different parts of the solver for each value of $C_{\max}$. Using $C_{\max} = 0.2$ as the reference value, $C_{\max} = 0.05$ takes approximately 4.04 times as long, $C_{\max} = 0.1$ approximately 1.88, and $C_{\max} = 0.4$ approximately 0.39. For each value, the percentage of time taken by each constituent part is remarkably consistent: the coupling take approximately 71% of the total time, interFoam 22%, and FNPFFoam 6% for each value of $C_{\max}$. This pattern can be seen in Figure 5.34(a) which illustrates the relationship between increasing $C_{\max}$ and the consequent increase in computational time for each part of the solver.

However, arguably more useful is Figure 5.34(b) which shows the the relationship between computational time and the total number of time steps for each corresponding value of $C_{\max}$. This clearly shows a linear relationship between the number of time steps and computational time. Moreover, it can crudely be deduced that halving the value $C_{\max}$ leads to a doubling in the number of time steps N, which consequently leads a doubling of computational time. This is approximately the case for $C_{\max} = 0.05$, 0.1, and 0.2, but 0.4 is a slight outlier. This information is useful then in deciding what value of $C_{\max}$ is actually best. Specifically, *is the increase in accuracy from halving C_{max} worth doubling the computational time?*. The answer to this is of course case dependent and discretionary, but for this case, it is clear that the original value $C_{\max} = 0.2$ strikes the best balance between accuracy and efficiency.

Again, one final thing to note is that the integrated model will never be solely used for wave propagation: its primary purpose is for wave-structure interaction. In those cases, as will be seen in Chapter 6, the interFoam time is far higher. For solely wave propagation, the FNPFFoam solver is sufficient and that is clearly much more efficient.

$C_{\max}$	0.05	0.1	0.2	0.4
Coupling time (s)	37,672	17587	9310	3592
interFoam time (s)	11,995	5389	2948	1150
FNPF time (s)	3106	1539	811	301
Total (s)	52,773	24,515	13,069	5043

Table 5.21: Time taken by different parts of the solver for each value of $C_{\max}$ in the long case.

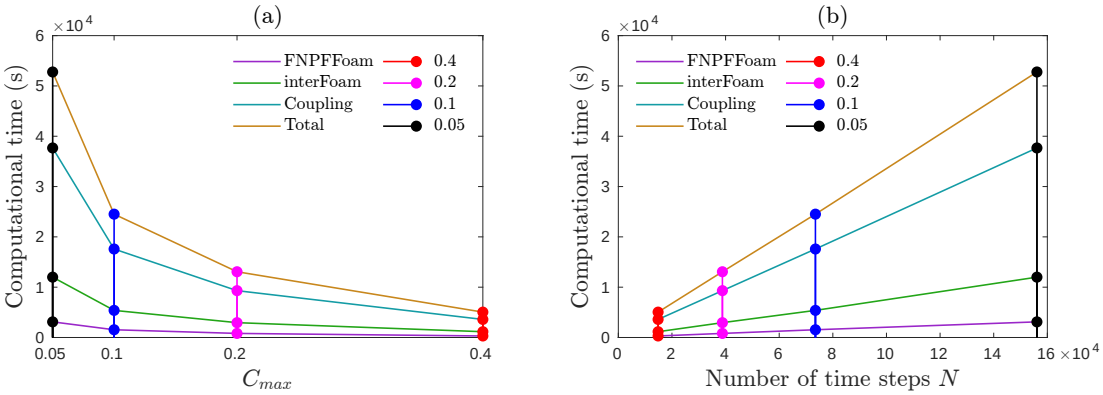

Figure 5.34: (a) Relationship between $C_{\max}$ and computational time for different parts of the IntegratedFoam model. (b) Relationship between number for time steps N and computational time for differing values of $C_{\max}$ and for different parts of the IntegratedFoam model.

5.3.3.4 Effects of changing $C_{\max}$ on the free-surface elevation and computational time in the short case

The geometric and computational setup is the same as the short case in the Section 5.3.1.5, with Ω_{OZ} and Ω_{DZ} both chosen as 1 wavelength long. The corresponding dimensions and mesh configurations are shown in Tables 5.15 and 5.16. Again the same FNPFFoam setup and input parameters are used and there is a sole wave gauge at $x = 64$ m.

Figure 5.35 shows the normalised crest and trough amplitude errors over time at the sole wave gauge for varying values of $C_{\max}$. The crest errors ϵ^a_{crest} are shown in Figure 5.35(a) and the trough errors ϵ^a_{trough} are shown in Figure 5.35(b). Both of these figures show strange results. Counter intuitively, the errors for $C_{\max} = 0.05$ is much greater than the other values, with the crest error being particularly bad. The other results are similar to each other. Figure 5.36 then shows the corresponding phase shift errors ϵ^θ_{crest} and ϵ^θ_{trough}. The shifts shown here are similar and small, but the $C_{\max} = 0.05$ trough shift is comfortably the worst. This behaviour can perhaps be explained by the major increase in the number of time step N that occurs when decreasing $C_{\max}$. It is possible that the dissipation becomes more prominent because it has more opportunities to occur. Moreover, the implicit Euler method used in interFoam is also only first order. However, this behaviour was obviously not present in the long case. This indicates that it may have something to do with the damping from Ω_{OZ} and Ω_{DZ} and how it affects the wave solution in the small Ω_{NS}. Regardless, this is something that would have to be considered in wave-structure interaction problems.

The computational times are also shown in Table 5.22, from which a similar pattern can be seen as in the long case.

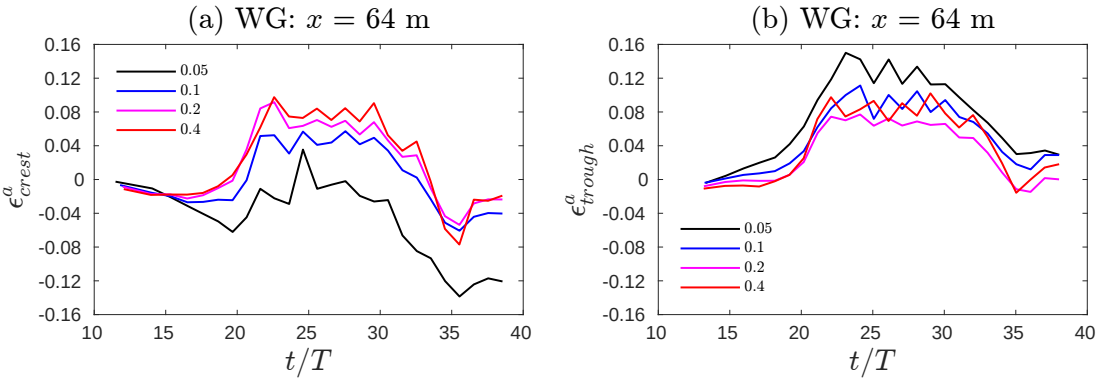

Figure 5.35: Normalised crest and trough amplitude errors ϵ^a_{crest} and ϵ^a_{trough} for $C_{\max} = 0.05$, 0.1, 0.2, and 0.4 at wave gauge (WG) $x = 64$ m in the short case.

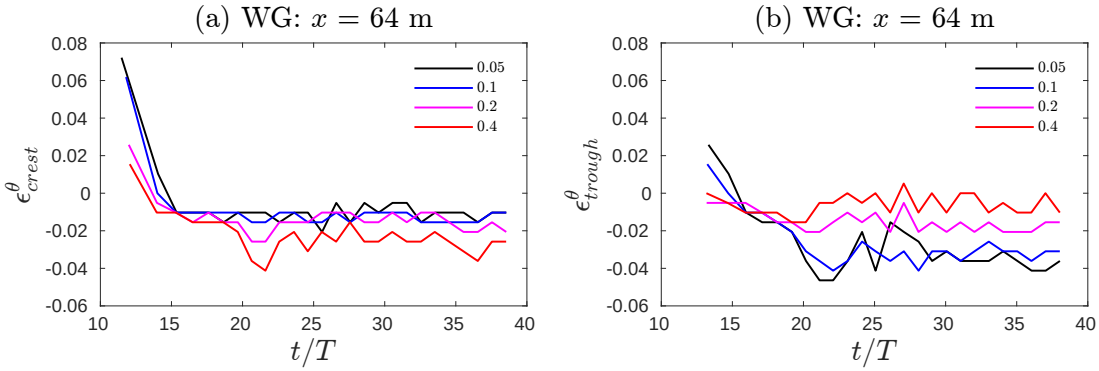

Figure 5.36: Normalised crest and trough phase shifts $\epsilon^{\theta}_{crest}$ and $\epsilon^{\theta}_{trough}$ for $C_{\max} = 0.05$, 0.1, 0.2, and 0.4 at wave gauge (WG) $x = 64$ m in the short case.

$C_{\max}$	0.05	0.1	0.2	0.4
Coupling time (s)	24773	12132	6161	3276
interFoam time (s)	4475	2283	1169	617
Total (s)	29248	14415	7330	3893

Table 5.22: Time taken by different parts of the solver for each value of $C_{\max}$ in the short case.

6

Wave-Structure Interaction

In Chapter 5, the ability of the IntegratedFoam model to accurately and efficiently model fifth-order Stokes wave propagation was thoroughly tested. However, as mentioned in Chapter 1, the main emphasis of the present work is for IntegratedFoam to model wave interaction with offshore renewable structures, e.g., fixed monopile foundations and wave energy converter devices. Therefore, in this chapter, the accuracy and efficiency of IntegratedFoam is validated through such test cases. In addition, the new stabilised model is also test through 2-D and 3-D wave shoaling cases.

6.1 Wave shoaling

A key aspect of ocean and coastal engineering is understanding how different coastal processes affect the characteristics of propagating waves. For example, wave energy converters close to the shore have to take into account the loss in available energy due to refraction, whereas arrays of bottom-fixed wind turbines need to take into account the affects of diffraction around neighbouring turbines. A critical process that will be considered in this work is wave shoaling, a process that transforms waves as they propagate into shallower water. It is caused by a change in group velocity—defined in Section 5.1.1—that occurs when waves enter shallower water and the water particle paths become more elliptical. This change in group velocity is not then accompanied by a change in energy flux, meaning that the wave height and steepness have to instead increase to ensure that there is conservation of energy. This increase in wave height and steepness will then obviously also lead to wave breaking if it goes past the critical breaking limit.

Wave shoaling also provides a good example of where integrated hydrodynamic models are particularly advantageous in terms of efficiency. For example, say there is a fixed oscillating water column type WEC device on a coast where the water depth decreases over a long distance. The actual hydrodynamic modelling of the WEC would have to be done using a N-S solver, but capturing the shoaling of incident waves over a large distance using such a solver would be practically unfeasible so the input wave conditions would not be known. However, the nonlinear transformation of propagating waves over this large distance could be done efficiently by an FNPF solver, but it could not model the WEC device. Therefore, a combination of the two would clearly be advantageous and is why this wave shoaling test case is important.

In this section, both 2-D and 3-D wave shoaling cases are first considered to validate the stabilised FNPF model. Each case will establish how accurately the model can capture the transformation of propagating waves that occurs due to variable bathymetry. For the 2-D case, this is due to interaction with a submerged structure, whereas for the 3-D case, this is due to changing bottom topography. Even though the constituent FNPF solver is only used in 2D in IntegratedFoam, a 3-D example is still considered here to validate the stabilised model in 3D.

6.1.1 2-D wave shoaling

This test case is based on the experiments described by Beji and Battjes (1993, 1994) [3, 4] which investigated how interaction with a submerged trapezoidal bar affected wave propagation. The NWT in this case has dimensions $x \times y \in [0, 30] \times [-0.4, 0]$ (m), but also has the aforementioned trapezoidal bar at the bottom boundary—as illustrated in Figure 6.1. Two sets of input wave parameters, B1 and B2, both listed in Table 6.1 are used. Input B1 corresponds to the set used in Beji and Battjes (1994) [4], whilst B2 corresponds to the set used in Beji and Battjes (1993) [3]. Note that the input waves B2 are approximately 4.6 times steeper than B1. Thus, the mesh configuration used for each is also different to account for the increased wave steepness

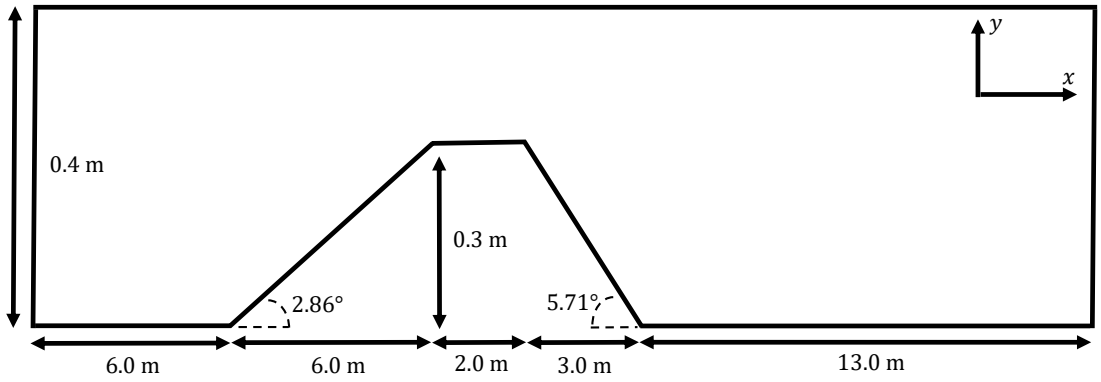

Figure 6.1: Sketch of numerical wave tank for the 2-D wave shoaling test case (not to scale).

Case ID	Height: H(m)	Period: T(s)	Wavelength: λ(m)	Water depth: h(m)	Steepness: H/λ
B1	0.02	2.02	3.737	0.4	0.005352
B2	0.036	1	1.4637	0.4	0.02460
W1	0.039	1	1.4957	0.4572	0.02607
W2	0.015	2	3.9095	0.4572	0.003837
W3	0.0212	2	3.9095	0.4572	0.005423

Table 6.1: Wave parameters for 2-D and 3-D shoaling cases.

Mesh	Configuration $x \times y \times z$
2D_M1	$1500 \times 20 \times 1$
2D_M2	$3000 \times 20 \times 1$
3D_M1	$1750 \times 30 \times 50$
3D_M2	$1750 \times 30 \times 100$

Table 6.2: Mesh configurations for 2-D and 3-D shoaling cases

and to ensure there is sufficient mesh resolution. For B1, configuration 2D_M1 listed in Table 6.2 is used, whereas for B2, configuration 2D_M2 is used. With both of these configurations, the mesh is not uniform. Instead, it is refined in the x-direction to increase resolution in the region $x \in [11, 21]$ (m) where the wave shoaling phenomenon is significant. Furthermore, the mesh is again refined in the y-direction as was the case in the wave propagation test cases. Finally, the Lin et al. (2021) [90] model to which the stabilised model is validated against sets $\beta_{FODC} = 0.2$ in the damping scheme with a frequency of 1 time step to ensure stability.

Considering input B1 first, Figure 6.2 shows the time histories of free-surface elevation for the stabilised model, Lin et al. (2021) [90] model, and experimental solution of Beji and Battjes (1994) [4] at various wave gauges in the NWT. Again, it must be emphasised that the key point to acknowledge here is that no numerical damping is required to ensure stability for this case. In terms of accuracy, it can be seen from Figure 6.2 that the present results at WG1: $x =$

2.0 m are practically identical to the experimental solution and Lin et al. (2021) [90] results, meaning that the target waves are produced well in the relaxation zone. Then from WG2: $x =$ 12.5 m to WG8: $x = 21.0$ m, the expected increase in amplitude and nonlinearity due to the presence of the submerged bar is clearly observed, with good agreements shown between the stabilised model and experimental solution. At WG's 5–8, the present results actually seem over predicted compared to the experimental data. However, this might be reasonable given that the more accurate potential flow simulation might over predict due to the absence of fluid viscosity.

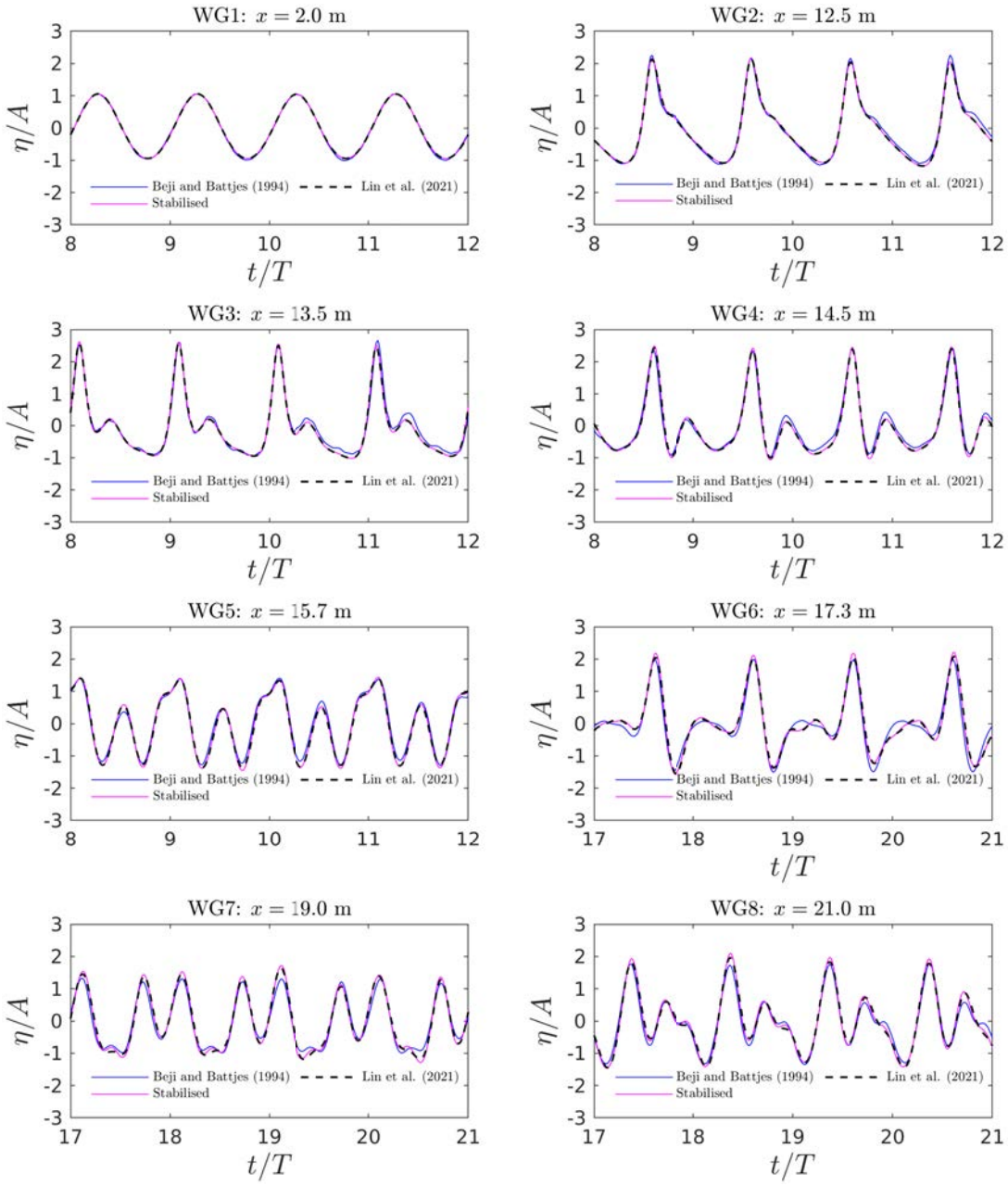

Figure 6.2: Time histories of free-surface elevation for the stabilised model, Lin et al. (2021) [90] model, and experimental solution of Beji and Battjes (1994) [4] at various wave gauges in the NWT for input B1.

Moving on to input B2, Figure 6.3 shows the analogous results plotted with the experimental solution of Beji and Battjes (1993) [3]. Again, the solution is stable and no numerical damping is required. In terms of accuracy, the results at WG1: $x = 6.0$ m—just before the submerged bar—agree well with the experimental solution and are identical to the Lin et al. (2021) [90] results. Then from WG2: $x = 12.0$ m to WG4: $x = 14.0$ m—where the shoaling effects predominately occur—the expected increase in amplitude is again clearly observed, with good agreements with the experimental solution and Lin et al. (2021) [90] results. Lastly, at WG5: $x = 15.0$ m and WG6: $x = 16.0$ m, strong nonlinear effects can be observed and slight discrepancies between the stabilised model and experimental solution emerge. However, this is to be expected due to the high nonlinearity.

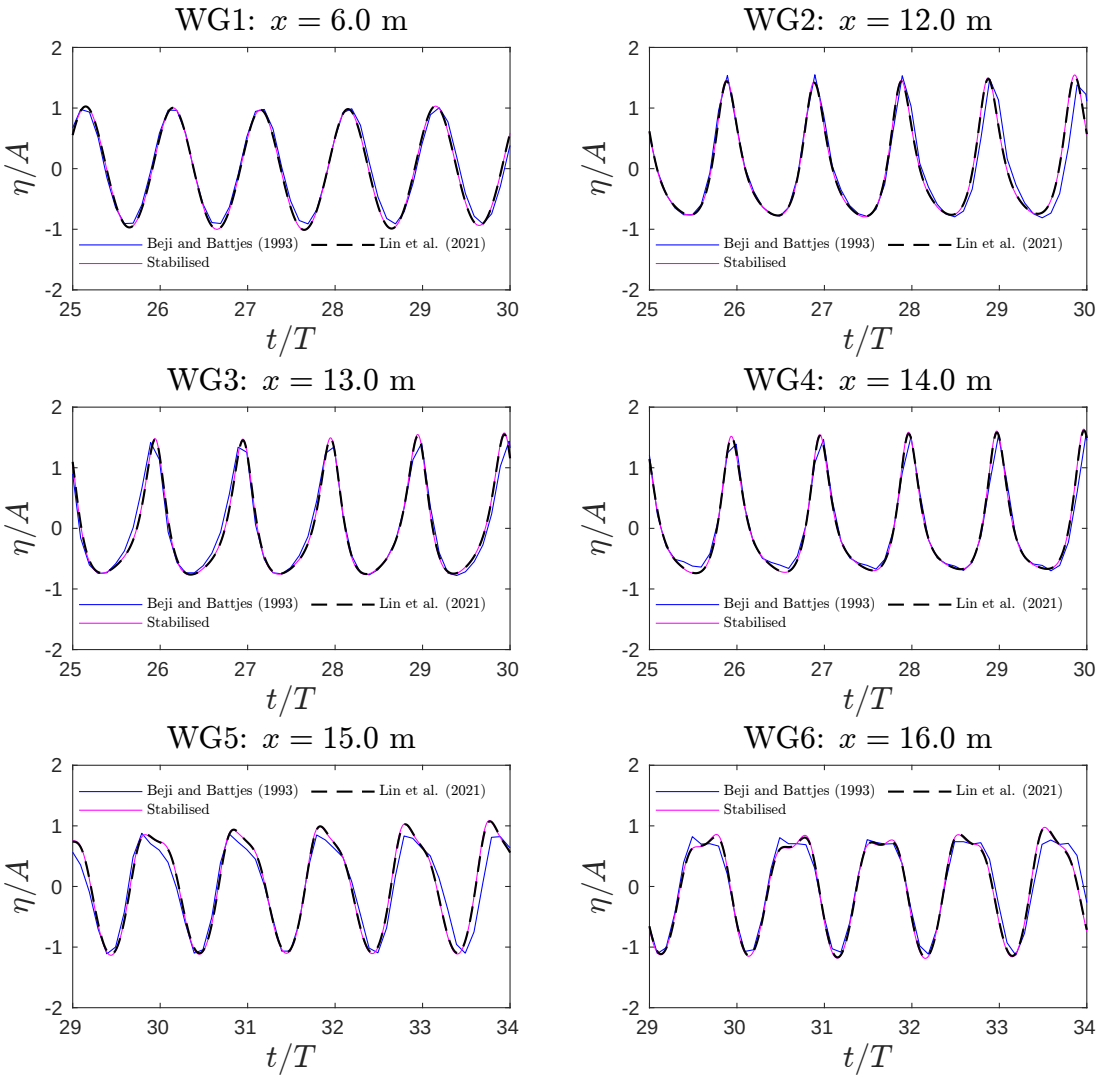

Figure 6.3: Time histories of free-surface elevation for the stabilised model, Lin et al. (2021) [90] model, and experimental solution of Beji and Battjes (1993) [3] at various wave gauges in the NWT for input B2.

It can be concluded then from this case that the stabilised model is able to accurately simulate the transformation of propagating waves that occurs due to interaction with a submerged structure, as well as capturing the ensuing highly nonlinear effects. This is all without using numerical damping and without the appearance of the sawtooth instability.

6.1.2 3-D wave shoaling

In this test case, it is established how accurately the stabilised model can capture the transformation of propagating waves that occurs due to variable bathymetry in 3D. The case is based on the experiments carried out by Whalin (1971) [143] in which the bottom topography is changing due to a submerged semi-circular slope. This will test the ability of the stabilised model to capture 3-D nonlinear effects associated with wave transformation. The NWT in this case has dimensions $x \times y \times z \in [0,\, 35] \times [-h(x,z),\, 0] \times [0,\, 6.096]$ (m), where $h(x,z)$ is defined as

$$h(x,z) = \begin{cases} 0.4572, & 0 \leq x \leq 10.67 - G(z), \\ 0.4572 + \frac{1}{25}(10.67 - G(z) - x), & 10.67 - G(z) < x < 18.29 - G(z), \\ 0.1524, & 18.29 - G(z) \leq x \leq 35.0, \end{cases} \tag{6.1}$$

where $G(z) = \sqrt{z(6.096 - z)}$. For this case, three different sets of wave parameters are used: W1, W2, and W3—all listed in Table 6.1. For W2 and W3, mesh configuration 3-D_M1 listed in Table 6.2 is used, whereas for W1 configuration 3-D_M2 is used. This increased number of cells for W1 is down to the increased steepness and nonlinearity: W1 is approximately 6.8 times steeper than W2—the least steep. Again, as was with the 2-D shoaling case, the mesh is refined in the x and y directions to increase resolution in the shoaling area and free surface respectively.

From the results, the first thing to note is that the simulation is stable for each of W1, W2, and W3. Figures 6.4(a)–6.4(c) then show the first three harmonic components—obtained by Fast Fourier Transform—along the streamwise central line of the NWT for the stabilised model, Shao and Faltinsen (2014) [123], Engsig-Karup (2009) [37], and experimental results of Whalin (1971) [143]. Overall, for all three inputs, good agreements are seen between the stabilised model results and those of the other cited works, even for the steepest input W1 (Figure 6.4(a)). In addition, for W3, Figures 6.5(a)–6.5(d) show snapshots of the free surface at various times during the simulation. Figure 6.5(a) shows the 2-D waves generated in the relaxation zone propagating towards the semi-circular slope. Figures 6.5(b)–6.5(d) then show the waves becoming steeper and transforming due to the presence of the slope before being damped out of the tank completely. What can be concluded then from this case is that the stabilised model is able to accurately simulate the transformation of propagating waves that occurs due to interaction with changing bottom topography, as well as capturing the ensuing three-dimensional nonlinear wave effects. Again, this is all without using numerical damping and without the appearance of the sawtooth instability.

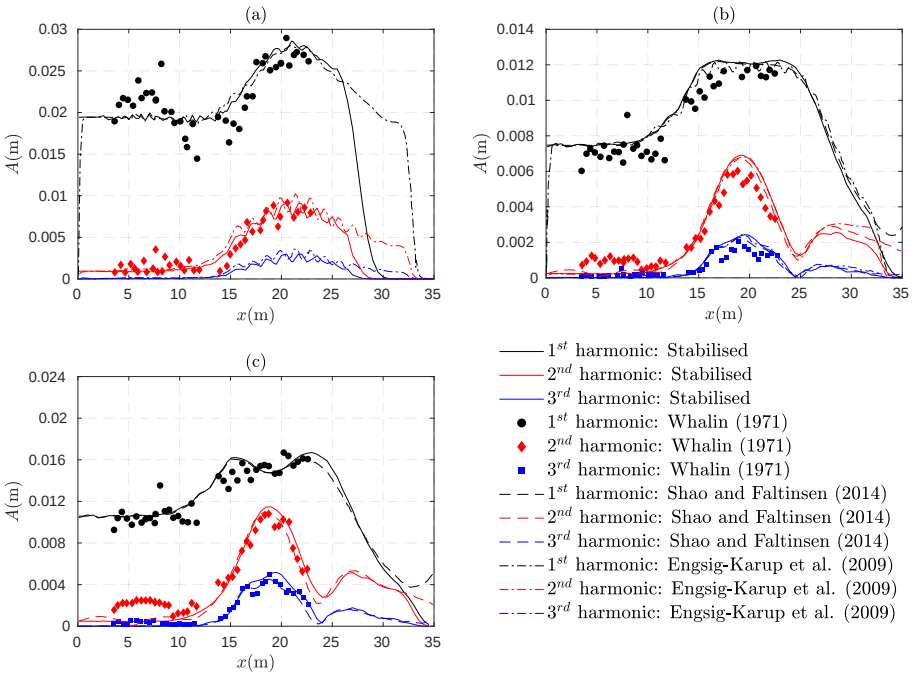

Figure 6.4: Harmonic components of numerical results from the stabilised model, Shao and Faltinsen (2014) [123], Engsig-Karup et al. (2009) [37], and experimental results of Whalin (1971) [143] at the streamwise central line of the NWT: (a.) input W1, (b.) input W2, (c.) input W3.

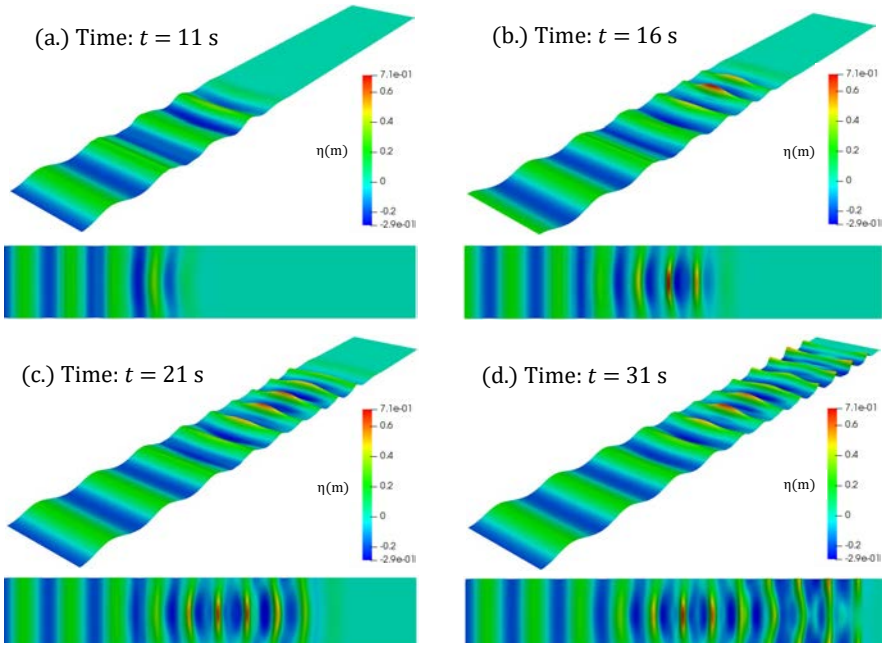

Figure 6.5: Snapshots of the free surface for input W3 at times (a.) 11 seconds (s), (b.) 16 s, (c.) 21 s, and (d.) 31 s. (Not to scale—exaggerated 20 times in the y-direction).

6.2 Regular wave interaction with a 2-D floating body

6.2.1 Geometric and computational setups

This first IntegratedFoam test case considers the wave-structure interaction of fifth-order Stokes waves with a 2-D T-shaped floating body which is considered as a simplified midship section with superstructure. The case itself is based on the physical and numerical experiments of Zhao and Hu [153]. Readers are referred to [153] for a detailed description of both these experiments; only the corresponding computational setup for the new integrated model is outlined here. The geometric setup is shown in Fig. 6.6. The water depth is 0.4 m meaning that $\Omega_{\text{FNPF}} = [0,\ 12.3] \times [-0.4,\ 0]$ (m) and the N-S domain $\Omega_{\text{NS}} = [5,\ 9] \times [-0.4,\ 0.573]$ (m). To be in agreement with the experiments, the width in the transverse direction is also 0.3 m but is only one computational cell thick—meaning the case is still 2D. The T-shaped floating body is placed in Ω_{NS} at a distance of 7 m away from the inlet and, as in the experiments, is restrained to only heave and roll motions. The relevant mechanical characteristics of the body are also clearly labelled in Fig. 6.6 and are listed in Table 6.4. The input wave parameters are also shown in Table 6.3. The mesh configuration for Ω_{FNPF} is $x \times y = 420 \times 15$ and for Ω_{NS} is $x \times y = 320 \times 78$. These were established given the mesh sensitivity analyses for FNPFFoam and IntegratedFoam in Chapter 5. In addition, the simulation time is 30 s and $C_{\max} = 0.2$ (again consequent to the analysis in Chapter 5). Moreover, the overlapping zone is chosen to be one wavelength long so that $\Omega_{\text{OZ}} = [5,\ 6.4637]$ (m). For validation, a wave gauge is placed at $x = 5.1$ m (WG1) and a pressure gauge is placed on the superstructure at a height of 0.01 m from the deck, at the seaward face. The heave and roll motions of the body are also measured with the heave being measured as the vertical displacement of the centre of rotation. The simulation is done on 10

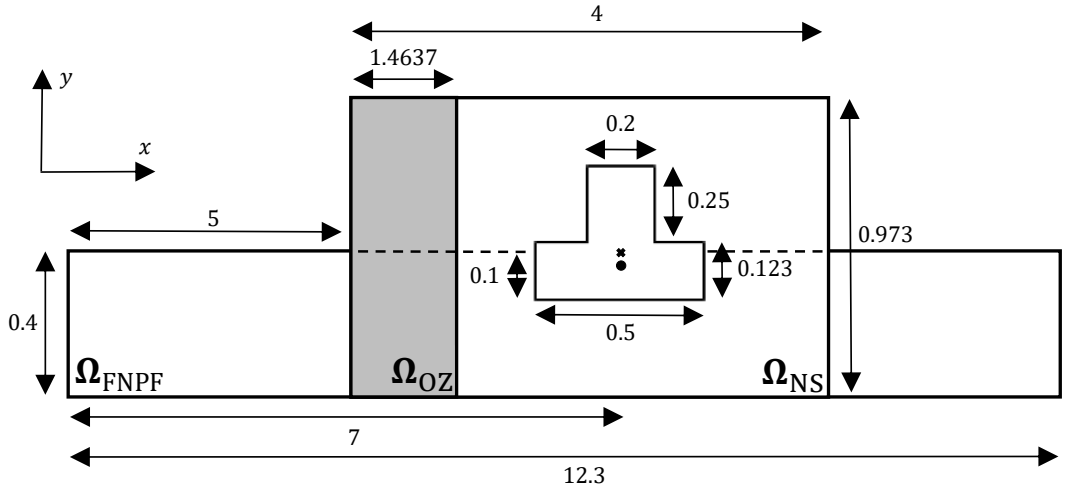

Figure 6.6: Schematic of the 2-D numerical wave tank in the floating body test case (not to scale). The black cross marks the centre of rotation and the dot marks the centre of mass. All dimensions are in meters.

Wave	Amplitude: A(m)	Period: T(s)	Wavelength: λ(m)	Water depth: h(m)
Stokes 5^{th}	0.031	1	1.4637	0.4

Table 6.3: Wave parameters for the generated fifth-order Stokes waves.

Characteristic	Value
Mass: m (kg)	15
Centre of mass: CM (m)	$(x, y, z) = (7,\ -0.0204,\ 0.15)$
Centre of rotation: CR (m)	$(x, y, z) = (7,\ 0,\ 0.15)$
Roll moment of inertia: I_{zz} (kg$\cdot$ m^2)	0.3417

Table 6.4: Mechanical Characteristics of the 2-D floating body.

processors with 4 being assigned to the coupling. Lastly, for comparison, the test case is also done using solely interFoam under the same conditions using 10 processors.

6.2.2 Numerical results

Figure 6.7(c) then shows the time histories of free-surface elevation at WG1 for IntegratedFoam, the experimental Zhao and Hu solution [153], the numerical Zhao and Hu solution [153], and also the solely interFoam solution. Overall, IntegratedFoam shows a fair agreement with the experimental solutions, more so than the numerical results of Zhao and Hu. The solely interFoam results appear to be even better. This makes sense given that the IntegratedFoam model relaxes out the wave response from the floating body in Ω_{OZ} with the incoming wave from Ω_{FNPF}, whereas interFoam takes the response into account and records the corresponding interference that causes the experimental solution to increase in amplitude after approximately $t/T = 20$.

Figures 6.7(a) and 6.7(b) then also show the time histories of the roll and heave motions respectively. The heave motion shows very good agreements with the experimental solutions. However, the roll motion generally underestimates the magnitude compared to the the experimental measurement, especially in the clockwise direction. Similar results can be seen at the pressure gauge: Figure 6.8 shows the computed and measured pressures on the floating body. Overall, the present results are similar to the numerical work of Zhao and Hu but are underestimated compared to the experimental results. The laboratory measurement of Zhao and Hu has an upward shift of around 100 Pa; this is likely due to a sudden change in temperature caused by incoming water on the pressure sensor [101]. However, the solely interFoam solution also shows similar behaviour. This indicates that the problem here is not necessarily with the coupling but rather the interFoam and motion solver setup. For example, even though the mesh used is appropriate for an accurate wave solution, it may not be fine on enough around the structure to accurately calculate the water volume and pressure on the seaward facing deck, consequently

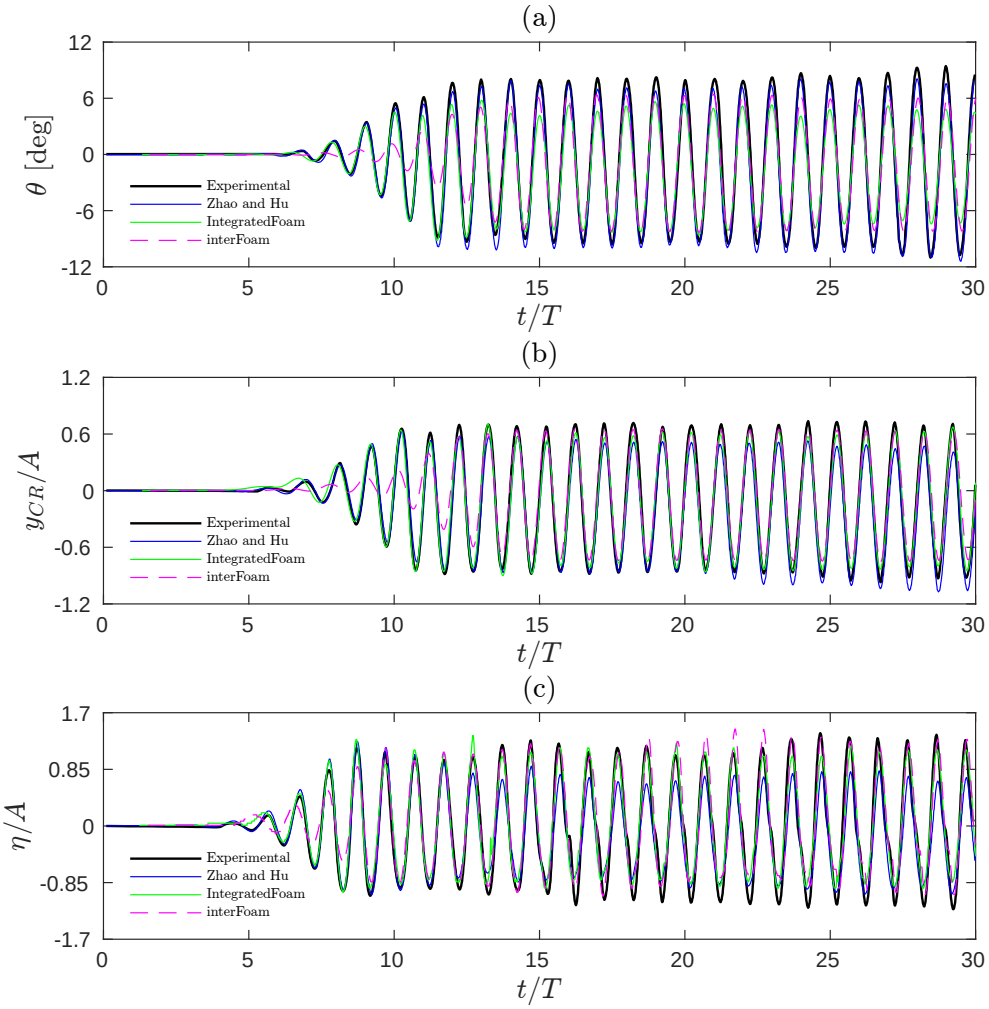

Figure 6.7: Time histories of (a) roll motion, (b) heave motion, and (c) free-surface elevation for IntergratedFoam, interFoam, the experimental Zhao and Hu solution [153], and the numerical Zhao and Hu solution [153].

leading to inaccurate roll angle measurements. A better approach may be to refine the mesh and concentrate computational cells around the structure; although, this would majorly increase the computational time. In addition, it could be that the parameters of the motion solver in interFoam are not optimally calibrated to produce the most accurate solution. A turbulence model could even be introduced to more accurately calculate the pressure distribution on the deck. Figure 6.8 shows the computed and measured pressures on the floating body. Overall, the present results are similar to the numerical work of Zhao and Hu but are underestimated compared to the experimental results. The laboratory measurement of Zhao and Hu has an upward shift of around 100 Pa; this is likely due to a sudden change in temperature caused by incoming water on the pressure sensor [101]. However, all these theories do not explain why the heave motion is very accurate. Indeed, all the above theories were tried and tested and still failed to accurately represent the roll motion. This indicates a limitation of the interFoam solver itself and will be discussed more in Section 6.4.

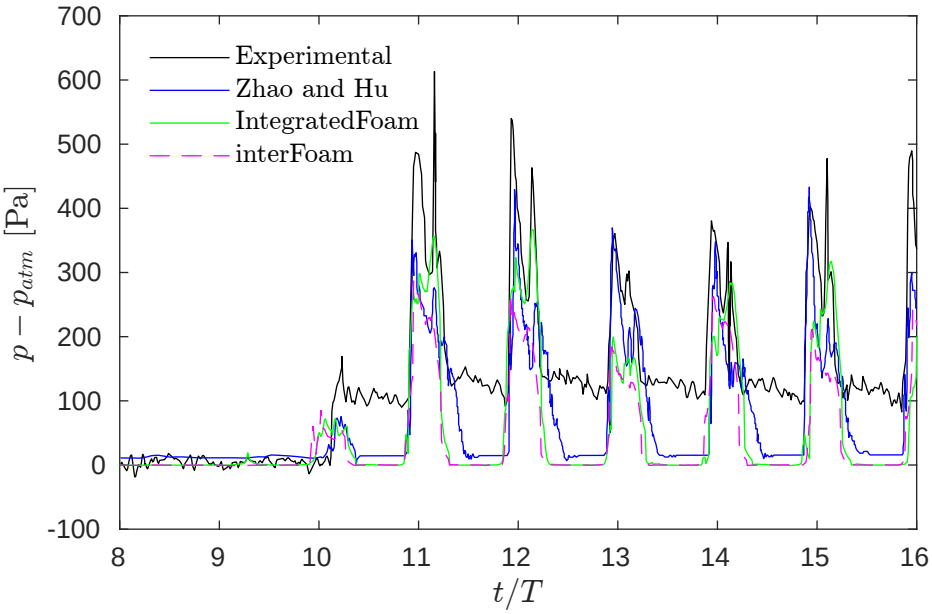

Figure 6.8: Time histories of pressure, measured 0.01 m above deck, for IntegratedFoam, interFoam, the experimental Zhao and Hu solution [153], and the numerical Zhao and Hu solution [153].

As mentioned in the introduction, the whole point in developing integrated models is to achieve better computational efficiency—whilst retaining similar levels of accuracy—that would be achieved when solely using Navier-Stokes models for wave-structure interaction problems. In respect of accuracy, it can be concluded form the floating body example that the IntegratedFoam model does well. However, with respect to computational efficiency, the IntegratedFoam is definitively superior. Indeed, Table 6.5 lists the time taken by each part of the IntegratedFoam solver. In contrast to the wave propagation examples in Chapter 5, interFoam now takes up the majority of computational time at 56%, whereas the coupling takes up 35% and FNPFFoam 9%. As a result, it can safely be assumed from this that if interFoam were used for the entire test case, it would take considerably longer. This is confirmed by the actual interFoam computational time which was 11,832 s—almost exactly 3 times as long. Therefore, it is proven through this simple 2-D wave-structure interaction test case that IntegratedFoam can produce similar results to interFoam but can do it much faster. Moreover, as hypothesised in Chapter 5, this speedup is expected to be even greater for cases in 3D.

	Coupling	interFoam	FNPFFoam	Total
Computational time (s)	1366	2207	365	3938

Table 6.5: Time taken by different parts of the solver in 2-D floating body case.

6.3 Focused wave-interaction with a fixed cylinder

As mentioned throughout this work, the primary objective here is to model wave interaction with offshore renewable structures, with one such example being fixed monopile foundations that are used in the construction of fixed offshore wind turbines. In the introduction it was mentioned that fixed structures constitute almost all offshore wind capacity currently installed globally, with the majority of planning approved capacity also being fixed. Technology is also advancing: the turbines themselves are getting larger, both in terms of blade size and overall structure size; the depth at which they are located is becoming greater; and more advanced materials are being used in their construction. This is leading to greater efficiency in electricity generation, making them more cost effective in the long term, but is inevitably leading to higher short term production costs. Therefore, it still remains vital that survivability is a key consideration in the design process for overall long-term performance.

The marine area in which fixed offshore wind turbine are usually deployed can be subject to extreme wave conditions, conditions that are also likely to become more frequent and random in the coming decades due to climate change. Extreme wave events can involve waves that hold enormous amounts of energy, so a structure will need to be able to withstand the force subjected during any such event, even if it is relatively rare. In Section 5.1 it was explained how and why these extreme wave events occur, and a method for replicating them in a numerical wave tank (NWT) was described; namely, generating focused waves using NewWave theory. In this section, focused waves will again be used to replicate these extreme wave events to see if the new IntegratedFoam model can accurately compute the hydrodynamic load on a fixed cylinder, as well as correctly predict the flow around the cylinder before and after interaction.

6.3.1 Experimental setup

In the present work, the test cases released for the comparative study in ISOPE 2020 (Sriram et al. (2021) [127]) involving focused wave interaction with a fixed cylinder are considered. In the physical experiments, outlined in detail in Sriram et al. (2021) [126], two-dimensional unidirectional focused waves were generated using second-order wavemaker theory in a three-dimensional wave tank. The tank in question was 110.0 m long, 2.2 m wide, and 2.0 m deep, with a working water depth of 0.7m. A wavemaker was placed at one end and a beach at the other. In addition to this, a cylinder of diameter 0.22 m and height 1 m was positioned so that its centre was at a distance 24.88 m away from the wave maker and 1.085 away from the front wall (hence is slightly off centre). The focused waves were generated using 32 components derived from a constant steepness spectrum, which is slightly different to the test case in Section 5.2.6. Thorough details of this spectrum can be found in Sriram et al. (2015) [125], but it is essentially dependent on the 'amplitude gain parameter' G_a that determines the amplitude A_i of each wave component, i.e.,

$$A_i = \frac{\pi G_a}{k_i}, \tag{6.2}$$

where k_i is the wavenumber of each component corresponding to a given frequency f_i. Therefore, rather than the amplitude of the focused wave being constant (A_I in Equation (5.17) in Section 5.1.4), the steepness S of the focused wave is instead constant, i.e.,

$$S = \sum_{i=1}^{N} a_i k_i. \tag{6.3}$$

The wave parameters for the two test cases considered in this work, 1 and 3, are listed in Table 6.6. The Table also lists the focusing location $x_f = 23$ m and focusing time $t_f = 38$ s.

Case	Frequency band (Hz)	f_P (Hz)	N	G_a	x_f (m)	t_f (s)
1	$f \in [0.34,\ 1.02]$	0.68	32	0.001	23	38
3	$f \in [0.34,\ 1.02]$	0.68	32	0.003	23	38

Table 6.6: Input focused wave parameters for the fixed cylinder test cases.

6.3.2 Geometric setup

The geometric setup for IntegratedFoam is shown in Figures 6.9 and 6.10. In this work, only wave gauges (WG) 4–7 from the original experiments are used: their locations are listed in Table 6.7 and are displayed on Figure 6.10(a). Wave gauge 4 is specifically chosen to validate the numerical focused wave in FNPFFoam and wave gauges 5, 6, and 7 are to capture the transformation of the focused wave, as it passes and interacts with the cylinder, in interFoam. The PGs are all listed in Table 6.8 and shown on Figure 6.10(b). The pressure gauges are arranged as they are to validate the hydrodynamic load at a wide range of positions on the cylinder. The generated focused waves are unidirectional and 2D, hence, $\Omega_{\mathrm{FNPF}} = [0,\ 110] \times [-0.7,\ 0] \times [0,\ 2.2]$, where there is a single cell of width 2.2 in the transverse direction. Moreover, in the same way as Section 5.2.6, the characteristic wave of the focused wave group is taken as the wave corresponding to the peak amplitude for that group, which in this case is $\lambda_p = 7.287$ m. This characteristic wavelength is clearly quite large compared to the area of interest around the cylinder where all the WGs are located, so it would not make sense for the size of the overlapping zone Ω_{OZ} to equal λ_p as it has in every other test case so far. Doing this would make the overall size of Ω_{NS} large relative to the area of interest as well, undoubtedly decreasing the overall efficiency of the model. An analogous argument could then also be made for the damping zone Ω_{DZ}, only further decreasing the efficiency. Therefore, in this case, both Ω_{OZ} and Ω_{DZ} are instead approximately $1/2\lambda_p = 3.644$ (the exact values vary slightly depending on the mesh density). As was seen through the analysis in Section 5.3.1, this does not lead to any significant difference in accuracy of the coupling, particularly given that the area of interest is small—$\Omega_{\mathrm{NS}} \backslash (\Omega_{\mathrm{OZ}} \cup \Omega_{\mathrm{DZ}})$ is approximately only 20% the size of Ω_{NS}. It follows then that $\Omega_{\mathrm{NS}} = [20.5,\ 29.5] \times [-0.7,\ 0.3] \times [0,\ 2.2]$ with $\Omega_{\mathrm{OZ}} = [20.5,\ 24.144] \times [-0.7,\ 0.3] \times [0,\ 2.2]$ and $\Omega_{\mathrm{DZ}} = [25.856,\ 29.5] \times [-0.7,\ 0.3] \times [0,\ 2.2]$. All these dimensions are shown in Table 6.9.

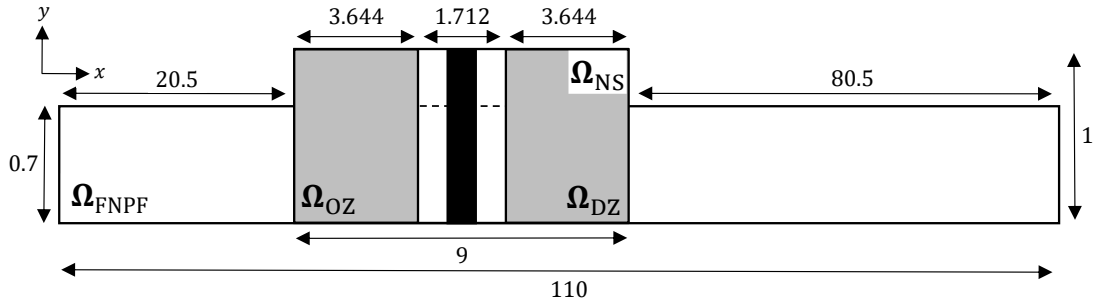

Figure 6.9: Schematic in the xy-plane of the IntegratedFoam numerical wave tank used in the fixed cylinder test cases (not to scale). The black rectangle represents the cylinder and all dimensions are in meters.

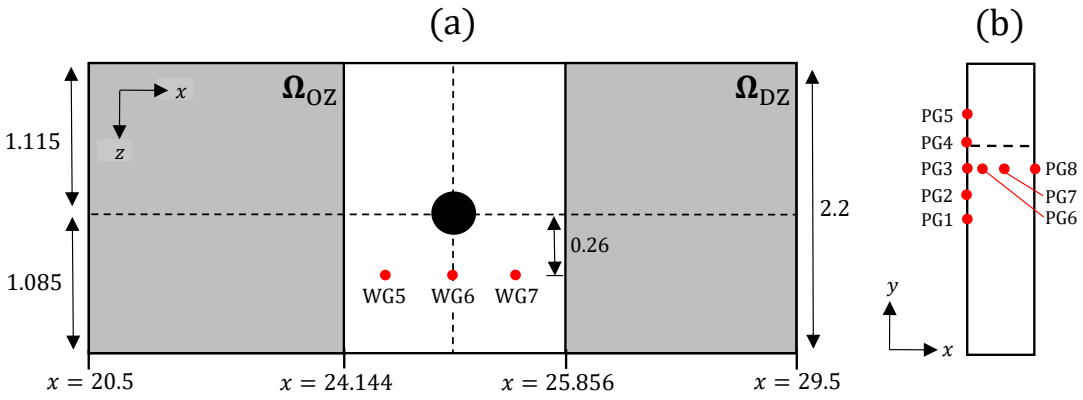

Figure 6.10: (a) Schematic in the xz-plane of Ω_{NS}, and locations of wave gauges 5–7, in the fixed cylinder test cases. All dimensions in meters. (b) Locations of all pressure gauges on the surface of the cylinder. The dashed line indicates the still water level $y = 0$.

Wave Gauge	4	5	6	7
Location (x, z) (m)	(14.428, 1.115)	(24.31, 1.375)	(24.88, 1.375)	(25.585, 1.375)

Table 6.7: Wave gauge locations in the fixed cylinder test cases. Note that wave gauge 4 is only in Ω_{FNPF}.

Pressure Gauge	1	2	3	4	5	6	7	8
x-location (m)	24.77	24.77	24.77	24.77	24.77	24.776634	24.88	24.99
y-location (m)	-0.285	-0.185	-0.085	0.015	0.115	-0.085	-0.085	-0.085
z-location (m)	1.115	1.115	1.115	1.115	1.115	1.077378	1.005	1.115

Table 6.8: Pressure gauge locations on the surface of the cylinder.

Domain	Dimensions (m)
Ω_{FNPF}	$[0,\ 110] \times [-0.7,\ 0] \times [0,\ 2.2]$
Ω_{NS}	$[20.5,\ 29.5] \times [-0.7,\ 0.3] \times [0,\ 2.2]$
Ω_{OZ}	$[20.5,\ 24.144] \times [-0.7,\ 0.3] \times [0,\ 2.2]$
Ω_{DZ}	$[25.856,\ 29.5] \times [-0.7,\ 0.3] \times [0,\ 2.2]$

Table 6.9: Dimensions of each domain and zone in the fixed cylinder test cases.

6.3.3 Case 1

6.3.3.1 Computational setup for Ω_{FNPF}

Before running Case 1, a mesh sensitivity study in an empty wave tank is needed to find the optimal mesh configuration for both Ω_{FNPF} and Ω_{NS}. As always, two things have to be kept in mind: accuracy and efficiency. Considering Ω_{FNPF} first, a good starting point would be trying a similar mesh configuration to the Ning et al. (2009) [111] cases in Section 5.2.6. In both of those cases, 20–30 cells per wavelength in the x-direction was sufficient for accurate solutions. In addition, 10 cells were used in the y-direction and were refined so that the cell at the top had vertical depth 1/10 of the cell at the bottom. Given that the generated focused wave in Case 1 is of similar steepness to the Ning cases, and given that the water depth is 1.75 times that of the Ning cases, an initial 2-D mesh configuration of $x \times y = 378 \times 15$ is chosen, constituting approximately 25 cells per wavelength. The mesh in the y-direction is again refined in the same way. This configuration is listed as configuration 'A' in Table 6.10 and is listed with four other configurations used in the sensitivity study.

Domain	ID	Configuration $x \times y$	Cells per λ
Ω_{FNPF}	A	378×15	25
Ω_{FNPF}	B	755×15	50
Ω_{FNPF}	C	755×10	50
Ω_{FNPF}	D	755×30	50
Ω_{NS}	E	125×50	100
Ω_{NS}	F	250×50	200
Ω_{NS}	G	500×50	400
Ω_{NS}	H	750×50	600
Ω_{NS}	I	250×25	200
Ω_{NS}	J	250×100	200

Table 6.10: Mesh configurations used in mesh sensitivity studies for Case 1.

The x-direction is considered first using meshes A and B where mesh B has double the number of cells per wavelength. Figures 6.11 and 6.12 then show the time histories of free-surface elevation for meshes A and B at WGs 4 and 5, along with the experimental solution of Sriram et al. (2021) [126]. At WG4, a slight difference can be seen between the two meshes at around 32.3 s before the point of peak amplitude, but they are very similar thereafter. However, there is a significant difference at WG5, which is just after the focus location $x_f = 23$ m. Figure 6.11(a) shows that mesh A fails to accurately predict the peak amplitude of the focused wave, something seen more clearly in Figure 6.11(b). In contrast, mesh B predicts the peak amplitude, and overall shape in the requested time range, with minimal difference to the experimental. Therefore, the solution has clearly converged using mesh B which constitutes 50 cells per wavelength in the horizontal direction.

In the y-direction, three meshes are considered: B, which has 15 cells in the y-direction; C, which has 10; and D, which has 30. The density in the x-direction is the same for each as per the 50 cells per wavelength that was found optimal previously. Figures 6.13 and 6.14 then show the time histories of free-surface elevation for meshes C, B, and D, along with the experimental solution of Sriram et al. (2021) [126]. Almost no differences in the solutions can be seen at WG4, but at WG5 slight discrepancies can be seen for mesh C compared to B, D, and the experimental. Moreover, there is no visible difference in solutions between meshes B and D, so mesh B—constituting 15 cells in the y-direction—is chosen. Therefore, to conclude, mesh B is chosen as the Ω_{FNPF} mesh configuration for Case 1.

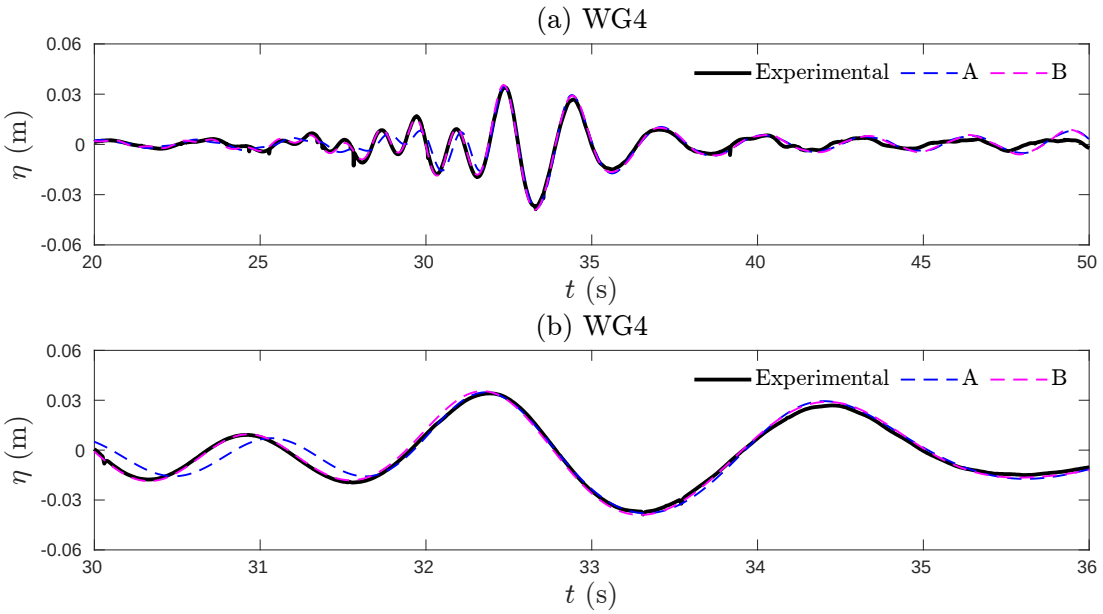

Figure 6.11: Case 1 FNPFFoam time histories of free-surface elevation for meshes A and B at wave gauge 4 (WG4), along with the experimental solution of Sriram et al. (2021) [126]: (a) $t \in [20,\ 50]$, (b) $t \in [30,\ 36]$.

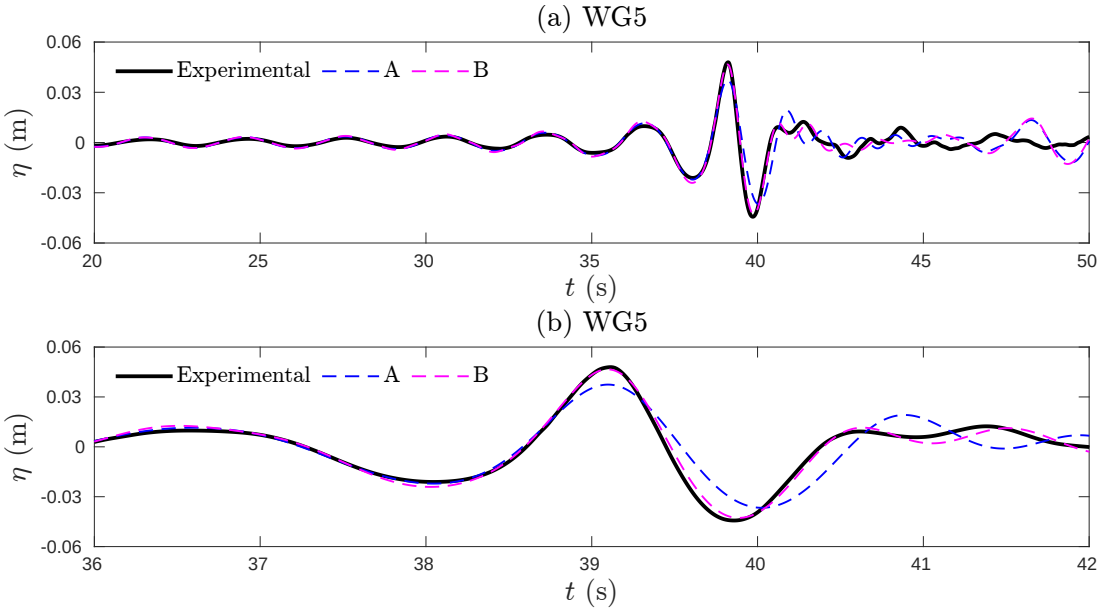

Figure 6.12: Case 1 FNPFFoam time histories of free-surface elevation for meshes A and B at wave gauge 5 (WG5), along with the experimental solution of Sriram et al. (2021) [126]: (a) $t \in [20,\ 50]$, (b) $t \in [36,\ 42]$.

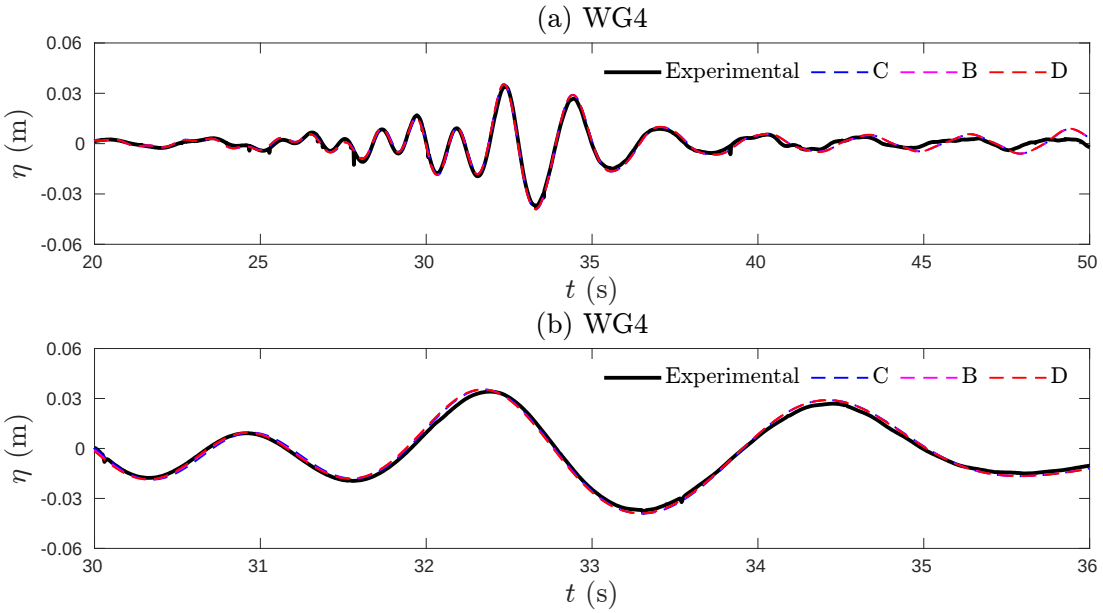

Figure 6.13: Case 1 FNPFFoam time histories of free-surface elevation for meshes C, B, and D at wave gauge 4 (WG4), along with the experimental solution of Sriram et al. (2021) [126]: (a) $t \in [20,\ 50]$, (b) $t \in [30,\ 36]$.

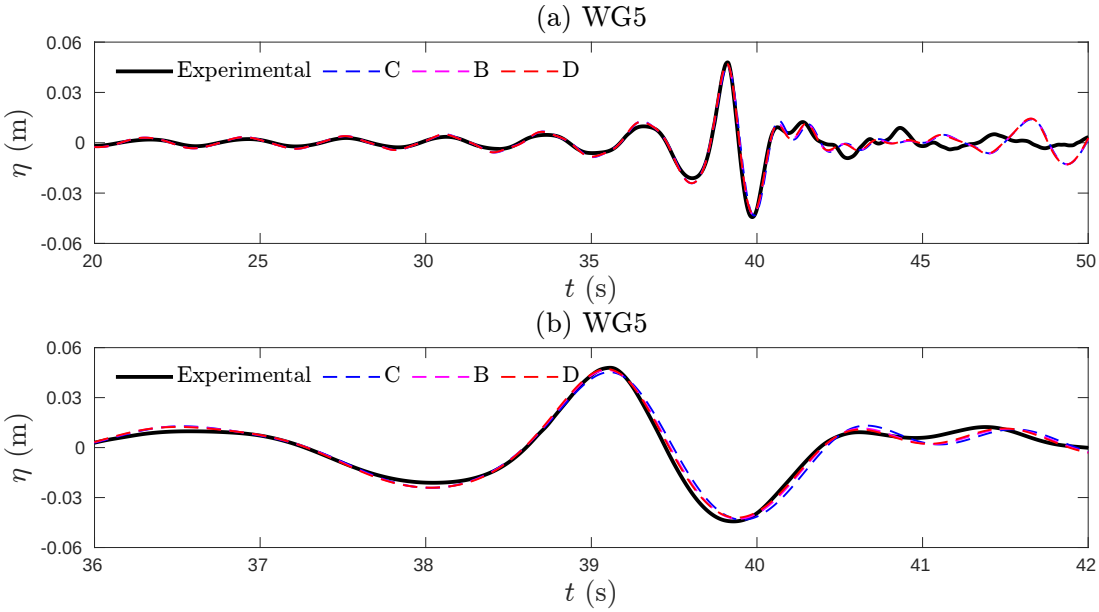

Figure 6.14: Case 1 FNPFFoam time histories of free-surface elevation for meshes C, B, and D at wave gauge 5 (WG5), along with the experimental solution of Sriram et al. (2021) [126]: (a) $t \in [20,\ 50]$, (b) $t \in [36,\ 42]$.

6.3.3.2 Computational setup for Ω_{NS}

The computational setup for Ω_{NS} is determined slightly differently. A mesh sensitivity can of course be done using IntegratedFoam without the cylinder present and using the optimal setup for Ω_{FNPF} found previously. However, this disregards the fact that the cylinder is the key part of the interFoam domain, and the mesh ultimately has to fit around it. A well-chosen mesh will not only need to be smooth, structured, and provide a convergent wave solution, but will also need to ensure that there is sufficient resolution on and around the cylinder so that wave elevation and pressure can be calculated accurately. Furthermore, the input focused wave is 2D, but the case is 3D, so the density in the z-direction also has to be determined, and this can not be done through any such study here. Therefore, the general structure of Ω_{NS}, with a randomly chosen coarse mesh density, is constructed first in order to fit the cylinder. However, a mesh sensitivity study is then conducted without the cylinder to ensure that the wave solution is convergent. The constructed mesh is then refined so that the correct mesh density required for a convergent wave solution is achieved and so that the resolution is sufficient on and around the cylinder. Note that the sensitivity study is conducted using a 2-D interFoam domain to save computational time.

Figure 6.15 then shows the initially constructed Ω_{NS} mesh. Considering just the xz-plane first (A and B), it can be seen that an annulus shape is constructed around the cylinder such that its inner radius r has length equal to the radius of the cylinder (0.11 m) and its outer radius R has length 0.5 m. A finite number of cells are then generated by constructing a finite number of annuli with outer radius length less than R, along with a finite number of radii of

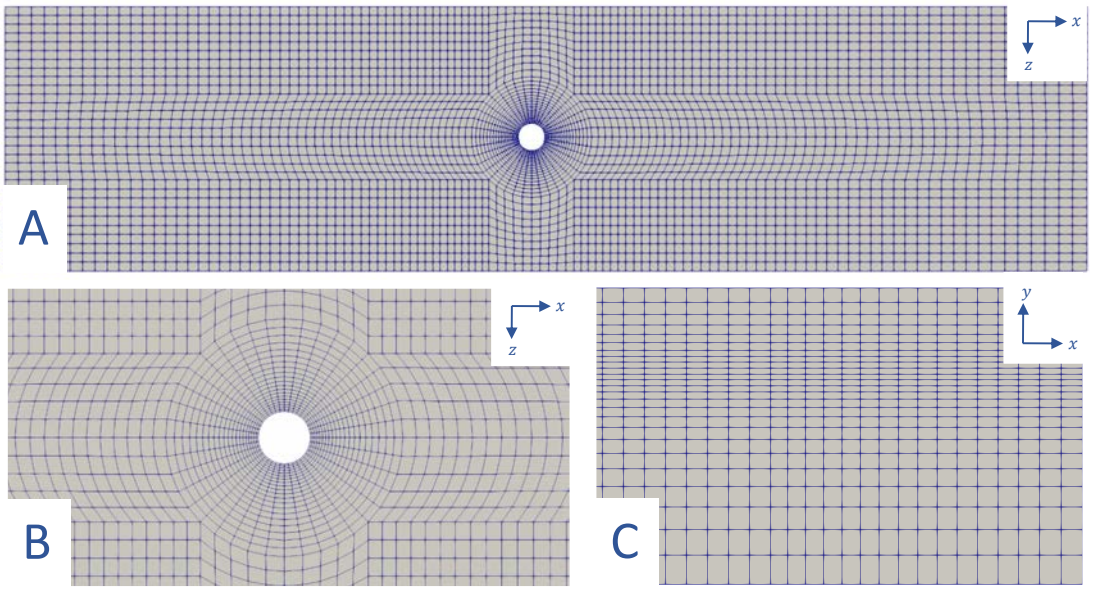

Figure 6.15: Initially constructed Ω_{NS} mesh in the xz-plane (A and B) and the xy-plane (C).

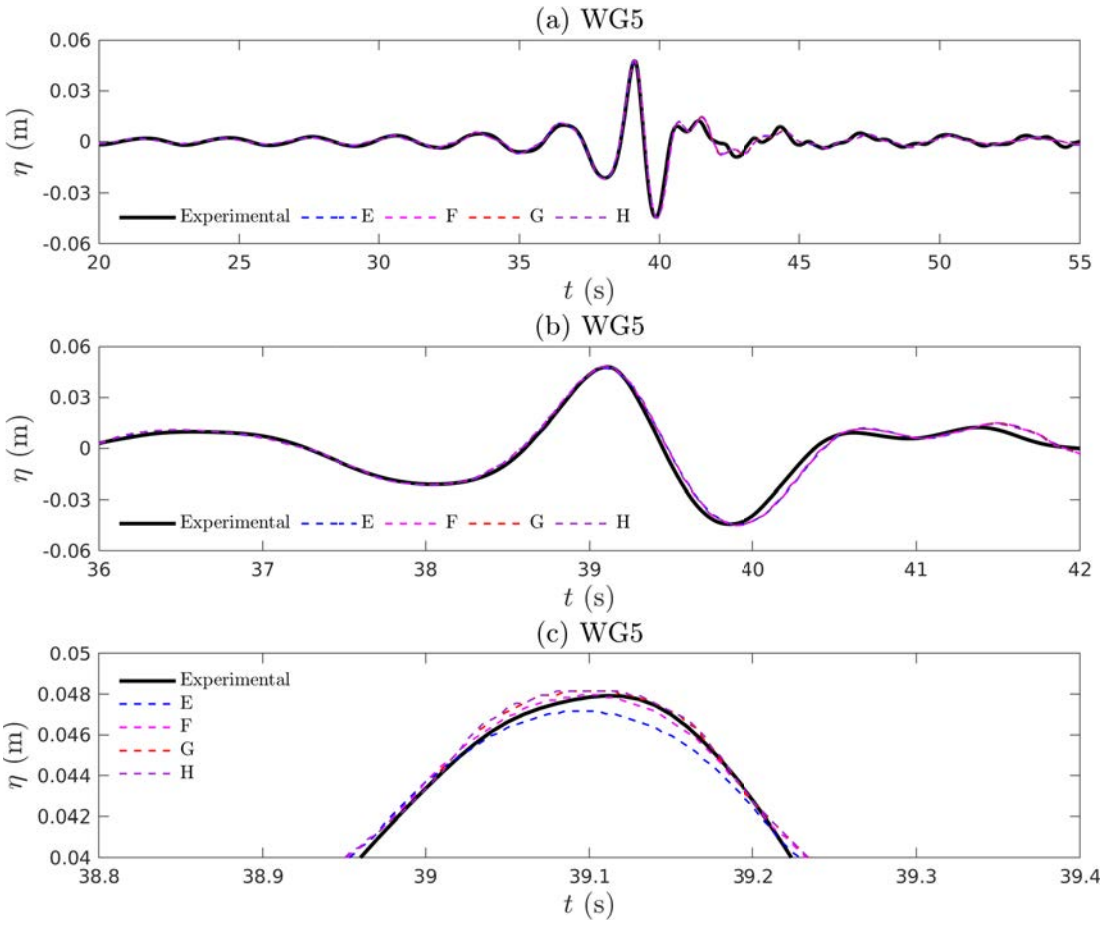

Figure 6.16: Case 1 IntegratedFoam time histories of free-surface elevation for meshes E, F, G, and H at wave gauge 5 (WG5), along with the experimental solution of Sriram et al. (2021) [126]: (a) $t \in [20,\ 55]$, (b) $t \in [36,\ 42]$, (c) $t \times \eta \in [38.8,\ 39.4] \times [0.04,\ 0.05]$.

length R. Increasing/decreasing the number of annuli/radii then controls the density of the mesh in the larger annular region around the cylinder. The rest of the mesh is then composed of eight 'blocks' in which the mesh can be constructed with a regular structure that fits around the annular region. In addition to the xz-plane, the mesh in the y-direction is refined so that 20% of cells are concentrated in the region $y \in [-0.05,\ 0.05]$ within which the focused wave reaches peak amplitude. The remaining cells then also stretched to fit around the region, as shown in Figure 6.15 C. This is the basic mesh structure that will be used for both cases in this section.

Now moving on to the mesh sensitivity study for Ω_{NS}, four different meshes—E–H in Table 6.10—are considered to test convergence in the x-direction. These constitute 100, 200, 400, and 600 cells per wavelength, picked using information gathered from the prior examples in Chapter 5. A constant density of 50 cells in the y-direction is also chosen given prior examples. Figure 6.16 then shows the time histories of free-surface elevation for meshes E–H at WG5, along with the experimental solution of Sriram et al. (2021) [126]. Figures 6.16(a) and Figure 6.16(b) show no discernible difference between the meshes but Figure 6.16(c) shows a slight difference between the coarsest mesh E and the others. This suggests that mesh E may be suitable for the test case; however, further investigations reveal that it does not allow for sufficient resolution around the cylinder to provide an accurate solution. Therefore, mesh F is chosen instead. Now considering the y-direction, three meshes are considered: I, F, and J in Table 6.10. These constitute 25, 50, and 100 cells respectively, with density in the x-direction being constant at 250 as found previously. Figure 6.17 then shows the time histories at WG5 along with the experimental solution. Mesh I clearly shows a considerable difference to both meshes F and J so this is disregarded and the reference mesh F is chosen. As an aside, the results here are impressive: it is clear that the IntegratedFoam can accurately reproduce this focused wave in Ω_{NS}, demonstrating that the coupling is accurate.

Figure 6.18 then shows the final Ω_{NS} mesh in which there are approximately 1.94 million cells in total. In the 2-D annular region around the cylinder, there are 60 anulli and 160 radii in total, resulting in 9600 cells in the xz-plane. Moreover, the cells are stretched so that the outer radius of the annulus closest to the cylinder is four times smaller than the outer radius of the annulus furthest from the cylinder. Multiplying by the mesh density in the y-direction then totals 480 thousand cells in the entire 3-D annular region. Outside the annular region, there are maximum 276 cells in the x-direction and 112 in the z-direction. This slight increase to the density found in the sensitivity study was required to fit the mesh and ensure proper resolution throughout the domain without major sudden changes in cell size. As mentioned previously, the mesh in the y-direction is refined so that 20% of cells are concentrated in the region $y \in [-0.05, 0.05]$. In addition to this, the mesh is stretched in the region $y \in [-0.7, -0.05]$ so that the cell at the top has vertical depth 1/4 of the cell at the bottom. Similar applies for the region $y \in [0.05,\ 0.3]$ where the cell at the top has 2.5 times the vertical depth of the cell at the bottom. Again, this is to ensure proper resolution and no sudden changes in cell size.

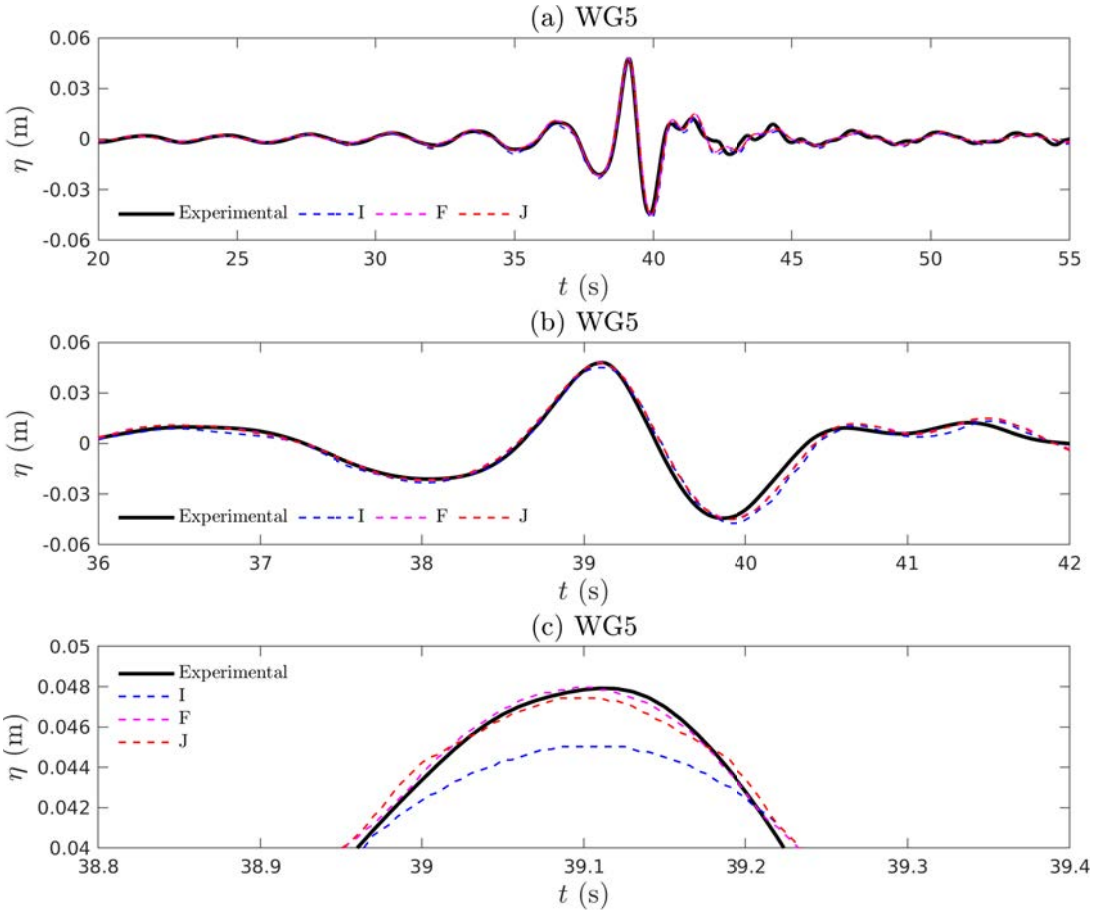

Figure 6.17: Case 1 IntegratedFoam time histories of free-surface elevation for meshes I, F, and J at wave gauge 5 (WG5), along with the experimental solution of Sriram et al. (2021) [126]: (a) $t \in [20,\ 55]$, (b) $t \in [36,\ 42]$, (c) $t \times \eta \in [38.8,\ 39.4] \times [0.04,\ 0.05]$.

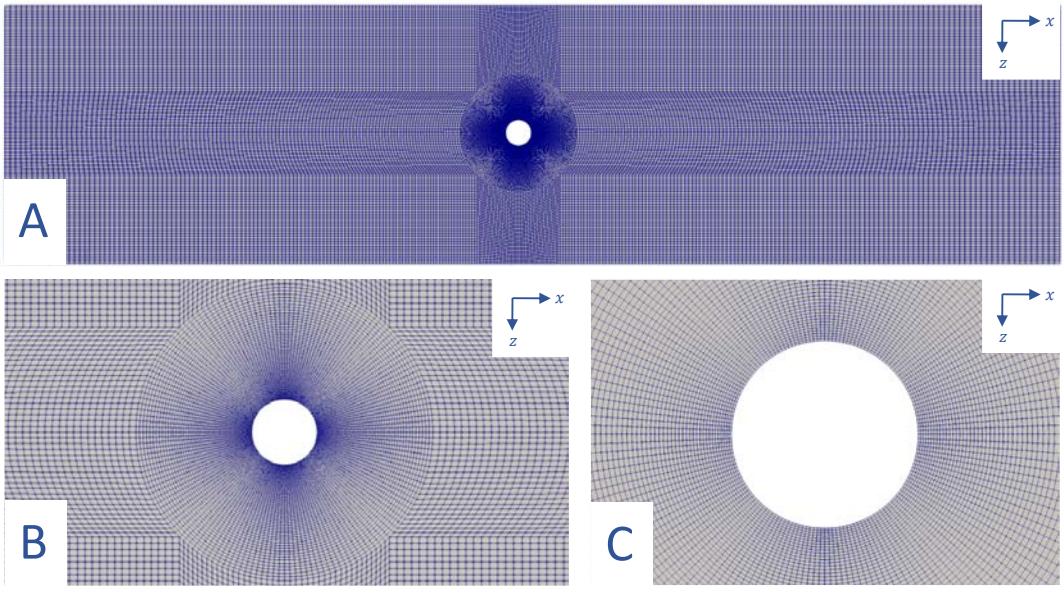

Figure 6.18: Final Ω_{NS} mesh in the xz-plane for Case 1.

6.3.3.3 Setup of remaining computational parameters

Following the analysis in Chapter 5, $C_{\max}$ is again set at 0.2. Moreover, given the analysis of computational time in Chapter 5, it is assumed that the coupling will take up the majority of the computational time. This assumption is backed up by the fact that the mesh is not moving here so additional interFoam time is not needed to solve the dynamic mesh equations as was the case with the floating body test case in Section 6.2. Furthermore, the input focused wave is not very steep, and there is no significant breaking on and around the cylinder. This means that less iterations will be needed to reach a convergent solution. Consequently, given all these factors, 17 out of 32 processors are assigned to the coupling.

6.3.3.4 Results for Case 1

Figure 6.19 then shows the time histories of free-surface elevation for IntegratedFoam and the experimental solution of Sriram et al. (2021) [126] at WGs 5–7. Very good agreements can be seen between the numerical and experimental results at every wave gauge, indicating that the IntegratedFoam model can accurately predict the free-surface location of the focused waves in this case, even after interaction with the cylinder.

Figure 6.20 also shows the time histories of the body-surface pressure for IntegratedFoam and the experimental solution of Sriram et al. (2021) [126] at PGs 2–8. Again, excellent agreements between then numerical and experimental results are achieved at every pressure gauge, demonstrating that the IntegratedFoam model is more than capable of accurately capturing the hydrodynamic load on the cylinder due interaction with the focused waves in this case.

In terms of computational time, Table 6.11 shows the time taken by different parts of the solver. It is clear that the coupling again takes up the majority of the time, 56% to be precise, followed by interFoam which takes up 42%, and FNPFFoam which takes up 2%. The proportion of time taken by the coupling is now less than the test cases in Chapter 5, but much less than 2-D floating structure case in Section 6.2. This means that the improvement in efficiency is limited for this case, but is still significant enough to warrant use of the IntegratedFoam solver. For example, it would obviously be unfeasible to use interFoam to the full scale of the experiments, i.e., a 110 m NWT, but even a NWT of length 29.5 m—i.e., from the inlet to the end of Ω_{NS}—would still be 3.3 times larger than Ω_{NS} using IntegratedFoam. Multiplying the interFoam time in Table 6.11 by 3.3 then gives a crude estimate of 64,899 as the expected interFoam time for such as example. This is of course not exact but gives a rough idea of what to expect.

	Coupling	interFoam	FNPFFoam	Total
Computational time (s)	29,084	21,633	1153	51,870

Table 6.11: Time taken by different parts of the solver in Case 1.

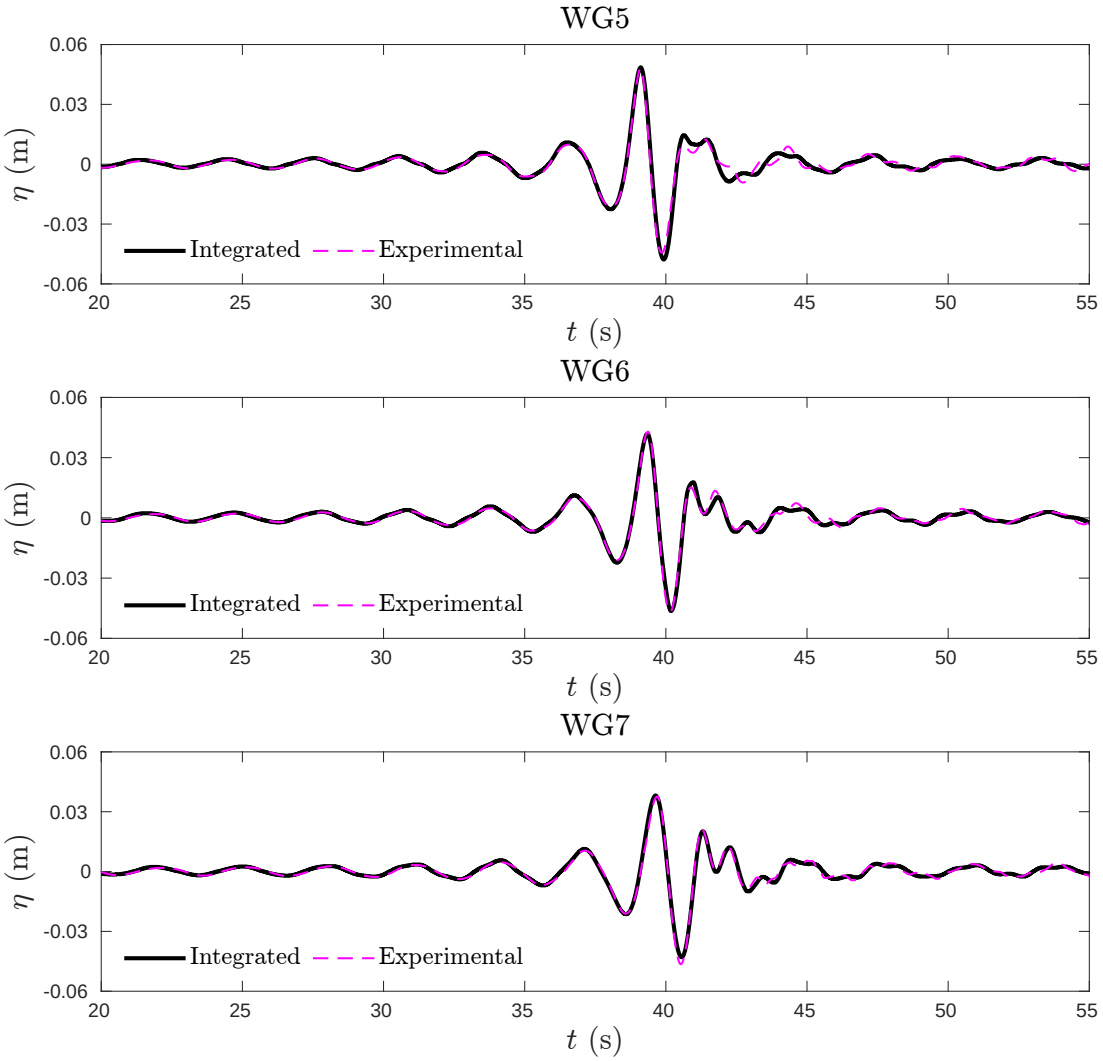

Figure 6.19: Case 1 time histories of free-surface elevation for IntegratedFoam, and the experimental solution of Sriram et al. (2021) [126], at wave gauges 5–7 (WG5–WG7).

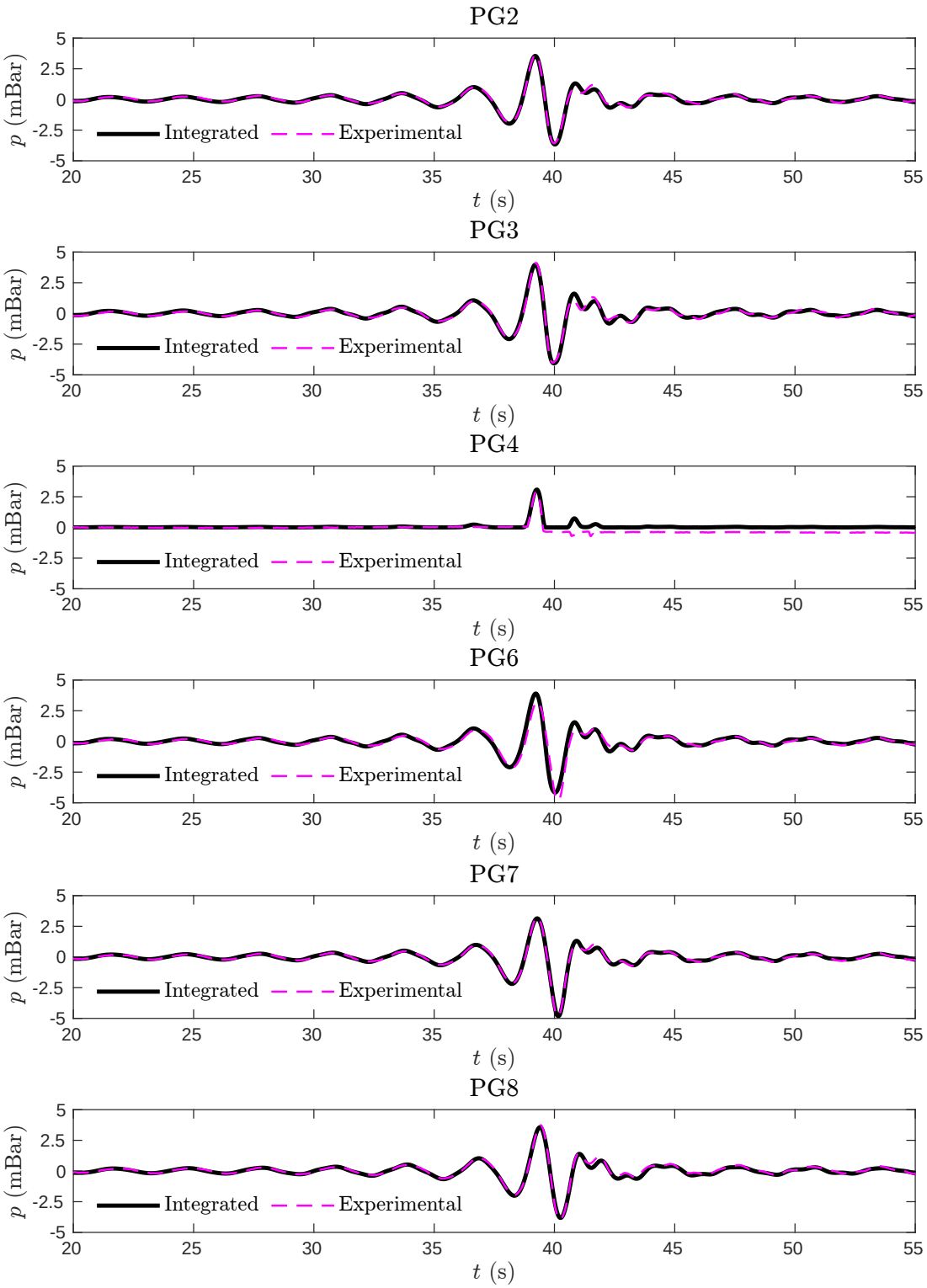

Figure 6.20: Case 1 time histories of body-surface pressure for IntegratedFoam, and the experimental solution of Sriram et al. (2021) [126], at pressure gauges 2–8 (PG2–PG8).

6.3.4 Case 3

6.3.4.1 Computational setup for $\Omega_{\mathbf{FNPF}}$

Analogous mesh sensitivity studies to Case 1 are now needed to find the optimal mesh configurations for Case 3. The wave in Case 3—as seen in Table 6.6—is much steeper than Case 1, so much finer meshes are expected for both Ω_{FNPF} and Ω_{NS}. Starting with Ω_{FNPF}, Table 6.12 lists the new meshes used in the sensitivity study. Figures 6.21 and 6.22 then show the time histories of free-surface elevation for meshes A, B, C, and D at WGs 4 and 5, along with the experimental solution of Sriram et al. (2021) [126]. At WG4 (Figure 6.21), no discernible difference can be seen between meshes B, C, and D, but mesh A shows a slight reduction in peak amplitude. This effect is amplified at WG5 (Figure 6.22) where a significant phase shift and reduction in amplitude is seen for mesh A. Moreover, a similar but less significant effect is also seen for mesh B but not meshes C and D, between which there is not a significant difference. Hence, mesh C is chosen for Ω_{FNPF}. Note that the y-direction is not considered here as previous work indicates that increased steepness primarily requires a greater density in the x-direction, particularly given that the water depth is still the same as Case 1. The accuracy of the results Figures 6.21 and 6.22 confirms this, as will the results that follow.

6.3.4.2 Computational setup for $\Omega_{\mathbf{NS}}$

The structure of Ω_{NS} for Case 3 is the same as in Case 1, i.e., the dimensions of the annular region around the cylinder are the same. However, the region in which cells are concentrated in the y-direction is now enlarged to $y \in [-0.15, 0.22]$ to account for the larger peak amplitude of the focused wave. Again, the mesh cannot be determined solely through a sensitivity study here as there are many factors in play. An additional challenge with this case compared to Case 1 is that significant breaking occurs on the cylinder after the focusing event, so the mesh needs to be fine enough around the cylinder to properly capture this by accurately calculating

Domain	ID	Configuration $x \times y$	Cells per λ
Ω_{FNPF}	A	755×15	50
Ω_{FNPF}	B	1510×15	100
Ω_{FNPF}	C	2277×15	150
Ω_{FNPF}	D	3036×15	200
Ω_{NS}	E	250×100	200
Ω_{NS}	F	375×100	300
Ω_{NS}	G	500×100	400
Ω_{NS}	H	750×100	600

Table 6.12: Mesh configurations used in mesh sensitivity studies for Case 3.

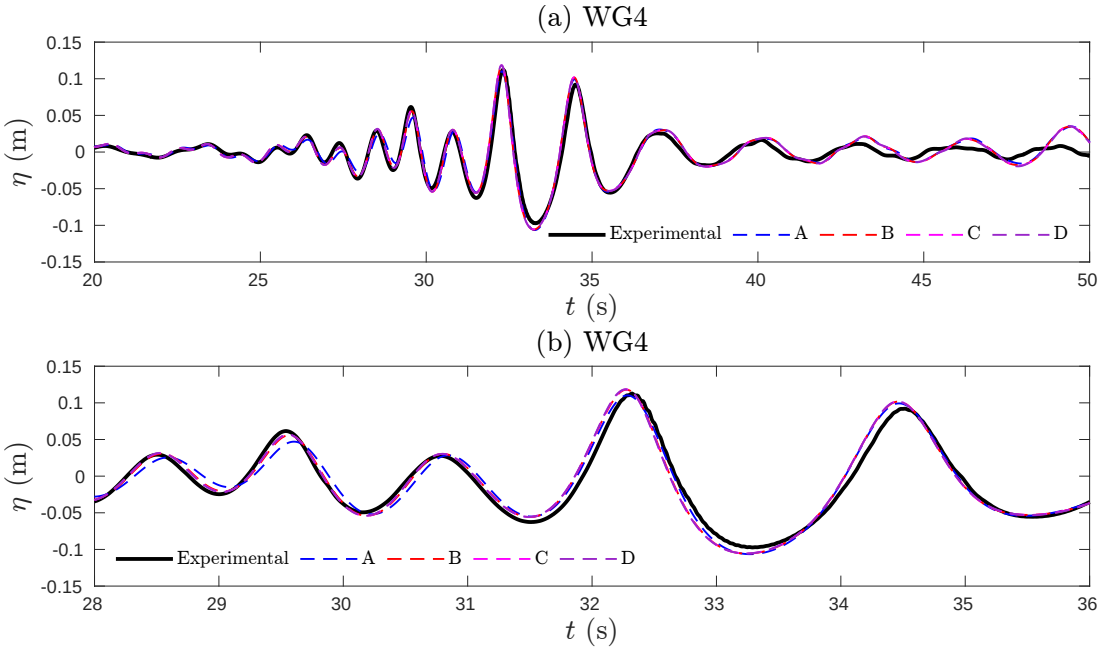

Figure 6.21: Case 3 FNPFFoam time histories of free-surface elevation for meshes A, B, C, and D at wave gauge 4 (WG4), along with the experimental solution of Sriram et al. (2021) [126]: (a) $t \in [20,\ 50]$, (b) $t \in [28,\ 36]$.

the water-volume fraction, velocity, and pressure. Given this, the density in the y-direction is doubled to 100 cells from 50 in Case 1. The wave solution in an empty tank was not found to not be much different between 50 and 100 cells, but during simulations with the cylinder it was found that 50 cells could not properly capture the breaking event accurately. Moreover, the simulation was actually taking longer to complete than when there were 100 cells because more corrector loops were needed in the solution procedure for the solution to converge. Given all this, a density of 100 cells is chosen in the y-direction and is kept constant throughout.

For the mesh sensitivity study in the x-direction, four different meshes—E–H in Table 6.12—are considered. These constitute 200, 300, 400, and 600 cells per wavelength. Figure 6.23 then shows the time histories of free-surface elevation for meshes E–H at WG5, along with the experimental solution of Sriram et al. (2021) [126]. Again, it is first noted that the results here are impressive: it is clear that the IntegratedFoam model can accurately reproduce this steeper focused wave in Ω_{NS}, demonstrating that the coupling is accurate. There are however very slight discrepancies between each mesh seen in Figure 6.23(c), but given that the increase in density between each mesh is so large, this is not significant. This means that mesh E, constituting approximately 200 cells per wavelength, could theoretically be used. However, recall that there is significant breaking on the cylinder, so a much finer mesh is needed in the annular region around the cylinder. Given this, mesh G, constituting approximately 400 cells per wavelength, is instead chosen as the reference mesh. However, given that the wave solution is convergent when the mesh density if half of this, some refinement is done to reduce the overall density whilst still keeping the same resolution. For example, the mesh is stretched so that close to

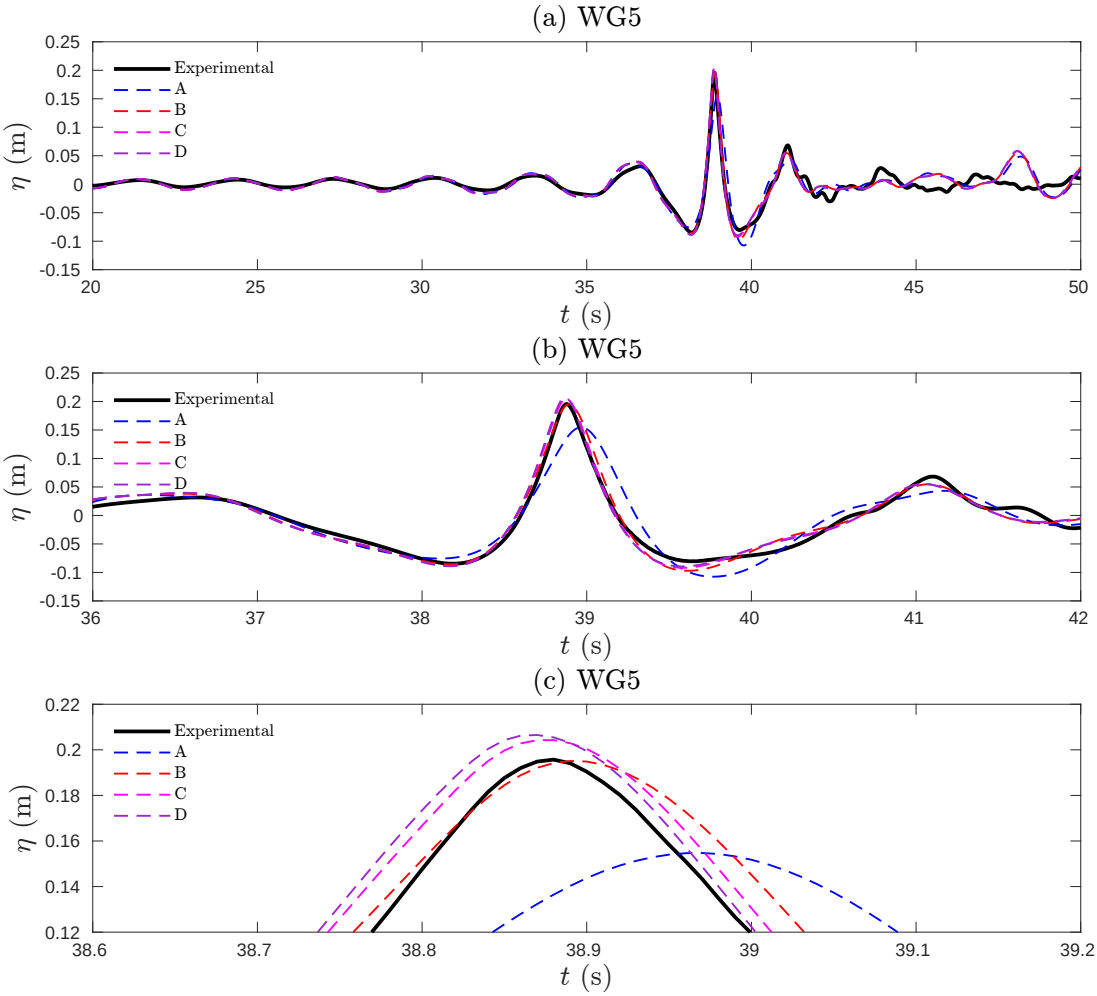

Figure 6.22: Case 3 IntegratedFoam time histories of free-surface elevation for meshes A, B, C, and D at wave gauge 5 (WG5) in Ω_{FNPF}, along with the experimental solution of Sriram et al. (2021) [126]: (a) $t \in [20,\ 50]$, (b) $t \in [36,\ 42]$, (c) $t \times \eta \in [38.6,\ 39.2] \times [0.12,\ 0.22]$.

the cylinder the cell width is the same as mesh G, but away from the cylinder the width is the same as in mesh E.

Figure 6.24 then shows the final Ω_{NS} mesh for Case 3 in which there are approximately 9.15 million cells in total—almost 5 times more than Case 1. In the 2-D annular region around the cylinder (B, C, and E), there are 100 annuli and 320 radii in total, resulting in 32 thousand cells in the xz-plane. Moreover, cells are stretched so that the outer radius of the annulus closest to the cylinder is eight times smaller than the outer radius of the annulus furthest from the cylinder. Multiplying by the mesh density in y-direction then totals 3.2 million cells in the entire 3-D annular region. Outside the annular region, there are maximum 434 cells in the x-direction and 152 in the z-direction. The mesh in the y-direction (D) is refined so that 64% of cells are concentrated in the region $y \in [-0.15,\ 0.22]$. In addition to this, the mesh is stretched in the region $y \in [-0.7,\ -0.15]$ so that the cell at the top has vertical depth 3/20 of the cell at the bottom. Similar applies for the region $y \in [0.22,\ 0.3]$ where the cell at the top has 2.5 times the vertical depth of the cell at the bottom.

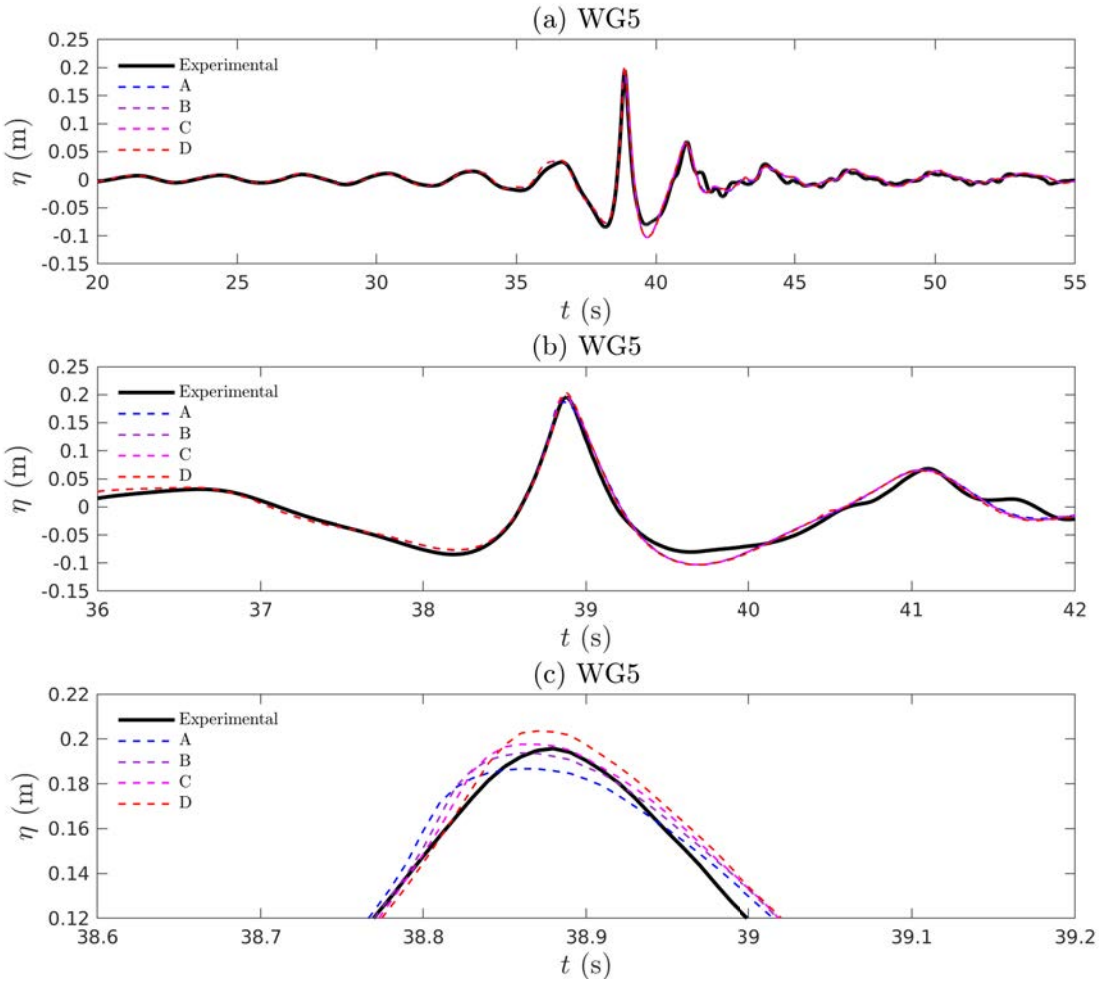

Figure 6.23: Case 3 IntegratedFoam time histories of free-surface elevation for meshes E, F, G, and H at wave gauge 5 (WG5) in Ω_{NS}, along with the experimental solution of Sriram et al. (2021) [126]: (a) $t \in [20,\ 55]$, (b) $t \in [36,\ 42]$, (c) $t \times \eta \in [38.6,\ 39.2] \times [0.12,\ 0.22]$.

6.3.4.3 Setup of remaining computational parameters

In contrast to Case 1, the input focused wave in this case is very steep and significant breaking is expected on and around the cylinder. Therefore, preliminary investigations, including the mesh sensitivity studies in the previous sections, suggest that a higher value of C_{max} can be used. This is because the time step step is driven to a very small value anyway due to the complex flow features associated with the wave breaking, regardless of the value of C_{max}. Therefore, a value of $C_{\text{max}} = 0.4$ is set instead. Moreover, the number of interFoam *innerCorrectors* and *alphaCorrectors*—each explained in Chapter 2—are increased from 3 to 5 to increase the stability of the solution. This inevitably increases the computational time so the increase in C_{max} will also aid efficiency. As a consequence of this wave breaking, a more even distribution of processors is required between the coupling and interFoam. Therefore, 17 out of 32 processors are assinged to the coupling in this case.

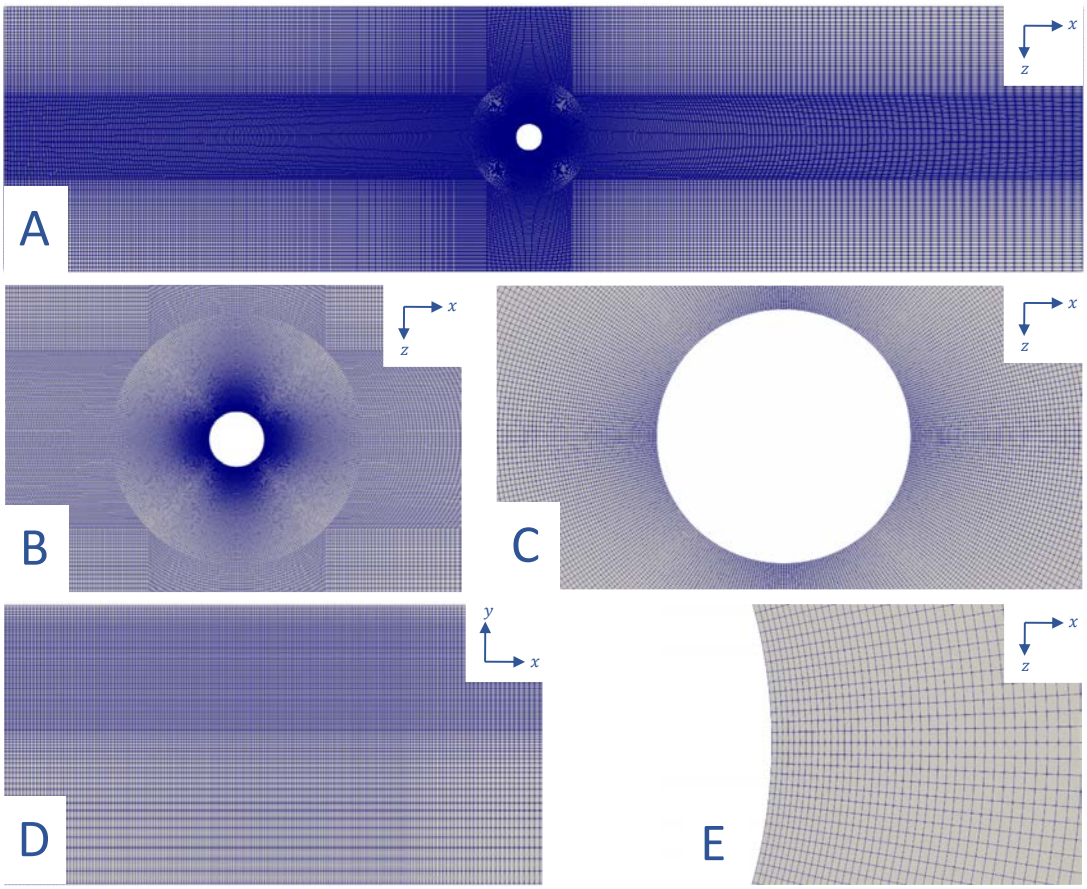

Figure 6.24: Final Ω_{NS} mesh for Case 3 in the xz-plane (A, B, C, and E) and the xy-plane (D).

6.3.4.4 Results for Case 3

Figure 6.25 then shows the time histories of free-surface elevation for IntegratedFoam and the experimental solution of Sriram et al. (2021) [126] at WGs 5–7. Good agreements can be seen between the numerical and experimental results at every wave gauge, indicating that the IntegratedFoam model can accurately predict the free-surface location of the focused waves in this steeper wave case. There are slight discrepancies at WG5 and WG6 after focusing event and subsequent impact with the cylinder. However, this may be expected given the complex flow field around the cylinder after impact. Figures 6.27 and 6.28 show snapshots at seven time instances around the focusing event. The aforementioned wave impact and consequent flow around the cylinder can clearly be observed. Moreover, spilling wave breaking can be seen to occur at snapshots $t = 39.2$ s and $t = 39.4$ s; this is in line with the experimental results and other numerical works. Figure 6.29 also shows snapshots of the free-surface velocity magnitude.

Figure 6.26 also shows the time histories of the body-surface pressure for IntegratedFoam and the experimental solution of Sriram et al. (2021) [126] at PGs 2–8. Again, good agreements between the numerical and experimental results are achieved at every pressure gauge, demonstrating that the IntegratedFoam model is more than capable of accurately capturing the hydrodynamic load on the cylinder due interaction with the steeper focused waves in this case.

The computational times for each part of the solver are shown in Table 6.13. It is clear that the sheer scale of the interFoam mesh used means both the interFoam and coupling time are very large. Further work should be done to find out whether such a fine mesh in the annular region around the cylinder is necessary; the same accuracy of results may be possible with a coarser mesh, significantly bringing down both coupling and interFoam time. However, interFoam still takes the majority of time here—contrary to Case 1. As previously mentioned, this is mostly down to the finer mesh but also the extra iterations needed to solve the fine scale flow features due to wave impact with the cylinder. This is an unfortunate downside of high-fidelity flow models and is at the heart of why integrated models like IntegratedFoam are important. Indeed, if solely interFoam had been used in this test case to the same scale as IntegratedFoam, it is clear that the computational time would be a magnitude greater and practically unfeasible. Hence, in this sense, IntegratedFoam has achieved a marked improvement in computational efficiency.

	Coupling	interFoam	FNPFFoam	Total
Computational time (s)	970,366	1,144,860	10,042	2,125,268

Table 6.13: Time taken by different parts of the solver in Case 3.

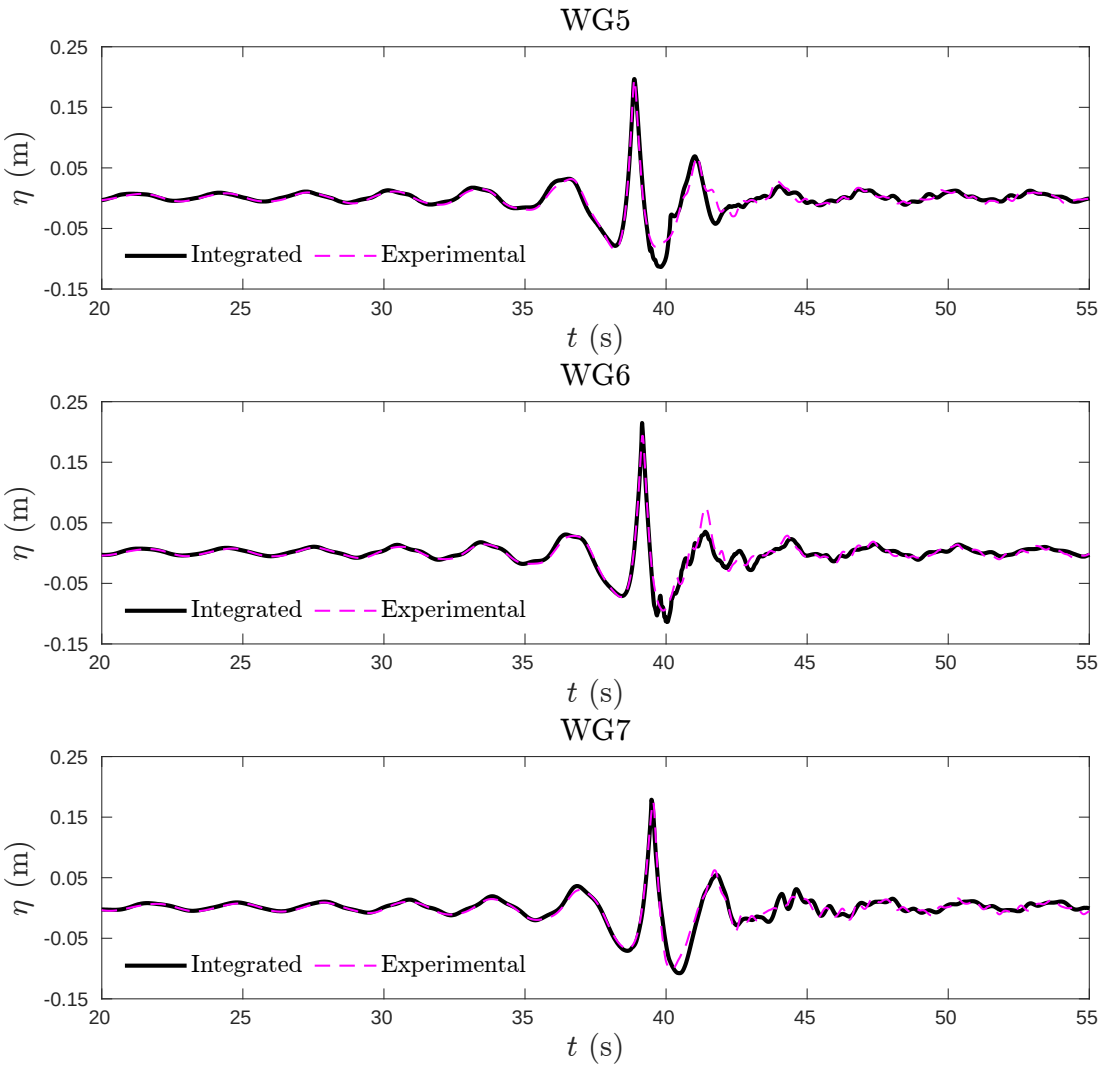

Figure 6.25: Case 3 time histories of free-surface elevation for IntegratedFoam, and the experimental solution of Sriram et al. (2021) [126], at wave gauges 5–7 (WG5–WG7).

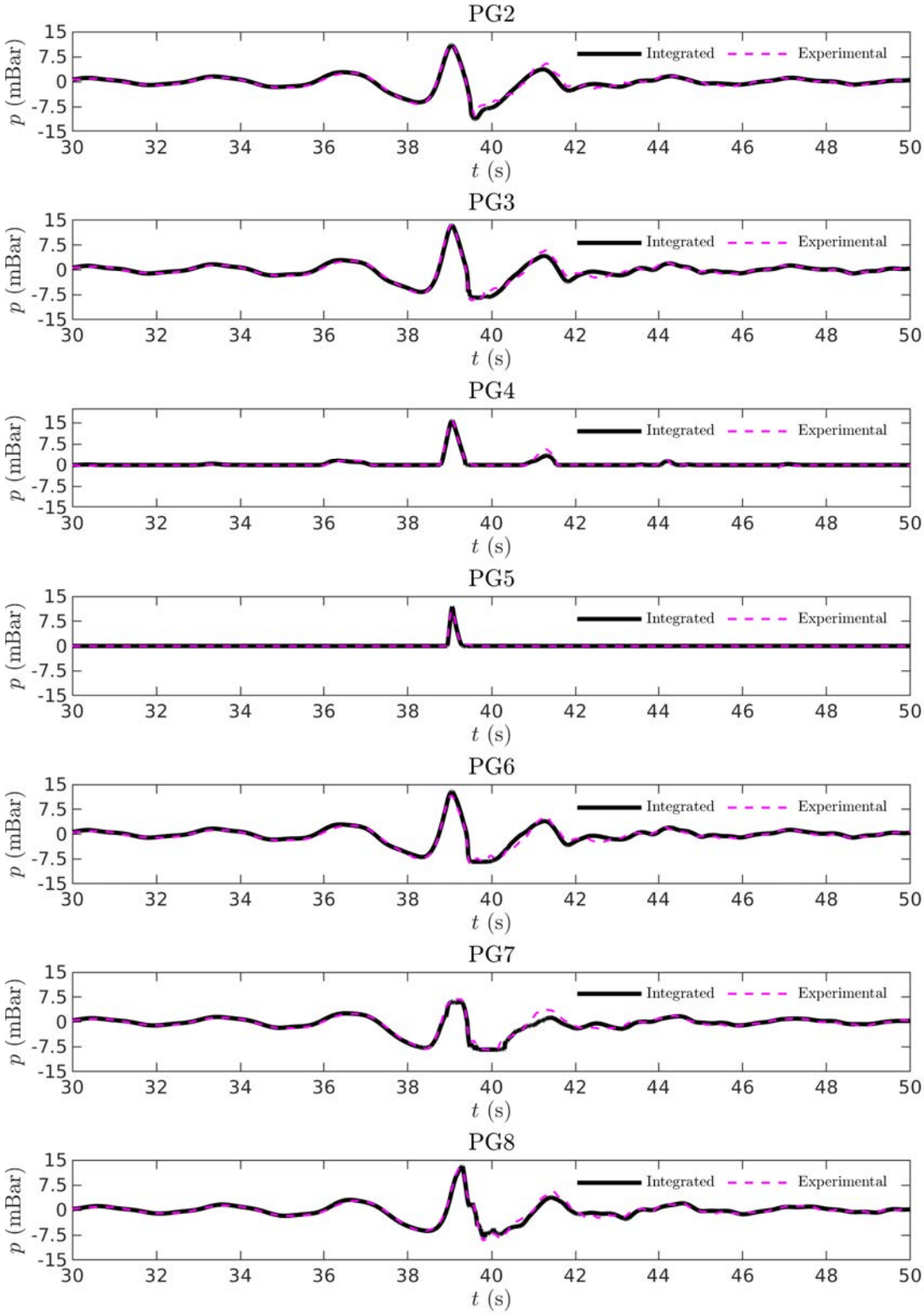

Figure 6.26: Case 3 time histories of body-surface pressure for IntegratedFoam, and the experimental solution of Sriram et al. (2021) [126], at pressure gauges 2–8 (PG2–PG8).

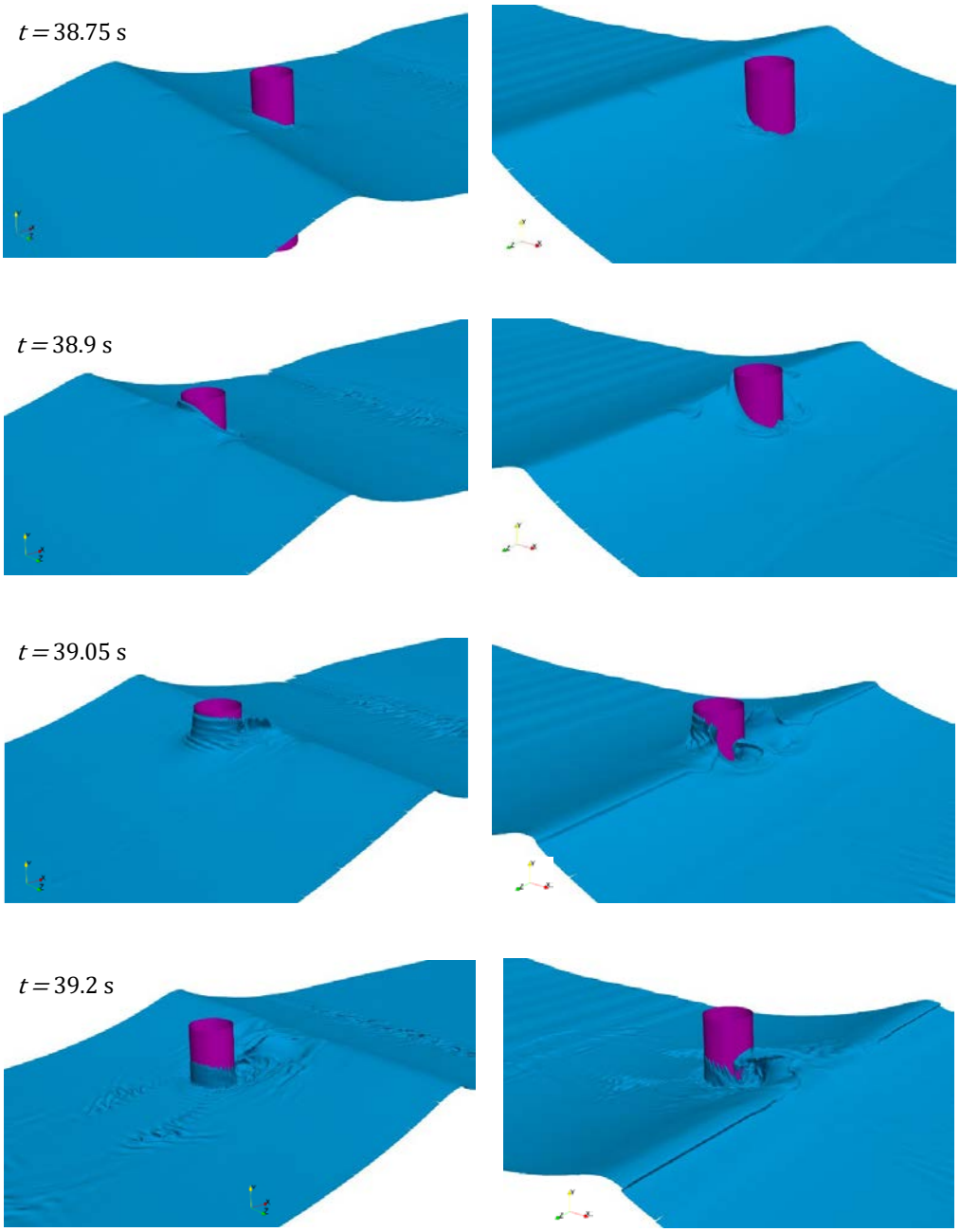

Figure 6.27: Snapshots of the free-surface profile at $t = 38.75$, 38.9, 39.05, and 39.2 s in Case 3. The wave propagates from left to right. Left panel: front left view. Right panel: rear left view.

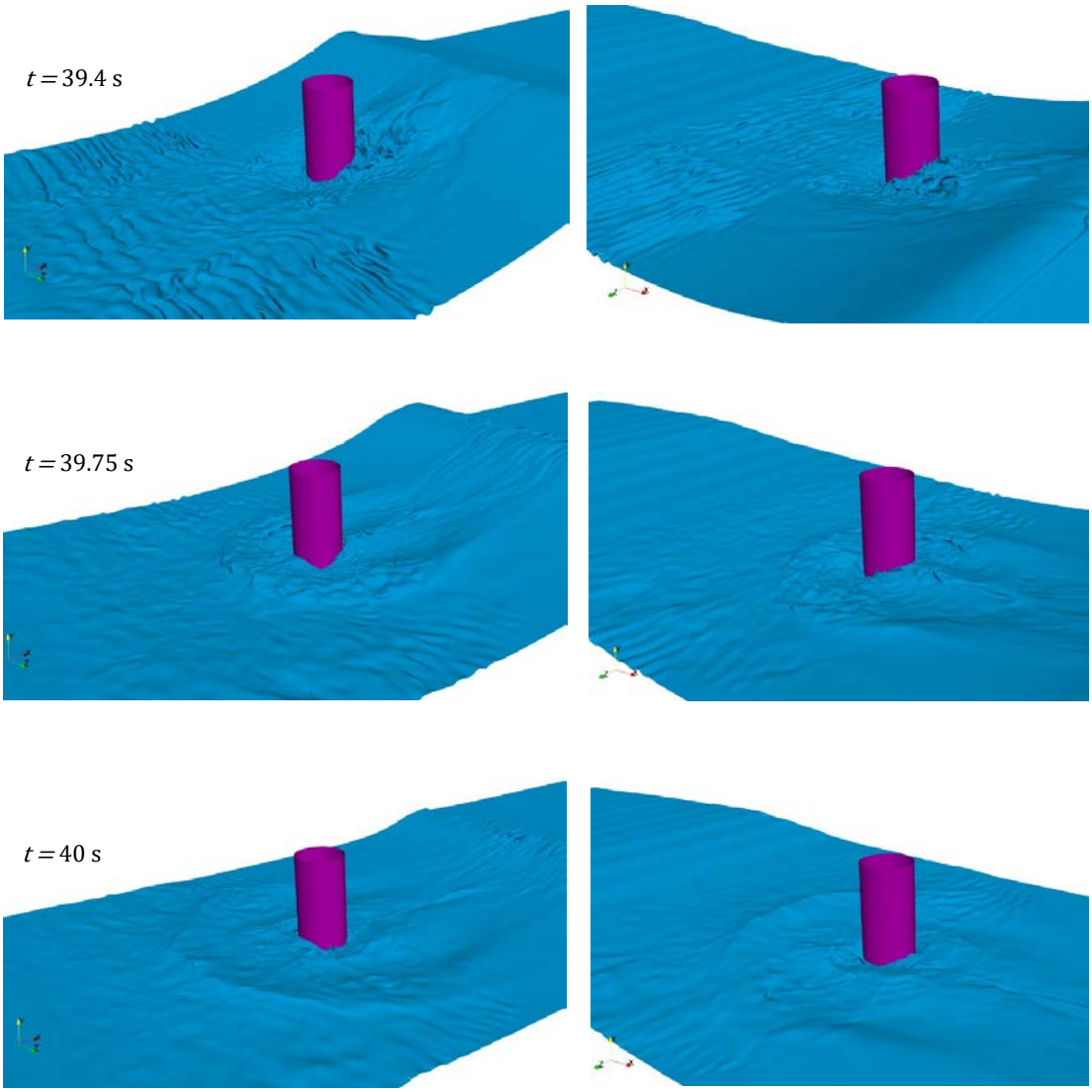

Figure 6.28: Snapshots of the free-surface profile at t = 39.4, 39.75, and 40 s in Case 3. The wave propagates from left to right. Left panel: front left view. Right panel: rear left view.

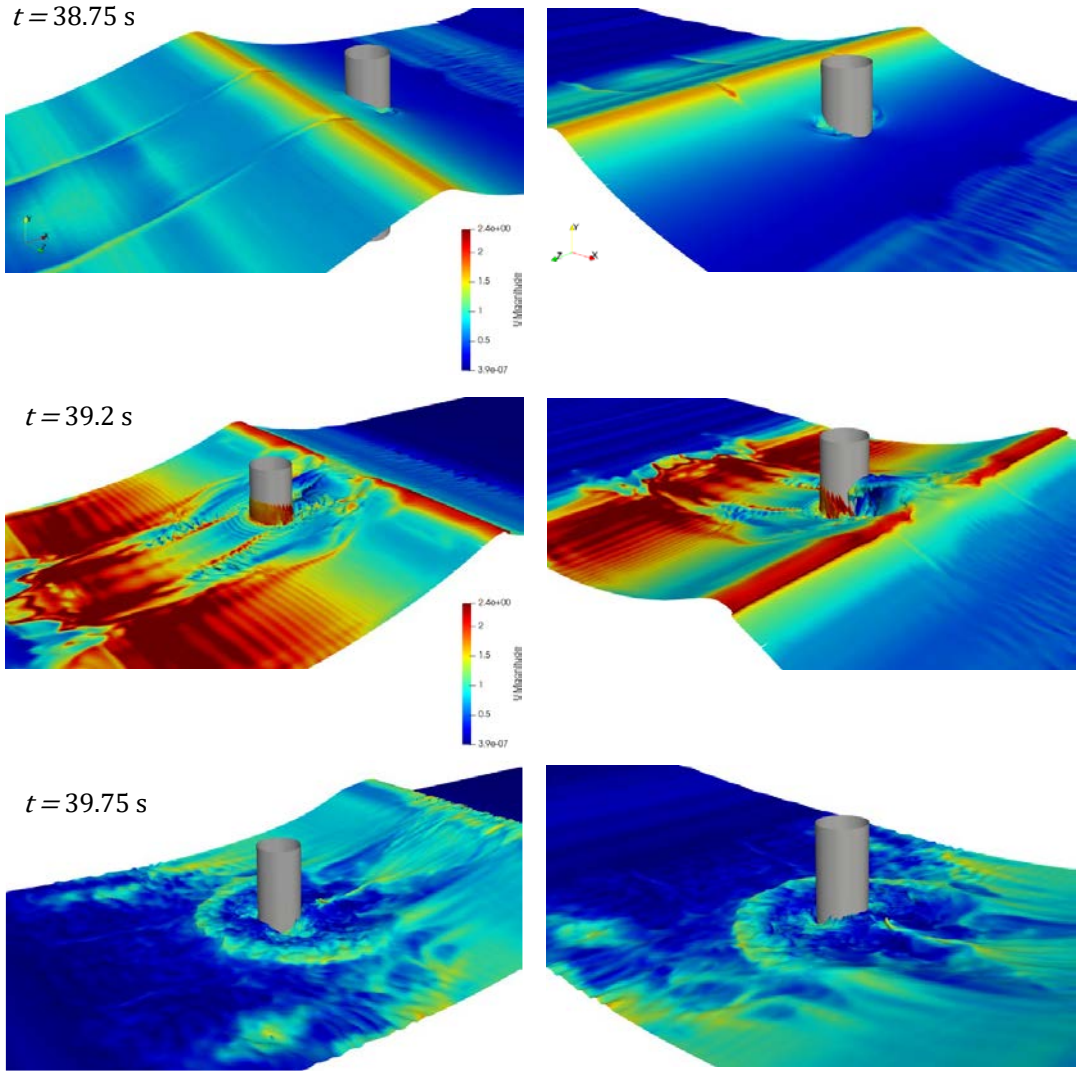

Figure 6.29: Snapshots of free-surface velocity magnitude at t = 38.75, 39.2, and 39.75 s in Case 3. The wave propagates from left to right. Left panel: front left view. Right panel: rear left view.

6.4 Focused wave-interaction with a point absorber wave energy converter

Wave power is, as of yet, a widely untapped form of renewable energy. The fundamental idea is to extract energy from ocean waves through a wave energy converter (WEC) device and accompanied power take-off system. The main types of wave energy converters are oscillating water columns, overtopping devices, and oscillating bodies. Oscillating bodies have long been the main attention of research, with the most common being 'point absorbers'. In general, these types of devices consist of a moored fully submerged or floating structure that oscillates near the free surface in response to incident waves from all directions. The relative heave motion of the body with respect to a base on the seabed is converted into electrical power through a power take-off system. However, other sorts of point absorbers exist, such as the famous Salters duck (Salter (1974) [120]). This device instead used its relative pitching motion, rather than heaving, to generate electrical power through an in-built hydraulic power take-off system.

Wave power development has always faced severe technical and engineering challenges involving survivability, seriously affecting long-term performance. Similar to monopile structures, any WEC device needs to be able withstand the forces subjected on them from extreme ocean waves. However, unlike monopile foundations, WECs also have to extract some of the enormous amounts of energy contained in these waves and convert it into electricity. The complexity of this process makes wave energy conversion one of the most challenging aspects of offshore engineering. As of yet, no commercially viable WEC projects that solve the practical and financial problems involved have been successful. However, wave energy continues to be a major area of research due to the potentially unlimited supply of renewable energy that can be harnessed.

Similar to the monopile foundations in the previous section, hydrodynamic modelling of these wave energy converter devices in the face of extreme wave events is a key part of the design process. Hence, in this section, focused wave will again be used to replicate these extreme wave events to see if the new IntegratedFoam model can accurately predict the motion of a 3-D moored point absorber WEC after interaction with the focused wave.

6.4.1 Experimental setup

In the present work, the CCP-WSI Blind Test Series 2: 'Focused wave interactions with floating structures' [15] is considered. In the physical experiments, two-dimensional unidirectional focused waves were generated in a 3-D wave tank. The tank in question was 35 m long and 15.5 m wide, with a working water depth of 3 m. A wavemaker was placed at one end and a beach at the other. In addition to this, a simplified WEC device is placed at a distance 14.8 m away from the wavemaker. In the experiments, two different shaped WECs were used: a hemispherical-bottomed cylinder and a cylinder with a moon pool. Only the former is considered in this work and is illustrated in Figure 6.30. The corresponding mechanical characteristics

of the WEC are also listed in Table 6.14. The mooring line was attached to the bottom of the hemispherical part of the WEC and anchored to the bottom of the wave tank. It had stiffness 67 N/m with and rest length of 2.199 m. The focused waves were generated using 244 components derived from the Pierson-Moskowitz spectrum referenced in Section 5.1.3 and through the same methodology as in Section 5.1.4. In the experiments, three sets of waves parameters were used, but in the present work only 'Case 1' is considered. The corresponding focused wave parameters are listed in Table 6.15. It should be noted that the focus location x_f is the same as the centre of the WEC and the focusing time is chosen to be the same as the experimental results. A number of wave gauges were also placed in the wave tank; the ones relevant in this work will be listed in the next section in relation to the IntegratedFoam geometry rather than the experimental geometry.

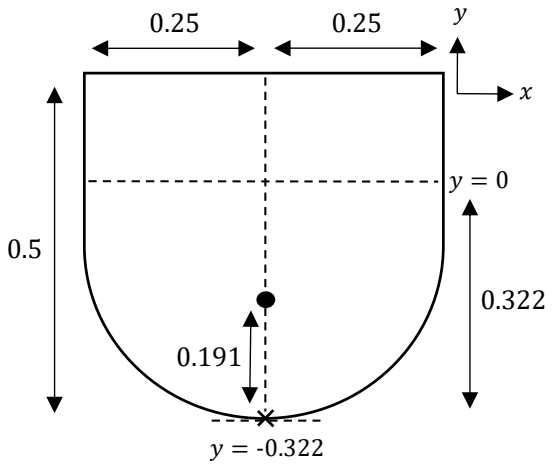

Figure 6.30: Schematic in the xy-plane of the hemispherical-bottomed wave energy converter (WEC). All dimensions are in metres.

Characteristic	Value
Mass: m (kg)	43.674
Centre of mass: CM (m)	$(x, y, z) = (14.8,\ -0.131,\ 0)$
Roll moment of inertia: I_x (kg·m^2)	1.620
Yaw moment of inertia: I_y (kg·m^2)	1.143
Pitch moment of inertia: I_z (kg·m^2)	1.620
Draft: d (m)	0.322

Table 6.14: Mechanical Characteristics of the hemispherical-bottomed wave energy converter (WEC).

Case	A_I (m)	Frequency band (Hz)	f_P (Hz)	H_s (m)	x_f (m)	t_f (s)
1	0.25	$f \in [0.101563,\ 2]$	0.3578	0.274	14.8	45.13

Table 6.15: Input focused wave parameters for the wave energy converter (WEC) test case: A_I is the input focused wave amplitude, f_p is the peak frequency, H_s is the significant wave height, x_f is the focusing location, and t_f is the focusing time.

6.4.2 Geometric setup

The geometric for IntegratedFoam is shown in Figures 6.31 and 6.32. In this work, only WGs 1, 3, 5, and 8 from the original experiments are used: their locations, all along the $z = 0$ centreline, are listed in Table 6.16. Note that all wave gauges lie in both Ω_{FNPF} and Ω_{NS}. Similar to the cylinder test case, the generated focused waves are unidirectional and 2D, so a 2-D FNPFFoam domain can be used. Hence, $\Omega_{\text{FNPF}} = [0,\ 35] \times [-3,\ 0] \times [-7.75,\ 7.75]$ (m), where there is a single cell of width 15.5 m in the transverse direction. Moreover, in the same way as previous examples, the characteristic wave of the focused wave group is taken as the wave corresponding to the peak amplitude for that group, which in this case is $\lambda_p = 11.276$ m. This characteristic wavelength is clearly quite large compared to the size and location of the WEC, so similar to the cylinder test case, the length of Ω_{OZ} and Ω_{DZ} are set to $1/2\lambda_p = 5.638$ m. As was seen through the analysis in Section 5.3.1 and during the cylinder test case in Section 6.3, this may lead to slight discrepancies in the solution, but should be minimal due to the small area of interest around the WEC. Moreover, the computational time potentially saved would be significant. It follows then that $\Omega_{\text{NS}} = [8.75,\ 23.138] \times [-3,\ 1.3] \times [-1.4,\ 1.4]$ (m) with $\Omega_{\text{OZ}} = [8.75,\ 14.35] \times [-3,\ 1.3] \times [-1.4,\ 1.4]$ (m) and $\Omega_{\text{DZ}} = [17.5,\ 23.138] \times [-3,\ 1.4] \times [-1.4,\ 1.4]$ (m). All these dimensions are shown in Table 6.17. Note that the upper y-limit here is necessary for the stability of mesh morphing in interFoam. Moreover, the z-limits are chosen for the same reason, whilst also taking into account efficiency and minimising any effects of reflection from the front and back walls. Lastly, the mooring line is modelled as a linear spring with stiffness 67 N/m and rest length 2.199 m. It is attached to bottom of the WEC at $(x, y, z) = (14.8,\ -0.322,\ 0)$ (m) and anchored to the bottom of the NWT at $(x, y, z) = (14.8,\ -3,\ 0)$ (m). Finally, the simulation time is 50.3 s (the requested time window in the CCP-WSI (2020) [15] case was $t \in [35.3,\ 50.3]$ (s)).

Wave Gauge	1	3	5	8
x-location (m)	10.55	12.8	14.8	17.55

Table 6.16: Wave gauge locations in the WEC test case. Note that wave gauge 5 is the focusing location.

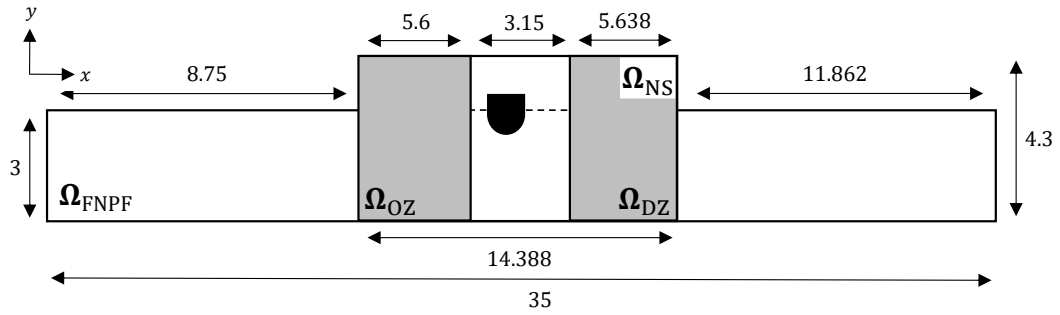

Figure 6.31: Schematic in the xy-plane of the IntegratedFoam numerical wave tank used in the wave energy converter (WEC) test case (not to scale). All dimensions are in metres.

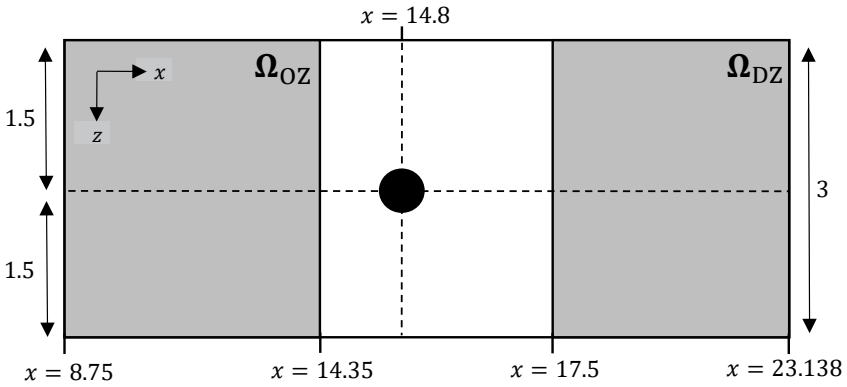

Figure 6.32: Schematic in the xz-plane of Ω_{NS} in the wave energy converter (WEC) test case (not to scale). All dimensions in metres.

Domain	Dimensions (m)
Ω_{FNPF}	$[0,\ 35] \times [-3,\ 0] \times [-7.75,\ 7.75]$
Ω_{NS}	$[8.75,\ 23.138] \times [-3,\ 1.3] \times [-1.4,\ 1.4]$
Ω_{OZ}	$[8.75,\ 14.35] \times [-3,\ 1.3] \times [-1.4,\ 1.4]$
Ω_{DZ}	$[17.5,\ 23.138] \times [-3,\ 1.3] \times [-1.4,\ 1.4]$

Table 6.17: Dimensions of each domain and zone in the WEC test case.

6.4.3 Computational setup for Ω_{FNPF}

Before running the case, a mesh sensitivity study in an empty wave tank is needed to find the optimal mesh configuration for both Ω_{FNPF} and Ω_{NS}. Considering Ω_{FNPF} first, a good starting point again would be trying a similar mesh configuration to the Ning et al. (2009) [111] cases in Section 5.2.6. In both of those cases, 20–30 cells per wavelength in the x-direction was sufficient for accurate solutions. In addition, 10 cells were used in the y-direction and were refined so that the cell at the top had vertical depth 1/10 of the cell at the bottom. The water depth in this

case is 6 times larger, so more cells are clearly needed in the y-direction. However, the steepness is only slightly larger than case NING1, so intial 2-D mesh configuration of $x \times y = 75 \times 15$ is chosen, constituting approximately 25 cells per wavelength. The mesh in the y-direction is again refined in the same way. This configuration is listed as configuration 'A' in Table 6.18 and is listed with two other configurations used in the sensitivity study.

Figure 6.33 then shows the time histories of free-surface elevation for meshes A, B, and C at the focusing location WG5, along with the experimental solution from CCP-WSI (2020) [15]. Meshes B and C reproduce the peak amplitude very well, but mesh A shows a slight discrepancy at the peak amplitude. All meshes also show a slight overestimation of the troughs either side of the peak amplitude. Nevertheless, good agreements are shown between the FNPFFoam solutions using meshes B and C and the experimental solution, hence mesh B—constituting approximately 32 cells per wavelength—is chosen. Figure 6.34 then shows the time histories of free-surface elevation for B at WGs 1, 3, 5, and 8, along with the experimental solution at each wave gauge. Overall, good agreements can be seen between each solution at every wave gauge. However, some discrepancies can be seen after about 49 s; this can most likely be down to slight reflection from Ω_{DZ} as predicted.

Domain	ID	Configuration $x \times y$	Cells per λ
Ω_{FNPF}	A	75×15	25
Ω_{FNPF}	B	100×15	32
Ω_{FNPF}	C	120×10	39

Table 6.18: Mesh configurations used in empty-tank Ω_{FNPF} mesh sensitivity studies in the wave energy converter (WEC) case.

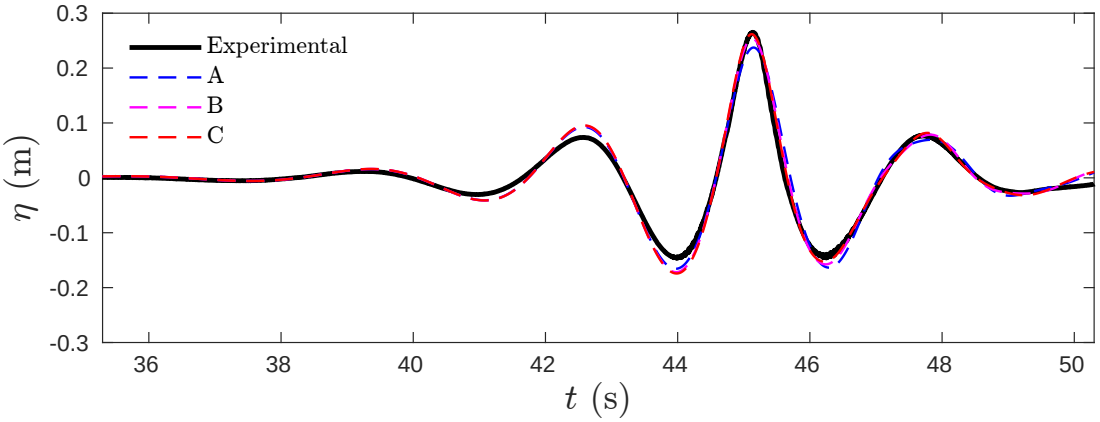

Figure 6.33: FNPFFoam time histories of free-surface elevation for meshes A, B, and C at wave gauge 5 (WG5), along with the experimental solution from CCP-WSI (2020) [15]: (a) $t \in [35,\ 55]$, (b) $t \in [40,\ 50]$.

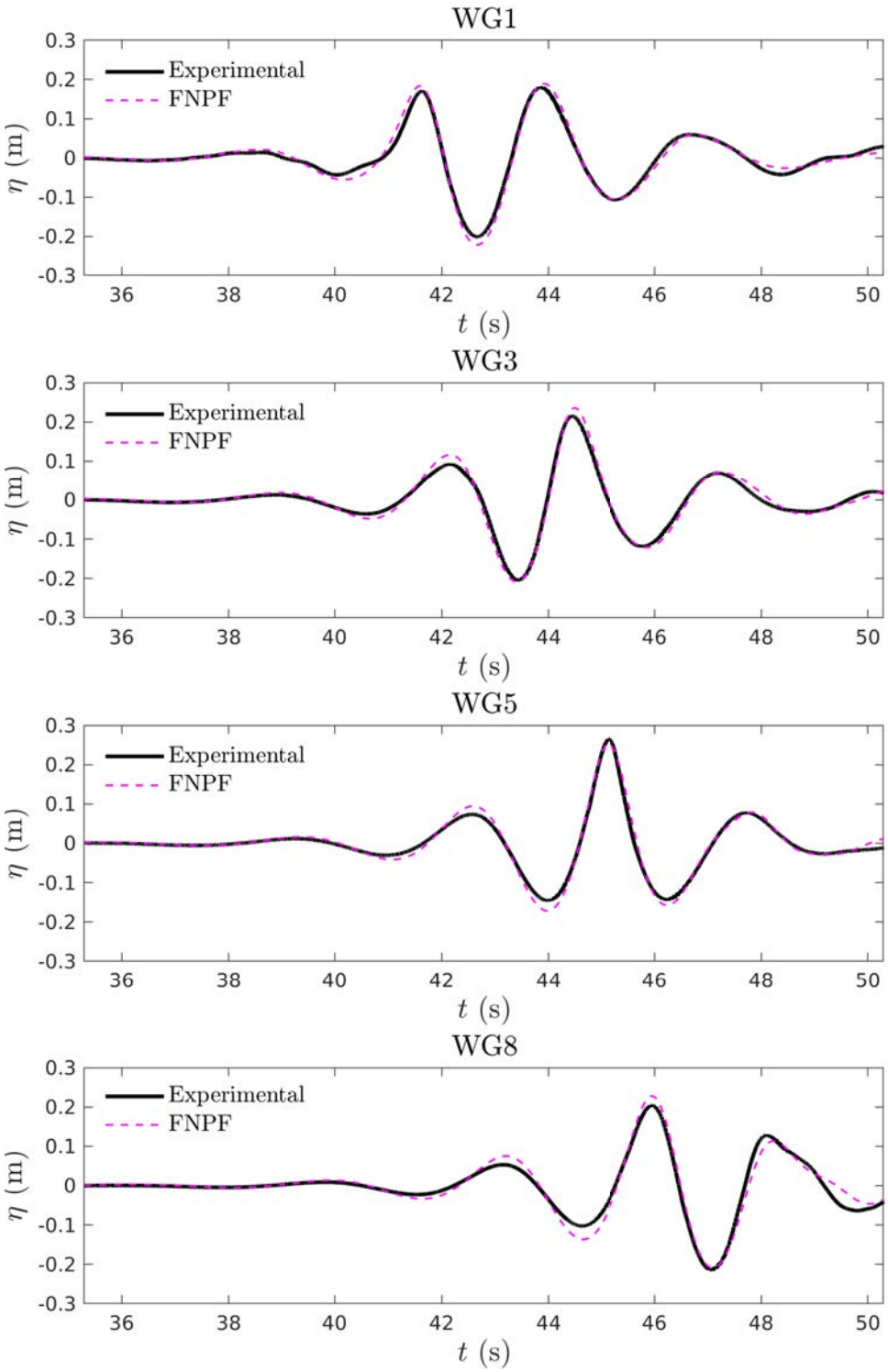

Figure 6.34: FNPFFoam time histories of free-surface elevation using mesh B at wave gauges (WGs) 1, 3, 5, and 8, along with the experimental solution from CCP-WSI (2020) [15].

6.4.4 Computational setup for Ω_{NS}

As in the cylinder test case, the computational setup for Ω_{NS} has to be determined slightly differently. A mesh sensitivity study can be done using IntegratedFoam without the WEC present and using the optimal setup for Ω_{FNPF} found previously, but the WEC also has to be meshed correctly and simultaneously fit into the background NWT mesh without any major issues. In particular, it needs to be refined enough so that the flow around and on the WEC can be calculated accurately whilst also not being too fine so as to excessively increase computational time. Indeed, it was seen in Section 6.2 that the dynamic mesh moving in interFoam takes up the majority of computational time in floating body examples; hence, the more refined the WEC mesh is, the more cells that will need moving, and the longer it will take. Therefore, as with the cylinder case, the mesh is constructed in three stages: an initial background hexahedral mesh is created, the WEC is then meshed from it, then the background mesh is refined as if the WEC were present through a mesh sensitivity study.

Starting with the initial background mesh, it is constructed to have the same dimensions as Ω_{NS} listed in Table 6.17 and has configuration $x \times y \times z = 210 \times 100 \times 76$. It is also refined so that, in the x-direction, 15% of cells are uniformly concentrated in the region $x \in [14.5,\ 15.1]$; in the y-direction, 50% of cells are uniformly concentrated in the region $y \in [-0.4,\ 0.4]$; and in the z-direction, 40% of cells are uniformly concentrated in the region $z \in [-0.4,\ 0.4]$. This is so that the mesh is fine enough in the region around the WEC and so that there is a smooth transition from the WEC mesh to background mesh. The remaining regions of the mesh are stretched in each direction for the same reason. This is illustrated in Figure 6.35 which shows the background mesh in the xy-plane (A) and the xz-plane (B). The concentration of cells in the region around the free surface and the WEC can clearly be seen. The *snappyHexMesh* utility

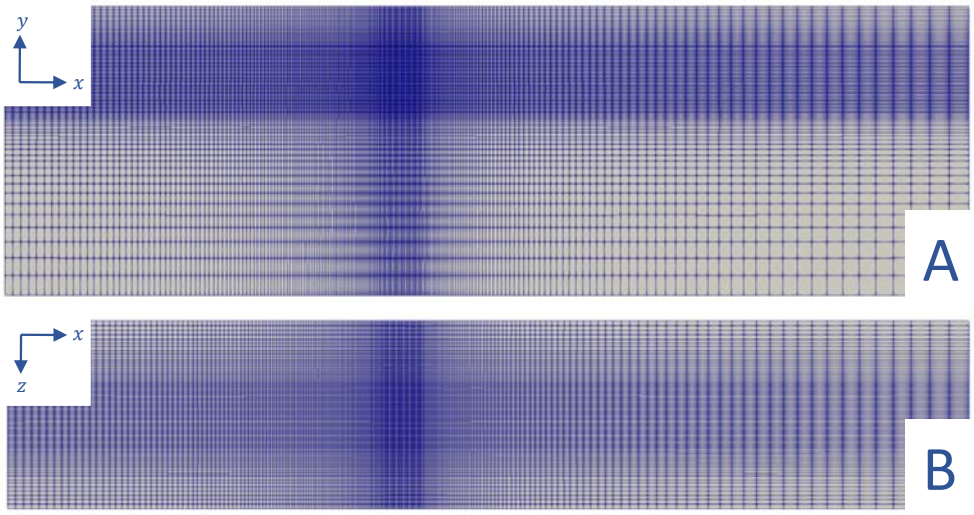

Figure 6.35: Initial background Ω_{NS} mesh in the xy-plane (A) and the xz-plane (B) in the wave energy converter (WEC) test case.

in OpenFOAM is then used to generate the WEC mesh from the initial background mesh: this is shown in Figure 6.36. There are 8606 faces in total that encompass the WEC surface. Figure 6.37 then shows a cross section (in the xy-plane) of the final constructed mesh in a small region around the WEC.

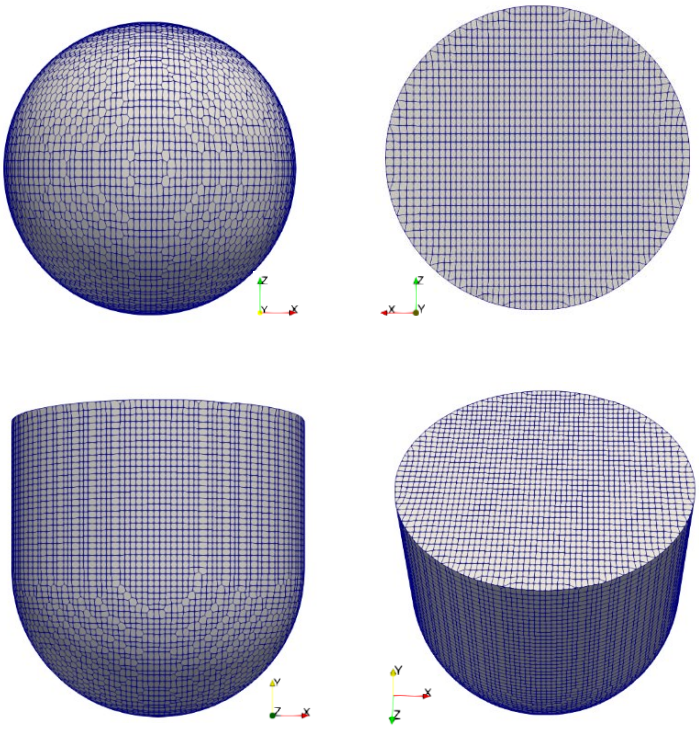

Figure 6.36: Wave energy converter (WEC) mesh.

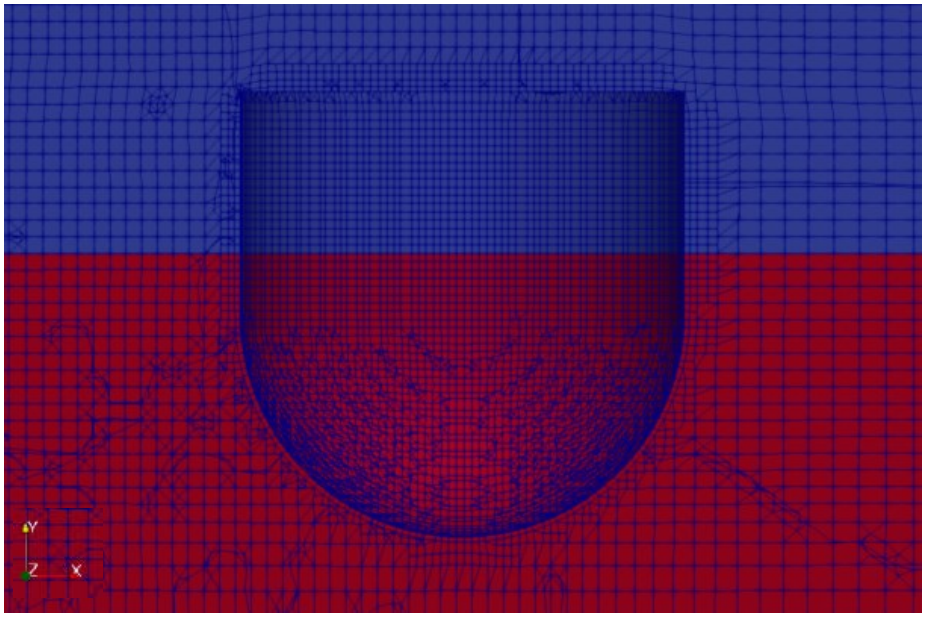

Figure 6.37: Cross section (in the xy-plane) of the final constructed mesh in a small region around the wave energy converter (WEC).

Now moving on to the mesh sensitivity study for Ω_{NS}, three different meshes—D–F in Table 6.10—are considered to test convergence in the x-direction. These constitute 100, 165, and 235 cells per wavelength. However, it should be remembered that the WEC mesh and the defined region surrounding it stays the same, so the increase/decrease in the number of mesh cells occurs in the two regions that do not include $x \in [14.5, 15.1]$. Figure 6.38 then shows the time histories of free-surface elevation for meshes D–F at WG5, along with the experimental solution of from CCP-WSI (2020) [15]. No discernible difference can be seen between each mesh, but a slight reduction in peak amplitude compared to the FNPFFoam solution in Figure 6.33 can be observed. Nevertheless, this indicates that mesh D can be used; however, this was actually found to cause problems with mesh distortion when used in the full test case. This is because the max distance the mesh can morph has to be set manually, and if the mesh density is not fine enough up to that max distance, severe distortion can occur. This is a classic problem with the interFoam solver: it is known to be sensitive to the size of deformations, particularly if the mesh quality is not good enough. Given this, mesh E is actually chosen. It should be noted that a mesh density between D and E may also provide stable and accurate solutions in this case but was not tested. This could be tried in future work. As an aside, the results here are impressive: it is clear that the IntegratedFoam can accurately reproduce this focused wave in Ω_{NS}, demonstrating that the coupling is accurate.

Domain	ID	Configuration $x \times y$	Cells per λ
Ω_{NS}	D	120×100	100
Ω_{NS}	E	210×100	165
Ω_{NS}	F	300×100	235

Table 6.19: Mesh configurations used in empty-tank Ω_{NS} mesh sensitivity studies in the wave energy converter (WEC) case.

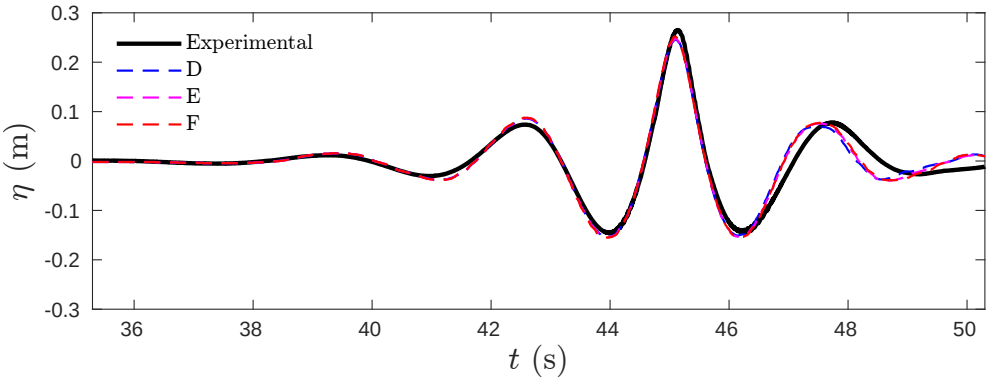

Figure 6.38: IntegratedFoam time histories of free-surface elevation for meshes D, E, and F at wave gauge 5 (WG5), along with the experimental solution from CCP-WSI (2020) [15]: (a) $t \in [35, 55]$, (b) $t \in [40, 50]$.

6.4.5 Setup of remaining computational parameters

Following the analysis in Chapter 5, $C_{\max}$ is again set at 0.2. Moreover, given the the 2-D floating body test case in Section 6.2, it is expected that interFoam will take up the majority of the computational time due to the moving mesh. Consequently, given all these factors, only 9 out of 32 processors are assigned to the coupling in the following simulation. Another parameter that is important in this case is the previously mentioned max mesh morphing distance. This has to be set correctly otherwise there could be severe mesh distortion that will cause the simulation to crash. Therefore, given that the the experimental WEC solutions are known from CCP-WSI (2020) [15], a max distance of 1 metre is selected.

6.4.6 Numerical results

6.4.6.1 Initial attempt

Figure 6.39 shows the IntegratedFoam time histories of surge displacement, heave displacement, pitch angle, and mooring force magnitude of the WEC, along with the experimental solution from CCP-WSI (2020) [15]. The first thing to note here is that the simulation actually crashes at approximately 48.95 s—close to the final time. The cause of the crash is severe mesh distortion around the WEC, but it is initially unclear what causes the distortion. The actual numerical results themselves are mixed. Figure 6.39(a) shows the surge displacement which is clearly significantly overestimated. The pitch angle (Figure 6.39(c)) is accurate in parts but does not decrease in amplitude as expected which may be down to the lack of viscous forces damping the oscillations (the simulation is laminar). In fact, the WEC actually starts oscillating at approximately 8 s, with the amplitude of oscillation steadily increasing throughout until the focusing time. It was shown in Section 6.2 that the pitch angle is hard to calculate correctly using interFoam so the inaccuracy in pitch can maybe be explained, but the reason for overestimation of surge is unclear. Nevertheless, these results may indicate a reason for the severe mesh distortion that causes the simulation to crash. However, the crash does not happen at the maximum point of surge, so it perhaps does not make sense for this to be reason. Moreover, the surge and pitch results are then directly contradicted by the heave displacement and mooring force magnitude, shown in Figures 6.39(b) and 6.39(d) respectively. These results are actually remarkably accurate. Furthermore, the wave solution at WG5 (shown in Figure 6.40) also does not show any major discrepancies that should cause a crash.

The cause was eventually found to be the yaw rotation and sway translation of the WEC. Recall that the WEC is able to move in all six degrees of freedom, so even though the input wave is 2D, it is still possible that 3-D motions may occur. Figure 6.41(b) shows the yaw rotation of the WEC which can clearly be seen to increase exponentially after approximately 25 s to a maximum of 6 degrees. In addition Figure 6.41(a) shows the sway displacement of the WEC which again increases sharply after the focusing time. This is clearly what caused the excessive mesh distortion. However, the cause of these motions is unclear; small yaw rotations

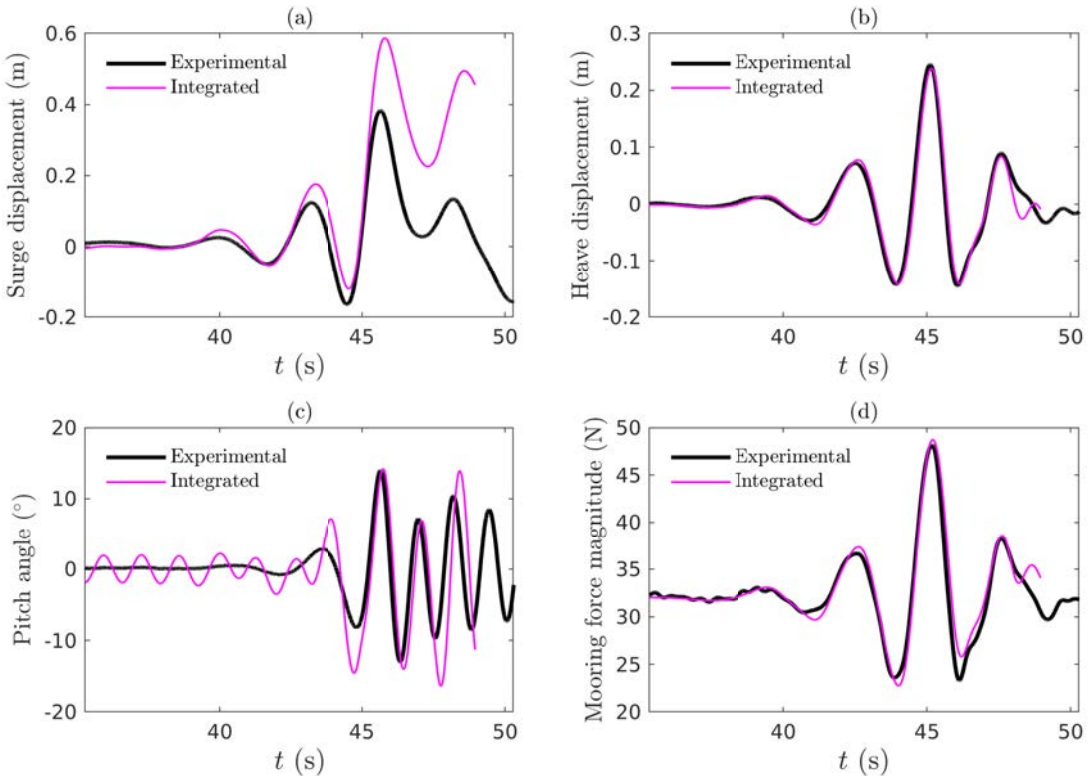

Figure 6.39: IntegratedFoam time histories of surge displacement (a), heave displacement (b), pitch angle (c), and mooring force magnitude (d) of the WEC, along with the experimental solution from CCP-WSI (2020) [15]. Initial attempt.

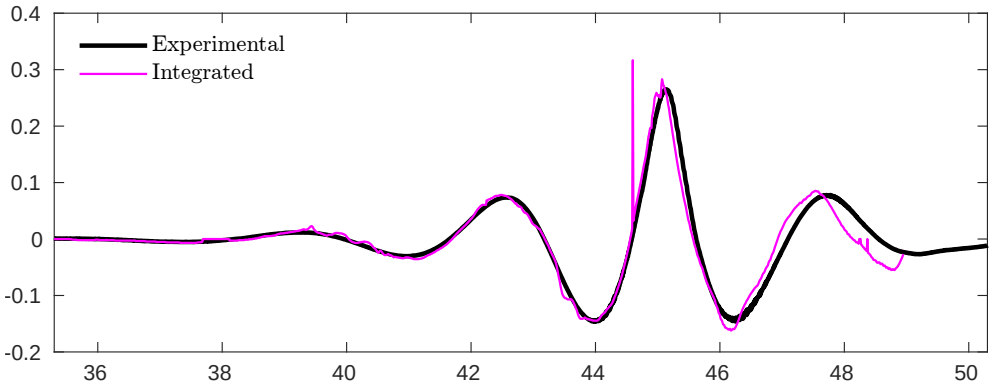

Figure 6.40: Time histories of free-surface elevation and the experimental solution from CCP-WSI (2020) [15] at wave gauge 5 (WG5).

and sway displacements may be expected given the complex flow around the WEC, but the exponential increase shown is most definitely unphysical. One possibility is reflection from the front and back walls, and maybe even Ω_{OZ} and Ω_{DZ}, that comes about due to the oscillations of the WEC that can be seen in Figure 6.39(c). However, an investigation was then done by bringing the focusing time forward to 12.13 s rather than 45.13—before any significant oscillations occurred—but the results were similar. The cause of the oscillations is also still unclear, but it is most likely down to a meshing problem, i.e. the mechanical characteristics

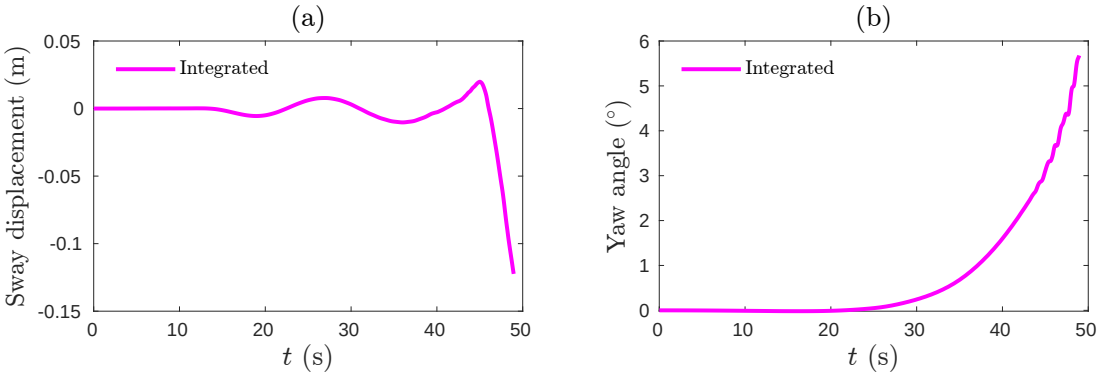

Figure 6.41: IntegratedFoam time histories of sway displacement (a) and yaw angle (b) of the WEC in the initial attempt.

of the WEC may not be exact with regards to the spatial discretisation, leading to unstable initial conditions. Indeed, the velocity at the start of the simulation seems to be unstable with the WEC moving from the start. This could potentially be solved by refining the mesh on and around the WEC, but would significantly increase the computational time. Meshing issues also most likely explain the overestimated surge displacement. Indeed, surge motion is caused by the rapid acceleration and deceleration of the WEC due the hydrodynamic load imposed by the focused wave as it passes. A poor mesh on-and-around the WEC will lead to an inaccurate pressure solution on its boundary and consequently inaccurately predict the correct acceleration of the WEC.

6.4.6.2 Refined attempt

Given that the unphysical yaw rotation and sway translation was found to be the cause of the crash, the WEC was then constrained to translation only in the xy-plane and rotation only in pitch. Moreover the max mesh morphing distance is increased slightly to 1.1 m. Figure 6.42 then shows the IntegratedFoam time histories of surge displacement, heave displacement, pitch angle, and mooring force magnitude of the WEC, along with the experimental solution from CCP-WSI (2020) [15]. This time the simulation does not crash and reached the final time of 50.3 s. Moreover, the surge displacement (Figure 6.42(a)) does not show as significant overestimation as before and even decays with a similar pattern to the experimental results. In fact, the surge results are actually similar to other OpenFOAM results from CCP-WSI blind tests in Ransley et al. (2021) [117] and Ransley et al. (2020) [118]. The pitch angle (Figure 6.42(c)) again shows significant oscillations that lead to the rotation being out of step with the experimental results. However, the amplitude of pitch is much more similar to the experimental than the previous attempt. The heave displacement and mooring force magnitude, shown in Figures 6.42(b) and 6.42(d) respectively are again accurate; although, the max displacement and max mooring force magnitude are slightly underestimated. For the mooring, this is perhaps expected given the motion has been constrained so the force component in the z-direction is zero.

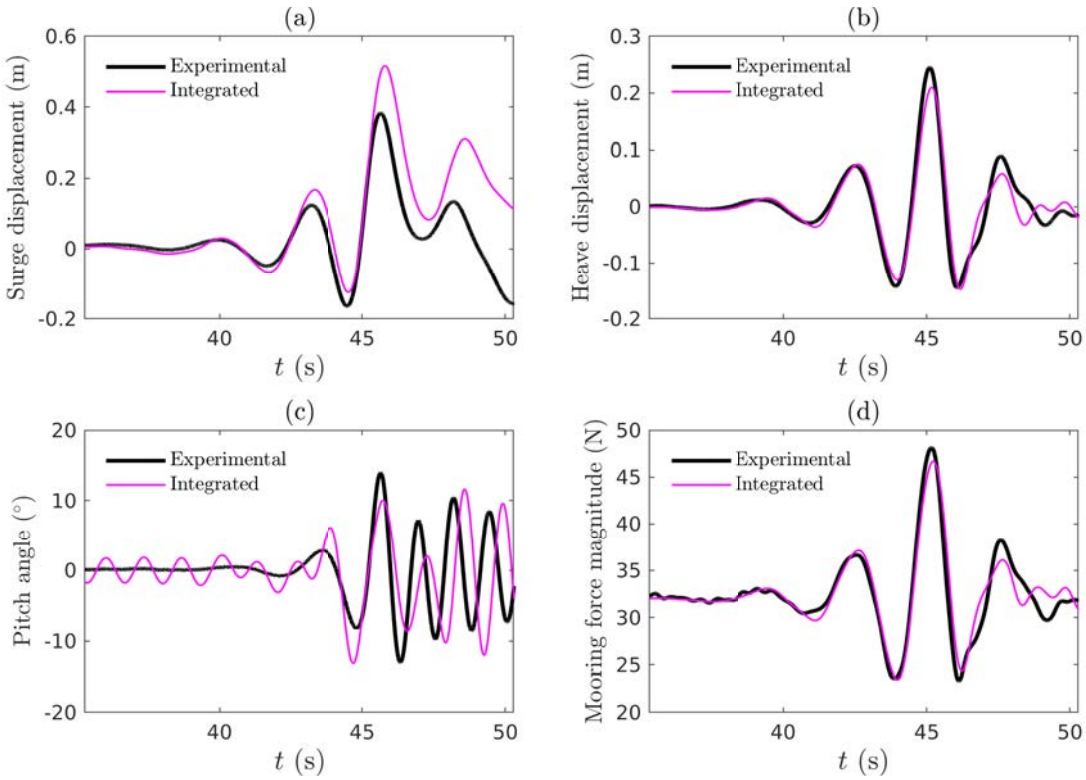

Figure 6.42: IntegratedFoam time histories of surge displacement (a), heave displacement (b), pitch angle (c), and mooring force magnitude (d) of the WEC, along with the experimental solution from CCP-WSI (2020) [15]. Refined attempt.

6.4.6.3 Analysis of computational time

Table 6.20 lists the time taken by each part of the IntegratedFoam solver. As hypothesised in Chapter 5 and in Section 6.2, the time saved by using the IntegratedFoam solver in this 3-D example is starkest of all test cases in this work. Indeed, interFoam takes approximately 85% of total computational time, whereas the coupling only takes 10%. As a result, it can safely be assumed that, if interFoam were used for the entire test case to the same scale, it would take considerably longer. Hence, in this sense IntegratedFoam has achieved a marked increase in computational efficiency.

	Coupling	interFoam	FNPFFoam	Total
Computational time (s)	25,960	212,532	12,259	250,751

Table 6.20: Time taken by different parts of the solver in the wave energy converter (WEC) test case.

6.4.6.4 Concluding remarks

It is clear from this test case that the IntegratedFoam coupling is accurate. Indeed, the wave solution was shown to be accurate through the mesh sensitivity studies and the WG5 results with the WEC actually present. Moreover, it was shown to substantially improve computational efficiency. Nevertheless, there were evidently also problems, but those problems were undoubtedly due to the computational setup of the interFoam solver and not the coupling itself. For example, the mesh distortion that caused the crash in the initial attempt is an inherent disadvantage of using mesh morphing solvers like interFoam for cases like this. An alternative option would be to couple the FNPF solver with the overset solver 'overInterDyMFoam' in OpenFOAM. Using an overset mesh has the major advantage over the standard dynamic mesh in that it allows for much larger linear and angular displacement. This greater flexibility in motion means it would be more applicable to complex wave-structure interaction problems like this WEC case, as Lin et al. (2021) [88] demonstrated for this specific case. Therefore, the logical next step for future work would be to create a separate *overset* version of IntegratedFoam: there is no coding or computing reason why this would not be possible. Regardless, the interFoam solver, whether by itself or as a constituent part of an integrated model, has been shown to produce good results for this example, i.e., Wang (2020) [136] and Brown (2021) [13]. This means that it should be possible for the IntegratedFoam model to do so as well, it is only a matter of having the correct computational setup and refining the motion solver parameters correctly. For example, as hypothesised previously, the mesh could be refined better so that the initial conditions are not unstable. Moreover, the max mesh morphing distance can be increased so that the distortion is not as prominent. However, this would invariably also increase computational time so that would have to be factored in.

7

Conclusion

7.1 Summary of research outcomes

7.1.1 Development and validation of a new finite volume–finite volume integrated hydrodynamic model

In the present work, a new integrated hydrodynamic modelling framework for large-scale and long-time wave-structure interaction problems is developed by coupling the finite-volume-based fully-nonlinear potential-flow (FNPF) solver by Lin et al. (2021) [90] with the native OpenFOAM incompressible 'interFoam' solver in a numerical wave tank (NWT). This new model, named IntegratedFoam, has the primary advantage that each constituent solver has been developed in the same numerical framework (OpenFOAM), and consequently, are both also based on the same numerical method, i.e., the finite-volume method (FVM). Moreover, given that OpenFOAM is open source, the major benefit of IntegratedFoam is that it can readily be used by researchers as a more efficient model for complex wave-structure interaction problems than the native incompressible solver 'interFoam'. The coupling procedure follows a domain decomposition approach in which an overlapping relaxation zone is utilised to implement a one-way coupling. The method for transferring information is simple, and the coupling accurate. Indeed, given that both solvers have been developed in OpenFOAM and are finite-volume-based, only a method to calculate the volume fraction from the free-surface elevation has to be implemented: the velocity and pressure are already calculated as part of the FNPF solution and can be transferred accordingly—simplifying things greatly and avoiding unwanted errors. In addition, existing advanced OpenFOAM functionalities make the required interpolation easy, handily solving the problem of non-conforming meshes. The relaxation zone then also ensures the coupling process is stable and accurate through a smooth transition from the FNPF solution to the N-S solution, as well as by absorbing any reflected waves.

The new IntegratedFoam model is first validated through a series of 2-D fifth-order Stokes wave propagation test cases. In particular, the sensitivity of IntegratedFoam to its main coupling parameters—namely, length of the overlapping relaxation zone Ω_{OZ} and the max Courant number $C_{\max}$—is tested. Associated sensitivity to length of the damping zone Ω_{DZ} and mesh density is also tested. Two specific cases are considered: long ($\Omega_{\mathrm{NS}} > 6$ wavelengths) and short ($\Omega_{\mathrm{FNPF}} < 2.5$ wavelengths), with the short being more representative of what is expected in wave-structure interaction test cases.

1. It is found in the long case that the waves are successfully transferred from Ω_{FNPF} and accurately reproduced in Ω_{NS} for each length of Ω_{OZ} ($1/2\lambda$, λ, and 2λ). Analysis of computational time indicates that the coupling for 2-D test cases takes the majority of time. However, it is noted that for solely wave propagation, IntegratedFoam would never be used as the FNPFFoam solver is much more efficient. Short case results show that the long-term behaviour of the wave solution in Ω_{NS} is very accurate for each length of Ω_{OZ}. An analysis of computational time indicates the same pattern as in the long case.

2. It is also found found in the long case that increasing the length Ω_{DZ} results in less reflection and better accuracy. However, the extent to which this is the case is not discernible. At most it is concluded that a length $\Omega_{\mathrm{DZ}} = 1/2\lambda$ should not be used if it can be avoided. No major differences in computational time are seen. The short case indicates the same for both accuracy and time.

3. Long case results show that, in general, a smaller value of $C_{\max}$ leads to a more accurate solution, particularly over a larger scale. However, the difference between the solutions for $C_{\max} = 0.05$, 0.1, and 0.2 is small—$C_{\max} = 0.4$ is the main outlier. The results also show a linear relationship between the number of time steps and computational time. Short case results show counter-intuitive behaviour in that $C_{\max} = 0.05$ shows the greatest error. This is hypothesised to be due to a combination of factors; namely, the major increase in the number of time steps leading to more opportunities for the dissipation to occur, the implicit Euler method is only first order, and the effects of reflection from Ω_{OZ} and Ω_{DZ}.

4. Mesh sensitivity results recommend 120 cells per wavelength in the x-direction to ensure sufficient solution accuracy over a large scale and for long time. Computational times indicate that the coupling and interFoam times are both exponentially increasing as the number of cells increases, but the coupling time increases faster.

The primary purpose of developing such an integrated model is to significantly improve the computational efficiency of high-fidelity open-source models, such as interFoam, when used to model wave interaction with offshore renewable structures, e.g., fixed monopile foundations, wave energy converter devices, or floating offshore wind turbines. This is all whilst retaining solution accuracy and the ability to calculate things such as hydrodynamic loads or six degree of freedom motions. To see whether this is the case for the new IntegratedFoam model, it is validated through three wave-structure interaction test cases.

1. The first is fifth-order Stokes waves interaction with a 2-D T-shaped floating body—a simplified midship section with a superstructure. It is found that the new IntegratedFoam model accurately predicts the heave motion of the structure, but the roll rotation is generally underestimated. However, using solely the interFoam solver produces similar results, but takes almost 3 times longer. Therefore, it is proven through this simple 2-D wave-structure interaction test case that IntegratedFoam can produce similar results to interFoam but can do it much faster.

2. The second is focused wave interaction with a fixed 3-D cylinder—a simplified monopile foundation. It is found that the new IntegratedFoam model accurately predicts the free-surface elevation after interaction with the cylinder; moreover, it is also more than capable of accurately capturing the hydrodynamic load on the cylinder. This is the case for two input focused waves, the second much steeper than the first. In both cases an improvement in efficiency is observed, with the steeper case—in which wave breaking on the cylinder is significant—showing a more substantial improvement.

3. The third case is focused wave interaction with a 3-D wave energy converter (WEC) device. It is found that the heave displacement and mooring force magnitude in particular show very good agreements with the experimental results. However, the pitch rotation experiences unphysical oscillations that affect the stability of the dynamic mesh solver in interFoam. As a result, the surge motion is also overestimated. Regardless, the computational efficiency is significantly increased; the interFoam part of the model takes approximately 85% of computational time, hence if interFoam were used for the entire test case at the same scale, the time taken would be many magnitudes higher.

7.1.2 Introduction of a new stabilisation technique for FNPF models

In conjunction with the primary objective of developing a new integrated hydrodynamic model, a new stabilisation method for finite-volume or finite-difference FNPF models has also been developed. The purpose for this is to avoid using cumbersome low-order damping techniques, such as the fourth-order damping correction scheme in the original Lin et al. (2021) [90] model, that can potentially cause superfluous dissipation and energy loss in the numerical wave tank (NWT). Analysing the characteristics of the nonlinear boundary condition equations shows that the kinematic boundary condition (KBC) equation is advection dominated, meaning that a second-order scheme motivated by a TVD approach is developed.

It is found that the new method eliminates the sawtooth instability in every instance for which it occurs in the original Lin et al. (2021) [90] model. Furthermore, it is demonstrated through a variety of validation test cases that the stabilised model is accurate, with good agreements shown with existing numerical, experimental, and analytical results. In particular, it tested through fifth-order Stokes wave propagation and focused wave propagation. The fifth-order Stokes cases also test the model for mesh sensitivity, temporal sensitivity, and choice of flux limiter function. A density of 50 cells per wavelength is consequently recommended as well as a value of $C_{\max} = 0.2$ which gives the best balance between accuracy and efficiency. The flux limiter comparison justifies the use of the Van Albada 2 (VA2) limiter. Wave shoaling tests cases are also considered to test the ability of the model to capture the transformation of propagating wave due to variable bathymetry: results for this are also accurate. An evaluation of the new model's performance in terms of energy conservation is also given; indeed, it is shown that the stabilised model is much better suited to large-scale and long-time simulations than the Lin et al. (2021) [90] model—vindicating the desire to be free from using numerical damping as a stabilisation technique. Overall, these results improve the suitability of the FNPF model to be the constituent FNPF solver in an integrated model.

7.2 Recommendations for future work

The advantages on the new IntegratedFoam model, its applicability to offshore renewable wave-structure interaction problems, and its consequent improvement to efficiency has been demonstrated. Therefore, the objectives of this work have achieved. However, some limitations are apparent and improvements can be made.

1. **Improve the efficiency of the coupling**

   As seen in the dynamic mesh test cases of Sections 6.2 and 6.4, the interFoam part of IntegratedFoam far exceeds the coupling and FNPF computational times. However, for static mesh cases like the fixed cylinder case in Section 6.3, the coupling time as a proportion of the total time is much higher. This can clearly be improved. The reason is largely due to the inefficiency of the algorithm for finding host/donor mesh cells during the domain connectivity information (DCI) stage of the coupling. The current algorithm has to search every mesh cell in Ω_{FNPF} for every cell in Ω_{OZ} in order to find the correct donor cells. This is clearly not efficient (although, it is still much faster than the OpenFOAM `findCell` function that performs the same task). Implementation of a more efficient algorithm would be beneficial and markedly improve efficiency for static mesh cases.

2. **Improve the damping technique in $\Omega_{\mathbf{DZ}}$**

   The damping technique currently utilised in Ω_{DZ} is very crude as it forces (through relaxation) the value of the velocity $\mathbf{u}$ and water-volume fraction α to zero whilst forcing the pressure p to the atmospheric pressure value. This has been shown in this and other works to not be the most effective way of avoiding reflection. Other techniques, such as a active wave absorption, may decrease the reflection from Ω_{DZ}, which then has the further advantage of reducing the overall size of Ω_{NS} and increasing efficiency.

3. **Improve the handling of mesh deformations**

   As seen in the WEC test case in Section 6, mesh distortion is an inherent disadvantage of using mesh morphing solvers like interFoam. For it to work correctly, the computational setup has to be near perfect and the motion solver parameters have to be set correctly. Failure to do so can lead to unstable initial conditions and unpyhsical motion. An alternative option would be to couple the FNPF solver with the overset solver 'overInterDyMFoam' in OpenFOAM. Using an overset mesh has the major advantage over the standard dynamic mesh in that it allows for much larger linear and angular displacement. This greater flexibility in motion means it would be more applicable to complex wave-structure interaction problems like this WEC case, as Lin et al. (2021) [88] demonstrated for this specific case. Therefore, the logical next step for future work would be to create a separate *overset* version of IntegratedFoam: there is no coding or computing reason why this would not be possible. Nevertheless, the correct computational setup and parameter setup for the mesh morphing version of interFoam can still be found for the WEC case.

Hence, this should be done first.

4. **Improve the method for parallel decomposition**

   For every test case in this work, the parallel decomposition is implemented through intuition and/or trial and error. The number of processors assigned to the coupling is of particular importance. For example, for the first cylinder test case in Section 6.3, the number of processors assigned to the coupling was inexact and the load balance across all processors was not as efficient as it could be. This then led to the coupling taking longer than expected. However, an alternative decomposition in which the load balance across processors assigned to the coupling was more even then led to the interFoam time, and time overall, being larger. Improving the overall efficiency of the coupling will make this issue less important, but a more methodical procedure for parallel decomposition should still be considered.

5. **Apply IntegratedFoam to other offshore renewable applications**

   If all the prior improvements can be achieved, the IntegratedFoam model should then be able to accurately and efficiently model much more complex wave-structure interactions with offshore renewable structures. For example, one of the key forms of renewable energy technology mentioned in the introduction was floating offshore wind. Lin et al. (2021) [89] applied the overset interFoam solver to evaluate the dynamic response of floating offshore wind turbines (FOWTs) under the action of regular and focused waves. If the IntegratedFoam model can be extended with the overset version of interFoam, this FOWT test case should be the next step.

Bibliography

[1] W. Bai and R. Eatock-Taylor. "Fully nonlinear simulation of wave interaction with fixed and floating flared structures". In: *Ocean engineering* 36.3-4 (2009), pp. 223–236. DOI: 10.1016/J.OCEANENG.2008.11.003.

[2] W. Bai and R. Eatock-Taylor. "Numerical simulation of fully nonlinear regular and focused wave diffraction around a vertical cylinder using domain decomposition". In: *Applied Ocean Research* 29.1-2 (2007), pp. 55–71. DOI: 10.1016/J.APOR.2007.05.005.

[3] S. Beji and J.A. Battjes. "Experimental investigation of wave propagation over a bar". In: *Coastal Engineering* 19.1-2 (1993), pp. 151–162. DOI: 10.1016/0378-3839(93)90022-Z.

[4] S. Beji and J.A. Battjes. "Numerical simulation of nonlinear wave propagation over a bar". In: *Coastal Engineering* 23.1-2 (1994), pp. 1–16. DOI: 10.1016/0378-3839(94)90012-4.

[5] E. Berberović, N.P. van Hinsberg, S. Jakirlić, I.V. Roisman, and C. Tropea. "Drop impact onto a liquid layer of finite thickness: Dynamics of the cavity evolution". In: *Physical Review E* 79.3 (2009), p. 036306. DOI: 10.1103/PHYSREVE.79.036306.

[6] H. Bihs, M.A. Chella, A. Kamath, and Ø.A. Arntsen. "Numerical investigation of focused waves and their interaction with a vertical cylinder using REEF3D". In: *Journal of Offshore Mechanics and Arctic Engineering* 139.4 (2017). DOI: 10.1115/1.4036206.

[7] H. Bihs, A. Kamath, M.A. Chella, A. Aggarwal, and Ø.A. Arntsen. "A New Level Set Numerical Wave Tank with Improved Density Interpolation for Complex Wave Hydrodynamics". In: *Computers & Fluids* 140 (2016), pp. 191–208. DOI: 10.1016/J.COMPFLUID.2016.09.012.

[8] H. Bihs, W. Wang, C. Pákozdi, and A. Kamath. "REEF3D::FNPF - A Flexible Fully Nonlinear Potential Flow Solver". In: *Journal of Offshore Mechanics and Arctic Engineering* 142 (Jan. 2020), pp. 1–12. DOI: 10.1115/1.4045915.

[9] H.B. Bingham and H. Zhang. "On the accuracy of finite-difference solutions for nonlinear water waves". In: *Journal of Engineering Mathematics* 58.1 (2007), pp. 211–228. DOI: 10.1007/S10665-006-9108-4.

[10] A. Brandt. "Multi-level adaptive solutions to boundary-value problems". In: *Mathematics of computation* 31.138 (1977), pp. 333–390. DOI: 10.1090/S0025-5718-1977-0431719-X.

[11] Carbon Brief. *Analysis: UK renewables still cheaper than gas, despite auction setback for offshore wind*. 2023. URL: https://www.carbonbrief.org/analysis-uk-renewables-still-cheaper-than-gas-despite-auction-setback-for-offshore-wind/ (visited on 09/26/2023).

[12] Britannica. *Three Gorges Dam*. 2023. URL: https://www.britannica.com/topic/Three-Gorges-Dam (visited on 09/25/2023).

[13] S.A. Brown, E.J. Ransley, and D.M. Greaves. "Assessing focused wave impacts on floating wave energy converters using OpenFOAM". In: *Proceedings of the Institution of Civil Engineers-Engineering and Computational Mechanics* 174.1 (2021), pp. 4–18. DOI: 10.1680/JENCM.19.00036.

[14] Eugeny Buldakov, Pablo Higuera, and Dimitris Stagonas. "Numerical models for evolution of extreme wave groups". In: *Applied Ocean Research* 89 (2019), pp. 128–140. DOI: 10.1016/j.apor.2019.05.013.

[15] CCP-WSI. *Focused wave interactions with floating structures (CCP-WSI Blind Test Series 2)*. 2020. URL: https://www.ccp-wsi.ac.uk/data_repository/test_cases/test_case_004.

[16] S. Chakrabarti. *Handbook of Offshore Engineering (2-volume set)*. Elsevier, 2005.

[17] H. Chen, L. Qian, Z. Ma, W. Bai, Y. Li, D. Causon, and C. Mingham. "Application of an overset mesh based numerical wave tank for modelling realistic free-surface hydrodynamic problems". In: *Ocean Engineering* 176 (2019), pp. 97–117. DOI: 10.1016/J.OCEANENG.2019.02.001.

[18] L.F. Chen, J. Zang, A.J. Hillis, G.C.J. Morgan, and A.R. Plummer. "Numerical investigation of wave-structure interaction using OpenFOAM". In: *Ocean Engineering* 88 (2014), pp. 91–109. DOI: 10.1016/J.OCEANENG.2014.06.003.

[19] D. Clamond and J. Grue. "A fast method for fully nonlinear water-wave computations". In: *Journal of Fluid Mechanics* 447 (2001), pp. 337–355. DOI: 10.1017/S0022112001006000.

[20] Intergovernmental Panel on Climate Change. *Urgent climate action can secure a liveable future for all*. 2023. URL: https://www.ipcc.ch/2023/03/20/press-release-ar6-synthesis-report/.

[21] D. Coles, A. Angeloudis, D. Greaves, G. Hastie, M. Lewis, L. Mackie, J. McNaughton, J. Miles, S. Neill, M. Piggott, D. Risch, B.E. Scott, C.E Sparling, T Stallard, P.R. Thies, S. Walker, D. White, R.H.J. Willden, and B.J. Williamson. "A review of the UK and British Channel Islands practical tidal stream energy resource". In: *Proceedings of the Royal Society A* 477.2255 (2021), p. 20210469. DOI: 10.1098/rspa.2021.0469.

[22] G. Colicchio, M. Greco, and O.M. Faltinsen. "A BEM-level set domain-decomposition strategy for non-linear and fragmented interfacial flows". In: *International journal for numerical methods in engineering* 67.10 (2006), pp. 1385–1419. DOI: 10.1002/nme.1680.

[23] Global Wind Energy Council. *Global Offshore Wind Report 2020*. 2020. URL: https://gwec.net/global-offshore-wind-report-2020/.

[24] Global Wind Energy Council. *Global Wind Report 2019*. 2020. URL: https://gwec.net/global-wind-report-2019/.

[25] Global Wind Energy Council. *Global Wind Report 2023*. 2023. URL: https://gwec.net/global-wind-report-2023/.

[26] S.M. Damián. "An Extended Mixture Model for the Simultaneous Treatment of Short and Long Scale Interfaces". PhD thesis. Universidad Nacional del Litoral, 2013.

[27] .B. Di Paolo, J.L. Lara, G. Barajas, and Í.J. Losada. "Wave and structure interaction using multi-domain couplings for Navier-Stokes solvers in OpenFOAM®. Part I: Implementation and validation". In: *Coastal Engineering* 164 (2021), p. 103799. DOI: 10.1016/j.coastaleng.2020.103799.

[28] F. Dias and T.J. Bridges. "The numerical computation of freely propagating time-dependent irrotational water waves". In: *Fluid Dynamics Research* 38.12 (2006), pp. 803–830. DOI: 10.1016/j.fluiddyn.2005.08.007.

[29] J.W. Dold. "An efficient surface-integral algorithm applied to unsteady gravity waves". In: *Journal of Computational Physics* 103.1 (1992), pp. 90–115. DOI: 10.1016/0021-9991(92)90327-U.

[30] J.W. Dold and D.H. Peregrine. "An Efficient Boundary Integral Method for Steep Unsteady Water Waves". In: *Numerical Methods for Fluid Dynamics II*. Oxford University Press, 1986, pp. 671–679.

[31] D.G. Dommermuth and D.K.P. Yue. "A high-order spectral method for the study of nonlinear gravity waves". In: *Journal of Fluid Mechanics* 184 (1987), pp. 267–288. DOI: 10.1017/S002211208700288X.

[32] Guohai Dong, Xiang Gao, Xiaozhou Ma, and Yuxiang Ma. "Energy properties of regular water waves over horizontal bottom with increasing nonlinearity". In: *Ocean Engineering* 218 (2020), p. 108159. DOI: 10.1016/j.oceaneng.2020.108159.

[33] G. Ducrozet, F. Bonnefoy, D. Le Touzé, and P. Ferrant. "HOS-ocean: Open-source solver for nonlinear waves in open ocean based on High-Order Spectral method". In: *Computer Physics Communications* 203 (2016), pp. 245–254. DOI: 10.1016/j.cpc.2016.02.017.

[34] Ember. *Global Electricity Review 2023*. 2023. URL: https://ember-climate.org/insights/research/global-electricity-review-2023/.

[35] Simec Atlantic energy. *MEYGEN*. 2023. URL: https://saerenewables.com/tidal-stream/meygen/ (visited on 09/25/2023).

[36] Department for Energy Security and Net Zero. *UK Energy In Brief 2023*. 2023. URL: https://www.gov.uk/government/statistics/uk-energy-in-brief-2023.

[37] A.P. Engsig-Karup, H.B. Bingham, and O. Lindberg. "An efficient flexible-order model for 3D nonlinear water waves". In: *Journal of Computational Physics* 228.6 (2009), pp. 2100–2118. DOI: 10.1016/J.JCP.2008.11.028.

[38] A.P. Engsig-Karup, C. Eskilsson, and D. Bigoni. "A stabilised nodal spectral element method for fully nonlinear water waves". In: *Journal of Computational Physics* 318 (Apr. 2016), pp. 1–21. DOI: 10.1016/j.jcp.2016.04.060.

[39] Allan P Engsig-Karup, Carlos Monteserin, and Claes Eskilsson. "A Mixed Eulerian-Lagrangian Spectral Element Method for Nonlinear Wave Interaction with Fixed Structures". In: *Water Waves* 1.2 (2019), pp. 315–342. DOI: 10.1007/s42286-019-00018-5.

[40] Equinor. *Equinor marks 5 years of operations at world's first floating wind farm*. 2022. URL: https://www.equinor.com/news/hywind-5-years-world-first-floating-wind-farm (visited on 09/26/2023).

[41] Equinor. *Equinor plans to launch GW-size floating wind concept in Scotland*. 2021. URL: https://www.equinor.com/news/archive/20211101-gw-size-floating-wind-concept-scotland (visited on 09/26/2023).

[42] J.D. Fenton. "A Fifth-Order Stokes Theory for Steady Waves". In: *Journal of waterway, port, coastal, and ocean engineering* 111.2 (1985), pp. 216–234. DOI: 10.1061/(ASCE)0733-950X(1985)111:2(216).

[43] M. Ferrand and J.C. Harris. "Finite volume arbitrary Lagrangian-Eulerian schemes using dual meshes for ocean wave applications". In: *Computers & Fluids* 219 (2021), p. 104860. DOI: 10.1016/J.COMPFLUID.2021.104860.

[44] P. Ferrant, L. Gentaz, B. Alessandrini, and D. Le Touzé. "A potential/RANSE approach for regular water wave diffraction about 2-D structures". In: *Ship Technology Research* 50.4 (2003), pp. 165–171. DOI: 10.1179/str.2003.50.4.004.

[45] G. Fourtakas, P.K. Stansby, B.D. Rogers, S.J. Lind, S. Yan, and Q.W. Ma. "On the Coupling of Incompressible SPH With a Finite Element Potential Flow Solver for Nonlinear Free Surface Flows". In: vol. All Days. International Ocean and Polar Engineering Conference. June 2017.

[46] D. Fructus, D. Clamond, J. Grue, and O. Kristiansen. "An efficient model for three-dimensional surface wave simulations: Part I: Free space problems". In: *Journal of computational physics* 205.2 (2005), pp. 665–685. DOI: 10.1016/j.jcp.2004.11.027.

[47] D.R. Fuhrman, P.A. Madsen, and H.B. Bingham. "Numerical Simulation of Lowest-Order Short-Crested Wave Instabilities". In: *Journal of Fluid Mechanics* 563 (2006), pp. 415–441. DOI: 10.1017/S0022112006001236.

[48] I. Galparsoro, I. Menchaca, J.M. Garmendia, A. Borja, A.D. Maldonado, G. Iglesias, and J. Bald. "Reviewing the ecological impacts of offshore wind farms". In: *npj Ocean Sustainability* 1.1 (2022), p. 1. DOI: 10.1038/s44183-022-00003-5.

[49] R.A. Gingold and J.J. Monaghan. "Smoothed particle hydrodynamics: theory and application to non-spherical stars". In: *Monthly notices of the royal astronomical society* 181.3 (1977), pp. 375–389. DOI: 10.1093/MNRAS/181.3.375.

[50] J. Gong, S. Yan, Q. Ma, and Y. Li. "Added resistance and seakeeping performance of trimarans in oblique waves". In: *Ocean engineering* 216 (2020), p. 107721. DOI: 10.1016/j.oceaneng.2020.107721.

[51] J. Gong, S. Yan, Q. Ma, and Y. Li. "Numerical simulation of fixed and moving cylinders in focusing wave by a hybrid method". In: *International Journal of Offshore and Polar Engineering* 31.01 (2021), pp. 102–111. DOI: 10.17736/IJOPE.2021.JC812.

[52] L. Greengard and V. Rokhlin. "A fast algorithm for particle simulations". In: *Journal of computational physics* 73.2 (1987), pp. 325–348. DOI: 10.1016/0021-9991(87)90140-9.

[53] C.J. Greenshields. *OpenFOAM User Guide*. English. Version 11. The OpenFOAM Foundation. July 11, 2023.

[54] S.T. Grilli, P. Guyenne, and F. Dias. "A fully non-linear model for three-dimensional overturning waves over an arbitrary bottom". In: *International journal for numerical methods in fluids* 35.7 (2001), pp. 829–867. DOI: 10.1002/1097-0363(20010415)35:7<829::AID-FLD115>3.0.CO;2-2.

[55] S.T. Grilli, J. Skourup, and I.A. Svendsen. "An efficient boundary element method for nonlinear water waves". In: *Engineering Analysis with Boundary Elements* 6.2 (1989), pp. 97–107. DOI: 10.1016/0955-7997(89)90005-2.

[56] Joel Guerrero. *OpenFOAM advanced training. Moving meshes, rigid body motion, adaptive mesh refinement, and overset meshes*. Mar. 2022. DOI: 10.6084/m9.figshare.19310492.v1. URL: https://figshare.com/articles/presentation/OpenFOAM_advanced_training_Moving_meshes_rigid_body_motion_adaptive_mesh_refinement_and_overset_meshes/19310492.

[57] S. Guignard, S.T. Grilli, R. Marcer, and V. Rey. "Computation of shoaling and breaking waves in nearshore areas by the coupling of BEM and VOF methods". In: *ISOPE International Ocean and Polar Engineering Conference*. ISOPE. 1999, ISOPE–I.

[58] F.C.W. Hanssen, J.B. Helmers, M. Greco, and Y. Shao. "A 3D fully-nonlinear potential-flow solver for efficient simulations of large-scale free-surface waves". In: *International Journal for Numerical Methods in Engineering* (2022). DOI: 10.1002/nme.7115.

[59] F.H. Harlow and J.E. Welch. "Numerical Calculation of Time-Dependent Viscous Incompressible Flow of Fluid with Free Surface". In: *The physics of fluids* 8.12 (1965), pp. 2182–2189. DOI: 10.1063/1.1761178.

[60] J.C. Harris, E. Dombre, M. Benoit, S.T. Grilli, and K.I. Kuznetsov. "Nonlinear Time-Domain Wave-Structure Interaction: A Parallel Fast Integral Equation Approach". In: *International Journal for Numerical Methods in Fluids* 94.2 (2022), pp. 188–222. DOI: 10.1002/fld.5051.

[61] A. Harten. "High resolution schemes for hyperbolic conservation laws". In: *Journal of Computational Physics* 49.3 (1983), pp. 357–393. ISSN: 0021-9991. DOI: 10.1016/0021-9991(83)90136-5.

[62] K.F. Hasselmann, T.P. Barnett, E. Bouws, H.C. Carlson, D.E. Cartwright, K. Enke, J.A. Ewing, H. Gienapp, D.E. Hasselmann, P. Kruseman, A. Meerburg, P.M. Müller, D.J. Olbers, K. Richter, W. Sell, and H. Walden. "Measurements of wind-wave growth and swell decay during the Joint North Sea Wave Project (JONSWAP)". In: *Ergaenzungsheft zur Deutschen Hydrographischen Zeitschrift, Reihe A* (1973).

[63] P. Higuera. "Application of computational fluid dynamics to wave action on structures". PhD thesis. Universidad de Cantabria, 2015.

[64] P. Higuera, E. Buldakov, and D. Stagonas. "Numerical Modelling of Wave Interaction With an FPSO Using a Combination of OpenFOAM® and Lagrangian Models." In: *ISOPE International Ocean and Polar Engineering Conference*. ISOPE. 2018, ISOPE–I.

[65] P. Higuera, E. Buldakov, and D. Stagonas. "Simulation of steep waves interacting with a cylinder by coupling CFD and Lagrangian models". In: *International Journal of Offshore and Polar Engineering* 31.01 (2021), pp. 87–94. DOI: 10.17736/IJOPE.2021.JC821.

[66] P. Higuera, J.L. Lara, and I.J. Losada. "Realistic wave generation and active wave absorption for Navier–Stokes models: Application to OpenFOAM®". In: *Coastal Engineering* 71 (2013), pp. 102–118. DOI: 10.1016/J.COASTALENG.2012.07.002.

[67] P. Higuera, J.L. Lara, and I.J. Losada. "Simulating coastal engineering processes with OpenFOAM®". In: *Coastal Engineering* 71 (2013), pp. 119–134. DOI: 10.1016/J.COASTALENG.2012.06.002.

[68] C.W. Hirt and B.D. Nichols. "Volume of fluid (VOF) method for the dynamics of free boundaries". In: *Journal of Computational Physics* 39.1 (1981), pp. 201–225. DOI: 10.1016/0021-9991(81)90145-5.

[69] L.H. Holthuijsen. *Waves in oceanic and coastal waters*. Cambridge university press, 2010.

[70] A. Iafrati and E.F. Campana. "A domain decomposition approach to compute wave breaking (wave-breaking flows)". In: *International journal for numerical methods in fluids* 41.4 (2003), pp. 419–445. DOI: 10.1002/FLD.448.

[71] IEA. *Share of OECD gross electricity production by source, 1974-2020p*. Licence: CC BY 4.0. 2021. URL: https://www.iea.org/data-and-statistics/charts/share-of-oecd-gross-electricity-production-by-source-1974-2020p (visited on 09/25/2023).

[72] IEA. *World Energy Outlook 2022*. International Energy Agency, 2022. URL: https://www.iea.org/reports/world-energy-outlook-2022.

[73] R.I. Issa. "Solution of the Implicitly Discretised Fluid Flow Equations by Operator-Splitting". In: *Journal of computational physics* 62.1 (1986), pp. 40–65. DOI: 10.1016/0021-9991(86)90099-9.

[74] R.I. Issa, A.D. Gosman, and A.P. Watkins. "The Computation of Compressible and Incompressible Recirculating Flows by a Non-Iterative Implicit Scheme". In: *Journal of Computational Physics* 62.1 (1986), pp. 66–82. DOI: 10.1016/0021-9991(86)90100-2.

[75] N.G. Jacobsen, D.R. Fuhrman, and J. Fredsøe. "A Wave Generation Toolbox for the Open-Source CFD Library: OpenFoam®". In: *International Journal for numerical methods in fluids* 70.9 (2012), pp. 1073–1088. DOI: 10.1002/fld.2726.

[76] C.F. Janssen, M. Krafczyk, and S.T. Grilli. "Modeling of Wave Breaking and Wave-Structure Interactions by Coupling of Fully Nonlinear Potential Flow and Lattice-Boltzmann Models". In: *ISOPE International Ocean and Polar Engineering Conference*. ISOPE. 2010, ISOPE–I.

[77] H. Jasak. "Dynamic mesh handling in OpenFOAM". In: *47th AIAA aerospace sciences meeting including the new horizons forum and aerospace exposition*. 2009, p. 341. DOI: 10.2514/6.2009-341.

[78] H. Jasak. "Error Analysis and Estimation for the Finite Volume Method with Applications to Fluid Flows". PhD thesis. Imperial College, University of London, 1996.

[79] H. Jasak, A. Jemcov, and Ž. Tuković. "OpenFOAM: A C++ Library for Complex Physics Simulations". In: *International workshop on coupled methods in numerical dynamics*. Vol. 1000. 2007, pp. 1–20.

[80] S. Jin and D. Greaves. "Wave energy in the UK: Status review and future perspectives". In: *Renewable and Sustainable Energy Reviews* 143 (2021), p. 110932. DOI: 10.1016/J.RSER.2021.110932.

[81] S. Kim, M. Yamashiro, and A. Yoshida. "A simple two-way coupling method of BEM and VOF model for random wave calculations". In: *Coastal Engineering* 57 (2010), pp. 1018–1028. DOI: 10.1016/j.coastaleng.2010.06.006.

[82] C. Lachaume, B. Biausser, P. Fraunié, S.T. Grilli, and S. Guignard. "Modeling of breaking and post-breakingwaves on slopes by coupling of BEM and VOF methods". In: *ISOPE International Ocean and Polar Engineering Conference*. ISOPE. 2003, ISOPE–I.

[83] B. Li and C.A. Fleming. "A three dimensional multigrid model for fully nonlinear water waves". In: *Coastal Engineering* 30.3-4 (1997), pp. 235–258. DOI: 10.1016/S0378-3839(96)00046-4.

[84] Q. Li, J. Wang, S. Yan, J. Gong, and Q. Ma. "A zonal hybrid approach coupling FNPT with OpenFOAM for modelling wave-structure interactions with action of current". In: *Ocean Systems Engineering* 8 (2018), pp. 381–407. DOI: 10.12989/ose.2018.8.4.381.

[85] Y. Li, J. Lu, S. Yan, Q. Ma, W. Asnim, H. Sun, and Z. Sulaiman. "Numerical Simulation of Interaction Between Focusing Waves and Cylinder Using qaleFOAM". In: *International Journal of Offshore and Polar Engineering* 31.01 (2021), pp. 36–44. DOI: 10.17736/IJOPE.2021.JC811.

[86] Z. Li, B. Bouscasse, G. Ducrozet, L. Gentaz, D. Le Touzé, and P. Ferrant. "Spectral Wave Explicit Navier-Stokes Equations for wave-structure interactions using two-phase Computational Fluid Dynamics solvers". In: *Ocean Engineering* 221 (2021), p. 108513. DOI: 10.1016/j.oceaneng.2020.108513.

[87] H. Lin and S.N. Atluri. "The Meshless Local Petrov-Galerkin (MLPG) Method for Solving Incompressible Navier-Stokes Equations". In: *CMES-Computer Modeling in Engineering and Sciences* 2.2 (2001), pp. 117–142. DOI: 10.3970/CMES.2001.002.117.

[88] Z. Lin, H. Chen, L. Qian, Z. Ma, D. Causon, and C. Mingham. "Simulating focused wave impacts on point absorber wave energy converters". In: *Proceedings of the Institution of Civil Engineers-Engineering and Computational Mechanics* 174.1 (2021), pp. 19–31. DOI: 10.1680/JENCM.19.00038.

[89] Z. Lin, L. Qian, and W. Bai. "A coupled overset CFD and mooring line model for floating wind turbine hydrodynamics". In: *Proceedings of the 31st International Ocean and Polar Engineering Conference*. 2021.

[90] Z. Lin, L. Qian, W. Bai, Z. Ma, H. Chen, J. Zhou, and H. Gu. "A Finite Volume Based Fully Nonlinear Potential Flow Model for Water Wave Problems". In: *Applied Ocean Research* 106 (2021), p. 102445. DOI: 10.1016/j.apor.2020.102445.

[91] S.J. Lind, R. Xu, P.K. Stansby, and B.D. Rogers. "Incompressible smoothed particle hydrodynamics for free-surface flows: A generalised diffusion-based algorithm for stability and validations for impulsive flows and propagating waves". In: *Journal of Computational Physics* 231.4 (2012), pp. 1499–1523. DOI: 10.1016/j.jcp.2011.10.027.

[92] Y. Liu, M. Xue, and D.K.P. Yue. "Computations of fully nonlinear three-dimensional wave-wave and wave-body Interactions. Part 2. Nonlinear waves and forces on a body". In: *Journal of Fluid Mechanics* 438 (2001), pp. 41–66. DOI: 10.1017/S0022112001004384.

[93] M.S. Longuet-Higgins and E. Cokelet. "The deformation of steep surface waves on water-I. A numerical method of computation". In: *Proceedings of the Royal Society of London. A. Mathematical and Physical Sciences* 350.1660 (1976), pp. 1–26. DOI: 10.1098/rspa.1976.0092.

[94] X. Lu, D.D.J. Chandar, Y. Chen, and J. Lou. "An overlapping domain decomposition based near-far field coupling method for wave structure interaction simulations". In: *Coastal Engineering* 126 (2017), pp. 37–50. DOI: 10.1016/J.COASTALENG.2017.04.009.

[95] R. Luquet, P. Ferrant, B. Alessandrini, G. Ducrozet, and L. Gentaz. "Simulation of a TLP in Waves using the SWENSE scheme". In: *ISOPE International Ocean and Polar Engineering Conference*. ISOPE. 2007, ISOPE–I.

[96] Q.W. Ma, G.X. Wu, and R.E. Taylor. "Finite element simulation of fully non-linear interaction between vertical cylinders and steep waves. Part 1: methodology and numerical procedure". In: *International Journal for Numerical Methods in Fluids* 36.3 (2001), pp. 265–285. DOI: 10.1002/FLD.131.

[97] Q.W. Ma, G.X. Wu, and R.E. Taylor. "Finite element simulations of fully non-linear interaction between vertical cylinders and steep waves. Part 2: numerical results and validation". In: *International Journal for Numerical Methods in Fluids* 36.3 (2001), pp. 287–308. DOI: 10.1002/FLD.133.

[98] Q.W. Ma and S. Yan. "QALE–FEM for numerical modelling of non-linear interaction between 3D moored floating bodies and steep waves". In: *International Journal for Numerical Methods in Engineering* 78 (May 2009), pp. 713–756. DOI: 10.1002/nme.2505.

[99] Q.W. Ma and S. Yan. "Quasi ALE finite element method for nonlinear water waves". In: *Journal of Computational Physics* 212 (Feb. 2006), pp. 52–72. DOI: 10.1016/j.jcp.2005.06.014.

[100] Z.H. Ma, L. Qian, P.J. Martínez-Ferrer, D.M. Causon, C.G. Mingham, and W. Bai. "An overset mesh based multiphase flow solver for water entry problems". In: *Computers & Fluids* 172 (2018), pp. 689–705. DOI: 10.1016/J.COMPFLUID.2018.01.025.

[101] P.J. Martínez Ferrer, D.M. Causon, L. Qian, C.G. Mingham, and Z.H. Ma. "A multi-region coupling scheme for compressible and incompressible flow solvers for two-phase flow in a numerical wave tank". In: *Computers & Fluids* 125 (2016), pp. 116–129. DOI: 10.1016/J.COMPFLUID.2015.11.005.

[102] S. Mayer, A. Garapon, and L.S. Sørensen. "A fractional step method for unsteady free-surface flow with applications to non-linear wave dynamics". In: *International Journal for Numerical Methods in Fluids* 28.2 (1998), pp. 293–315. DOI: 10.1002/(SICI)1097-0363(19980815)28:2<293::AID-FLD719>3.0.CO;2-1.

[103] A. Mehmood, D.I. Graham, K. Langfeld, and D.M. Greaves. "Numerical Simulation of Nonlinear Water Waves based on Fully Nonlinear Potential Flow Theory in OpenFOAM-Extend". In: *Proceedings of the Twenty-sixth (2016) International Ocean and Polar Engineering Conference*. International Society of Offshore and Polar Engineers, 2016.

[104] A. Mola, L. Heltai, and A DeSimone. "A stable and adaptive semi-Lagrangian potential model for unsteady and nonlinear ship-wave interactions". In: *Engineering Analysis with Boundary Elements* 37.1 (2013), pp. 128–143. ISSN: 0955-7997. DOI: 10.1016/j.enganabound.2012.09.005.

[105] J.J. Monaghan. "Simulating Free Surface Flows with SPH". In: *Journal of Computational Physics* 110.2 (1994), pp. 399–406. DOI: 10.1006/JCPH.1994.1034.

[106] C Monroy, G Ducrozet, F Bonnefoy, A Babarit, L Gentaz, and P Ferrant. "RANS Simulations of a Calm Buoy in Regular and Irregular Seas using the SWENSE Method". In: *International Journal of Offshore and Polar Engineering (IJOPE)* 21.4 (2011), pp. 264–271.

[107] C/ Monroy, G/ Ducrozet, P. Roux de Reilhac, L. Gentaz, P. Ferrant, and B. Alessandrini. "RANS Simulations of Ship Motions In Regular And Irregular Head Seas Using the SWENSE Method". In: *The Nineteenth International Offshore and Polar Engineering Conference*. OnePetro. 2009.

[108] United Nations. *Paris Agreement*. 2015. URL: https://treaties.un.org/Pages/ViewDetails.aspx?src=TREATY&mtdsg_no=XXVII-7-d&chapter=27&clang=_en (visited on 09/26/2023).

[109] N.M. Newmark. "A method of computation for structural dynamics". In: *Journal of the engineering mechanics division* 85.3 (1959), pp. 67–94. DOI: 10.1061/TACEAT.0008448.

[110] D.Z. Ning, B. Teng, R.E. Taylor, and J. Zang. "Numerical simulation of non-linear regular and focused waves in an infinite water-depth". In: *Ocean Engineering* 35.8-9 (2008), pp. 887–899. DOI: 10.1016/j.oceaneng.2008.01.015.

[111] D.Z. Ning, J. Zang, S.X. Liu, R.E. Taylor, B. Teng, and P.H. Taylor. "Free-surface evolution and wave kinematics for nonlinear uni-directional focused wave groups". In: *Ocean Engineering* 36.15-16 (2009), pp. 1226–1243. DOI: 10.1016/j.oceaneng.2009.07.011.

[112] S. Osher and J.A. Sethian. "Fronts Propagating with Curvature-Dependent Speed: Algorithms Based on Hamilton-Jacobi Formulations". In: *Journal of computational physics* 79.1 (1988), pp. 12–49. DOI: 10.1016/0021-9991(88)90002-2.

[113] B.T. Paulsen, H. Bredmose, and H.B. Bingham. "An efficient domain decomposition strategy for wave loads on surface piercing circular cylinders". In: *Coastal Engineering* 86 (2014), pp. 57–76. DOI: 10.1016/J.COASTALENG.2014.01.006.

[114] A. Pecher and J.P. Kofoed. *Handbook of Ocean Wave Energy*. Springer Nature, 2017. DOI: 10.1007/978-3-319-39889-1.

[115] C. Pérez-Collazo, D. Greaves, and G. Iglesias. "A review of combined wave and offshore wind energy". In: *Renewable and sustainable energy reviews* 42 (2015), pp. 141–153. DOI: 10.1016/J.RSER.2014.09.032.

[116] W.J. Pierson Jr and L. Moskowitz. "A proposed spectral form for fully developed wind seas based on the similarity theory of SA Kitaigorodskii". In: *Journal of geophysical research* 69.24 (1964), pp. 5181–5190. DOI: 10.1029/JZ069I024P05181.

[117] E.J. Ransley, S.A. Brown, M. Hann, D.M. Greaves, C. Windt, J. Ringwood, J. Davidson, P. Schmitt, S. Yan, J.X. Wang, J. Wang, Q. Ma, Z. Xie, G. Giorgi, J. Hughes, A.J. Williams, I. Masters, Z. Lin, H. Chen, L. Qian, Z. Ma, Q. Chen, H. Ding, J. Zang, J. van Rij, Y. Yu, Z. Li, B. Bouscasse, G. Ducrozet, and H.B. Bingham. "Focused wave interactions with floating structures: A blind comparative study". In: *Proceedings of the Institution of Civil Engineers-Engineering and Computational Mechanics* 174.1 (2021), pp. 46–61. DOI: 10.1680/JENCM.20.00006.

[118] E.J. Ransley, S. Yan, S.A. Brown, M.R. Hann, D.I. Graham, C. Windt, P. Schmitt, J. Davidson, J.V. Ringwood, P. Musiedlak, J. Wang, J.X. Wang, Q. Ma, Z. Xie, N. Zhang, X. Zheng, G. Giorgi, H. Chen, Z. Lin, L. Qian, Z. Ma, W. Bai, Q. Chen, J. Zang, H. Ding, L. Cheng, J. Zheng, H. Gu, X. Gong, Z. Liu, Z. Yuan, D. Wan, H.B. Bingham, and D.M. Greaves. "A Blind Comparative Study of Focused Wave Interactions with Floating Structures (CCP-WSI Blind Test Series 3)". In: *International Journal of Offshore and Polar Engineering* 30.01 (2020), pp. 1–10. DOI: 10.17736/ijope.2020.jc774.

[119] H. Rusche. "Computational Fluid Dynamics of Dispersed Two-Phase Flows at High Phase Fractions". PhD thesis. Imperial College London (University of London), 2003.

[120] S. Salter. "Wave power". In: *Nature* 249.5459 (1974), pp. 720–724. DOI: 10.1038/249720a0.

[121] A. Savitzky and M.J.E. Golay. "Smoothing and differentiation of data by simplified least squares procedures". In: *Analytical chemistry* 36.8 (1964), pp. 1627–1639. DOI: 10.1021/AC60319A045.

[122] E. Serin, P. Andres, R. Martin, A. Shah, and A. Valero. *Seizing sustainable growth opportunities from tidal stream energy in the UK*. London School of Economics and Political Science, 2023. URL: https://www.lse.ac.uk/granthaminstitute/publication/seizing-sustainable-growth-opportunities-from-tidal-stream-energy-in-the-uk/.

[123] Y. Shao and O. Faltinsen. "A harmonic polynomial cell (HPC) method for 3D Laplace equation with application in marine hydrodynamics". In: *Journal of Computational Physics* 274 (2014), pp. 312–332. DOI: 10.1016/j.jcp.2014.06.021.

[124] Y. Shao, Z. Zheng, H. Liang, and J. Chen. "A consistent second-order hydrodynamic model in the time domain for floating structures with large horizontal motions". In: *Computer-Aided Civil and Infrastructure Engineering* (2022). DOI: 10.1111/mice.12782.

[125] V Sriram, T Schlurmann, and S Schimmels. “Focused wave evolution using linear and second order wavemaker theory”. In: *Applied Ocean Research* 53 (2015), pp. 279–296. DOI: 10.1016/J.APOR.2015.09.007.

[126] V. Sriram, S. Agarwal, and T. Schlurmann. “Laboratory study on steep wave interactions with fixed and moving cylinder”. In: *International Journal of Offshore and Polar Engineering* 31.01 (2021), pp. 19–26. DOI: 10.17736/IJOPE.2021.JC808.

[127] V. Sriram, S. Agarwal, S. Yan, .Z. Xie, S. Saincher, T. Schlurmann, Q. Ma, T. Stoesser, Y. Zhuang, B. Han, et al. “A comparative study on the nonlinear interaction between a focusing wave and cylinder using state-of-the-art solvers: Part A”. In: *International Journal of Offshore and Polar Engineering* 31.01 (2021), pp. 1–10. DOI: 10.17736/IJOPE.2021.JC820.

[128] V. Sriram, Q.W. Ma, and T. Schlurmann. “A hybrid method for modelling two dimensional non-breaking and breaking waves”. In: *Journal of Computational Physics* 272 (2014), pp. 429–454. DOI: 10.1016/j.jcp.2014.04.030.

[129] G.G. Stokes. “On the theory of oscillatory waves”. In: *Trans Cambridge Philos Soc* 8 (1847), pp. 441–473.

[130] P.K. Sweby. “High Resolution Schemes Using Flux Limiters for Hyperbolic Conservation Laws”. In: *SIAM journal on numerical analysis* 21.5 (1984), pp. 995–1011. DOI: 10.1137/0721062.

[131] P.S. Tromans, A.R. Anaturk, and P. Hagemeijer. “A new model for the kinematics of large ocean waves-application as a design wave”. In: *ISOPE International Ocean and Polar Engineering Conference*. ISOPE. 1991, ISOPE–I.

[132] O. Ubbink. “Numerical prediction of two fluid systems with sharp interfaces”. PhD thesis. Imperial College, University of London, 1997.

[133] U.K. Verfuss, R.R. Sinclair, and C. Sparling. *A review of noise abatement systems for offshore wind farm construction noise, and the potential for their application in Scottish waters*. Scottish Natural Heritage, 2019.

[134] H. Wang, C. Huang, and J. Wu. “Simulation of a 3D Numerical Viscous Wave Tank”. In: *Journal of Engineering Mechanics* 133.7 (2007), pp. 761–772. DOI: 10.1061/(ASCE)0733-9399(2007)133:7(761).

[135] J. Wang and Q.W. Ma. “Numerical techniques on improving computational efficiency of spectral boundary integral method”. In: *International Journal for Numerical Methods in Engineering* 102.10 (2015), pp. 1638–1669. DOI: 10.1002/nme.4857.

[136] J. Wang, S. Yan, Q. Ma, J. Wang, Z. Xie, and S. Marran. “Modelling of focused wave interaction with wave energy converter models using qaleFOAM”. In: *Proceedings of the Institution of Civil Engineers-Engineering and Computational Mechanics* 173.3 (2020), pp. 100–118. DOI: 10.1680/JENCM.19.00035.

[137] W. Wang, A. Kamath, C. Pakozdi, and H. Bihs. "Investigation of focusing wave properties in a numerical wave tank with a fully nonlinear potential flow model". In: *Journal of Marine Science and Engineering* 7.10 (2019), p. 375. DOI: 10.3390/jmse7100375.

[138] W. Wang, C. Pákozdi, A. Kamath, T. Martin, and H. Bihs. "Hydrodynamic Coupling of Viscous and Nonviscous Numerical Wave Solutions Within the Open-Source Hydrodynamics Framework REEF3D". In: *Journal of Offshore Mechanics and Arctic Engineering* 144.4 (2022), p. 041903. DOI: 10.1115/omae2021-62185.

[139] H.G. Weller. *A new approach to VOF-based interface capturing methods for incompressible and compressible flow*. Tech. rep. 2008.

[140] H.G. Weller. *Derivation Modelling and Solution of the Conditionally Averaged Two-Phase Flow Equations*. Tech. rep. TR/HGW/02. 2002.

[141] H.G. Weller, G. Tabora, H. Jasak, and C. Fureby. "A tensorial approach to computational continuum mechanics using object-oriented techniques". In: *Computers in physics* 12.6 (1998), pp. 620–631. DOI: 10.1063/1.168744.

[142] J. Westphalen, D.M. Greaves, C.J.K. Williams, A.C. Hunt-Raby, and J. Zang. "Focused waves and wave-structure interaction in a numerical wave tank". In: *Ocean Engineering* 45 (2012), pp. 9–21. DOI: 10.1016/J.OCEANENG.2011.12.016.

[143] R.W. Whalin. *The Limit of Applicability of Linear Wave Refraction Theory in a Convergence Zone*. Tech. rep. ARMY ENGINEER WATERWAYS EXPERIMENT STATION VICKSBURG MISS, 1971.

[144] G.X. Wu and R.E. Taylor. "Finite element analysis of two-dimensional non-linear transient water waves". In: *Applied Ocean Research* 16 (1994), pp. 363–372. DOI: 10.1016/0141-1187(94)00029-8.

[145] M. Xue, H. Xü, Y. Liu, and D.K.P. Yue. "Computations of fully nonlinear three-dimensional wave-wave and wave-body interactions. Part 1. Dynamics of steep three-dimensional waves". In: *Journal of Fluid Mechanics* 438 (2001), pp. 11–39. DOI: 10.1017/S0022112001004396.

[146] S. Yan and Q. Ma. "A hybrid approach coupling MLPG-R with QALE-FEM for modelling fully nonlinear water waves". In: *The 27th International Ocean and Polar Engineering Conference*. OnePetro. 2017.

[147] S. Yan, Q. Ma, W. Asnim, Z. Sulaiman, and H. Sun. "Comparative study on focusing wave interaction with cylinder using QALE-FEM and qaleFOAM". In: *The 30th International Ocean and Polar Engineering Conference*. OnePetro. 2020.

[148] S. Yan and Q.W. Ma. "Numerical simulation of fully nonlinear interaction between steep waves and 2D floating bodies using the QALE-FEM method". In: *Journal of Computational physics* 221.2 (2007), pp. 666–692. DOI: 10.1016/j.jcp.2006.06.046.

[149] S. Yan, Q.W. Ma, and J. Wang. "Quadric SFDI for Laplacian Discretisation in Lagrangian Meshless Methods". In: *Journal of Marine Science and Application* 19 (2020), pp. 362–380. DOI: 10.1007/s11804-020-00159-x.

[150] S. Yan, J. Wang, J. Wang, Q.W Ma, and Z. Xie. "Numerical simulation of wave structure interaction using QaleFOAM". In: *The 29th International Ocean and Polar Engineering Conference*. OnePetro. 2019.

[151] Z. Yu, X. Zheng, H. Hao, S. Yan, and Q. Ma. "Numerical Simulation of a Floating Offshore Wind Turbine in Waves Using qaleFOAM". In: *International Journal of Offshore and Polar Engineering* 32.01 (2022), pp. 39–48. DOI: 10.17736/ijope.2022.jc841.

[152] N. Zhang, S. Yan, X. Zheng, and Q. Ma. "A 3D Hybrid Model Coupling SPH and QALE-FEM for Simulating Nonlinear Wave-structure Interaction". In: *International Journal of Offshore and Polar Engineering* 30.01 (2020), pp. 11–19. DOI: 10.17736/ijope.2020.jc776.

[153] X. Zhao and C. Hu. "Numerical and Experimental Study on a 2-D Floating Body Under Extreme Wave Conditions". In: *Applied Ocean Research* 35 (2012), pp. 1–13. DOI: 10.1016/J.APOR.2012.01.001.

[154] B.Z. Zhou, G.X. Wu, and B. Teng. "Fully nonlinear wave interaction with freely floating non-wall-sided structures". In: *Engineering Analysis with Boundary Elements* 50 (2015), pp. 117–132. DOI: 10.1016/J.ENGANABOUND.2014.08.003.

A

Publications

- Ranjodh Rai, Zhihua Ma, Zaibin Lin, Wei Bai and Ling Qian. A stable free-surface boundary solution method for fully nonlinear potential flow models. *Applied Ocean Research* 134 (2023) 103500. doi:10.1016/j.apor.2023.103500.
- Ranjodh S. Rai, Zhihua Ma, Ling Qian, Wei Bai, Zaibin Lin, Anatoliy Khait. A New Integrated Finite Volume–Finite Volume Numerical Model for Wave-Structure Interactions. *Proceedings of the ASME 2023 42nd International Conference on Ocean, Offshore and Arctic Engineering.* Melbourne, Australia. June 11–16, 2023. doi:10.1115/OMAE2023-103590.